Enhancing Molecular Dynamics Simulations: From Trajectories to Reaction Rates

Inaugural-Dissertation
to obtain the academic degree

Doctor rerum naturalium (Dr. rer. nat.)

Submitted to the Department of Biology, Chemistry, Pharmacy of Freie Universität Berlin
by
Simon-Viktor Ghysbrecht

Berlin 2024

The research of this thesis was carried out between October 2018 and November 2024 under the supervision of Prof. Dr. Bettina Keller at the Institute of Chemistry and Biochemistry at Freie Universität Berlin.

First reviewer:
Prof. Dr. Bettina G. Keller
Department of Biology, Chemistry and Pharmacy
Physical & Theoretical Chemistry
Freie Universität Berlin

Second reviewer:
Prof. Dr. Beate Paulus
Department of Biology, Chemistry and Pharmacy
Physical & Theoretical Chemistry
Freie Universität Berlin

Date of defense: 05.02.2025

ACKNOWLEDGEMENTS

I would like to express my deepest gratitude to my supervisor, Prof. Dr. Bettina Keller, for giving me the opportunity to pursue my doctoral studies in her research group. I am immensely grateful for the mentorship and guidance she provided throughout my time there. Her scientific support, ability to provide clear direction for projects, and skillful leadership over the research group have greatly impressed me.

I would like to thank Prof. Dr. Beate Paulus for being my second reviewer, for her helpful scientific and non-scientific advice, and for the welcoming and supportive environment she fostered within the theoretical chemistry groups.

My sincere appreciation goes to the Keller group. I had many engaging scientific discussions with Dr. Luca Donati and Dr. Stefanie Kieninger, all of which greatly advanced my work. I also want to thank all other group members for creating such a comfortable work environment—I could not have asked for better colleagues.

A heartfelt thank you goes out to my friends, both in Berlin and in Belgium, for making these last years so enjoyable. Last but not least, I would like to thank my family, and especially my mother, for their unwavering support throughout my life in general and my doctoral studies specifically.

DECLARATION OF INDEPENDENCE

Herewith I certify that I have prepared and written my thesis independently and that I have not used any sources and aids other than those indicated by me.

ABSTRACT

Advanced methods for estimating reaction rates of rare events in molecular dynamics (MD) simulations are crucial for molecular processes like chemical reactions, nucleation, and protein folding. These processes commonly involve high energy barriers, making them infrequent and challenging to capture with conventional MD due to long waiting times. Some rare event methods apply enhanced sampling techniques where potential energy functions are biased to accelerate molecular transitions. In this thesis, different rare event methods employing enhanced sampling are introduced, applied and compared. A first case study focuses on thermal cis-trans isomerization of retinal, a crucial process in opsins involved in biological light responses. The enormous disparity between accessible simulation times (nanoseconds to microseconds depending on level of theory) and actual reaction times (hours to days) requires careful application of rate theories. Results from rare event methods based in both numerical sampling of transitions and effective dynamics were compared to results from transition state optimization followed by application of Eyring's transition state theory (TST). Numerical sampling, enabled by infrequent metadynamics simulation, yielded rates in good agreement with Eyring's TST, especially when the classical limit was enforced. Methods based in effective dynamics proved highly sensitive to the choice of reaction coordinate. Only after optimizing the reaction coordinate using adaptive path collective variables did rates approximate those from Eyring's TST well. Additionally, the thesis explores dynamical reweighting techniques, particularly Girsanov reweighting, to recover kinetics and reaction dynamics from biased simulations. Girsanov reweighting factors were derived for a number of integrators for underdamped Langevin dynamics. The reweighting factors were subsequently tested for a $[\text{Ca-Cl}]^+$ dimer system. The dissociation rates obtained from biased trajectories successfully estimated reference rates for the unbiased system, demonstrating the effectiveness of these methods for accurately recovering reaction dynamics as well as their potential for future reaction dynamics studies.

ZUSAMMENFASSUNG

Fortgeschrittene Methoden zur Abschätzung der Reaktionsraten von Rare-Events in molekulardynamischen (MD) Simulationen sind entscheidend für molekulare Prozesse wie chemische Reaktionen, Keimbildung und Proteinfaltung. Diese Prozesse beinhalten häufig hohe Aktivierungsenergien, wodurch sie selten auftreten und mit konventioneller MD aufgrund langer Wartezeiten schwer erfasst werden können. Einige Rare-Event-Methoden verwenden Enhanced-Sampling-MD-Simulationen, bei denen potentielle Energiefunktionen verzerrt werden, um molekulare Übergänge zu beschleunigen. In dieser Arbeit werden verschiedene Rare-Event-Methoden, die Enhanced-Sampling-MD-Simulationen nutzen, vorgestellt, angewendet und verglichen. Eine erste Fallstudie konzentriert sich auf die thermische Cis-Trans-Isomerisierung von Retinal, einem wichtigen Prozess in Opsinen, der an biologischen Lichtreaktionen beteiligt ist. Die enorme Diskrepanz zwischen zugänglichen Simulationszeiten (Nanosekunden bis Mikrosekunden, je nach Theorieebene) und tatsächlichen Reaktionszeiten (Stunden bis Tage) erfordert den sorgfältigen Einsatz von Reaktionsgeschwindigkeitstheorie. Ergebnisse von Rare-Event-Methoden, die sowohl auf numerischer Simulationen von Übergängen als auch auf effektiver Dynamik basieren, wurden mit Ergebnissen der Übergangszustandsoptimierung gefolgt von der Anwendung der Theorie des Übergangszustandes von Eyring verglichen. Die numerischen Übergangssimulationen, ermöglicht durch Infrequent-Metadynamics Simulationen, ergaben Raten, die gut mit der Eyring-Theorie übereinstimmten, insbesondere wenn das klassische Limit berücksichtigt wurde. Methoden, die auf effektiver Dynamik basieren, erwiesen sich als äußerst empfindlich gegenüber der Wahl der Reaktionskoordinate. Erst nach Optimierung der Reaktionskoordinate mittels adaptiver Pfadkollektivvariablen näherten sich die Raten gut den Ergebnissen der Eyring-Theorie an. Zusätzlich untersucht die Arbeit dynamische Rückgewichtungstechniken, insbesondere die Girsanov-Rückgewichtung, um Kinetiken und Reaktionsdynamiken aus verzerrten Simulationen wiederherzustellen. Girsanov-Rückgewichtungsfaktoren wurden für eine Reihe von Integratoren für unterdämpfte Langevin-Dynamik abgeleitet. Die Rückgewichtungs-faktoren wurden anschließend an einem $[\text{Ca-Cl}]^+$-Dimer-System getestet. Die aus den verzerrten Trajektorien gewonnenen Dissoziationsraten ergaben eine erfolgreiche Schätzung der Referenzraten für

das unverzerrte System und demonstrierten die Wirksamkeit dieser Methoden zur genauen Wiederherstellung der Reaktionsdynamik sowie ihr Potenzial für zukünftige Studien zur Reaktionsdynamik.

Contents

Chapter 1

Introduction

1.1 Background and Motivation

Computer Simulations Computer simulations play a pivotal role in natural science across many disciplines. In their core, simulations strive to faithfully replicate real-world physical processes. Their use extends far beyond mere replication, however, as they grant the extraordinary ability to exercise absolute and independent control over all variables, transcending the limitations of traditional experiments and reducing the need for costly laboratory equipment. Still, the computational cost of the simulations can pose limitations, often depending on factors such as the size of the system, the timescale of the simulation and the computational resources available. To make modeling practically feasible, simulations generally require abstractions and simplifications in description of the physical phenomena. The accuracy of a simulation heavily relies on the quality of the underlying mathematical models and assumptions. If these models are inaccurate or incomplete, the simulation results may not reflect reality in a reliable way. Therefore, one of the main tasks of computational scientists is estimating the validity of the models used for specific applications. Researchers continue to improve the simulation methods available, as well as the tools to analyse the generated data.

Molecular Dynamics Molecular dynamics (MD) are computer simulations of the movement and interactions of molecular systems specifically[1, 2]. By numerically solving the equations of motion for all the constituent atoms or particles in a system, a trajectory describing the molecular motion is attained[3]. Such a trajectory can essentially be considered a movie of how the molecule behaves in time. Getting quantitative predictions on molecular processes from these trajectories, however, warrants a meticulous statistical analysis of the trajectory data[4]. More specifically, dynamical trajectories are often used to sample probability distributions of configurations or events. In this way, one is able to devise meaningful assessments of molecular structures, thermodynamic properties or dynamics of the simulated (bio)molecular systems[5].

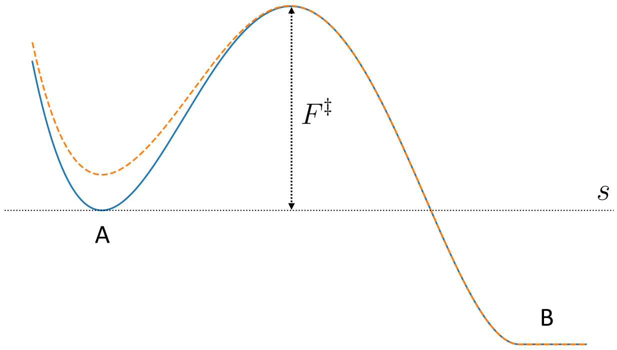

Figure 1.1: Energy scheme of an activated process, with reactant state A, product state B and activation energy barrier $F^{\ddagger}$ along a reaction coordinate s. The effective energy profile along s is shown in blue, while an example of a biased energy profile is shown in orange.

Rate Theories Of special interest in chemistry or physics are activated processes which require a relatively large activation energy to transpire. Typical examples include chemical reactions, nucleation processes or protein folding. The requirement to overcome the activation energy makes these processes relatively rare, which is why they are also referred to as rare events. Peters[6] remarked that rare events are not truly rare in the conventional sense of the word, as in principle, they happen around us all the time. The actual interpretation of rare events is that their rates are slow relative to other relaxation processes in the same systems. In other words, the system moves around within a reactant state A for a long time before 'suddenly' moving to a product state B, with the time it takes to transition from A to B once the transition is initiated being a lot shorter than the waiting time in A (Fig. 1.1). Small and inconsequential fluctuations away from equilibrium within reactant state A during this waiting time relax at much smaller timescales than the total time it takes before transitioning to B [4, 7]. For small proteins, for example, transition from an unfolded state A to a folded state B typically occurs on the order of microseconds (10^{-6} s) to milliseconds (10^{-3} s), while intramolecular vibrations within either the folded or unfolded states happen on the order of femtoseconds (10^{-15} s) to picoseconds (10^{-12} s). For larger and more complex proteins, it may require seconds to minutes or even hours to fold properly. In the context of molecular dynamics simulations, a rare event is usually understood as an event where the waiting time is too long for direct simulation. Extracting rates from MD simulations for these events is considered a complicated challenge, as the processes of interest are too infrequent to obtain sufficient statistics from straightforward unbiased simulation. Rate theories and rare event methods have been developed to estimate rates while avoiding the need for direct simulation of rare events[6,8]. Leveraging the time scale separation between waiting times and transition events, these methods enable computation of rates without fully simulating the long waiting periods. Different rate theories facilitate calculation of rates starting from information obtained a priori by other computational methods, such as saddle

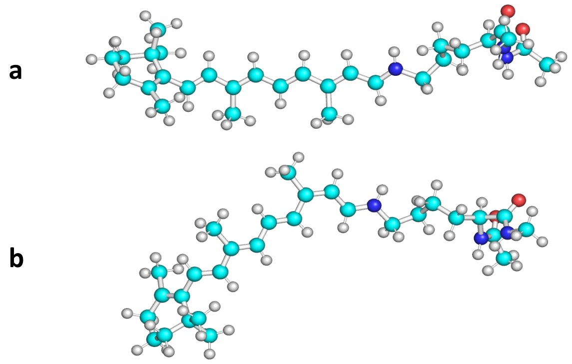

Figure 1.2: Configurations of the retinal cofactor connected to a lysine dipeptide. Configurations correspond to different isomerization states around the $C_{13}{=}C_{14}$ double bond; **a:** trans and **b:** cis. These can be considered reactant state A and product state B in thermal trans-cis isomerization (Fig. 1.1) or vice versa for cis-trans isomerization. Different rate theories were compared for isomerization rates, and an analysis of the reaction coordinate was performed.

point search[9, 10], computation of free energy surfaces[11], optimizing minimum free energy paths[12, 13] or converging reactive trajectories[7, 14]. Selecting the most suitable rare event method for a particular application is a difficult task. One of the main goals of this work is to evaluate different rare event methods for processes involving high activation energies. In particular, the thermal cis-trans isomerization in retinal compounds is studied as a model case.

Thermal Isomerization of Retinal Retinal is a polyene chromophore that functions as the key cofactor within the protein class known as opsins[15]. These proteins play an important role in many biological processes involving light, including in vision of higher life forms and in phototaxis of bacteria. The primary mechanism through which retinal engages with light involves a cis-trans isomerization event occurring over one of its double bonds within the polyene chain[16] (Fig. 1.2). This molecular transition underpins the photosensitive nature of opsins, enabling them to initiate key physiological responses upon exposure to light stimuli. Whereas the initial isomerization event is governed by photo-excitation, the full mechanism generally involves a return to the original state by a thermal back-isomerization step. Thermal isomerization is a rare event with a very large activation barrier[17, 18], with expected time scales of seconds to minutes or hours[19–21]. In this thesis, different rate theories are evaluated with regards to their ability to calculate thermal isomerization rates starting from MD simulations of the retinal compound. This constitutes a significant challenge, as the achievable simulation times are often many orders of magnitude lower than the actual reaction times. Of special interest is the assessment of the reaction mechanism, and closely related, the definition of a suitable reaction coordinate.

Dynamical Reweighting One strategy to investigate reaction mechanisms and estimate rates for rare events while avoiding long waiting times is to use enhanced sampling tech-

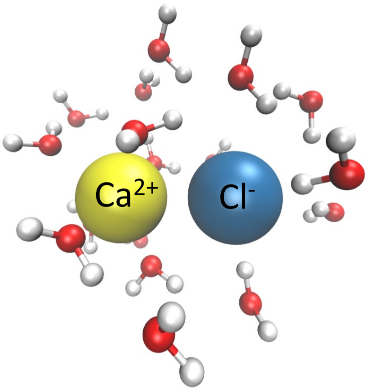

Figure 1.3: $[\text{Ca-Cl}]^+$ dimer in water. This system was used to test path reweighting for rate calculation by computing dissociation rates from the bounded state (A) to an unbounded state (B) with and without application of a bias to the reactant state (similar as in Fig. 1.1).

niques that apply a biasing force to artificially push the system out of the reactant state (Fig. 1.1). Many methods that bias the potential energy surface in MD simulations have been developed[1, 11]. While most of these methods focus on exploring new configurations, recent approaches increasingly seek to recover kinetics and reaction dynamics from the biased trajectories[22]. Dynamical reweighting techniques use statistical reweighting to correct the effects of the bias applied during sampling, allowing accurate estimation of unbiased dynamical properties such as reaction rates and transition times.

Path Reweighting Girsanov reweighting[23] is a dynamical reweighting technique that intends to express relative probabilities for a path generated at a biased potential to happen at the unbiased potential. Formulations of the path probability ratios depend on the choice of integrator used to generate the paths[22]. When dynamical paths have been sufficiently sampled, relative path probability ratios can reweight dynamic properties from biased simulations. This has the ability to considerably speed up sampling of reactive trajectories and calculate corresponding reaction rates. For the Euler-Maruyama integrator for overdamped Langevin dynamics, the path probability ratio has already been described[24–27]. Part of the work in this thesis focuses on expressing path probability ratios for different integrators for underdamped Langevin dynamics. The formulations for different integrators are subsequently tested on a simple molecular system consisting of a $[\text{Ca-Cl}]^+$ dimer in water (Fig. 1.3). Dissociation rates are calculated from trajectories sampled on a biased potential using dynamical reweighting, and compared to rates obtained from unbiased reference trajectories.

1.2 Research Questions and Structure

Eyring's Transition State Theory[28] (TST) remains the most widely used rate theory for estimating reaction rates, especially for processes with high activation energies. It's success lies in requiring only the free energy barrier and partition functions of reactant and transition state configurations[6], which can be computed with relatively low computational effort, without detailed molecular trajectories. Recent advancements in reactive force fields[29], neural network potentials[30], semi-empirical electronic structure methods[31–33] and QM/MM approaches[34] have made it increasingly feasible to simulate chemical reactions using molecular dynamics. By combining rate theory with enhanced sampling techniques, reaction rates can be estimated even for reactions with high energy barriers and complex mechanisms. However, moving from Eyring TST to MD-based rate estimates requires a fundamental shift in the theoretical framework through which the reaction is modeled. Consequently, it is essential to evaluate the applicability and performance of these different approaches. This thesis explores whether reaction dynamics of processes with high energy barriers can be accurately studied from trajectories generated with enhanced sampling techniques. The central research question is:

Can MD simulations combined with enhanced sampling techniques yield accurate rate constants for processes with high activation energies?

To address this question, the thermal cis-trans isomerization of retinal is used as a test system. Rate estimates obtained from enhanced sampling methods are compared with those from TST. Additionally, dynamical reweighting techniques are examined as a means to recover unbiased reaction dynamics from biased trajectories. Specifically, path reweighting is extended to integrators for underdamped Langevin dynamics and tested on a model system consisting of a $[\text{Ca-Cl}]^+$ dimer in water.

The structure of the thesis is as following. Chapter 1 introduces the central topics and outlines the structure of the thesis. Chapter 2 presents the most important theoretical concepts, including a brief overview of molecular dynamics (Section 2.1), an introduction to key enhanced sampling methods such as umbrella sampling and metadynamics (Section 2.2), an overview of the rate methods utilized in this thesis (Section 2.3), and an introduction to dynamical reweighting methods (Section 2.4). Chapter 3 presents the results of this thesis, including three papers. Additionally, a supporting information section is incorporated containing unpublished results. A short summary is given here, including more detailed research questions for each section:

Part A Reaction Mechanisms and Rates for Thermal Isomerization of Retinal

Paper A1: In this paper, rate constants and reaction mechanisms for thermal isomerization of retinal are investigated for two retinal analogues using ab-initio MD, where the self-consistent-charge Density functional tight-binding (DFTB) method is used to model the potential energy surface. Density Functional Theory (DFT) is used as a reference. We address the research questions:

1. How do rate constants compare between potential energy surfaces obtained from DFT and DFTB?
2. How do rate constants estimated from dynamical sampling compare to those from Eyring's transition state theory?

Paper A2: In this paper the reaction mechanism of thermal isomerization and the applicability of different rate theories is studied in more detail. Rate theories are first tested for a one-dimensional model potential and subsequently for a model retinal system using a classical force field. The research questions are:

1. How do rates from effective dynamics compare to rates from numerical sampling in one-dimensional model potentials?
2. How do rates from effective dynamics compare to rates from numerical sampling for thermal cis-trans isomerization in a retinal system modeled by a force field?
3. What is the influence of the choice of reaction coordinate?

Part B Path Reweighting for Underdamped Langevin Dynamics

Paper B1: In this paper, relative path probabilities for Girsanov reweighting in integrators from splitting methods for underdamped Langevin dynamics are derived. The following research questions are treated:

1. Can we formulate a general approach to predict whether the relative path probability for Langevin integrators from splitting methods obeys absolute continuity?
2. Can we formulate a general approach to derive the associated relative path probability?

Supporting Information for Part B: In this section, the reweighting factors derived above are tested numerically for dissociation rates of a $[\text{Ca-Cl}]^+$ dimer in water. Rates from biased simulations are compared to reference rates obtained from simulations at the unbiased potential.

Finally, Chapter 4 concludes the thesis and provides an outlook on potential future research directions.

Chapter 2

Theory

2.1 Molecular Dynamics

Obtaining access to the microscopic details of molecular motion enables a profound understanding of the processes these molecules are involved in. Given sufficient data are available, statistical mechanics theory can be used to generalize many microscopic events to macroscopic phenomena, and thus yields a definite connection between the microscopic and macroscopic world. Such connection is of high interest in many fields of application, including drug design, catalysis, material science and condensed-state physics. Whereas experimental detection of microscopic motion is challenging or often unattainable, computer simulations have made their introduction in modeling the dynamics of atoms and molecules[2, 3, 6].

Atoms and especially the particles they consist of are inherently quantum-mechanical in nature. A highly accurate description of molecules and the way they interact thus warrants application of the quantum mechanical laws of motion. However, while the field of quantum dynamics is an intense and fruitful area of research, solving the relevant equations remains a challenging task[5, 35]. Simulation methods developed to do so are generally computationally expensive to a degree that becomes prohibitive for larger systems. This is especially true when longer simulation times are required to obtain sufficient statistics on configurational prevalence as well as on conversions between them.

The Born-Oppenheimer (BO) approximation[5, 35, 36] takes advantage of the fact that the mass of the electron is much smaller than the mass of any of the nuclei to assume the electrons in a system move instantaneously and are entirely dependent on the motion of the nuclei. This approximation allows for separation of the electronic and nuclear degrees of freedom, enabling a more manageable analysis of the system. The electronic energy, also called the BO energy, is expressed as a function of the coordinates of the nuclei similar to a classical potential energy surface (PES). Using Ehrenfest's theorem[5, 35], the movement of molecules can then be modeled classically on this PES according to Newton's equations of motion.

Moving to a classical scheme evidently means dynamics become approximate as quantum effects get ignored. However, these effects generally only play a very minor role for atoms heavier than hydrogen. In fact, the classical nuclei approximation is anticipated to remain reasonably accurate even for hydrogen as long as no chemical bond is formed or broken[5].

2.1.1 Hamiltonian Dynamics

In classical mechanics, Newton's equations of motion are often reformulated into the Hamiltonian framework[37]. For a molecular system where N atoms have positions $\mathbf{q} = \{q_i\}_{i=1,\ldots,3N}$ and momenta $\mathbf{p} = \{p_i\}_{i=1,\ldots,3N}$

$$\begin{cases} \dot{q}_i &= \frac{\partial}{\partial p_i} H(\mathbf{q}, \mathbf{p}) = m_i^{-1} p_i \\ \dot{p}_i &= -\frac{\partial}{\partial q_i} H(\mathbf{q}, \mathbf{p}) = -\frac{\partial}{\partial q_i} V(\mathbf{q}). \end{cases} \tag{2.1}$$

The masses $\{m_i\}_{i=1,\ldots,3N}$ have been assigned per degree of freedom and one should thus keep in mind that $m_1 = m_2 = m_3$ is the mass of the first particle and so on. The Hamiltonian $H(\mathbf{q}, \mathbf{p}) = V(\mathbf{q}) + T(\mathbf{p})$ represents the total internal energy of the system and consist of the potential energy $V(\mathbf{q})$ plus the kinetic energy $T(\mathbf{p}) = \sum_{i=1}^{3N} p_i^2/2m_i$. The state space of the system at a time t is denoted as $\mathbf{x}(t) = \{\mathbf{q}(t), \mathbf{p}(t)\} \in \Gamma \subset \mathbb{R}^{6N}$. For a certain potential energy function $V(\mathbf{q})$, Hamiltonian dynamics will always propagate identical dynamics when starting from the same initial conditions $\mathbf{x}_0 = \{\mathbf{q}_0, \mathbf{p}_0\}$ at $t = 0$, i.e. dynamics are said to be deterministic. Moreover, the total internal energy along the trajectory is constant, and the Hamiltonian is said to be a constant of motion. Hamiltonian dynamics sample a microcanonical ensemble, often referred to as NVE because the amount of atoms N, the volume V and the internal energy $E = H(\mathbf{q}, \mathbf{p})$ are constant for all configurations in the ensemble.

Trajectories for Hamiltonian dynamics can be simulated by numerically integrating the equations in time. The most commonly used integrator for Hamiltonian mechanics is the Verlet integrator, but many other schemes exist[3].

2.1.2 Langevin Dynamics

Molecular systems of interest can rarely be considered as isolated entities, but instead customarily are surrounded by an environment influencing their behavior. In these cases, the internal energy isn't constant, as energy can be exchanged with the environment. A more suitable approach is to assume such system is in thermal equilibrium with its surroundings. For many situations of interest, especially in chemistry and biochemistry, the system can be considered immersed in a bulk of fluid with which it exchanges heat quickly, maintaining thermal equilibrium.

In Langevin dynamics, the model system surroundings are not explicitly incorporated but rather mimicked by including additional terms into the equations of motion[3]:

$$\begin{cases} \dot{q}_i &= m_i^{-1} p_i \\ \dot{p}_i &= -\frac{\partial}{\partial q_i} V(\mathbf{q}) - \xi p_i + \sqrt{2 k_B T \xi m_i} \eta_i(t). \end{cases} \tag{2.2}$$

Here, the term $-\xi p_i$ is the frictional drag, with ξ the collision rate (in units s^{-1}), also referred to as the friction coefficient. The frictional drag represents the systematic effect of dissipation due to the surroundings[5]. The term $\sqrt{2 k_B T \xi m_i} \eta(t)$ is a random collision force representing random impulses arising from the surroundings. $\eta_i(t) \in \mathbb{R}$ describes an uncorrelated Gaussian white noise with zero mean and unit variance

$$\langle \eta_i(t) \eta_j(t') \rangle = \delta_{ij} \delta(t - t') \tag{2.3}$$

and is scaled by the volatility $\sqrt{2 k_B T \xi m_i}$ where k_B is the Boltzmann constant and T is the temperature. Here, δ_{ij} is the Kronecker delta

$$\delta_{ij} = \begin{cases} 1 & \text{if} \quad i = j \\ 0 & \text{if} \quad i \neq j \end{cases} \tag{2.4}$$

and $\delta(t - t')$ is the Dirac delta function. The inclusion of the random term makes dynamics stochastic rather than deterministic.

The relationship between the dissipation through collision rate ξ and the fluctuation scaled by the volatility ensures thermal equilibrium, which is a manifestation of the so-called fluctuation-dissipation theorem[3, 5, 38]. Langevin dynamics thus sample a canonical ensemble of configurations, also known as an NVT ensemble since the temperature T is constant rather than the internal energy E as is the case in Hamiltonian dynamics. The equilibrium probability distribution in phase space for a canonical ensemble is given by the Gibbs-Boltzmann density

$$\rho_{\text{eq}}(\mathbf{q}, \mathbf{p}) = Z_{\text{can}}^{-1} e^{-\beta H(\mathbf{q}, \mathbf{p})} \tag{2.5}$$

where $\beta = (k_B T)^{-1}$ and the classical canonical partition function $Z_{\text{can}} = \int_{\Gamma_q} \int_{\Gamma_p} \mathrm{d}\mathbf{q} \mathrm{d}\mathbf{p} e^{-\beta H(\mathbf{q}, \mathbf{p})}$ with $\Gamma_q \subset \mathbb{R}^{3N}$ the space of all possible configurations $\mathbf{q}(t)$ and $\Gamma_p \subset \mathbb{R}^{3N}$ the space of all possible momenta $\mathbf{p}(t)$. Often, this distribution is split in a configuration and momentum part $\rho(\mathbf{q}, \mathbf{p}) = \nu(\mathbf{q}) \mu(\mathbf{p})$. The configurational distribution

$$\nu(\mathbf{q}) = Z_q^{-1} e^{-\beta V(\mathbf{q})} \tag{2.6}$$

is colloquially referred to as the Boltzmann distribution, with $Z_q = \int_{\Gamma_q} \mathrm{d}q e^{-\beta V(\mathbf{q})}$ the configurational canonical partition function. The distribution of momenta is Gaussian in each dimension of momentum space:

$$\mu(\mathbf{p}) = \prod_{i=1}^{3N} \sqrt{\frac{1}{2\pi m_i k_B T}} e^{-\frac{p_i^2}{2mk_BT}} \tag{2.7}$$

and is referred to as the Maxwell-Boltzmann distribution. The canonical probability distributions can be used to perform thermodynamic averaging. For a configuration dependent observable $O(\mathbf{q})$, we get

$$\begin{aligned} \langle O(\mathbf{q}) \rangle &= \int_{\Gamma_q} \mathrm{d}\mathbf{q}\, O(\mathbf{q}) \nu(\mathbf{q}) && (2.8) \\ &= \lim_{M\to\infty} \frac{1}{M} \sum_{i=1}^{M} O(\mathbf{q}_i) && (2.9) \end{aligned}$$

where in the last line, summation is performed over a high number of configurations that are statistically representative for the canonical ensemble. Langevin dynamics have the advantage of being ergodic[3], meaning that for long enough trajectories, eventually all configurations in configuration space Γ_q will be visited, and moreover they will be visited with a frequency proportional to the probability distribution. In other words, for long enough simulation times, time averaging becomes equivalent to ensemble averaging, and Eq. 2.9 can be applied directly to the trajectory points.

Langevin integrators used to generate time-discretized trajectories for Langevin dynamics (Eq. 2.2) will be discussed in Section 3.3 and its supplementary material.

2.1.3 Brownian Dynamics

A commonly discussed special case of Langevin dynamics is the high friction limit, where the inertial force $\dot{p}_i$ becomes negligible compared to the dissipation ξp_i. The equations of motion simplify to

$$\dot{q}_i = -\frac{1}{m_i \xi} \frac{\partial}{\partial q_i} V(\mathbf{q}) + \sqrt{\frac{2k_BT}{\xi m_i}} \eta_i(t). \tag{2.10}$$

The corresponding dynamics are referred to as overdamped Langevin dynamics or Brownian dynamics.

Complementary to equations of motion describing trajectories in configurational space, dynamics can also be described as a time evolution of probability densities $\rho(\mathbf{q}, t)$. For Brownian motion, evolution of probability densities is described by the Smoluchowski equation

$$\begin{aligned} \frac{\partial}{\partial t} \rho(\mathbf{q}, t) &= \sum_{i=1}^{3N} D_i \frac{\partial^2}{\partial q_i^2} \rho(\mathbf{q}, t) + \sum_{i=1}^{3N} m_i^{-1} \xi^{-1} \frac{\partial}{\partial q_i} \left(\rho(\mathbf{q}, t) \frac{\partial V(\mathbf{q})}{\partial q_i} \right) && (2.11a) \\ &= \mathcal{Q} \rho(\mathbf{q}, t) && (2.11b) \end{aligned}$$

where diffusion coefficients D_i are related to the collision rate through the Einstein-Smoluchowski equation:

$$D_i = \frac{k_B T}{m_i \xi}\,. \tag{2.12}$$

Whereas the equation of motion in configurational space (Eq. 2.10) is a stochastic differential equation, the Smoluchowski equation is a partial differential equation in time and thus time evolution of the probability density is deterministic. We mention similar equations for time evolution of probability densities exist for Hamiltonian and Langevin dynamics[3, 39] but are omitted here for the sake of brevity.

The most commonly used numerical integrator for Brownian dynamics (Eq. 2.10) is the Euler-Maruyama integrator[3].

2.1.4 Force fields

So far, we've discussed equations of motion for classical dynamics, while saying nothing about the form of the potential energy function $V(\mathbf{q})$. In principle, the potential energy function can be estimated *ab-initio* using electronic structure methods from quantum chemistry, where commonly electronic energies of configurations are calculated within the Born-Oppenheimer approximation. The corresponding potential energy functions can be calculated on the fly, while dynamics of the nuclei are still carried out classically as discussed above. This type of simulations, where the nuclei are treated classically while electronic structure is computed quantum mechanically, is generally referred to as ab-initio molecular dynamics. Electronic structure calculations, however, are ordinarily prohibitively expensive, and applicability of ab-initio MD is limited to smaller systems at shorter simulation times.

In order to increase calculation speeds, parametrized frameworks for the expression of the potential energy function $V(\mathbf{q})$ have been developed. The combination of the functional form of $V(\mathbf{q})$ and the parameter set needed to calculate it, is generally referred to as a force field. Most force fields use a similar makeup, splitting interactions in bonded and nonbonded parts[2, 5]:

$$V(\mathbf{q}) = V_{\text{nonbonded}}(\mathbf{q}) + V_{\text{bonded}}(\mathbf{q}). \tag{2.13}$$

The nonbonded potential in turn consists of a Coulombic part, designed to reproduce the electrostatic properties of the molecules, and a Lennard-Jones part, designed to emulate van der Waals interactions. For a system of N atoms:

$$V_{\text{nonbonded}}(\mathbf{q}) = \sum_{k=1}^{N}\sum_{l=k+1}^{N} \frac{Q_k Q_l}{4\pi\epsilon_0 r_{kl}} + \sum_{k=1}^{N}\sum_{l=k+1}^{N} 4\epsilon_{kl}\left[\left(\frac{\sigma_{kl}}{r_{kl}}\right)^{12} - \left(\frac{\sigma_{kl}}{r_{kl}}\right)^{6}\right] \tag{2.14}$$

where the first term is the Coulombic contribution with Q_k and Q_l the partial charges of atoms k and l respectively, r_{kl} the interatomic distances between them (which can be deduced from the positions $\mathbf{q}$) and ϵ_0 the vacuum permittivity. The second term is the Lennard-Jones 12-6 potential with parameters ϵ_{kl} and σ_{kl} representing the depth of the potential well and the size of the atoms involved respectively.

The bonded potential manages energetics within molecules and depends on how covalent bonds between atoms are asserted beforehand. Generally, they depend on bond distances l_i between covalently bonded atoms, bond angles θ_i between two neighboring covalent bonds and proper dihedrals ω_i and improper dihedrals ϕ_i between three neighboring covalent bonds. If the connectivity of the molecule is known, all these internal coordinates can be deduced from the positions $\mathbf{q}$ of the atoms. For bond stretching, bond angles and improper dihedral angles, the corresponding potential energy terms generally penalize deviations from reference values through harmonic potentials, while proper dihedrals are generally expressed using periodic potential contributions:

$$\begin{aligned} V_{\text{bonded}}(\mathbf{q}) = &\sum_{\text{bonds}} \frac{k_i^{(l)}}{2} (l_i - l_{i,0})^2 + \sum_{\text{angles}} \frac{k_i^{(\theta)}}{2} (\theta_i - \theta_{i,0})^2 \\ &+ \sum_{\text{proper}} \sum_{n} \frac{V_n}{2} (1 + \cos(n\omega_i - \gamma)) + \sum_{\text{improper}} \frac{k_i^{(\phi)}}{2} (\phi_i - \phi_{i,0})^2 \end{aligned} \tag{2.15}$$

where $l_{i,0}$, $\theta_{i,0}$ and $\phi_{i,0}$ are reference values for the bond lengths, bond angles and improper dihedrals respectively, and $k_i^{(l)}$, $k_i^{(\theta)}$ and $k_i^{(\phi)}$ are the spring constants of their harmonic potentials. Contributions from proper dihedral angles are commonly expressed as cosine series expansions, where n is the multiplicity, γ the phase factor and V_n can be considered the barrier height for a single term in the series. Because the bonded terms take care of interactions between covalently linked atoms close to each other, nonbonded interactions between atoms less than three covalent bonds away from each other are commonly not included.

All parameters including the reference values for internal coordinates and spring constants need to be parametrized. This can be done by picking combinations of these parameters in a way that simulation results match experimental data of choice, as different parameter combinations might optimize different experimental observables. Alternatively, parameters can also be derived from quantum mechanical modeling. For more details on the functional form as well as parametrization of force fields, I refer to Chapter 4 of Ref. 2 as well as to manuals of molecular dynamics software packages such as OpenMM[40] and GROMACS[41].

2.1.5 Collective Variables

Collective variables (CV) are descriptors of the system useful to the modeler to investigate its properties. A collective variable z_i can generally be defined in terms of the nuclear positions $\mathbf{q}$ through a mapping

$$z_i = \zeta_i(\mathbf{q}) \tag{2.16}$$

with $\zeta_i : \mathbb{R}^{3N} \rightarrow \mathbb{R}$. Examples include distances, dihedral angles, coordination numbers, root-mean square deviations or radii of gyration, but can also include non-trivial combinations of other variables. In the multidimensional generalization $\mathbf{z} = \{z_i\}_{i=1,\ldots,d} = \{\zeta_i(\mathbf{q})\}_{i=1,\ldots,d} = \zeta(\mathbf{q})$, collective variables span a subspace $\Gamma_z \subset \mathbb{R}^d$ where typically $d \ll 3N$, with $\zeta : \mathbb{R}^{3N} \rightarrow \mathbb{R}^d$. This so-called dimensionality reduction is often performed to attempt easier navigation and interpretation in the study of molecular behavior in terms of thermodynamics and kinetics as compared to the full-dimensional case.

The equilibrium distribution in the reduced space $\pi(\mathbf{z})$ can be reformulated from Eq. 2.6 as

$$\pi(\mathbf{z}) = Z_q^{-1} \int_{\Gamma_q} \mathrm{d}\mathbf{q} e^{-\beta V(\mathbf{q})} \prod_{i=1}^{d} \delta(\zeta_i(\mathbf{q}) - z_i) \tag{2.17}$$

where $\delta(\zeta_i(\mathbf{q}) - z_i)$ are Dirac delta functions. The free energy surface (FES) in $\mathbf{z}$ is defined as[6]

$$F(\mathbf{z}) = -k_B T \ln \pi(\mathbf{z}). \tag{2.18}$$

In case of sufficient sampling, $\pi(\mathbf{z})$ can be obtained directly by building a histogram in $\mathbf{z}$ over all configurations sampled and a subsequent normalization.

Reducing dimensionality inherently comes down to projecting out part of the information entailed in the potential energy surface, and interpretation of the resulting free energy surface should always be done with care. Collective variables which do not resolve distinct metastable states and transition states can severely misrepresent the energetics of molecular processes[42].

Often, sufficient sampling of the full CV space by direct unbiased simulation is impractical, and many methods have been established to obtain free energy profiles more quickly[11]. So-called enhanced sampling methods will be the subject of Section 2.2. In these methods the choice of CV space is commonly an important consideration, as unfortunate choices can severely slow down sampling.

2.1.6 Reaction Coordinates

In the mechanistic understanding of chemical reactions, it is generally key to identify a physically meaningful reaction coordinate which accurately describes the dynamical progress from the reactant to the product state. Commonly, reaction coordinates are one-dimensional collective variables in position space

$$s = s(\mathbf{q}), \tag{2.19}$$

but in principle they can also depend on momentum space coordinates. They should monotonically increase going from reactants to products along the reaction pathway[43].

All degrees of freedom orthogonal to the reaction coordinate are considered to comprise the bath. In many rate theories, the bath is replaced by one-dimensional friction in combination with random forces along the reaction coordinate. The high-dimensional problem is thus reduced to a one-dimensional Langevin dynamics[1] (Section 2.1.2), also referred to as *effective dynamics*. Here, the free energy in the reaction coordinate $F(s)$ is assumed to take the role of the potential energy governing drift. Furthermore, the effective friction term ξ as well as the reduced mass μ_s in s are important parameters in reducing the high-dimensional problem. Dynamics $s(t)$ generated by direct application of Eq. 2.2 to the one-dimensional reaction coordinate are then assumed to be equivalent with full-space dynamics projected on s.

For many processes of interest, the dynamics along the reaction coordinate are considered diffusive, and the overdamped limit of the Langevin equation is used (Section 2.1.3). This is typically the case for thermally activated transitions over energy barriers such as conformational transitions in biomolecules. In general, reaction coordinates will require position dependent friction, reduced mass and diffusion profiles $D(s)$ for an accurate description of the dynamics[43, 45–48]. In this case, a correction needs to be made to the equations of motion when using the free energy profile as effective potential energy function. The overdamped Langevin equation in Eq. 2.10 is now written as[49]:

$$\dot{s} = -\beta D(s)\frac{\partial F(s)}{\partial s} + \frac{\partial D(s)}{\partial s} + \sqrt{2D(s)}\,\eta(t) \tag{2.20}$$

with the diffusion coefficient along the reaction coordinate as given by the Einstein-Smoluchowski relation in Eq. 2.12 where the mass m needs to be substituted with the reduced mass along the reaction coordinate. The corresponding Smoluchowski equation is[47, 49]:

$$\begin{aligned}
\frac{\partial}{\partial t}\rho(s,t) &= \frac{\partial^2}{\partial s^2}\left[D(s)\rho(s,t)\right] + \frac{\partial}{\partial s}\left[\beta D(s)\rho(s,t)\frac{\partial F(s)}{\partial s} - \rho(s,t)\frac{\partial D(s)}{\partial s}\right] && \text{(2.21a)}\\
&= \frac{\partial}{\partial s}\left[D(s)e^{-\beta F(s)}\frac{\partial}{\partial s}\left(e^{\beta F(s)}\rho(s,t)\right)\right] && \text{(2.21b)}\\
&= \mathcal{Q}\rho(s,t)\,. && \text{(2.21c)}
\end{aligned}$$

Given a reaction coordinate, several methods to obtain the position dependent diffusion $D(s)$ can be found in literature[45, 50–52].

The choice of reaction coordinate can greatly influence the reliability of the effective dynamics and correspondingly the accuracy of calculated dynamical properties such as reaction rates. Theories to estimate rates will be the subject of Section 2.3. Finding good reaction coordinates is often a highly nontrivial task.

In terms of formal properties, the committor $p_B(\mathbf{q})$ can be considered an ideal reaction coordinate[43, 53]. $p_B(\mathbf{q})$ gives the probability of trajectories launched at $\mathbf{q}$ with momenta distributed according to Maxwell-Boltzmann (Eq. 2.7) to reach the product state B before

---

[1] Remark that the framework for effective dynamics described here assumes a clear separation of time scales between the reaction coordinate and the bath degrees of freedom. In case bath degrees of freedom exhibit slow correlated motion with regards to the reaction coordinate, effective one-dimensional dynamics are better described using a memory kernel as part of the friction in what is called the Generalized Langevin Equation (GLE)[6, 38, 44].

visiting the reactant state A. It is zero for configurations in the reactant state, one for configurations in the product state and varies from 0 to 1 along the transition pathway. Correspondingly, the committor maps the full configurational space to a single scalar coordinate p_B which quantifies the dynamical progress from A to B directly. It can be shown that the free energy surface and dynamics, when projected onto the committor, yield a one-dimensional model that perfectly preserves the reaction rate[6, 43]. Planes in configurational space with constant committor values are called isocommittor surfaces or isocommittor hyperplanes. The isocommittor surface at $p_B(\mathbf{q}) = 0.5$ is also called the stochastic separatrix. The stochastic separatrix commonly connects the transition state ensemble, encompassing configurations which coincide with dynamical bottlenecks. Although the committor is conceptually an ideal reaction coordinate, it is often impractical to work with, as it cannot be resolved at the molecular degrees of freedom and thus often does not facilitate mechanical insight[43].

2.2 Enhanced Sampling Methods

In a first instance, molecular dynamics are often used to obtain representative samples of configurations for the thermodynamic ensemble in which the simulation is performed. The obtained configurations can then be used to set up further thermodynamic study of the system, i.e. to determine stable states, to calculate thermodynamically averaged observables or to compute free energy profiles. As systems get more involved, however, potential energy surfaces grow more complicated. In cases where energy surfaces contain many local minima separated by high barriers, exploring all parts of configurational space might take a long time. Even with the use of parametrized force fields, computation times necessary to sample a statistically representative set of configurations can easily increase to a troublesome degree.

Enhanced sampling methods have been developed to increase sampling speeds in MD simulations while reproducing the equilibrium probability distribution of the system. Many approaches have been developed to enhance sampling, including adding additional potentials to the force field, sampling at higher temperatures, exchanging configurations between parallel simulations sampling different but related configurational space and more[11].

In this work, the main focus will be on enhanced sampling through application of an additional biasing potential to the potential energy function. The biasing potential steers the simulation away from states which have already been sufficiently sampled towards unexplored parts of the configurational space. Usually, the biasing potential is not applied to all degrees of freedom, but to a set of sensibly chosen collective variables. The biased potential energy function takes form

$$\widetilde{V}(\mathbf{q}) = V(\mathbf{q}) + U^{\text{bias}}(\zeta(\mathbf{q})) \tag{2.22}$$

where $U^{\text{bias}}(\zeta(\mathbf{q}))$ is the biasing potential, often simply referred to as the bias. Notice biased trajectories can only be propagated if the force from the biasing potential can be calculated, which requires access to the Jacobian matrix elements of the mapping functions $\zeta_i(\mathbf{q})$:

$$F_i^{\text{bias}} = -\frac{\partial}{\partial q_i} U^{\text{bias}}(\zeta(\mathbf{q})) = -\sum_{j=1}^{d} \left.\frac{\mathrm{d}U^{\text{bias}}}{\mathrm{d}z_j}\right|_{z_j=\zeta_j(\mathbf{q})} \frac{\partial}{\partial q_i}\zeta_j(\mathbf{q}) \qquad \forall\, i. \tag{2.23}$$

Similar to the unbiased case in Eqs. 2.6-2.8, sampling at the biased potential energy function will transpire at a biased probability distribution $\widetilde{\nu}(\mathbf{q}) = \widetilde{Z}_q^{-1} \exp\left(-\beta \widetilde{V}(\mathbf{q})\right)$ with $\widetilde{Z}_q = \int_{\Gamma_q} \mathrm{d}\mathbf{q} \exp\left(-\beta \widetilde{V}(\mathbf{q})\right)$, while the biased ensemble average of an observable $O(\mathbf{q})$ is written as $\langle O(\mathbf{q})\rangle_{\widetilde{\nu}} = \int_{\Gamma_q} \mathrm{d}\mathbf{q}\, O(\mathbf{q})\widetilde{\nu}(\mathbf{q})$. Ensemble averages for biased and unbiased potential energy functions are related through[11]

$$
\begin{aligned}
\langle O(\mathbf{q}) \rangle &= \int_{\Gamma_q} \mathrm{d}\mathbf{q}\, O(\mathbf{q}) \nu(\mathbf{q}) && (2.24a) \\
&= \int_{\Gamma_q} \mathrm{d}\mathbf{q}\, O(\mathbf{q}) \frac{\nu(\mathbf{q})}{\widetilde{\nu}(\mathbf{q})} \widetilde{\nu}(\mathbf{q}) && (2.24b) \\
&= \left\langle O(\mathbf{q}) \frac{\nu(\mathbf{q})}{\widetilde{\nu}(\mathbf{q})} \right\rangle_{\widetilde{\nu}} . && (2.24c)
\end{aligned}
$$

The ratio of probability distributions can be expressed as

$$
\begin{aligned}
\frac{\widetilde{\nu}(\mathbf{q})}{\nu(\mathbf{q})} = \frac{Z_q}{\widetilde{Z}_q} \frac{e^{-\beta \widetilde{V}(\mathbf{q})}}{e^{-\beta V(\mathbf{q})}} &= \frac{\int_{\Gamma_q} \mathrm{d}\mathbf{q} e^{-\beta V(\mathbf{q})}}{\int_{\Gamma_q} \mathrm{d}\mathbf{q} e^{-\beta \widetilde{V}(\mathbf{q})}} \cdot e^{-\beta U^{\mathrm{bias}}(\zeta(\mathbf{q}))} && (2.25a) \\
&= \frac{\int_{\Gamma_q} \mathrm{d}\mathbf{q} e^{-\beta \widetilde{V}(\mathbf{q})} e^{\beta U^{\mathrm{bias}}(\zeta(\mathbf{q}))}}{\int_{\Gamma_q} \mathrm{d}\mathbf{q} e^{-\beta \widetilde{V}(q)}} \cdot e^{-\beta U^{\mathrm{bias}}(\zeta(\mathbf{q}))} && (2.25b) \\
&= \left\langle e^{\beta U^{\mathrm{bias}}(\zeta(\mathbf{q}))} \right\rangle_{\widetilde{\nu}} e^{-\beta U^{\mathrm{bias}}(\zeta(\mathbf{q}))} && (2.25c)
\end{aligned}
$$

Notice a completely equivalent derivation can be done in the reduced space spanned by collective variables $\mathbf{z} = \zeta(\mathbf{q})$, where $\widetilde{\pi}(\mathbf{z})/\pi(\mathbf{z})$ takes the same form as Eq. 2.25c. Filling in yields

$$
\begin{aligned}
\langle O(\mathbf{q}) \rangle &= \frac{\left\langle O(\mathbf{q}) e^{\beta U^{\mathrm{bias}}(\zeta(\mathbf{q}))} \right\rangle_{\widetilde{\nu}}}{\left\langle e^{\beta U^{\mathrm{bias}}(\zeta(\mathbf{q}))} \right\rangle_{\widetilde{\nu}}} && (2.26a) \\
&= \lim_{M \to \infty} \frac{\sum_{i=1}^{M} O(\mathbf{q}_i) e^{\beta U^{\mathrm{bias}}(\zeta(\mathbf{q}_i))}}{\sum_{i=1}^{M} e^{\beta U^{\mathrm{bias}}(\zeta(\mathbf{q}_i))}} . && (2.26b)
\end{aligned}
$$

Consequently, for sufficiently long trajectories, the ergodic property can be used to estimate the unbiased ensemble average of $O(\mathbf{q})$ from biased trajectories.

It is important to notice that in what has been discussed above, the biasing potential $U^{\mathrm{bias}}(\mathbf{z})$ is predetermined and static, and convergence times for reweighting in Eqs. 2.26 will depend strongly on the overlap between the biased and unbiased distributions of configurations[11]. Choosing a suitable biasing potential is not an easy enterprise, as it is generally not clear before sampling how the energy landscape as a function of $\mathbf{z}$ looks like. As a matter of fact, the free energy profile $F(\mathbf{z})$ as defined in Eq. 2.18 is often considered one of the main results of enhanced sampling methods. A bad choice of biasing potential can insufficiently speed up sampling of the configuration space, as energy barriers might look different than anticipated. Alternatively, unfortunate choices can also ruin overlap between biased and unbiased configurational distributions and correspondingly impede convergence of the thermodynamical reweighting.

A range of methods have been developed to carry out enhanced sampling in a way that negates the necessity of predefining a single static biasing potential[54–58]. In umbrella sampling (Section 2.2.1), harmonic restraints are used to force the system to explore different regions of collective variable space $\mathbf{z}$. While the harmonic restraints themselves are static, reweighting methods have been constructed that allow combining configurations from different trajectories at different restraint positions to estimate the unbiased population distribution over the whole configurational space. In other words, configurations sampled at effectively different biasing potentials can be used to estimate a single free energy surface.

In adaptive biasing potential simulations, the biasing potential is no longer static, but is adapted on-the-fly during simulations using information from the trajectory itself. Hence, the bias can be considered to 'learn' an optimal shape as dynamics progress. Metadynamics (Section 2.2.2) is a widely used adaptive biasing potential method where the bias is evolved to eventually cancel out the free energy surface in collective variables $\mathbf{z}$. A more complete overview of enhanced sampling methods and corresponding references can be found in Ref. 11.

2.2.1 Umbrella Sampling

In umbrella sampling (US)[54], harmonic restraint potentials are applied to localize sampling to a specific region $S_i \subset \Gamma_s$ of the collective variable space $\mathbf{z}$:

$$U_i^{\text{bias}}(\mathbf{z}) = \frac{1}{2} k_i \left(\mathbf{z} - \mathbf{z}_i\right)^2 \tag{2.27}$$

where k_i is the harmonic spring constant and $\mathbf{z}_i$ is a point in S_i around which one wishes to sample. A trajectory simulated under a harmonic restraint $U_i^{\text{bias}}(\mathbf{z})$ can in principle be reweighted directly using Eqs. 2.25-2.26. Because the restraints confine trajectories to a localized part of collective variable space, however, the rest of the space is usually hardly sampled. Consequently, the biased and unbiased configurational distributions will differ too much, and reweighting does not converge to the full-space unbiased equilibrium distribution in any reasonable timespan.

The weighted histogram analysis method (WHAM)[59] is a maximum likelihood method to estimate the population distribution $\pi(\mathbf{z})$ using configurations from n_{t} trajectories generated at different restraint potentials $\left\{U_i^{\text{bias}}(\mathbf{z})\right\}_{i=1,\ldots,n_{\text{t}}}$, also referred to as windows. In WHAM, the collective variable space is discretized in n_{b} bins, and the number of frames N_{ij} from trajectory i belonging to bin j is counted. The maximum likelihood estimate of the unbiased probability for bin j is[11, 60]

$$P_j = \frac{\sum_{i=1}^{n_{\text{t}}} N_{ij}}{\sum_{i=1}^{n_{\text{t}}} N_i^{\text{steps}} C_i e^{-\beta U^{\text{bias}}(\mathbf{z}_j)}} \tag{2.28}$$

where N_i^{steps} is the total amount of steps in trajectory i, $\mathbf{z}_j$ is a representative point for bin

j in collective variable space and

$$C_i = \frac{1}{\sum_{j=1}^{n_\mathrm{b}} e^{-\beta U^{\mathrm{bias}}(\mathbf{z}_j)} P_j} . \tag{2.29}$$

Eqs. 2.28 and 2.29 can be solved iteratively, for example by calculating the P_j values first using Eq. 2.28 and an initial guess for the C_i values. The resulting probabilities are then used to calculate the C_i's using Eq. 2.29, which can then be used to calculate the probabilities again. This iterative scheme is repeated until probabilities converge and we obtain a probability distribution $\mathbf{P} = \{P_j\}_{j=1,\ldots,n_\mathrm{b}}$ which is a discretized estimate of the unbiased probability density $\pi(\mathbf{z})$. Binless extensions for free energy estimation using WHAM have also been introduced[61].

The ability to combine trajectory data from several windows with different restraints allows sampling of a larger part of collective variable space with smaller simulation time. Within one window, sampling is localized to a specific part of collective variable space, and thus windows must be spread out to cover the area of interest in its entirety. At the same time, however, WHAM only converges if the windows sufficiently overlap[62]. Calculating the probability distribution and corresponding free energy surface using US thus requires a strategic choice of the parameters involved, i.e. the positions $\mathbf{z}_i$ of the restraints for each window, as well as the spring constants k_i and amount of simulations steps per window N_i^{steps}. Estimation of errors on the free energy surface calculated using WHAM can be done using bootstrapping[63], either by generating bootstrapped trajectories or by bootstrapping complete histograms[64].

For trajectories simulated under harmonic restraints, a value for the diffusion coefficient can be calculated using Hummers method[45]. For a one-dimensional collective variable z, Hummers formulation for the diffusion coefficient from a single trajectory is:

$$D(z = \langle z \rangle) = \frac{\mathrm{var}(z)}{\tau_z} \tag{2.30}$$

where $\tau_z = \int_0^\infty \langle \delta z(t) \delta z(0) \rangle \, \mathrm{d}t / \mathrm{var}(z)$ with $\delta z(t) = z(t) - \langle z \rangle$. Notice neither the spring constant k_i nor the position z_i of the harmonic restraint enters the equations. When multiple trajectories simulated using harmonic restraints at a series of different z_i are available, as is the case when doing umbrella sampling in combination with WHAM, the diffusion coefficient in Eq. 2.30 can be calculated for different values of z. If enough data points are available, diffusion coefficients $D(z)$ for any value of z can be estimated from interpolation.

2.2.2 Metadynamics

Metadynamics (MetaD)[55] is an enhanced sampling method where an adaptive biasing potential is added to a set of collective variables $\mathbf{z} = \{z_i\}_{i=1,\ldots,d}$ with the intention of pushing dynamics to regions of configurational space which have not been sampled yet. The time dependent biasing potential $U^{\mathrm{bias}}(\mathbf{z}, t)$ consists of a sum of repulsive Gaussian kernels which are deposited in collective variable space at a predetermined rate. For a time in interval $\tau_G m \leq t < \tau_G(m+1)$, the bias is given by:

$$U^{\mathrm{bias}}(\mathbf{z}, t) = U_m(\mathbf{z}) = \sum_{k=1}^{m} W_k \exp\left(-\frac{1}{2}\sum_{i=1}^{d}\frac{(z_i - z_{k,i})^2}{\sigma_i}\right) \tag{2.31}$$

where τ_G is the deposition rate time interval, W_k is the height of the Gaussian at the k'th deposition, σ_i the standard deviation of the deposited Gaussian functions in the dimension of the i'th collective variable and $z_{k,i}$ is the value of z_i at the time of depositing the k'th Gaussian, i.e. at time $t = k\tau_G$. When a trajectory finds itself in a deep potential energy well which would ordinarily be slow to escape from, for example, the adaptive bias steadily fills the well with deposited Gaussians ultimately speeding up escape significantly. With time, the deposited Gaussians fill out the full free energy surface and sampling ideally becomes diffusive in the corresponding collective variable space.

In the original formulation of metadynamics, the Gaussian height W_k is kept constant and thus independent of k. In this case, the biasing potential converges in time oscillating around the negative of the free energy surface $-F(\mathbf{z})$ plus a constant. As a consequence, the free energy surface can be estimated by taking the negative of the average of the bias, but starting the averaging only from a time where the free energy surface can be considered filled[11, 42].

The oscillations of the biasing potential upon convergence are proportional to the height of the Gaussian kernels. They can therefore be decreased by reducing the Gaussian height W_k in the course of the simulation in an appropriate way[42]. In well-tempered metadynamics (WT-MetaD)[65], the height of the Gaussians is chosen to be proportional to a decaying exponential function of the biasing potential already deposited in the currently visited point of the CV space:

$$W_k = W_0 \exp\left(-\frac{1}{1-\gamma}\beta U_{k-1}(\mathbf{z}_k)\right) \tag{2.32}$$

where W_0 is the initial height and the exponential factor can be considered a scaling factor decreasing the height of the deposited Gaussian kernels if the biasing potential at the corresponding kernel center is already high, where $U_{k-1}(\mathbf{z})$ is the biasing potential after $k-1$ depositions with $U_0 = 0$. γ is generally referred to as the bias factor. Low values for γ speed up scaling leading to faster decreasing Gaussian heights, while high values for γ slow down scaling, meaning the heights of the deposited Gaussian kernels decrease slower. Conventional metadynamics corresponds to the limit $\gamma \to \infty$.

The biasing potential in well-tempered metadynamics does not converge to $-F(\mathbf{z})$ but instead has been shown to converge to[66]:

$$U^{\text{bias}}(\mathbf{z},t) = -\left(1-\frac{1}{\gamma}\right)F(\mathbf{z})\,. \tag{2.33}$$

Contrary to conventional metadynamics, the bias potential does not oscillate upon convergence, but instead asymptotically reaches a quasi-equilibrium state. Eq. 2.33 can therefore be used to estimate the FES directly from the biasing potential $U^{\text{bias}}(\mathbf{z},t)$ at a time t where the bias can be considered converged. Practically, convergence can be checked by comparing free energy surfaces obtained using Eq. 2.33 at different times t while aligning their minima to zero.

The free energy surface can also be obtained from well-tempered metadynamics simulations by applying reweighting methods. These methods have the additional advantage of being capable of estimating free energy profiles and population distributions in collective variables which have not been biased during the metadynamics run. Reweighting methods have been developed where the time dependence of the bias potential is taken into account[67,68]. Alternatively, free energy profiles and probability densities can be estimated by using the final biasing potential $U^{\text{bias}}(\mathbf{z},t=t_{\text{final}})$ to reweight trajectories from well-tempered metadynamics through direct application of Eq. 2.26 [69]. The assumption made in this case is that the biasing potential has not changed during the simulation, which is evidently untrue for adaptive biasing potential methods such as metadynamics. The asymptotic convergence of the biasing potential, however, means that for the biggest part of the trajectory, the change to the biasing potential becomes negligible, and the bias is effectively constant. In practice, one often removes the initial part of the metadynamics trajectory where the bias still significantly changes, and subsequently reweights the rest of the trajectory points with the final bias. It is generally good procedure to compare the free energy surface $F(\mathbf{z})$ obtained from reweighting methods to the one obtained from analyzing the bias potential directly through Eq. 2.33.

Error estimates for free energy profiles obtained from metadynamics can be calculated using block analysis[42].

2.2.3 Path Adaptive Sampling

Complicated dynamics can often not be accurately described using traditional internal coordinates such as distances or angles. Therefore, enhanced sampling methods frequently adopt more complicated collective variables that are better suited to describe the reaction dynamics. For many processes, however, finding a single CV which faithfully describes the progress of the dynamics (i.e. a reaction coordinate) is a challenging task. In this case, free energy surfaces in multiple CVs can be generated to get a more comprehensive understanding of the system's behavior and explore the multidimensional landscape of the dynamics. For most free energy methods, however, the number of CVs is limited as a higher number leads to prohibitively high computational effort. In practical applications, methods like metadynamics and umbrella sampling are limited to three to four CVs[11], depending on the complexity of the system and the computational resources available. Methods to extend the number of CVs have been proposed[70, 71].

One approach which has been successful in describing complicated dynamics on a single CV are path based schemes. In these schemes, a larger CV space is projected onto a carefully chosen path CV. The path CV is generally represented by a parameterized curve connecting the initial and final states of the system, aiming to capture complicated dynamics using a one-dimensional parameter. This one-dimensional parameter can be considered a formulation of a reaction coordinate as introduced in Section 2.1.6.

Central is of course the formulation of a suitable path in CV space. Different algorithms to find reaction paths have been proposed, often based on steepest descent starting from an initial guess and converging toward a minimum free energy path (MFEP). Examples are schemes using a string method[12, 72] or using metadynamics with path-like variables[13, 73].

An alternative formulation[53] allows the use of a flexible, adaptive path described in a predefined set of collective variables $\mathbf{z} = \{z_i\}_{i=1,\dots,d} \in \Gamma_z \subset \mathbb{R}^d$ to converge to an estimate of the average transition path between two stable states instead. This path follows the average transition flux density under following assumptions[53, 74].

1. The average transition path can be represented by a parametrized curve $\mathbf{s}(\sigma) : \mathbb{R} \to \mathbb{R}^d$ in collective variable space, with $\mathbf{s}(0)$ located in the reactant state and $\mathbf{s}(1)$ in the product state.

2. In the vicinity of the path, the isocommittor hyperplanes S_σ are perpendicular to the path $\mathbf{s}(\sigma)$ for all values of σ.

3. In the vicinity of the path, the transition flux density can be represented by the configurational probability $\pi(\mathbf{z})$ as defined in Eq. 2.17.

In the first assumption, the path parameter $\sigma(\mathbf{z}) : \mathbb{R}^d \to [0, 1]$ projects CV space on a value between zero and one, which in its turn parametrizes the curve $\mathbf{s}$. This mapping should be done in a way that each point $\mathbf{z}$ in CV space is projected onto the specific value of σ for which $\mathbf{s}(\sigma)$ corresponds to the point on the path closest to $\mathbf{z}$. The second assumption allows for expressing the average transition path as:

$$\mathbf{s}(\sigma) = \int_{S_\sigma} \mathrm{d}S_\sigma \mathbf{z}' p_\sigma(\mathbf{z}') \tag{2.34}$$

where p_σ is the flux probability density at the isocommittor surface perpendicular to $\mathbf{s}(\sigma)$, which using the third assumption can be obtained from the probability density $\pi(\mathbf{z})$.

Under the assumptions listed above, the average transition path can in principle be obtained directly by constructing histograms of $\mathbf{z}$ in the isocommittor surfaces after MD runs, given isocommittor surfaces can be established and are sufficiently sampled. More practically, a guess transition path $\mathbf{s}_g(\sigma_g)$ parameterized by guess path parameter $\sigma_g = \sigma(\mathbf{z})\big|_{\mathbf{s}_g}$ can be chosen, and the probability distribution in the corresponding orthogonal hyperplanes S_{σ_g} can be estimated during MD runs by replacing the ensemble average in Eq. 2.34 by a time average using the ergodic property:

$$\langle \mathbf{z} \rangle_{\sigma_g} = \lim_{t\to\infty} \frac{1}{t} \int_0^t \int_{S_{\sigma_g}} \mathbf{z}'(t') \mathrm{d}S_{\sigma_g} \mathrm{d}t' \,. \tag{2.35}$$

The guess path can then be converged to the average transition path in an iterative procedure by relocating the guess path at regular time intervals to the accumulative average density, i.e. by iteratively setting the new path to the calculated averages at each isocommittor surface, $\mathbf{s}_g = \langle \mathbf{z} \rangle_{\sigma_g}$. The numerical implementation of this method requires definition of a discrete version of the paths in collective variable space, that is, path curves are expressed through a number M of nodes $\mathbf{s}_g(\sigma_g, t) \to \left\{ \mathbf{s}_j^{t_i} \right\}_{j=1,\dots,M}$. Here, j labels the nodes and t_i represents the discrete time parameter denoting the current path update step. For expressions of the geometrical mapping of points $\mathbf{z}$ in collective variable space to path parameter σ_g in discrete paths, as well as formulations for path updates to the current accumulative average, I refer to the original reference, Ref. 53, or to a recent review article, Ref. 74.

For rare events, hypersurfaces S_{σ_g} away from the stable states will be poorly sampled during simulation. Therefore, adaptive biasing methods such as metadynamics can be applied to the guess path parameter σ_g to speed up sampling. While metadynamics biasing makes dynamics more diffusive along the current guess path, the orthogonal degrees of freedom are being explored and accumulative averaging can be performed and paths can be updated as before. While the path is being updated, the metadynamics will keep adding layers of Gaussian potentials to the total bias in σ_g, correcting discrepancies inherited from the previous path guesses when the path was still moving through higher regions of the FES in collective variable space[53]. Ultimately, both the path and the adaptive bias will converge, producing a final estimate for the average transition path as well as the corresponding free energy profile. Notice that, in principle, other enhanced sampling methods such as umbrella sampling can be used to locate the average transition path[74]. Evidently, the converged path CV can also be used directly rather than adaptive (i.e. without updating the path) as a CV in further analysis.

Care has to be taken using average transition paths in systems where transitions from the reactant to product state can happen over multiple clearly distinct pathways. In these cases, the actual average transition path can be a bad representation of the physical pathways the transitions happen over, and it makes more sense to converge distinct pathways separately, averaged over the relevant parts of CV space only. Moreover, for certain systems, free energy landscapes can be quite rugged, and transition from a reactant to a product state can occur via various close and ill-defined pathways. This can severely hinder convergence towards an average transition path, as the path evolution becomes flexible as guess paths tend to wander during the adaptive path simulations. To avoid sampling multiple distinct pathways within the same adaptive path simulation, a harmonic restraint potential can be set on the distance from the path $\|\mathbf{s}_g(\sigma_g(\mathbf{z})) - \mathbf{z}\|$. Also referred to as a 'tube potentials', these restraints are used to block 'bifurcations' away from the pathways of interest, which can also be useful if landscapes are very rugged.

The spring constant of the harmonic restraint is an important parameter for optimizing path convergence as well as for the quality of the resulting paths. Evidently, spring constants need to be chosen as a compromise between a) keeping trajectories from wandering too far from the path into areas corresponding to other pathways and b) still allowing enough freedom to efficiently sample the average density in the degrees of freedom orthogonal to the path within the area of the pathway of interest. From a conceptual point of view, the size of the tube restraint controls the extent the degrees of freedom orthogonal to the path (but within CV space) can be explored, and thus influences the entropic contribution of the rest of CV space to the free energy along the path[74]. In the limit of an infinitesimally narrow tube potential, no entropic contributions are included, and the path converges to the MFEP closest to the initial path. Wider tubes go back to the more path density based description of average transition paths.

Once an estimate for the average transition path $\mathbf{s}_g$ has been obtained, the path parameter $\sigma_g(\mathbf{z})$ can be used as a reaction coordinate for further analysis including free energy methods to determine $F(\sigma_g)$ and subsequent application of rate theories.

Enhanced sampling techniques such as metadynamics and umbrella sampling increase sampling speeds and allow for exploration of configuration space to an extent that would be computationally prohibitive in case of unbiased MD. By introducing a biasing potential, the trajectory is encouraged to explore regions which would otherwise scarcely be visited, and reweighting procedures have been developed to retrieve the unbiased population distributions and free energy profiles useful for thermodynamic averaging or other physical analysis of the molecular system. Path collective variables can be used to reduce the number of CVs that need to be included in the biased sampling, while taking into account some of the complexities of the multidimensional dynamics. In the discussions so far, MD has mainly been used as a tool for generating ensembles, i.e. for creating a representative set of configurations of the system under specific thermodynamic conditions. In many molecular problems, modelers are especially interested in inherently dynamical features, such as reaction rates and mechanisms.

The next section will treat theory on how to calculate rates in molecular dynamics, both for unbiased simulations as for simulations where dynamics have been enhanced.

2.3 Rate Theory

Determining reaction mechanisms and estimating rates is a central objective in computational chemistry. Dynamical properties, however, are generally considered more difficult to compute than thermodynamic properties, for which the main obstacle often amounts to sufficient sampling of configurational space. Quantitative predictions of rates are persistently strenuous, especially when activation energies are high and systems of study become more involved. Many molecular processes involve rare events, where transitions are too infrequent to be accurately examined in the computationally accessible timescales of direct atomistic simulation. Therefore, a bulk of more resourceful sampling methods and rate theories have been developed to be able to formulate rates from MD simulations on timescales much higher than the actual simulation times. Still, due to the highly complex nature of dynamics, these methods are often restricted in their applicability, and many factors can appear as potential sources of error.

The most well-known source of error in calculations of rates is the exponential magnification of errors in the activation barrier. Unfortunately, even for relatively small errors this can create order of magnitude differences between rates obtained from computation versus experiment. Meanwhile, the force fields involved in describing the underlying energetics of dynamical processes are customarily parametrized to match equilibrium properties away from the activated state[6]. As systems get more involved, additional complications arise, more closely related to the nature of the dynamics as opposed to errors in the energy calculations. In these cases, the complexity of the energy surface hampers designation of functional transition states or reaction coordinates required for most rate theories, and a high number of potential reaction paths might need be considered.

In the quantum chemistry community, the most widely used rate method is Eyring's transition state theory[28]. Eyring's formulations are especially interesting for smaller molecules in vacuum, since strong assumptions are made regarding the shape of the potential energy surface. Within these assumptions, one only needs access to a limited amount of configurations representing the reactant and transition states to calculate rate constants. Finding these configurations, especially transition states, is not always straightforward, especially when dimensionality increases[10, 75–77]. Nonetheless, the limited amount of energy calculations allows for ab-initio electronic structure methods to be applied, and depending on the quality of the quantum chemical methods used, a more accurate estimate of the activation barrier is attainable.

For more complicated systems such as for larger biomolecules, the energy landscapes become more rugged and the approximations quickly brake down. Consequently, different strategies are used to determine rates for such systems, typically involving actual dynamics simulations. In these cases, electronic structure methods become computationally prohibitive and parametrized force fields are used. Depending on the size of the system, the computational resources at hand and the simulation methods used, different schemes allow for more dynamics based approaches to rate calculation, unlocking application to systems which violate the assumptions of Eyring's transition state theory.

For small energy barriers, reactions can be simulated directly, and mean first passage times (Section 2.3.1) and corresponding rates can be obtained by averaging. Alternatively, time correlation functions can be used to determine rates in the reactive flux formalism (Section 2.3.2). For complicated dynamics involving multiple metastable states, more involved methods such as Markov State Models (Section 2.3.3) can be adopted.

As energy barriers increase, crossing events become less frequent and getting sufficient statistics on their occurrence requires longer trajectories up until the point it becomes computationally prohibitive. In that case, other strategies need to be used to estimate rates of reaction events. These methods span a continuum of different approaches, and any attempt to classify them into discrete classes will be inaccurate at the classification boundaries. With this in mind, there are two distinct approaches to determine transition rates:

1. analyze the free energy surface
2. stimulate, count and reweight transitions.

Transition state theory (Section 2.3.4) or Kramers' theory (Section 2.3.5) as well as discretization approaches to the Fokker-Planck equation (Section 2.3.7) are examples of the first approach. These methods rely on models of effective dynamics in a reduced dimensional space, for which the FES is presumed to be available. Infrequent metadynamics (Section 2.4.1), path reweighting (Section 2.4.2) and transition path sampling[14, 78] are examples for the second approach. These methods involve direct numerical sampling using molecular dynamics, but transitions from the reactant to product state are artificially accelerated. Statistical methods are then employed to accurately estimate reaction rates from the enhanced sampling data. Reactive flux methods such as the Bennett-Chandler approach[79–81] can be considered a combination of both approaches.

These methods have extensively been used for transitions demanding complicated reaction coordinates often characterized by broad transition states or involving multiple possible reaction pathways. A typical test case is the conformational transition of alanine dipeptide in vacuum or solution[26,82–88]. Rates have also been calculated for protein folding[89–91], ligand binding[92–95], base-pairing transitions in DNA[74,96–98], crystal nucleation[49,99–101], and many more[6].

2.3.1 Mean First Passage Times

Imagine we are interested in transitions between two states A and B:

$$A \rightleftharpoons B\,. \tag{2.36}$$

An example could be a solution of N noninteracting particles which can occupy two conformational states. In case there is good separation of timescales, that is, if the timescales associated to the relaxation within the conformational states (τ_{mol}) is a lot smaller than the timescale on which the system must wait, on average, in one conformational state before undergoing a transition to another state (τ_{rxn}), the relaxation behaviour can be described with a linear rate law[102]:

$$\frac{\mathrm{d}}{\mathrm{d}t} N_A(t) = -k_{AB} N_A(t) + k_{BA} N_B(t) \tag{2.37a}$$

$$\frac{\mathrm{d}}{\mathrm{d}t} N_B(t) = k_{AB} N_A(t) - k_{BA} N_B(t)\,. \tag{2.37b}$$

Here, $N_A(t)$ and $N_B(t)$ are the number of particles at a time t in states A and B respectively, with $N = N_A(t) + N_B(t)$, while k_{AB} is the microscopic rate of transitioning from state A to B, and k_{BA} analogously the microscopic rate from B to A.

In MD simulations, states are generally designated by choosing a suitable reaction coordinate s and defining a value $s^{\ddagger}$ separating state A where $s \leq s^{\ddagger}$ from state B where $s > s^{\ddagger}$. The states are often represented by occupation functions

$$h_A(s(t)) = \begin{cases} 1 & \text{if} \quad s(t) \leq s^{\ddagger} \\ 0 & \text{if} \quad s(t) > s^{\ddagger} \end{cases} \qquad h_B(s(t)) = \begin{cases} 0 & \text{if} \quad s(t) \leq s^{\ddagger} \\ 1 & \text{if} \quad s(t) > s^{\ddagger} \end{cases}. \tag{2.38}$$

To simplify notation, occupation functions will be denoted with their time dependence only: $h_A(t) = h_A(s(t))$ and $h_B(t) = h_B(s(t))$. It should be remembered that the time dependence is implicit and the actual explicit dependence is on the position along the reaction coordinate at that time $s(t)$. Nonequilibrium ensemble averages of the occupation functions at a time t can be related to the number of particles $\langle h_A(t)\rangle_{\mathrm{ne}} = N_A(t)/N$ and analogous for B. The phenomenological rate law can then be written as:

$$\frac{\mathrm{d}}{\mathrm{d}t} \langle h_A(t)\rangle_{\mathrm{ne}} = -k_{AB} \langle h_A(t)\rangle_{\mathrm{ne}} + k_{BA} \langle h_B(t)\rangle_{\mathrm{ne}} \tag{2.39a}$$

$$\frac{\mathrm{d}}{\mathrm{d}t} \langle h_B(t)\rangle_{\mathrm{ne}} = k_{AB} \langle h_A(t)\rangle_{\mathrm{ne}} - k_{BA} \langle h_B(t)\rangle_{\mathrm{ne}}\,. \tag{2.39b}$$

which can be solved[6, 7, 102] as

$$\langle h_A(t)\rangle_{\mathrm{ne}} = \langle h_A\rangle + \left(\langle h_A(0)\rangle_{\mathrm{ne}} - \langle h_A\rangle\right) e^{-kt} \tag{2.40a}$$

$$\langle h_B(t)\rangle_{\mathrm{ne}} = \langle h_B\rangle + \left(\langle h_B(0)\rangle_{\mathrm{ne}} - \langle h_B\rangle\right) e^{-kt} \tag{2.40b}$$

where $\langle h_A\rangle$ is the standard equilibrium ensemble average of $h_A(t)$ corresponding to the equilibrium molecular fraction of state A with $\lim_{t\to\infty} \langle h_A(t)\rangle_{\mathrm{ne}} = \langle h_A\rangle$. The new rate constant $k = k_{AB} + k_{BA}$ is known as the phenomenological rate constant as it describes the effective exponential asymptotic relaxation towards equilibrium which could be observed in experiment. The timescale connected to the phenomenological rate $\tau_{\text{rxn}} = 1/k$ is often referred to as the reaction time and was already mentioned in the separation of timescales assumption above.

When the energy barrier between state A and B is sufficiently low to sample a lot of transitions between the states from an unbiased trajectory, rates can be estimated from mean first passage times (MFPT). The trajectory can be partitioned into segments during which it stays in the same state, i.e. starting from when it enters the state up until when the state is exited again. From these segments, the mean first passage times $\tau_{\text{MFPT},A\to B}$ for going from state A to B and $\tau_{\text{MFPT},B\to A}$ for going from B to A are calculated:

$$\tau_{\text{MFPT},A\to B} = \frac{1}{M_A}\sum_{i=1}^{M_A} t^{(i)}_{A\to B} \qquad \text{and} \qquad \tau_{\text{MFPT},B\to A} = \frac{1}{M_B}\sum_{i=1}^{M_B} t^{(i)}_{B\to A} \tag{2.41}$$

with $t^{(i)}_{A\to B}$ the time of the i-th segment recorded in state A and analogous for $t^{(i)}_{B\to A}$, and M_A and M_B the amount of segments in state A and B respectively. The microscopic rates can then be computed using

$$k^{\text{MFPT}}_{AB} = \frac{1}{\tau_{\text{MFPT},A\to B}} \qquad \text{and} \qquad k^{\text{MFPT}}_{BA} = \frac{1}{\tau_{\text{MFPT},B\to A}}\,. \tag{2.42}$$

2.3.2 Reactive Flux Formalism

The indicator functions allow easy formulation of the conditional probability to find a system in state B at time t provided it was in state A at time 0:

$$C_{AB}(t) = \frac{\langle h_A(0)h_B(t)\rangle}{\langle h_A\rangle} \tag{2.43}$$

where $\langle \dots \rangle$ indicates ensemble averaging over equilibrium initial conditions. In case of separation of timescales, it can be shown[4,79] from Onsager's regression hypothesis[103] that the time correlation function $C_{AB}(t)$ grows linearly with time in a time regime $\tau_{\text{mol}} < t \ll \tau_{\text{rxn}}$ according to $C_{AB}(t) \approx k_{AB}t$. More details about the derivation are given in Appendix A.1. The time derivative of $C_{AB}(t)$ is called the reactive flux

$$k^{\text{RF}}_{AB}(t) \equiv \frac{\mathrm{d}}{\mathrm{d}t}C_{AB}(t)\,. \tag{2.44}$$

In the time regime $\tau_{\text{mol}} < t \ll \tau_{\text{rxn}}$, $k^{\text{RF}}_{AB}(t)$ has a horizontal plateau with height equal to the microscopic rate constant k_{AB}. For very long times, $C_{AB}(t)$ reaches $\langle h_B\rangle$ asymptotically in accordance with Eq. A.6, and consequently $k^{\text{RF}}_{AB}(t)$ goes to zero. At times below the molecular relaxation time τ_{mol}, $C_{AB}(t)$ will incorporate correlations in microscopic motion including recrossing effects, and consequently the reactive flux $k^{\text{RF}}_{AB}(t)$ can be unstable in this regime. A sketch of $k^{\text{RF}}_{AB}(t)$ as a function of time is given in Fig. 2.1.

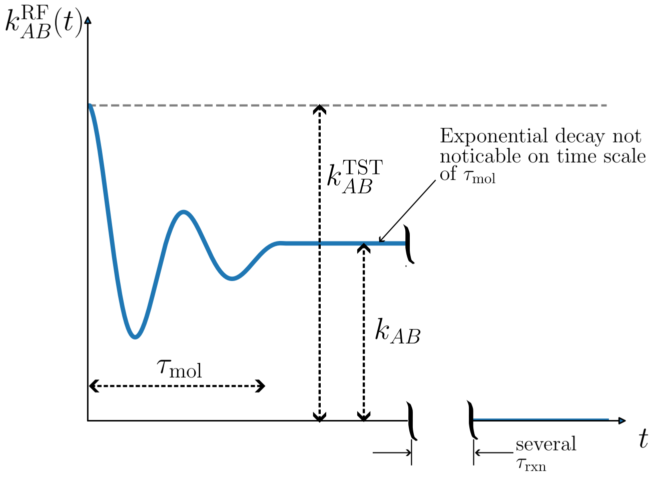

Figure 2.1: Sketch of behaviour of $k_{AB}^{\mathrm{RF}}(t)$ as a function of time. Based on similar figures in Refs. [4, 7].

Carrying out the time derivative to the time correlation function gives an expression of the reactive flux in terms of the velocity along the reaction coordinate s:

$$k_{AB}^{\mathrm{RF}}(t) = \frac{\left\langle \dot{s}(0)\delta\left(s(0) - s^{\ddagger}\right) h_B(s(t))\right\rangle}{\langle h_A \rangle} \tag{2.45}$$

where the dot notation signifies a time derivative and $\delta\left(s(0) - s^{\ddagger}\right)$ is the Dirac delta function. The derivation can be found in Appendix A.2. This formulation of the reactive flux gives a more intuitive interpretation of its meaning. The flux can be considered as the average velocity in the reaction coordinate $\dot{s}$ at the dividing surface defined by $s = s^{\ddagger}$, with the additional condition that the system is in state B a time t later. For small times $t < \tau_{\mathrm{mol}}$, the system might not have settled 'definitively' in state B yet, and still recross to state A, making the velocity averaging unreliable. Commonly such recrossings originate from interactions of the reaction coordinate with other degrees of freedom[7, 43]. For times larger than the molecular relaxation time τ_{mol}, the system should have relaxed in either state A or state B, and the reactive flux is expected to reach a plateau value equal to the microscopic rate k_{AB} before decaying to zero in the long time limit. Notice the reactive flux formulations do not involve any underlying assumptions about the dynamics or thermodynamic ensemble, and thus is formally exact. The accuracy of the calculated rate only depends on definitions of the reactant and product states A and B, and the interpretation of the plateau region.

2.3.3 Markov State Models

More involved systems such as proteins and nucleic acid often show complex dynamics involving transitions between various long-lived metastable states through a multitude of reaction paths. Often, the existence and location of metastable states and barriers are not known beforehand, and determination of MFPTs is not achievable through direct measurement as in the previous section, even when dynamics are properly sampled. A more meticulous approach to investigate the dynamical behavior entails a partitioning of the configurational space into discrete cells and subsequently calculating rates or transition probabilities between the cells. In this way, the view of a single barrier crossing or trajectory path is abandoned in favor of an ensemble view of the dynamics. Of course, dynamical information can still be disguised within a single cell, i.e. when parts of configurational space that have an important distinction have been lumped together during discretization. A sufficiently fine partitioning can resolve this issue.

To obtain rate and transition matrices from continuous dynamics, configuration space Γ_q is divided in a disjoint decomposition of n_c cells Σ_i such that $\Gamma_q = \cup_{i=1}^{n_\mathrm{c}} \Sigma_i$. To do so, we define the characteristic function indicating cell i as

$$\chi_i\left(\mathbf{q}\right) = \begin{cases} 1 & \text{if} \quad \mathbf{q} \in \Sigma_i \\ 0 & \text{if} \quad \mathbf{q} \notin \Sigma_i \end{cases} \tag{2.46}$$

for $i = 1, \ldots, n_\mathrm{c}$. These can be considered higher-dimensional and multistate equivalents of the occupation functions defined in Eq. 2.38 in the previous section. Cell probabilities $\rho_i(t)$ of probability vectors $\boldsymbol{\rho}(t) \in \mathbb{R}^{n_\mathrm{c}}$ can be formulated as $\rho_i(t) = \int_{\Gamma_q} \mathrm{d}\mathbf{q}\, \chi_i(\mathbf{q})\rho(\mathbf{q}, t)$ and equilibrium probabilities π_i of equilibrium probability vector $\boldsymbol{\pi} \in \mathbb{R}^{n_\mathrm{c}}$ as $\pi_i = \int_{\Gamma_q} \mathrm{d}\mathbf{q}\, \chi_i(\mathbf{q})\nu(\mathbf{q}) = \langle \chi_i \rangle$ with $\nu(\mathbf{q})$ the equilibrium probability distribution defined in Eq. 2.6. The Fokker-Planck operator $\mathcal{Q}$ in the Smoluchowski equation (Eq. 2.11b) can be discretized in a Galerkin discretization[88, 104] to yield a $n_\mathrm{c} \times n_\mathrm{c}$ rate matrix $\mathbf{Q}$:

$$Q_{ij} = \frac{\langle \chi_j | \mathcal{Q}\chi_i \rangle_\nu}{\langle \chi_i | \chi_i \rangle_\nu} = \frac{1}{\pi_i} \langle \chi_j | \mathcal{Q}\chi_i \rangle_\nu \tag{2.47}$$

where the scalar product in weighted space $\langle u|v \rangle_\nu = \int_{\Gamma_q} u(\mathbf{q})v(\mathbf{q})\nu(\mathbf{q})\mathrm{d}\mathbf{q}$ was introduced. The discretized Fokker-Planck equation is then written as

$$\partial_t \boldsymbol{\rho}^T(t) = \boldsymbol{\rho}^T(t)\mathbf{Q}\,. \tag{2.48}$$

Given overdamped dynamics, the rate matrix thus indicates the probability per unit of time that transition occurs within an infinitesimally small time interval.

Assuming transitions between cells are Markovian, the rate matrix will be constant in time and independent of the initial probability. Eq. 2.48 can be solved as $\boldsymbol{\rho}^T(t) = \boldsymbol{\rho}^T(0)\exp\left(t\mathbf{Q}\right)$ which allows definition of the propagator

$$\mathbf{T}(\tau) = \exp\left(\tau\mathbf{Q}\right)\,. \tag{2.49}$$

The matrix element $T_{ij}(\tau)$ indicates the conditional probability for the system to be found in cell j given that it was in cell i at a fixed time τ before, and therefore $\mathbf{T}(\tau)$ is generally referred to as the *transition matrix.* Probability vectors can be propagated over a time τ according to

$$\boldsymbol{\rho}^T(t+\tau) = \boldsymbol{\rho}^T(t)\mathbf{T}(\tau)\,. \tag{2.50}$$

Because we have assumed Markovianity, probabilities at a later time $t + a\tau$ can also be obtained by repeated application of the transition matrix, which can be formulated as

$$\boldsymbol{\rho}^T(t+a\tau) = \boldsymbol{\rho}^T(t)\mathbf{T}^a(\tau)\,. \tag{2.51}$$

Eq. 2.51 is a formulation of the well-known Chapman-Kolmogorov equation[44]. It can be shown that a transition matrix generally has a unique stationary distribution $\boldsymbol{\pi} \in \mathbb{R}^n$, which remains unchanged under application of the transition matrix $\boldsymbol{\pi}^T = \boldsymbol{\pi}^T\mathbf{T}(\tau)$. For dynamics at thermal equilibrium, the transition matrix fulfills detailed balance $\pi_i T_{ij} = \pi_j T_{ji}$.

The transition matrix can be applied directly to propagate any density vector, and can thus be used to model evolution of nonequilibrium distributions in time. Alternatively, essential dynamical information about the conformation dynamics of the system can be obtained by studying the eigenvectors and eigenvalues of the transition matrices[105]. As explained in Appendix B.1, the largest eigenvalues $\lambda_i(\tau)$ of $\mathbf{T}(\tau)$ can be used to calculate implied timescales connected to exponential decay of nonequilibrium processes:

$$t_i = -\frac{\tau}{\ln \lambda_i(\tau)}\,. \tag{2.52}$$

For Markovian processes, the implied timescales do not depend on time τ. The corresponding leading eigenvectors can be considered the principal modes of probability flow between the system's metastable states, governing evolution of nonequilibrium probability densities $\boldsymbol{\rho}(t)$ towards the equilibrium probability $\boldsymbol{\pi}$. From Eq. 2.49 it follows that the rate matrix $\mathbf{Q}$ has the same eigenvectors as $\mathbf{T}(\tau)$, while its eigenvalues θ_i are related to those of the transition matrix through $\lambda_i(\tau) = \exp(\tau\theta_i)$. Consequently, the eigenvalues of the rate matrix are directly related to the implied timescales

$$t_i = -\frac{1}{\theta_i}\,. \tag{2.53}$$

The implied timescales (and corresponding rates) do not have a forward or backward direction, but should rather be considered as equivalents to the reaction time τ_{rxn} (or phenomenological rate constant k) considered in Section 2.3.1. In fact, as is shown in Appendix B.2, for a two-state system under Markovian assumptions, the implied timescale equals the reaction time $t_1 = \tau_{\text{rxn}}$.

Markov state models (MSM) estimate the transition matrix $\mathbf{T}(\tau)$ from one or multiple

MD trajectories. The matrix elements $T_{ij}(\tau)$ can be written as conditional probabilities[106]:

$$T_{ij}(\tau) = \mathcal{P}\left[\mathbf{q}(t+\tau) \in \Sigma_j \,|\, \mathbf{q}(t) \in \Sigma_i\right] \tag{2.54}$$

where τ is called the lag time. Using Bayes' theorem, Eq. 2.54 can be reformulated as[106,107]

$$\begin{aligned} T_{ij}(\tau) &= \frac{\mathcal{P}\left[\mathbf{q}(t+\tau) \in \Sigma_j \,\cap\, \mathbf{q}(t) \in \Sigma_i\right]}{\mathcal{P}\left[\mathbf{q}(t) \in \Sigma_i\right]} && \text{(2.55a)} \\ &= \frac{\langle \chi_j\left(\mathbf{q}(\tau)\right) \chi_i\left(\mathbf{q}(0)\right)\rangle}{\langle \chi_i \rangle} && \text{(2.55b)} \\ &= \frac{c_{ij}^{\text{corr}}(\tau)}{\pi_i} && \text{(2.55c)} \end{aligned}$$

where in Eq. 2.55b the ensemble averaging in the numerator is over equilibrium initial conditions[107]. This numerator can be interpreted as an equilibrium time-lagged correlation function $c_{ij}^{\text{corr}}(\tau)$ between indicator functions χ_j and χ_i. The matrix elements $T_{ij}(\tau)$ can thus be considered the multistate equivalents of the time correlation function used in the reactive flux formalism in Eq. 2.43. From the definitions of the indicator functions, it follows that $\sum_{i=1}^{n_\text{c}} c_{ij}^{\text{corr}}(\tau) = \pi_j$ and $\sum_{j=1}^{n_\text{c}} c_{ij}^{\text{corr}}(\tau) = \pi_i$ for any value of lag time τ.

For long enough MD trajectories, and in case $\mathbf{q}(t)$ is ergodic (Eq. 2.9), this correlation function can be expressed as

$$c_{ij}^{\text{corr}}(\tau) = \lim_{M\to\infty} \frac{1}{M} \sum_{k=1}^{M} \chi_i(\mathbf{q}_k)\chi_j(\mathbf{q}_{k+l}) \tag{2.56}$$

where $l\Delta t = \tau$ with Δt the time step of the trajectory. In practice, one often builds a count matrix $\mathbf{C}(\tau)$ where the matrix elements $C_{ij}(\tau)$ are calculated by counting transitions over a long trajectory from bin i to bin j within a time span τ

$$C_{ij}(\tau) = \sum_{k=1}^{n_\text{MD}-l} \chi_i(\mathbf{q}_k)\chi_j(\mathbf{q}_{k+l}) \tag{2.57}$$

with n_MD the total amount of time steps in the trajectory. The transition matrix elements can then be estimated as

$$T_{ij}(\tau) = \frac{C_{ij}(\tau)}{\sum_{j=1}^{n_\text{c}} C_{ij}(\tau)} \tag{2.58}$$

or, in other words, by row-normalizing the count matrix $\mathbf{C}(\tau)$.

At this point, it is important to consider that the Markovian assumption might be violated in the construction of MSMs. Mapping the (spatially) continuous dynamics $\mathbf{q}(t)$ onto a discrete set of cells Σ_i (Eqs. 2.54-2.55) generally makes the process non-Markovian. Local dynamical effects within the cells can make transition probabilities history dependent[2], and

---

[2] For example: it is completely conceivable that a system which has just entered cell j coming from cell i

the calculated implied timescales generally become dependent of lag time τ. Nonetheless, MSMs model these dynamics using a transition matrix where the Markovian property is assumed. In this context, formulations using the transition and rate matrices in Eqs. 2.49 and 2.51 are only approximations. Non-Markovianity effects introduce a discretization error[106] that makes both propagation of density vectors (Eq. 2.51) and timescale computation from eigenvector analysis (Eq. 2.52) approximate. In general, the error made will depend on:

- *Discretization:* larger cells will lump together more dynamics and consequently worsen Markovianity. A finer discretization will generally reduce the error. Moreover, discretization can be adapted to fit metastable states if they are known[106].
- *Collective variable space:* discretization is often chosen to depend only on a low number of specific collective variables. The CV space on which the discretization is build ideally incorporates all slow dynamics. Slow correlated motion not included in the resolved degrees of freedom will induce memory effects and worsen Markovianity, leading to larger errors.
- *Choice of lag time τ:* for short lag times $\tau < \tau_{\mathrm{mol}}$, the correlation function in Eq. 2.55b will incorporate correlation in local microscopic dynamics. These can introduce memory effects on short timescales which cause errors in determination of the slowest dynamical components. Therefore, transition matrices should be used and analyzed only at sufficiently high lag times $\tau > \tau_{\mathrm{mol}}$.

Commonly, convergence of the implied timescales of the slowest processes are monitored to check which lag time to use[106]. For small lag times, implied timescales are often severely underestimated, whilst an asymptotic convergence is expected as lag times get longer. For good choices of CVs and discretizations, the implied timescales converge faster, and the calculated timescales and eigenvectors become reliable representation of the system's slowest dynamical processes.

Notice that is often not obvious from the eigenvectors by themselves which bins will correspond to which metastable states. Methods for assigning bins to metastable states from the transition matrix eigenvectors can be found in literature[108, 109].

2.3.4 Transition State Theory

Transition state theory (TST) embodies a theoretical framework which allows formulation of relatively simple rate equations for chemical reactions starting from the free energy surface. In its most general form, the following key assumptions are made[6]:

1. Classical dynamics on a single Born-Oppenheimer PES

---

has a higher probability of returning to i than a system which has been in cell j for a longer time.

2. A dividing surface that separates reactants and products
3. States on the dividing surface are populated as though at equilibrium with reactants
4. Trajectories that cross the dividing surface lead directly to products with no recrossing events.

The first point is generally assumed in classical MD simulations. The second point had already been assumed in Sections 2.3.1 and 2.3.2 to formally define states A and B in mean first passage times and the reactive flux formulations. The third and fourth point are additional assumptions specific to TST, and form the basis of further simplifications in rate expressions.

In the one-dimensional formulation of TST, one assumes knowledge of the FES $F(s)$ in a one-dimensional reaction coordinate s. For a reaction $A \rightleftharpoons B$, the assumptions above allow for the following formulation of the rate constant[6, 8]:

$$k_{AB}^{\mathrm{TST}} = \frac{1}{2} \langle |\dot{s}| \rangle_{\ddagger} \exp\left(-\beta \Delta F^{\ddagger}\right) . \tag{2.59}$$

Here, $\langle |\dot{s}| \rangle_{\ddagger}$ is the averaged absolute velocity along s at the transition state and $\Delta F^{\ddagger} = F(s^{\ddagger}) - F_A$ with $s^{\ddagger}$ the value of s at the transition state and $F_A = -\beta^{-1} \ln \left[l_s^{-1} \int_A \mathrm{d}s \exp\left(-\beta F(s)\right) \right]$ the free energy of the reactant well. Derivations of Eq. 2.59 typically commence by formulating an equilibrium constant between the reactant state and an activated complex at the transition state. From the activated complex, the trajectories are assumed to move to the product state B at a frequency related to the average velocity along the reaction coordinate. However, the expression can also be derived directly from the reactive flux formalism as is shown in Appendix A.3.

If we approximate the free energy near the reactant state A by a harmonic potential

$$F(s) = F(s_A) + \frac{1}{2} \mu_s \omega_A^2 (s - s_A)^2 \qquad \text{for} \qquad s \in A \tag{2.60}$$

where μ_s is the effective mass in the reaction coordinate and ω_A is the angular frequency, and, since we assume thermal equilibrium of the dividing surface, we let

$$\langle |\dot{s}| \rangle_{\ddagger} \approx \langle |\dot{s}| \rangle = \frac{\int_{-\infty}^{+\infty} \mathrm{d}\dot{s} \exp\left(-\beta \mu_s \dot{s}^2/2\right) \cdot |\dot{s}|}{\int_{-\infty}^{+\infty} \mathrm{d}\dot{s} \exp\left(-\beta \mu_s \dot{s}^2/2\right)} = \sqrt{\frac{2 k_B T}{\pi \mu_s}} \tag{2.61}$$

where the Maxwell-Boltzmann distribution was used, we obtain:

$$k_{AB}^{\mathrm{TST}} = \frac{\omega_A}{2\pi} \exp\left(-\beta F^{\ddagger}\right) \tag{2.62}$$

where $F^{\ddagger} = F(s^{\ddagger}) - F(s_A)$ is the free energy barrier measured from the bottom of state A (and thus defined differently from $\Delta F^{\ddagger}$). Eq. 2.62 is often referred to as *one-dimensional harmonic transition state theory* or *simple transition state theory* and corresponds to Eq. 3.5

in Ref. 8.

Formulations of the TST rate in full dimensional space for a general multidimensional potential energy surface $V(\mathbf{q})$ have been derived and are available in literature, see for example Eqs. 3.6 and 3.13 in Ref. 8. For the special case of a nonlinear reaction coordinate coupled to N_{dof} orthogonal vibrational degrees of freedom, the rate constant takes the form[110]:

$$k_{AB}^{\mathrm{TST}} = \frac{1}{2\pi} \frac{\prod_{i=0}^{N_{\mathrm{dof}}} \omega_A^{(i)}}{\prod_{i=1}^{N_{\mathrm{dof}}} \omega_{\ddagger}^{(i)}} \exp\left(-\beta E_b\right) . \tag{2.63}$$

Here, $\omega_A^{(i)}$ and $\omega_{\ddagger}^{(i)}$ are the angular frequencies in the ith vibrational degree of freedom of the reactant and transition states respectively, and $E_b = V(s^{\ddagger}) - V(s_A)$ is the potential energy barrier. $i = 0$ denotes the nonlinear reaction coordinate while all higher indices refer to the coupled vibrational degrees of freedom.

Using the harmonic partition functions for the reactant and transition state in the classical limit:

$$Z_A = \prod_{i=0}^{N_{\mathrm{dof}}} \left(\frac{k_B T}{\hbar \omega_A^{(i)}} \right) \qquad \text{and} \qquad Z^{\ddagger} = \prod_{i=1}^{N_{\mathrm{dof}}} \left(\frac{k_B T}{\hbar \omega_{\ddagger}^{(i)}} \right) \tag{2.64}$$

we can rewrite the TST rate:

$$k_{AB}^{\mathrm{TST}} = \frac{k_B T}{h} \frac{Z^{\ddagger}}{Z_A} \exp\left(-\beta E_b\right) . \tag{2.65}$$

Assuming equilibrium between reactant and transition state, the corresponding equilibrium constant can be written in terms of the partition functions, $K^{\ddagger} = \frac{Z^{\ddagger}}{Z_A} \exp\left(-\beta E_b\right)$, which allows the rate constant to be formulated as

$$k_{AB}^{\mathrm{TST}} = \frac{k_B T}{h} \exp\left(-\beta \Delta A^{\ddagger}\right) . \tag{2.66}$$

where we used the well-known relation between the equilibrium constant and free energy $K^{\ddagger} = \exp\left(-\beta \Delta A^{\ddagger}\right)$ with $\Delta A^{\ddagger}$ the Helmholtz free energy difference between the transition and reactant states. Notice the reaction coordinate degree of freedom is excluded in the transition state partition function in Eq. 2.64 and should thus also be excluded in the transition state free energy calculation[6]. Care has to be taken not to confuse Eqs. 2.62 and 2.66. The prefactors differ, and the free energies have been defined in different ways: $F^{\ddagger}$ is the free energy barrier measured from the bottom of the reactant well to the top of the barrier, equivalent to E_b in full dimensional space, whereas $\Delta A^{\ddagger}$ can be considered the full free energy difference between reactant and transition states. The prefactor of one equation should not be used in combination with the exponential factor of the other.

The TST rate equations above have been derived within the realm of classical mechanics (assumption 1.), and thus do not incorporate effects of quantization such as zero-point energies (ZPE). One approach to incorporate these effects is to substitute the classical partition functions in Eq. 2.65 by their quantum variants[3]. The corresponding equation is commonly referred to as the *Eyring equation*[28].

To calculate rates using the Eyring equation, geometry optimization algorithms are used to determine the molecular configurations of the reactant state minimum and transition state saddle point on the potential energy surface. The quantum partition function analogons in Eq. 2.65 can then be calculated using a local quadratic approximation for both configurations[4], where the frequencies of the vibrational modes are obtained by taking the square root of the corresponding eigenvalues of the mass-weighted Hessian[114]. Because in principle only two configurations need to be found and analyzed, it is relatively easy to evaluate Eq. 2.65. Moreover, it will give surprisingly accurate rate constants whenever the dynamical bottleneck of the activated process is a clearly distinguishable high saddle on the molecular PES[6]. Consequently, the Eyring equation is frequently used in the quantum chemistry community (see for example refs. 113,115–117). Evaluation of the Eyring equation and its classical equivalent (also called the high-temperature limit), as well as the connection between the quantum and the classical partition functions are described in more detail in Section 3.1 and its supporting information.

For complicated potential energy surfaces with more rugged energy landscapes, the local quadratic approximation around a single reactant state minimum and transition state saddle point will no longer yield an accurate enough description of the reaction dynamics. In this case, sampling a free energy profile $F(s)$ in a one-dimensional reaction coordinate and applying simple TST using Eq. 2.62 might yield a better result. Determining the free energy as a function of the reaction coordinate $F(s)$, however, generally requires dynamical calculations in combination with enhanced sampling methods. Notice that simple TST still uses a harmonic approximation, but only in the reactant state free energy profile along the reaction coordinate. Furthermore, as potential energy surfaces and corresponding dynamics become more involved, the fundamental no-recrossing assumption of TST also becomes less tangible. In the following sections we discuss rate theories improving on the assumptions of TST.

2.3.5 Kramers' Theory

Kramers' rate theory describes chemical reactions as one-dimensional diffusive processes in reaction coordinate s. A particle of mass μ_s moves on the free energy surface $F(s)$ starting

---

[3] A fully rigorous quantum prescription for determining rate constants necessitates solving the time dependent Schrödinger equation, which is often done by working out the complete state-to-state reactive scattering problem[35]. Substituting in the quantum partition functions does not suffice for a fully quantum mechanical prescription, as, for example, it does not account for nuclear tunneling[111] important in proton transfer reactions[5].

[4] Additionally, the translational, rotational and electronic partition functions will need to be calculated, see Refs. 112, 113.

from a harmonic reactant well (denoted as state A) moving over a parabolic barrier driven by the Langevin equation (Eq. 2.2). Let us assume that the minimum of the harmonic well potential is located at $s = s_A$ as in Eq. 2.60 and the barrier is located at $s = s^\ddagger = 0$, with $s_A < s^\ddagger$ and

$$F(s) = F(s^\ddagger) - \frac{1}{2}\mu_s\omega_\ddagger^2\left(s - s^\ddagger\right)^2 = F(s^\ddagger) - \frac{1}{2}\mu_s\omega_\ddagger^2 s^2 \qquad \text{for} \qquad s \approx s^\ddagger\,, \tag{2.67}$$

where $\omega_\ddagger$ is the angular frequency of the parabolic barrier. At this point, let us consider the barrier $F^\ddagger = F(s^\ddagger) - F(s_A)$ to be significantly larger than the thermal noise, i.e. $\beta^{-1} \ll F^\ddagger$ so there is separation of timescales between relaxation in reactant state (τ_{mol}) and the escape time (τ_{rxn}). We assume the friction coefficient is constant, and additionally presume a steady-state non-equilibrium flux from state A to state B and vice versa, maintained by a source which generates a new trajectory every time that the particle crosses the barrier and is absorbed by a sink at the other side of the barrier [8]. This assumption replaces the requirement for thermal equilibrium between reactant and transition state in transition state theory. Under these assumptions, Kramers derived rates k_{AB}^{Kra} for different friction regimes[6, 8].

1. **Weak friction limit.** If $\xi\omega_\ddagger^{-1} < \left(\beta F^\ddagger\right)^{-1} \ll 1$, the deterministic forces dominate the diffusive forces (*energy diffusion limited regime*), and the energy of the system is almost constant. Under these conditions, the escape rate from the reactant state A reads

$$k_{AB}^{\mathrm{Kra}} = \xi\beta I(F^\ddagger)\frac{\omega_A}{2\pi}\exp\left(-\beta F^\ddagger\right)\,, \tag{2.68}$$

   where we have introduced the abbreviated action variable at energy $F^\ddagger$,

$$I(F^\ddagger) = \frac{2\pi F^\ddagger}{\omega_A}\,. \tag{2.69}$$

   Notice that for a two-state system, i.e. for a free energy surface with two harmonic wells, a particle that acquires sufficient energy to escape one well may, on account of the weak friction, bounce back and forth until it stabilizes in one of either wells. This will influence the effective rate of transitioning from state A to B, as we do not want to include escapes from A that end up back in A a short time later. Therefore, the rate in Eq. 2.68 is commonly multiplied with the probability of ending up in state B once an escape from A is registered. Expressions can be found in Ref. 8 or alternatively in Section 3.2 and its supporting information below.

2. **Moderate-to-high friction limit.** If $\xi\omega_\ddagger^{-1} > \left(\beta F^\ddagger\right)^{-1}$, the diffusive forces are stronger than the deterministic force defined by the free energy function. This is known

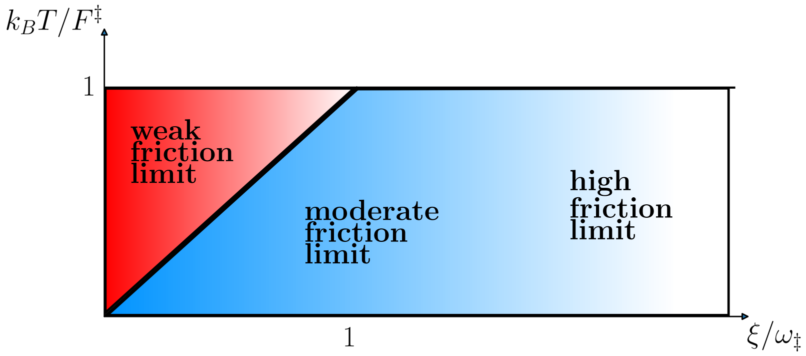

Figure 2.2: Regime of validity of Kramers rate formula (Fig. 15 in Ref. 8).

as the diffusion-dominated regime and the Kramers rate constants is

$$k_{AB}^{\text{Kra}} = \frac{\xi}{\omega_\ddagger}\left(\sqrt{\frac{1}{4}+\frac{\omega_\ddagger^2}{\xi^2}}-\frac{1}{2}\right)\frac{\omega_A}{2\pi}\exp\left(-\beta F^\ddagger\right), \tag{2.70}$$

3. **High friction limit.** If $\xi\omega_\ddagger^{-1} \gg \left(\beta F^\ddagger\right)^{-1}$, then Eq. 2.70 converges to

$$k_{AB}^{\text{Kra}} = \frac{\omega_\ddagger}{\xi}\frac{\omega_A}{2\pi}\exp\left(-\beta F^\ddagger\right). \tag{2.71}$$

In the high friction limit, the diffusive forces dominate the deterministic forces (*spatial diffusion limited regime*, also shortly called the *diffusive regime*), and dynamics are often referred to as being *overdamped*. In this regime, Langevin dynamics converge to Brownian dynamics as was explained in Section 2.1.3. Trajectories are propagated according to Eq. 2.10 while the probability density behaves according to Eq. 2.11a.

Fig. 2.2 summarizes under which conditions the friction regimes hold. Notice that in each of the friction regimes, the rates (Eqs. 2.68-2.71) are easily expressed as a function of the simple TST rate of Eq. 2.62:

$$k_{AB}^{\text{Kra}} = \kappa\frac{\omega_A}{2\pi}\exp\left(-\beta F^\ddagger\right) = \kappa k_{AB}^{\text{TST}} \tag{2.72}$$

where κ is referred to as the transmission coefficient and is a number between zero and one. We remark that in all equations so far, it was assumed the friction and diffusion coefficients are position independent. Despite the assumption of constant friction, Kramers' equations are routinely applied to systems with position dependent friction, in which case the value at the barrier $\xi^\ddagger$ is used in the rate equations. Evidently this constitutes an approximation of the true dynamics. Methods which incorporate full diffusion profiles are discussed below.

2.3.6 Pontryagin Rate

Kramers' expressions allow for rate calculations over different friction regimes under assumptions of parabolic barriers and constant friction coefficients. In the high friction regime specifically, however, an exact rate expression can be derived for any shape of the barrier and considering a position dependent friction coefficient. In the high friction limit and for position dependent diffusion, trajectories are described by Eq. 2.20. From the associated density evolution in Eq. 2.21, one derives the exact escape rate[118]:

$$k_{AB}^{\mathrm{Pon}} = \left\{ \int_{s_A}^{s_B} \mathrm{d}s' \left[\frac{1}{D(s')} e^{\beta F(s')} \int_{-\infty}^{s'} \mathrm{d}s'' \, e^{-\beta F(s'')} \right] \right\}^{-1} . \tag{2.73}$$

In literature, Eq. 2.73 is often quite generically referred to as the formula for mean first passage time for diffusion over a barrier (which is inverted to get the rate) or the escape rate. For the sake of clarity, we shall refer to it as the *Pontryagin rate equation* after Ref. 118. Inserting the parabolic approximation and assuming constant diffusion in Eq. 2.73 yields Kramers' rate equation in the high friction limit (Eq. 2.71).

2.3.7 Grid-Based Models for Discretization of the Fokker-Planck Operator

In grid-based models, the rate matrix $\mathbf{Q}$ is estimated directly from the free energy surface and the diffusion profile of the system[88, 104]. Unlike for MSMs, no calculations of correlation functions are necessary, and thus no actual trajectories are required.

Using a uniform Voronoi tessellation[88, 104] of configurational space using n_c cells, the rate matrix is obtained from a discretization of the Fokker-Planck operator $\mathcal{Q}$ as in Eq. 2.47. The integral in Eq. 2.47, however, is too high-dimensional to solve directly. Moreover, the numerator cannot be calculated using correlation functions as was done for the transition matrix elements in Eq. 2.54. Instead, the Gauss theorem is used to write rates between neighboring cells as a surface integral over the flux, weighted by the Boltzmann density of the intersecting surface[88]. This Boltzmann weight between adjacent Voronoi cells Σ_i and Σ_j can be estimated as the geometric average $\sqrt{\nu(\mathbf{q}_j)\nu(\mathbf{q}_i)}$, which is why this specific formulation of grid-based method is referred to as the square-root approximation (SqRA). Here, $\nu(\mathbf{q})$ is the equilibrium distribution and $\mathbf{q}_i$ and $\mathbf{q}_j$ are the positions of the centers of cells Σ_i and Σ_j respectively. Furthermore, the flux between cells is assumed to be constant, i.e. the flux is assumed not to depend on the potential energy but on the discretization of the space instead. Under sufficiently fine discretization, the rate matrix elements can then be approximated from the equilibrium probability, the diffusion profile $D(\mathbf{q})$, the area of the intersecting surfaces between cells S_{ij}, the volume of the cell V_i and the Euclidean distance between the centers of the cell $h_{ij} = \|\mathbf{q}_j - \mathbf{q}_i\|$:

$$Q_{ij} = \begin{cases} D_{ij}\frac{\mathcal{S}_{ij}}{\mathcal{V}_i h_{ij}}\frac{\sqrt{\nu(\mathbf{q}_j)\nu(\mathbf{q}_i)}}{\nu(\mathbf{q}_i)} & \text{if } i \neq j \text{ and cells adjacent} \\ 0 & \text{if } i \neq j \text{ and cells not adjacent} \\ -\sum_{l=1,l\neq i}^{n_\mathrm{c}} Q_{il} & \text{if } i = j \end{cases} \tag{2.74}$$

where $D_{ij} = \left(D(\mathbf{q}_j) - D(\mathbf{q}_i)\right)/2$.

As mentioned, the rate matrix Q has the same eigenvectors as the transition matrix $\mathbf{T}(\tau)$ used in MSMs (under Markovian assumptions, see Section 2.3.3). The eigenvalues θ_i of the rate matrix are related to those of the transition matrix through $\theta_i = -\ln\lambda_i/\tau$ and consequently, implied timescales can be calculated directly using Eq. 2.53. The rate matrix can also be used to estimate microscopic rates directly by introducing a column vector $\boldsymbol{\tau}_j$ of size n_c containing the mean first passage times $\tau_{\mathrm{MFPT},i\to j}$ from starting cells with centers $\mathbf{q}_i$ (with $i = 1, \ldots, n_\mathrm{c}$) to the cell with center $\mathbf{q}_j$. Given the rate matrix $\mathbf{Q}$, the vector $\boldsymbol{\tau}_j$ solves the partial differential equation

$$\mathbf{Q}\,\boldsymbol{\tau}_j = -\mathbf{1}\,, \tag{2.75}$$

subject to the boundary condition $\tau_{\mathrm{MFPT},j\to j} = 0$ as in Ref. 119. Solving the linear matrix equation (Eq. 2.75) yields the MFPTs and rates from all cells with centers $\mathbf{q}_i$ to cell with center $\mathbf{q}_j$

$$k_{ij}^{\mathrm{SqRA}} = \frac{1}{\tau_{\mathrm{MFPT},i\to j}}\,. \tag{2.76}$$

In case it is known which cells j belong to the product state B, the boundary condition can be extended to calculate MFPTs to the full product state. This is done by setting $\tau_{\mathrm{MFPT},j\to j} = 0$ for all j belonging to B before solving the linear matrix equation in Eq. 2.75. If it is also known which cells i belong to the reactant state A, the resulting MFPTs $\tau_{\mathrm{MFPT},i\to j}$ can be averaged over reactant state equilibrium conditions:

$$\tau_{\mathrm{MFPT},A\to B} = \sum_{i\in A}\pi_{A,i}\,\tau_{\mathrm{MFPT},i\to j} \tag{2.77}$$

where

$$\pi_{A,i} = \pi_i/\sum_{i\in A}\pi_i\,. \tag{2.78}$$

This yields an average time $\tau_{\mathrm{MFPT},A\to B}$ and corresponding rate $k_{AB}^{\mathrm{SqRA}} = 1/\tau_{\mathrm{MFPT},A\to B}$ which can be compared directly to rates obtained from rare event methods above.

2.4 Dynamical Reweighting

In the previous Section, methods to estimate rate constants for molecular transitions were introduced. Some methods required sampling of transitions through direct (unbiased) simulations of the molecular dynamics. Alternatively, methods based in effective dynamics in one or lower dimensional spaces were presented. These generally required knowledge of the free energy and diffusion profiles in order to estimate rate constants.

In this Section, we introduce methods to estimate rates obtained from biased molecular dynamics trajectories. Similar as for the enhanced sampling methods in Section 2.2, biasing the potential energy function can stimulate transitions and speed up sampling. While for enhanced sampling methods, this is done to generate a representative ensemble of configurations, the methods introduced here aim to reweight dynamical properties. In other words, the aim is to determine transition times at the unbiased potential from trajectories generated at a biased potential (Fig. 1.1).

2.4.1 Infrequent Metadynamics

Infrequent metadynamics[120] (InMetaD) is a method to calculate transition times based on the related well-tempered metadynamics method introduced in Section 2.2.2. The biasing potential (Eq. 2.22) is identical in both methods and is given by Eqs. 2.31-2.32. In infrequent metadynamics, the molecular system is initialized in a state A from which a WTMetaD simulation is run until a transition to a different state B occurs. At that point, the biased transition time $\widetilde{t}^{(i)}_{A\to B}$ is recorded, where i denotes the index of the InMetaD run. The unbiased transition time $t^{(i)}_{A\to B}$ can be estimated by scaling the biased time according to an acceleration factor $\alpha^{(i)}$

$$t^{(i)}_{A\to B} = \alpha^{(i)} \cdot \widetilde{t}^{(i)}_{A\to B} \,. \tag{2.79}$$

In other words, the acceleration factor links the biased transition time to the transition time for the unbiased potential, and can be calculated as follows[57, 120, 121]

$$\begin{aligned} \alpha^{(i)} &= \left\langle e^{\beta U^{\text{bias}}(\mathbf{z},t)} \right\rangle_i && \text{(2.80a)} \\ &= \frac{1}{\widetilde{t}^{(i)}_{A\to B}} \int_0^{\widetilde{t}^{(i)}_{A\to B}} \mathrm{d}t\, e^{\beta U^{\text{bias}}(\mathbf{z},t)} \,, && \text{(2.80b)} \end{aligned}$$

where $\langle \dots \rangle_i$ denotes ensemble averaging over the trajectory at the biased potential up to the time of transition $\widetilde{t}^{(i)}_{A\to B}$, as expressed in the time-averaging in the second line. This expression is derived based on transition state theory (Section 2.3.4) and assumes no bias is present in the TS region until transition occurs. Consequently, the deposition rate is kept low during InMetaD runs (i.e. lower than the expected time spent in the TS region). By combining Eqs. 2.79 and 2.80b, the unbiased transition time can also be expressed as[22, 122]

$$t^{(i)}_{A\to B} = \int_0^{\widetilde{t}^{(i)}_{A\to B}} \mathrm{d}t \, e^{\beta U^{\text{bias}}(\mathbf{z},t)} \tag{2.81a}$$

$$= \Delta t \sum_{j=1}^{n^{(i)}_{\text{MD}}} e^{\beta U^{\text{bias}}(\mathbf{z}(t_j),t_j)} \,. \tag{2.81b}$$

In Eq. 2.81b, the time-integral is written as a sum over the time-discretized steps of the trajectory, with $t_j = j\Delta t$ the time at the j-th time step and $n^{(i)}_{\text{MD}}$ the total number of MD steps to perform the transition $\widetilde{t}^{(i)}_{A\to B} = n^{(i)}_{\text{MD}}\Delta t$.

Mean first transition times $\tau_{\text{MFPT},A\to B}$ can be estimated by repeating InMetaD simulations a number M_A times (i.e. for $i = 1, \ldots, M_A$) and averaging as in Eqs. 2.41. However, since escape times from long-lived metastable states are expected to follow Poisson statistics, more accurate mean transition times can be calculated by fitting the empirical cumulative distribution function (ECDF) of unbiased transition times to the theoretical cumulative distribution function (TCDF)[85]

$$P\left(t_{A\to B}\right) = 1 - \exp\left(-\frac{t_{A\to B}}{\tau_{\text{MFPT},A\to B}}\right) . \tag{2.82}$$

for $\tau_{\text{MFPT},A\to B}$. This has the additional advantage of allowing back-calculation of how well the ECDF follows a Poisson distribution, by generating a large amount of new data points from the fitted TCDF and performing a Kolmogorov-Smirnov (KS) test. The KS test estimates the probability that two sets of data (in this case the original set of calculated unbiased transition times and the newly generated data set) were produced by the same distribution, and generally a cutoff p-value of 0.05 is taken in literature[85].

2.4.2 Path Reweighting

Many modern rare event methods are based in a path ensemble description of dynamics[7]. In molecular dynamics, numerical integrators are applied to generate time-discretized paths x of $n + 1$ states

$$\mathrm{x} = (\mathbf{x}_0, \mathbf{x}_1, \ldots, \mathbf{x}_n) \tag{2.83}$$

where Δt is the time step of the integrator, $\mathbf{x}_k = (\mathbf{q}_k, \mathbf{p}_k) \in \Gamma$ is the state at time $k\Delta t$ with positions $\mathbf{q}_k$ and momenta $\mathbf{p}_k$ and $\mathcal{T} = n\Delta t$ is the total simulation time of the path. We denote the space containing all such possible paths as $\mathcal{S} = \Gamma^{n+1}$. The discussion here is restricted to paths from stochastic integrators which discretize the equation of motion for Langevin dynamics.

For an ensemble of paths of length $\mathcal{T}$ generated at potential energy function $V(\mathbf{q})$, a path probability density $\mathcal{P}\left[\mathrm{x}\right] = p(\mathbf{x}_0)\mathcal{P}\left[\mathrm{x} \,|\, \mathbf{x}_0\right]$ can be defined, where for equilibrium conditions $p(\mathbf{x}_0)$ corresponds to the Gibbs-Boltzmann distribution in Eq. 2.5. Due to the Markovian property of the Langevin integrators, the conditional probability can be written as

$$\mathcal{P}\left[\mathrm{x}\,|\,\mathbf{x}_0\right] = \mathcal{P}\left[\mathbf{x}_1, \ldots, \mathbf{x}_n | \mathbf{x}_0\right] = \prod_{k=0}^{n-1} p(\mathbf{x}_{k+1}|\mathbf{x}_k) \tag{2.84}$$

where the single-step transition probabilities $p(\mathbf{x}_{k+1}|\mathbf{x}_k)$ depend on the choice of Langevin integrator. The path probability density $\mathcal{P}[\mathrm{x}]$ is normalized, i.e.

$$\int_{\mathcal{S}} \mathcal{D}\mathrm{x}\, \mathcal{P}\left[\mathrm{x}\right] = \int_{\mathbf{x}_0 \in \Gamma} \int_{\mathbf{x}_1 \in \Gamma} \cdots \int_{\mathbf{x}_n \in \Gamma} \mathrm{d}\mathbf{x}_0 \mathrm{d}\mathbf{x}_1 \ldots \mathrm{d}\mathbf{x}_n \mathcal{P}\left[\mathrm{x}\right] = 1 \tag{2.85}$$

where the discrete path integral $\int_{\mathcal{S}} \mathcal{D}\mathrm{x}$ is introduced. If the path probability density is available, path expectation values can be calculated for path observables $s[\mathrm{x}] : \mathcal{S} \to \mathbb{R}$ as

$$\begin{aligned} \langle s \rangle &= \int_{\mathbf{x}_0 \in \Gamma} \int_{\mathbf{x}_1 \in \Gamma} \cdots \int_{\mathbf{x}_n \in \Gamma} \mathrm{d}\mathbf{x}_0 \mathrm{d}\mathbf{x}_1 \ldots \mathrm{d}\mathbf{x}_n \mathcal{P}\left[\mathrm{x}\right] s[\mathrm{x}] && \text{(2.86a)} \\ &= \int_{\mathcal{S}} \mathcal{D}\mathrm{x}\, \mathcal{P}\left[\mathrm{x}\right] s[\mathrm{x}]\,. && \text{(2.86b)} \end{aligned}$$

For sufficiently large N, these path expectation values can be calculated by averaging over a set of paths $\{\mathrm{x}_1, \ldots, \mathrm{x}_N\}$ that have been sampled according to $\mathcal{P}[\mathrm{x}]$:

$$\langle s \rangle = \lim_{N\to\infty} \frac{1}{N} \sum_{r=1}^{N} s[\mathrm{x}_r]\,. \tag{2.87}$$

The aim of path reweighting (also called Girsanov reweighting[23, 26, 87]) is to reweight path probabilities for trajectories at a simulation potential $V_{\mathrm{sim}}(\mathbf{q})$ to probabilities for the same trajectories at a target potential

$$\widetilde{V}_{\mathrm{tar}}(\mathbf{q}) = V_{\mathrm{sim}}(\mathbf{q}) + U(\mathbf{q}) \tag{2.88}$$

where $U(\mathbf{q})$ will be referred to as the perturbation potential.[5] If the ratio of the respective path probabilities is known, expectation values for path observables can be estimated at a target potential from trajectories generated at a simulation potential. The ratio of probabilities can be split up into what can roughly be considered a thermodynamical and a dynamical part

$$\frac{\widetilde{\mathcal{P}}\left[\mathrm{x}\right]}{\mathcal{P}\left[\mathrm{x}\right]} = \frac{\widetilde{p}(\mathbf{x}_0)}{p(\mathbf{x}_0)} \cdot \frac{\widetilde{\mathcal{P}}\left[\mathrm{x}\,|\,\mathbf{x}_0\right]}{\mathcal{P}\left[\mathrm{x}\,|\,\mathbf{x}_0\right]} = g(\mathbf{x}_0) \cdot M\left[\mathrm{x}\,|\,\mathbf{x}_0\right] \tag{2.89}$$

---

[5] Notice that notation of the target potential in Eq. 2.88 is similar to that of the biased potential for enhanced sampling in Eq. 2.22. This is done in order to follow convention from literature in both cases. Care needs to be taken, however, since, while conceptually similar, in certain cases interpretation might differ. If the sole purpose is to employ enhanced sampling to speed up transitions, the simulation potential often includes a bias in the reactant state, and thus corresponds to the biased potential in enhanced sampling. In this case, the target potential corresponds to the unbiased potential, while the perturbation potential is the negative of the biasing potential $U(\mathbf{q}) = -U^{\mathrm{bias}}(\mathbf{q})$.

Integrator	$\Delta\eta_k$	Reference
Euler-Maruyama	$\sqrt{\frac{\Delta t}{2k_BT\xi m}}\nabla U(\mathbf{q}_k)$	Ref. 26
ISP	$\sqrt{\frac{1}{k_BT\xi^2 m}}\frac{1-\exp(-\xi\Delta t)}{\sqrt{1-\exp(-2\xi\Delta t)}}\nabla U(\mathbf{q}_k)$	Ref. 27

Table 2.1: Formulations of $\Delta\eta_k$ for different integrators.

where for thermal equilibrium conditions

$$g(\mathbf{x}_0) = \frac{\widetilde{p}(\mathbf{x}_0)}{p(\mathbf{x}_0)} = \frac{Z_q}{\widetilde{Z}_q} e^{-\beta U(\mathbf{q}_0)} \,. \tag{2.90}$$

Notice the thermodynamical reweighting factor $g(\mathbf{x}_0)$ is the same as the one used for reweighting thermodynamic ensemble averages (Eqs. 2.24-2.26).

The conditional path probability ration $M\left[\mathrm{x}\,|\,\mathbf{x}_0\right]$ depends on the dynamical properties of the system and consequently on the integrator used to generate the path. The conditional path probability ratio for the Euler-Maruyama scheme[3, 24] for overdamped Langevin dynamics has been reported many times[24–26, 87, 123, 124]. More recently, an expression for $M\left[\mathrm{x}\,|\,\mathbf{x}_0\right]$ has been derived for a specific integrator[125] for underdamped Langevin dynamics[27].

The relative conditional path probability density can be expressed[26] in terms of the random numbers η_k of the integrator as well as the random number difference[27] $\Delta\eta_k$ which depends on the gradient of the bias $\nabla U(\mathbf{q}_k)$:

$$M\left[\mathrm{x}\,|\,\mathbf{x}_0\right] = \frac{\widetilde{P}\left[\mathrm{x}\,|\,\mathbf{x}_0\right]}{P\left[\mathrm{x}\,|\,\mathbf{x}_0\right]} = \exp\left(-\sum_{k=0}^{n-1} \eta_k \cdot \Delta\eta_k\right) \cdot \exp\left(-\frac{1}{2}\sum_{k=0}^{n-1} \left(\Delta\eta_k\right)^2\right) \,. \tag{2.91}$$

This formulation allows for easy on-the-fly calculation of reweighting factors by recording η_k and $\Delta\eta_k$ during simulation at the simulation potential. The expression for the random number difference $\Delta\eta_k$ depends on the stochastic integrator. Expressions derived for the Euler-Maruyama integrator for overdamped Langevin dynamics and for the ISP integrator for underdamped Langevin dynamics are shown in Tab. 2.1.

If reweighting factors $g(\mathbf{x}_0)$ and $M\left[\mathrm{x}\,|\,\mathbf{x}_0\right]$ are accessible, path expectation values can be reweighted

$$\widetilde{\langle s \rangle} = \int \mathcal{D}\mathrm{x}\, \widetilde{\mathcal{P}}[\mathrm{x}] s[\mathrm{x}] = \int \mathcal{D}\mathrm{x}\, g(\mathbf{x}_0) M\left[\mathrm{x}\,|\,\mathbf{x}_0\right] \mathcal{P}[\mathrm{x}] s[\mathrm{x}] \,. \tag{2.92}$$

In other words, if path space has been sufficiently sampled, path expectation values at a target potential $\widetilde{V}$ can be calculated from trajectories generated at a simulation potential V. In case we have a sufficiently large set of paths $\{\mathrm{x}_1, \ldots, \mathrm{x}_N\}$ at simulation potential, i.e. according to $\mathcal{P}[\mathrm{x}]$, target path expectation values can be calculated as:

$$\widetilde{\langle s \rangle} = \lim_{N\to\infty} \frac{1}{N} \sum_{r=1}^{N} g(\mathbf{x}_{r,0}) M\left[\mathrm{x}_r \,|\, \mathbf{x}_{r,0}\right] s[\mathrm{x}_r] \tag{2.93}$$

where $g(\mathbf{x}_{r,0}) M\left[\mathrm{x}_r \,|\, \mathbf{x}_{r,0}\right]$ is the relative weight of path x_r at target potential $\widetilde{V}$ with $\mathbf{x}_{r,0}$ the paths starting state.

The Girsanov reweighting factors can readily be used to reweight the transition matrices from Markov state models described in Section 2.3.3. Notice the correlation function in the numerator of Eq. 2.54 can be rewritten using path probability formulations as

$$c_{ij}^{\mathrm{corr}}(\tau) = \int_{\mathcal{S}} \mathcal{D}\mathrm{x}\, \chi_j\left(\mathbf{q}(\tau)\right) \cdot \mathcal{P}[\mathrm{x}] \cdot \chi_i\left(\mathbf{q}(0)\right) \tag{2.94}$$

where integration happens over all paths x of length τ. Applying Eq. 2.87 retrieves Eq. 2.56. The correlation function can consequently be reweighted to a target potential $\widetilde{V}$ using the reweighting factors

$$\begin{aligned} \widetilde{c_{ij}}^{\mathrm{corr}}(\tau) &= \int_{\mathcal{S}} \mathcal{D}\mathrm{x}\, \chi_j\left(\mathbf{q}(\tau)\right) \cdot \widetilde{\mathcal{P}}[\mathrm{x}] \cdot \chi_i\left(\mathbf{q}(0)\right) && (2.95\mathrm{a}) \\ &= \int_{\mathcal{S}} \mathcal{D}\mathrm{x}\, \chi_j\left(\mathbf{q}(\tau)\right) \cdot g(\mathbf{x}_0) M\left[\mathrm{x} \,|\, \mathbf{x}_0\right] \mathcal{P}[\mathrm{x}] \cdot \chi_i\left(\mathbf{q}(0)\right) && (2.95\mathrm{b}) \end{aligned}$$

which as in Eq. 2.93, can be written as

$$\widetilde{c_{ij}}^{\mathrm{corr}}(\tau) = \lim_{N\to\infty} \frac{1}{N} \sum_{r=1}^{N} g(\mathbf{x}_{r,0}) M\left[\mathrm{x}_r \,|\, \mathbf{x}_{r,0}\right] \chi_i\left(\mathbf{q}_{r,0}\right) \chi_j\left(\mathbf{q}_{r,\tau}\right) \,. \tag{2.96}$$

$\mathbf{q}_{r,0}$ and $\mathbf{q}_{r,\tau}$ are the positions of the initial and final states of path x_r, i.e. the positions at time 0 and τ respectively. In practice, paths are often sampled from a long equilibrium trajectory by counting transitions from cell i to cell j in a lag time τ and building a count matrix as in Eq. 2.57. Notice that an equivalent strategy can be used here, providing that each count has to be weighted by the relevant weighting factor. For a long trajectory of n_{MD} time steps, the reweighted count matrix takes form

$$\widetilde{C_{ij}} = \sum_{k=1}^{n_{\mathrm{MD}}-l} g(\mathbf{x}_k) M\left[\mathrm{x}_k^{\tau} \,|\, \mathbf{x}_k\right] \chi_i\left(\mathbf{q}_k\right) \chi_j\left(\mathbf{q}_{k+l}\right) \tag{2.97}$$

where $\tau = l\Delta t$ with Δt the time step, and $\mathrm{x}_k^{\tau} = (\mathbf{x}_k, \mathbf{x}_{k+1}, \ldots, \mathbf{x}_{k+l})$ the part of the long trajectory starting at time $k\Delta t$ and ending at $(k+l)\Delta t = k\Delta t + \tau$. The reweighted transition matrix can then be calculated by row normalizing as in Eq. 2.58.

Girsanov reweighting has been used in combination with the continuum path ensemble maximum caliber approach to formulate new force field optimization strategies[126] as well as in a new slow CV discovery method[127].

Chapter 3

Publications

3.1 Paper A1

"Thermal isomerization rates in retinal analogues using ab-initio molecular dynamics"

S. Ghysbrecht, B. G. Keller
J. Comput. Chem., **2024**, *45(16)*, 1390-1403

DOI: 10.1002/jcc.27332
URL: https://doi.org/10.1002/jcc.27332
Preprint: https://doi.org/10.48550/arXiv.2312.10520

Contributions:
Simon Ghysbrecht and Bettina Keller conceived the project and wrote the manuscript. S.G. performed the computational work and produced figures and tables containing the resulting data. S.G. wrote the detailed computational setup in the second chapter of the SI. B.K. produced Figs. 5 and 6 as well as Tab. 1, and wrote the overview on transition state theories in the first chapter of the SI. Both authors contributed to the the final version of the manuscript.

Summary

Retinal proteins are light-sensitive membrane proteins that serve as key components in vital biological processes such as vision or bacterial phototaxis[15]. In general these proteins consist of a retinal chromophore surrounded by seven trans-membrane helices. Upon photoabsorption, a fast trans-cis isomerization in the retinal initiates structural changes guiding the protein through functional states. Thermal back-isomerization returns the protein to its dark state, a slower process with timescales ranging from seconds to hours[19–21].

In this paper, we study reaction mechanisms and corresponding rate constants of thermal isomerization over the $C_{13}{=}C_{14}$ double bond of the retinal cofactor (Fig. 1 in the article). We focus on two retinal analogues at 300 K in the gas phase. The Born-Oppenheimer (BO) potential energy surface (PES) is modeled by the self-consistent-charge density functional tight-binding (DFTB) method[128], while density functional theory (DFT) with the B3LYP functional[129, 130] and 6-31G* basis set[131] is included as a reference. Despite being computationally efficient, DFTB has been demonstrated to be reasonably accurate in modeling retinal analogues[132–134]. Leveraging DFTB, ab-initio molecular dynamics (MD) simulations with timescales in the order of hundreds of nanoseconds become accessible, enabling application of dynamical sampling-based approaches for estimating free energy surfaces and rate constants.

Thermal cis-trans isomerization in the retinal analogues in the gas phase is expected to align well with the assumptions of transition state theory (TST). Therefore, within its level of theory, Eyring TST is anticipated to provide accurate rate constants that can serve as a benchmark for dynamical sampling-based approaches. Additionally, identifying the transition state configuration is expected to be achievable at both the DFT level and DFTB levels, facilitating the comparison of TST rates between these methods. This enables the exploration of the following research questions:

1. How do rate constants compare between potential energy surfaces obtained from DFT and DFTB?
2. How do rate constants estimated from dynamical sampling compare to those from Eyring TST?

Previous studies have examined potential energy barriers for cis-trans isomerization in the retinal analogues using both DFT and DFTB methods[132, 133], with their findings well reproduced in the study here. Roughly, DFTB underestimates potential energy barriers by approximately 5 to 10 kJ/mol compared to DFT. This translates in Eyring TST rates being one to two orders of magnitude higher for DFTB ($2 \times 10^{-4}\,\mathrm{s}^{-1}$) as compared to DFT ($2 \times 10^{-5}\,\mathrm{s}^{-1}$).[1] In addition to Eyring TST where rates are calculated using the quantum

---

[1] Rates between brackets are given for cis-to-trans isomerization in pSb5 and serve as an example. Similar trends are seen in trans-to-cis rates as well as for rates in pSb1, see Tabs. 2 and 3 in the paper.

partition functions, rates can also be calculated in the high-temperature limit formulation of TST (Eq. 2.63), see Section 2.3.4. Rates in the high-temperature limit are consistently around three times lower ($6 \times 10^{-5}\,\mathrm{s}^{-1}$ for DFTB) than those obtained from Eyring TST. The error stemming from the high-temperature limit thus is small compared to the uncertainty arising from the model of the PES.

Rate constants from dynamical sampling are computed using two main approaches. In the first approach, infrequent metadynamics runs are carried out biasing the $C_{13}{=}C_{14}$ dihedral angle φ. Rates from infrequent metadynamics ($1 \times 10^{-4}\,\mathrm{s}^{-1}$) are found to match rates from TST in the high-temperature limit very well. In a second approach, enhanced sampling techniques are used to sample the free energy and diffusion profiles along φ. Rates are then computed by Kramers' equation ($2 \times 10^{-1}\,\mathrm{s}^{-1}$) and Pontryagin's equation ($3 \times 10^{-1}\,\mathrm{s}^{-1}$). Remarkably, rates obtained through these methods are several orders of magnitude higher than those derived from TST. This is a more considerable difference even than the uncertainty due to the model of the PES.

In both MD simulations employing DFTB and constrained optimizations at the DFT level, we observe neighboring dihedral angles to be correlated to φ. Particularly notable is the out-of-plane wagging of substituents on the C_{13} and C_{14} atoms. These observations suggest that the isomerization mechanism involves a coordinated motion beyond mere rotation around φ. Hence, relying solely on φ as a one-dimensional reaction coordinate may not be sufficient to accurately describe the reaction dynamics. Effective dynamics-based methods heavily rely on the definition of the reaction coordinate, which could contribute to the observed disparities in rate calculations. This is investigated in more depth in the next section.

Received: 19 December 2023 | Revised: 31 January 2024 | Accepted: 2 February 2024
DOI: 10.1002/jcc.27332

RESEARCH ARTICLE

Journal of COMPUTATIONAL CHEMISTRY WILEY

Thermal isomerization rates in retinal analogues using Ab-Initio molecular dynamics

Simon Ghysbrecht | **Bettina G. Keller**

Department of Biology, Chemistry and Pharmacy, Freie Universität Berlin, Berlin, Germany

Correspondence
Bettina G. Keller, Department of Biology, Chemistry and Pharmacy, Freie Universität Berlin, Arnimallee 22, 14195 Berlin, Germany.
Email: bettina.keller@fu-berlin.de

Funding information
Deutsche Forschungsgemeinschaft (DFG), Grant/Award Number: SFB 1114

[Correction added after first online publication, March 9, 2024: Equation (3a) has been revised.]

Abstract

For a detailed understanding of chemical processes in nature and industry, we need accurate models of chemical reactions in complex environments. While Eyring transition state theory is commonly used for modeling chemical reactions, it is most accurate for small molecules in the gas phase. A wide range of alternative rate theories exist that can better capture reactions involving complex molecules and environmental effects. However, they require that the chemical reaction is sampled by molecular dynamics simulations. This is a formidable challenge since the accessible simulation timescales are many orders of magnitude smaller than typical timescales of chemical reactions. To overcome these limitations, rare event methods involving enhanced molecular dynamics sampling are employed. In this work, thermal isomerization of retinal is studied using tight-binding density functional theory. Results from transition state theory are compared to those obtained from enhanced sampling. Rates obtained from dynamical reweighting using infrequent metadynamics simulations were in close agreement with those from transition state theory. Meanwhile, rates obtained from application of Kramers' rate equation to a sampled free energy profile along a torsional dihedral reaction coordinate were found to be up to three orders of magnitude higher. This discrepancy raises concerns about applying rate methods to one-dimensional reaction coordinates in chemical reactions.

KEYWORDS
DFT, DFTB, Kramers, metadynamics, rate theory, retinal, square-root approximation, umbrella sampling

1 | INTRODUCTION

Precise models of chemical reactions, encompassing reaction mechanisms and precise rate constants, are critical for a nuanced understanding of reactions occurring in nature, laboratory experiments, and industrial processes. Yet, computational models of chemical reactions remain challenging, because the transition state of a reaction has to be calculated using a highly accurate model of the Born-Oppenheimer potential energy surface (PES). This usually involves evaluating the electronic structure and explicitly calculating the electronic energy at each nuclear configuration. Thus, the current standard to calculate reaction rate constants remains Eyring transition state theory (TST),[1] which requires only calculations at a few select points along the PES. However, Eyring TST makes strong assumptions for the shape of the PES and the dynamics on this PES and is therefore limited to small to medium sized systems in the gas phase.

Eyring TST defines the transition state as a saddle point on the PES, assumes an equilibrium between reactant state *A* and transition state *TS* and models the PES at *A* and *TS* by a harmonic approximation.[2] The dynamics of the nuclei are treated quantum mechanically. The most prominent error source is the accuracy of the energy barrier, which enters the equation for the rate exponentially. But the assumptions are easily violated if (*i*) the saddle point of the PES does not coincide with the bottleneck of the reaction (i.e., the free energy maximum along the optimal reaction coordinate), (*ii*) the PES at *A* or at *TS* is anharmonic, (*iii*) the reaction coordinate has a strong curvature in the configurational space, or (*iv*) the reactant state exhibits multiple minima.

These violations occur in systems with many degrees of freedom, in particular if these degrees of freedom are very mobile. Then the reactant state may comprise multiple molecular conformations and various vibrational modes may couple to the reactive vibrational mode. The situation is further complicated if the reaction occurs in solution or if the reactants otherwise strongly interacts with their environment, for example, in a catalysed reaction. To model reactions for these systems, one shifts to a classical description of the nuclear dynamics and samples the reaction using molecular dynamics (MD) simulations.[3]

The simplest estimator for a reaction rate constant from a MD simulation is to count the number of transition from reactant state *A* to product state *B*. However, since the accessible simulation times are orders of magnitude smaller than the mean first passage times even of very fast reactions, one uses enhanced sampling protocols to increase the statistics. A wide variety of methods to recover accurate rate constants and mechanisms from these sped-up simulations have been proposed.[2,4] They broadly fall into two categories: (*i*) dynamical reweighting methods[5] sample the reaction on a biased PES and reweight the transition count, (*ii*) reaction coordinate based methods define a one-dimensional reaction coordinate *s*[6] and calculate the rate constant from an effective dynamics on this reaction coordinate. Besides the definition of a reaction coordinate, the second approach involves the calculation of the free energy surface (FES)[7] and diffusion profile[8] via MD simulations.

Kramers' rate theory[9] is the most prominent example for this second approach. It assumes separation of timescales and models the FES at *A* and *TS* by a harmonic approximation. These two assumptions may be relaxed by using Pontryagin's rate theory.[10] In both cases, the dynamics are modelled by a stochastic classical equation of motion. Infrequent metadynamics[11] is an example for the first approach. The method assumes separation of timescales, but does not use a harmonic approximation. The dynamics are modelled and simulated in the full configurational space using either a deterministic or a stochastic classical equation of motion.

Owing to recent progress in electronic structure calculations[12–14] and quantum mechanics/molecular mechanics approaches,[15] the development of reactive force fields,[16] and the emergence of neural network potentials,[17] chemical reactions will increasingly be modeled through simulations rather than through Eyring TST. Thus, models of chemical reactions in large molecular systems with complex environments come within reach. However, moving from Eyring TST to sampling-based rate estimates involves a considerable reconstruction of the theoretical foundation through which the reaction is modelled. Most importantly, the quantum mechanical description of the nuclear degrees of freedom is replaced by a classical approximation. Furthermore, the search for a transition state *TS* is replaced by a statistical estimate of the transition count (first approach) or by the search for an optimal reaction coordinate. It is not obvious how these changes influence the accuracy with which the reaction rate constant can be determined.

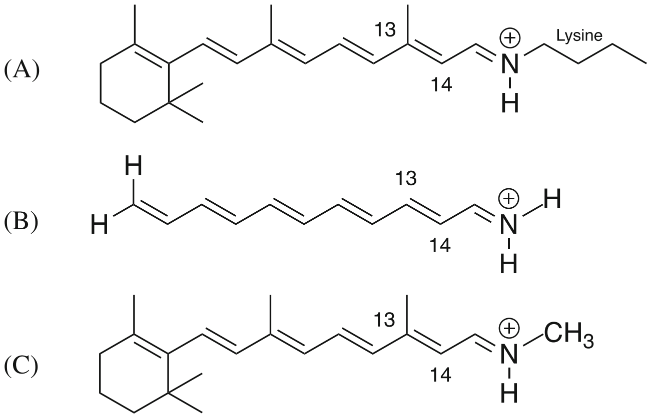

FIGURE 1 Structures of retinal compounds: (A) Retinal cofactor attached to lysine chain, (B) pSb5 and (C) pSb1.

The first aim of this study is to explore and to quantify the influence of these approximations on the estimate of a reaction rate constant. As test reactions we choose the thermal cis-trans isomerization in two analogues of retinal: pSb5 and pSb1 (Figure 1). When modelled in vacuum, the thermal cis-trans isomerization over a C=C double bond fulfills the assumptions of Eyring TST well. Additionally, it is an unimolecular reaction, so that the encounter complex of the reactants does not need to be modelled. Thus for this specific system, we expect that Eyring TST yields an accurate rate constant, which can serve as a reference for more approximate TST models or for sampling-based approaches. On the other hand, the reaction energy barrier is high and the two molecules are large enough for non-trivial coupling between vibrational modes, so that the two test systems pose a reasonable challenge for sampling-based approaches.

Extensive literature has addressed the precise modeling of the potential energy surface (PES) for the cis-trans isomerization in retinal,[18] as well as for retinal analogues.[19–21] We here model the PES by self-consistent-charge density-functional tight-binding method with a third-order expansion of the total energy around a reference density (DFTB3)[12,22] and include density functional theory (DFT)[23,24] as a reference. This allows us to explore the sensitivity of the reaction rate constant to variations in both the rate model and the underlying PES. Thus, as a second aim of the study, we ask whether the precision of the activation energy is indeed the most pivotal parameter when calculating a reaction rate constant.

2 | THEORY

We here summarize the rate theories used in this study. For a more in-depth exploration of rate theories, please refer to References 2, 4, and section I of the supplementary material.

2.1 | Eyring TST

The cis-trans isomerization around a C=C double bond is a unimolecular reaction

$$A \xrightarrow{k_{AB}} B, \tag{1}$$

which, according to the theory of the activated complex, is modeled as

$$A \rightleftharpoons AB^{\ddagger} \rightarrow B \tag{2}$$

where A is the reactant state, B is the product state and $AB^{\ddagger}$ is the activated complex. The critical assumption in Equation (2) is that reactant and transition state configurations are in equilibrium. Eyring TST[1] models this equilibrium by statistical thermodynamics and arrives at the following equation for the reaction rate:[2,4]

$$k_{AB}^{\mathrm{Eyr}} = \frac{RT}{h}\frac{\tilde{q}_{AB^{\ddagger}}}{q_A}\exp\left(-\frac{E_b}{RT}\right) \tag{3a}$$

$$= \frac{RT}{h}\exp\left(-\frac{\Delta F^{\ddagger}}{RT}\right) \tag{3b}$$

where R is the ideal gas constant, T is the temperature, and h is the Planck constant in molar units. See section I of the supplementary material.

The free energy difference $\Delta F^{\ddagger}$ between the $AB^{\ddagger}$ and A can be calculated from the molecular partition function at the transition state $\tilde{q}_{AB^{\ddagger}}$ and the molecular partition function at the reactant state q_A:

$$\Delta F^{\ddagger} = E_b - RT\ln\left(\frac{\tilde{q}_{AB^{\ddagger}}}{q_A}\right) \tag{4}$$

where E_b is the potential energy barrier, that is, the potential energy difference between the reactant minimum and the maximum of the energy barrier. The partition functions are calculated relative to the electronic ground state energy of the respective configurations. The tilde symbol in $\tilde{q}_{AB^{\ddagger}}$ indicates that, for $AB^{\ddagger}$, the vibrational contribution corresponding to the reaction coordinate is excluded in the free energy calculation.

We calculate and report potential and free energies in units of $\mathrm{J\,mol^{-1}}$, correspondingly the thermal energy is also reported as a molar quantity: RT. If units of energy are used for potential and free energies, R should be replaced by the Boltzmann constant $k_B = R/N_A$ in Equations (3) and (4) and all of the following equations. N_A is the Avogadro constant.

The molecular partition functions are determined by separating their translational, rotational, vibrational and electronic degrees of freedom. Each part is treated using appropriate quantum mechanical models, that is, particle-in-a-box for translational, rigid rotor for rotational and harmonic oscillator for vibrational degrees of freedom. In the case of a unimolecular reaction, the contributions of the translational degrees of freedom to the free energy difference in Equation (4) will cancel. We assume $q_{\mathrm{el}} = 1$ for all situations, that is, the electronic ground state energy level is non-degenerate, and any contributions from higher electronic states can be ignored. With these approximations, the free energy difference (Equation 4) of the cis-trans isomerization can be decomposed as

$$\Delta F^{\ddagger} = E_b + \Delta F_{\mathrm{rot}} + \Delta F_{\mathrm{vib}} \tag{5}$$

where

$$\Delta F_{\mathrm{rot}} = -RT\ln\left[\frac{q_{AB^{\ddagger},\mathrm{rot}}}{q_{A,\mathrm{rot}}}\right] \tag{6a}$$

$$\Delta F_{\mathrm{vib}} = -RT\ln\left[\frac{\tilde{q}_{AB^{\ddagger},\mathrm{vib}}}{q_{A,\mathrm{vib}}}\right] \tag{6b}$$

define the rotational and vibrational free energy difference. $q_{A,\mathrm{rot}}$ and $q_{AB^{\ddagger},\mathrm{rot}}$ are the rotational partition functions of A and $AB^{\ddagger}$. $q_{A,\mathrm{vib}}$ and $\tilde{q}_{AB^{\ddagger},\mathrm{vib}}$ are the vibrational partition functions of A and $AB^{\ddagger}$, where the tilde symbol indicates that the reactive vibrational mode has been excluded from vibrational partition function of $AB^{\ddagger}$. See section I of the supplementary material.

2.2 | High-temperature TST

If the thermal energy RT is large compared to the energy difference of the vibrational states, the following high-temperature approximation to Eyring TST may be used

$$k_{AB}^{\mathrm{Eyr}} \approx k_{AB}^{\mathrm{ht}} = \frac{\prod_{k=1}^{3N-6}\nu_{A,k}}{\prod_{k=1,k\neq r}^{3N-6}\nu_{AB^{\ddagger},k}}\exp\left(-\frac{E_b}{RT}\right) \tag{7}$$

where the frequencies $\nu_{A,k}$ and $\nu_{AB^{\ddagger},k}$ correspond to the harmonic frequencies at the reactant and transition state respectively. Note that the frequency of the reactive vibrational mode $\nu_{AB^{\ddagger},r}$ is excluded from the product.

Equation (7) can be brought into the form of Equation (3b) by setting

$$\Delta F^{\ddagger} \approx \Delta F^{\ddagger,\mathrm{ht}} = E_b - RT\ln\left(\frac{\tilde{q}^{\mathrm{ht}}_{AB^{\ddagger},\mathrm{vib}}}{q^{\mathrm{ht}}_{A,\mathrm{vib}}}\right) = E_b + \Delta F^{\mathrm{ht}}_{\mathrm{vib}} \tag{8}$$

where $\tilde{q}^{\mathrm{ht}}_{AB^{\ddagger},\mathrm{vib}}$ and $q^{\mathrm{ht}}_{A,\mathrm{vib}}$ are the high-temperature approximations to the vibrational partition functions of A and $AB^{\ddagger}$. In deriving Equations (7) and (8), one assumes that the moments of inertia of the reactant and TS configuration are approximately the same and thus the rotational contribution to the $\Delta F^{\ddagger}$ is negligible. Additionally, one neglects the vibrational zero-point energy and takes the continuum limit of the vibrational partition function. See section I of the supplementary material.

The high-temperature TST can also be derived by treating the partition functions in Equations (3a) and (4) classically and using a harmonic approximation for the PES. See section I of the supplementary material. Equations (7) and (8) thus constitute the link between a quantum mechanical and a classical treatment of the activated complex.

2.3 | Infrequent metadynamics

A statistical estimate for the reaction coordinate rate constant is obtained via the mean first-passage time τ_{AB}

$$k_{AB} = \frac{1}{\tau_{AB}}, \tag{9}$$

where τ_{AB} is the average time it takes for the system to reach the product state B from the reactant state A. The relation between k_{AB} and τ_{AB} stated in Equation (9) relies on a separation of timescales between the timescale of equilibration within A and the much slower timescale of equilibration between A and B. From MD simulations on the PES $V(\mathbf{x})$, where $\mathbf{x}$ is the molecular configuration, τ_{AB} can be calculated as the arithmetic mean of the first-passage times from A to B.[2] However, a better statistical accuracy is obtained by fitting a the cumulative distribution function of a Poisson process[25]

$$P(\tau_{AB,i}) = 1 - \exp\left(-\frac{\tau_{AB,i}}{\tau_{AB}}\right) \tag{10}$$

to the cumulative distribution histogram of these fist passage times. In Equation (10), $\tau_{AB,i}$ is the i first-passage time observed in the simulation and τ_{AB} is the MFPT and acts as a fitting parameter, which is inserted into Equation (9) to obtain the reaction rate.

Infrequent metadynamics[11] is a method to calculate transition times for systems in which the mean first-passage times is larger than the accessible simulation time. The molecular system is prepared in the reactant state A and a time dependent bias function $U(\mathbf{x},t)$ is introduced that increases in strength as the simulation proceeds and pushes the system over the barrier into state B. One terminates the simulation and records the biased transition time $\tau^{\mathrm{InMetaD}}_{AB,i}$, where i is the index of the infrequent metadynamics simulation. Each accelerated first-passage time is then reweighted to the corresponding physical first-passage time by a discretized time-integral over the length of the trajectory[11,26–28]

$$\tau_{AB,i} = \Delta t \sum_{k=1}^{T_i} \exp\left(\frac{U(\mathbf{x}_{i,k}, k\Delta t)}{RT}\right), \tag{11}$$

where Δt is the time step of the trajectory, T_i is the total number of time steps in the ith trajectory, $\mathbf{x}_{i,k}$ is the kth configuration in this trajectory, and $t = k\Delta t$ is the corresponding time. This reweighting assumes that no bias has been deposited on the transition state, which is approximately ensured by the slow deposition of the infrequent metadynamics protocol.[29]

Equation (11) is derived from the Equation (3b), that is, the method assumes that the reaction proceeds via an activated complex. In contrast to Eyring TST, partition functions q_A and $q_{AB^\ddagger}$ are treated classically. The derivation considers a statistical estimate of $q_{AB^\ddagger}/q_A$ from MD simulation data, which has the advantage that no harmonic approximation is needed. See section I of the supplementary material.

2.4 | Reaction coordinate based rate theories

In reaction coordinate based rate theories, one assumes that the system evolves according to a diffusive dynamics along a reaction coordinate $s(\mathbf{x})$. This approach requires the free energy surface (FES) along $s(\mathbf{x})$, which is defined as:[2]

$$F(s) = -RT \ln \pi(s) \tag{12}$$

where $\pi(s)$ is the equilibrium distribution in s:

$$\pi(s) = Z_{\mathbf{x}}^{-1} \int_{\Gamma_{\mathbf{x}}} \mathrm{d}x \exp\left(-\frac{V(\mathbf{x})}{RT}\right) \delta(s(\mathbf{x}) - s). \tag{13}$$

$Z_{\mathbf{x}}$ the configurational partition function, $\Gamma_{\mathbf{x}}$ is the configurational space, and $\delta(s(\mathbf{x}) - s)$ is the Dirac delta function.

The interaction of the internal degrees of freedom with the effective dynamics along s is modelled as a thermal bath, that is, by a friction and random force which are balanced by the Einstein relation. The friction force can be scaled by a friction coefficient or collision rate ξ (with units time^{-1}).

The following two rate theories assume separation of timescales which can be quantified in terms of the FES as $F^\ddagger_{AB} \gg RT$, where $F^\ddagger_{AB} = F(s_{AB^\ddagger}) - F(s_A)$ is the difference of the FES between the FES minimum in the reactant state and the maximum of the free energy barrier. We remark that the location of the free energy maximum $s_{AB^\ddagger}$ does not necessarily coincide with a saddle point in the PES.

In Kramers' rate theory,[2,4,9] the reactant and product state, as well as the maximum of the FES are modelled using a harmonic approximation of the FES around these extrema. In the medium-to-high friction regime, one obtains the following analytical expression for the reaction rate constant

$$k^{\mathrm{Kra}}_{AB} = \frac{\xi}{\omega_\ddagger}\left(\sqrt{\frac{1}{4} + \frac{\omega_\ddagger^2}{\xi^2}} - \frac{1}{2}\right) \frac{\omega_A}{2\pi} \exp\left(-\frac{F^\ddagger_{AB}}{RT}\right) \tag{14}$$

where ω_A is the angular frequency of the harmonic approximation in the reactant state A, and $\omega^\ddagger$ is the angular frequency of the harmonic approximation at the maximum of the free energy barrier.

By relaxing the harmonic approximation one obtains Pontryagin's expression for the rate constant:[10]

TABLE 1 Overview of the model assumptions for different reaction rate models.

	Equation	Activated complex	Separat. of timescales	Harmonic approx.	High T	QM versus CM	TS versus RC	Sampling	Further assumptions
Eyring TST	3b	✓	–	✓	–	QM	TS	–	
High T TST	7	✓	–	✓	✓	QM/CM	TS	–	
InMetaD	11	✓	✓	–	✓	CM	(RC)	✓	Poisson statistics No bias on TS
Pontryagin	15	–	✓	✓	✓	CM	RC	✓	High friction
Kramers	14	–	✓	–	✓	CM	RC	✓	Medium-to-high friction

Abbreviations: CM, classical mechanics; QM, quantum mechanics; RC, reaction coordinate; TS, transition state.

$$k_{AB}^{\mathrm{Pon}} = \left\{ \int_{s_A}^{s_B} \mathrm{d}s' \left[\frac{1}{D(s')} e^{\beta F(s')} \int_{-\infty}^{s'} \mathrm{d}s'' \, e^{-\beta F(s'')} \right] \right\}^{-1} \tag{15}$$

where $\beta = 1/RT$, and $D(s) = \frac{RT}{\mu_q \xi(s)}$. $D(s)$ is the position dependent diffusion profile, which arises from the position dependent friction coefficient $\xi(s)$. μ_q is a effective molar mass. $D(s)$ can be estimated form MD simulations following Reference 8. Note that, while Equation (14) is valid in the intermediate and in the high friction regime, Equation (15) is only valid in the high friction regime, where the effective dynamics can be modelled by overdamped Langevin dynamics. Equation (15) is often quite generically referred to as the formula for the mean first-passage time (MFPT) for diffusion over a barrier (which is inverted to get the rate) or the escape rate. For the sake of clarity, we shall refer to it as the Pontryagin rate equation after Reference 10.

The assumptions of the reaction rate models introduced in this section are summarized in Table 1. We remark that all sampling-based approaches use the high-temperature approximation, and that infrequent metadynamics needs a reaction coordinate to apply the bias, but not for the actual estimate for the rate constant.

3 | MODEL SYSTEMS AND POTENTIAL ENERGY SURFACE

pSb5 and pSb1 (Figure 1B,C) are model compounds for retinal. In proteins, retinal is covalently linked to a lysine side chain via a protonated Schiff base (Figure 1A). In pSb5 (naming following Reference 18), the β-ionone ring and methyl substituents as well as the lysine chain have been removed. In pSb1 (naming following Reference 18), the β-ionone ring and methyl substituents remain but the lysine chain has been replaced by a methyl group. Both compounds have been used as models for retinal in previous studies.[18–20,30–34]

Our goal is to evaluate various rate theories for two model compounds on a specific potential energy surface. Here, we outline our selection of the electronic structure method for PES calculation. Even though most computational models emphasize photo-isomerization in electronically excited states, our focus centers on the thermal isomerization within the electronic ground state.

A critical point in modelling the thermal isomerization is the highly correlated π-electron system along the retinal polyene chain, which allows for two possible pathways for the cis-trans isomerization. In the first pathway, the double bond is broken homolytically when the torsion angle reaches ca. 90 degrees, creating a transition state with diradical character. In the second pathway, cis-trans isomerization over the double bond occurs through charge transfer, with the electrons moving towards the protonated imine in the transition state.

From quantum chemical methods that account for dynamic electron correlation, there is little consensus as to whether cis-trans isomerization in molecules with three conjugated double bonds proceeds via a charge-transfer or a diradical mechanism.[21,35–37] However, DFT studies of retinal and related systems[18,20,32–34] conclude that the isomerization over double bonds in the polyene chains proceeds through a charge-transfer pathway if the Schiff-base is protonated. Since both pSb5 and pSb1 feature a protonated Schiff-base, the charge-transfer pathway seems to be a reasonable assumption for the isomerization of the $C_{13}{=}C_{14}$ double bond in our model compounds. In a charge-transfer pathway, electrons stay paired (closed-shell) during isomerization, and we thus do not necessarily need an electronic structure method that models unpaired electrons.

Ab-initio MD simulations of the thermal isomerization in retinal at the level of DFT are limited to simulation times in the order 1 ns to 10 ns, which is not enough to converge a free energy surface. An alternative is the self-consistent-charge tight-binding density-functional method (DFTB),[12,22] whose computational cost is 2–3 orders of magnitude lower than DFT, thus giving access to much longer simulation timescales. DFTB is an approximation to DFT based on expansion of the total energy around a reference density,[22] where DFTB3[12] includes the third order of the expansion. Even though spin polarization has been introduced for DFTB,[38–40] most applications are based on restricted DFT and cannot model unpaired electrons.

For retinal compounds, DFTB-predicted structures are in good agreement with NMR experiments.[41] Relative to DFT, DFTB yields a reasonable description of the torsional properties of retinal not only in the gas phase,[34] but also in the protein environment.[18,42,43] Torsional barriers for the $C_{13}{=}C_{14}$ bond in retinal compounds are slightly underestimated (about 2 kcal mol^{-1}) when using DFTB as compared to DFT/B3LYP.

More approximate potential energy functions, including semi-empirical methods such as AM1 or PM3, overestimate the delocalization more dramatically than DFTB.[34] In empirical force fields, the delocalization can be modelled by imposing the bond lengths along the polyene chain. But since these potential energy functions use fixed partial atomic charges, they are not well suited to describe the charge-shift in the polyene chain during the isomerization, and consequently the isomerization is highly sensitive to the choice of these charges.

Since DFTB strikes a suitable balance between the accuracy of the potential energy function and the computational cost of conducting ab-initio MD simulations, we use will use it in our simulations. For rate theories that do not require sampling, we include calculations at the level of unrestricted DFT/B3LYP/6-31G* for comparison to a higher level of theory.

4 | RESULTS

4.1 | Free energy surface and diffusion profile

The potential energy functions of pSb5 and pSb1 are high-dimensional functions of 72 and 156 internal degrees of freedom, respectively. With MD simulations, one can characterize these high-dimensional energy functions in more manageable, lower-dimensional collective variable spaces using free energy surfaces (FES) and diffusion profiles.

Figure 2 shows the FES (Equation 12) along the $C_{13}{=}C_{14}$ torsion angle φ, as estimated from umbrella sampling[44] (US) and well-tempered metadynamics[29,45] (MetaD) simulations using ab-initio MD with the DFTB3 method. The line thickness shows the statistical error in the estimated FES.

A full rotation around φ yields two barriers which, as expected, have the same absolute height. The vertical rotational barriers are $F^{\ddagger}_{t\to c} \approx 89\,\mathrm{kJ\,mol^{-1}}$ and $F^{\ddagger}_{c\to t} \approx 81\,\mathrm{kJ\,mol^{-1}}$ for pSb5 and $F^{\ddagger}_{t\to c} \approx 79\,\mathrm{kJ\,mol^{-1}}$ and $F^{\ddagger}_{c\to t} \approx 75\,\mathrm{kJ\,mol^{-1}}$ for pSb1 (both from MetaD1 in Figure 2). The rotational barrier in pSb5 is slightly higher than in pSb1, because the tertiary C_{13} in pSb1 stabilizes the positive charge at the charge-transfer transition state better than the secondary C_{13} in pSb5.[19,20] As usual for a carbon double bond, the trans state at $\varphi = \pi$ rad is slightly more stable than the cis state at $\varphi = 0$ rad, however the stabilization is larger in pSb5 (9.43 ± 1.20 kJ mol^{-1}) than in pSb1 (2.70 ± 1.23 kJ mol^{-1}). A possible explanation might be that in the trans state of pSb1, the methyl group at C_{13} sterically interacts with the hydrogens at C_{15}, which destabilizes this conformation.

The effective dynamics along a reaction coordinate are suitably modelled by stochastic dynamics with position dependent diffusion constant. The dependence of the diffusion constant on the collective variable is due to the dynamics in the orthogonal degrees of freedom and due to the curvature of the collective variable. The diffusion profile in Figure 2 show the form that is expected for a dihedral angle rotations. Note that the estimate of the diffusion constant fails in the barrier region, because of the sharpness of the barriers.

In pSb1, umbrella sampling and metadynamics yield essentially the same FES for various parameter settings (Figure 2B). By contrast, estimates of the FES for pSb5, and especially the relative stability of the cis state, depends on the method that is used to construct the FES and on the parameter settings (Figure 2A). Additionally, the metadynamics simulations converge much slower for pSb5 than for pSb1. Convergence of the metadynamics simulation can be checked by monitoring the estimated free-energy difference between cis and trans state ΔF as function of simulation time (Figure 3A), or by monitoring average errors in block analysis[46] as a function of block size (Figure 3B).

The kinks in the lines in Figure 3A correspond to transitions between cis and trans state during the metadynamics build-up. The larger and less frequent kinks in the simulations for pSb5 compared to those for pSb1 imply that the bias builds up within one state longer before moving to the other. Slow convergence can be caused by correlated motion in degrees of freedom orthogonal to the biased coordinate, which in this case is the $C_{13}{=}C_{14}$ dihedral φ.

4.2 | Correlated degrees of freedom

Using MD simulations, correlation between various collective variables can be assessed. In the case of pSb1, previous research in Ref. 18 documented correlations between the $C_{13}{=}C_{14}$ dihedral angle and adjacent dihedral angles along the minimum energy path, that is, at 0 K. In Figure 4, the correlations at 300 K are presented for both pSb5 and pSb1. These correlation plots were generated from US simulations, with each color in the plot representing a different umbrella potential. Crosses represent the minimum energy path calculated at unrestricted DFT/B3LYP/6-31G*.

The MD simulations at DFTB3 follow closely the B3LYP/6-31G* minimum energy path, which substantiates that DFTB faithfully represents the DFT-PES of these two molecules. However, there is considerable thermal fluctuations around the minimum energy path. For the single-bond dihedrals C_{12}-C_{13} and C_{14}-C_{15}, the spread is ± 0.4 rad ($\approx \pm 23$ degrees), whereas for the improper torsions the spread is ± 0.2 rad ($\approx \pm 11$ degrees). Overall, we find that the correlation extends to the neighboring single bond, but not to the improper dihedrals at C_{12} and C_{15}. We observed a certain level of correlation to the C_{15}-N double bond along the minimum energy paths. However, this correlation is obscured by thermal fluctuations at 300 K (see Figure S1 in the supplement).

The most remarkable feature of the correlations plots are the sudden jumps at the transition states ($\varphi = +\pi/2$ rad and $\varphi = -\pi/2$ rad). The improper dihedral angles at C_{13} and C_{14} represent the planarity at these sp^2-carbon atoms, with $\chi = 0$ rad representing a planar conformation. Consider the improper torsion at C_{14} when approaching the transition state at $\varphi = -\pi/2$ rad from the trans-state, the local conformation at C_{14} bends out of plane up to 20 degrees (0.35 rad, minimum energy value). At the transition state, it suddenly inverts to an

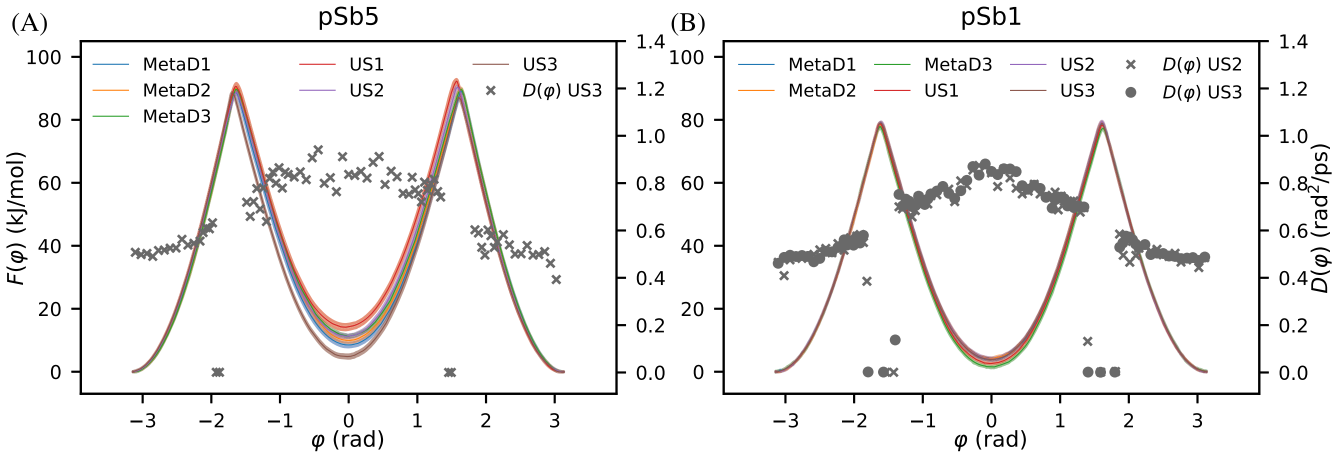

FIGURE 2 Free energy surfaces $F(\varphi)$ and diffusion profiles $D(\varphi)$ along $C_{13}{=}C_{14}$ dihedral angle φ for (A) pSb5 and (B) pSb1 from metadynamics (MetaD) and umbrella sampling (US) using DFTB3. Parameters for MetaD and US simulations are reported in Tables 4 and 5. Free energy curves are filled between plus and minus one standard error.

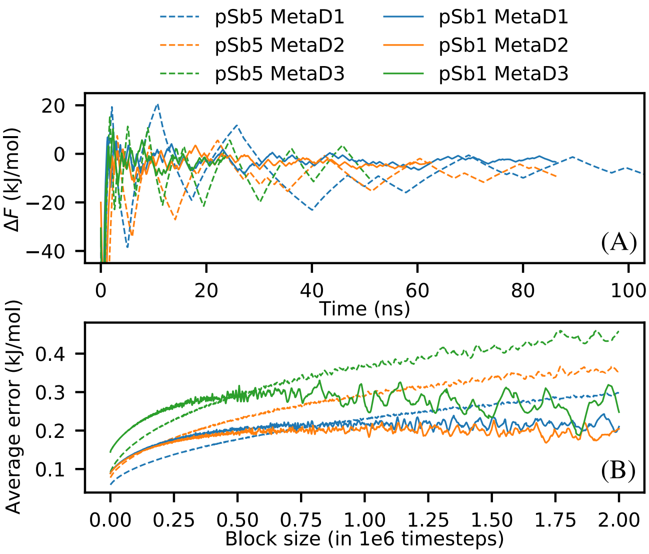

FIGURE 3 (A) Convergence of free energy difference $\Delta F = F_{\mathrm{cis}} - F_{\mathrm{trans}}$ from metadynamics bias as a function of simulation time for pSb5 (dashed) and pSb1 (full). (B) Convergence of the average errors from block averaging analysis as a function of block size for the same simulations as above.

out-of-plane distortion of -20 degrees. On top of the out-of-plane wagging at C_{14}, the substituent at N (H for pSb5 and CH_3 for pSb1) slightly rotates. The concerted motion is illustrated in Figure 5, where structures of pSb1 nearing the transition state ($\varphi \approx -90$ degrees) from cis (orange structure, $\varphi = -60$ degrees) and from trans (red structure, $\varphi = -120$ degrees) are aligned along the C_{13}, C_{15} and N atoms. Note that the out-of-plane wagging at C_{14} contributes to the correlation between $C_{13}{=}C_{14}$ dihedral and C_{14}-C_{15} dihedral.

C_{13} shows a similar out-of-plane wagging as C_{14}. However, while at C_{14} we do not find any difference between pSb5 and pSb1, the correlation of the $C_{13}{=}C_{14}$ dihedral to the improper dihedral at C_{13} and the C_{13}-C_{12} torsion is less pronounced in pSb1 than in pSb5. Presumably, the methyl substituent hinders the out-plane motion at C_{13} in pSb1 compared to C_{14} in the same molecule and thus interrupts the correlation.

4.3 | Rates for the DFTB3 potential energy surface

With a model of the free energy surface of pSb5 and pSb1 and good understanding of the reaction mechanism, we are ready to discuss the reaction rate constants for the thermal isomerization at the level of DFTB3 (Tables 2 and 3). Transition states for both compounds were optimized using the Nudged Elastic Band (NEB) method. NEB optimization converged well for pSb5, but was very sensitive to the choice of the NEB parameters (spring constants, maximal force, amount of nodes) for pSb1.

4.3.1 | Eyring TST

In pSb5, the potential energy barrier E_b for trans→cis reaction is $112.2\,\mathrm{kJ\,mol^{-1}}$, which is in good agreement with the previously reported value of $27.5\,\mathrm{kcal\,mol^{-1}} = 115.1\,\mathrm{kJ\,mol^{-1}}$.[34] The barrier for cis → trans reaction is about $7.7\,\mathrm{kJ\,mol^{-1}}$ lower, which implies that the cis reactant state is slightly higher in energy than the trans state. This aligns closely with the free energy difference of 8 to $10\,\mathrm{kJ\,mol^{-1}}$ between cis and trans states in pSb5 (Figure 2). For pSb1, the potential energy barriers have about equal height (93.7 and $91.1\,\mathrm{kJ\,mol^{-1}}$) and are about $10\,\mathrm{kJ\,mol^{-1}}$ lower than for pSb5. Again, this aligns closely with the FES along φ for this molecule.

In each of the four reactions, the free energy difference $\Delta F^{\ddagger}$ at $T = 300\,\mathrm{K}$ is about 8 to $12\,\mathrm{kJ\,mol^{-1}}$ lower than E_b due to the vibrational and rotational contribution to the free energy difference. For pSb5, the Eyring TST rates are $8.30 \cdot 10^{-6}\,\mathrm{s^{-1}}$ for the trans → cis

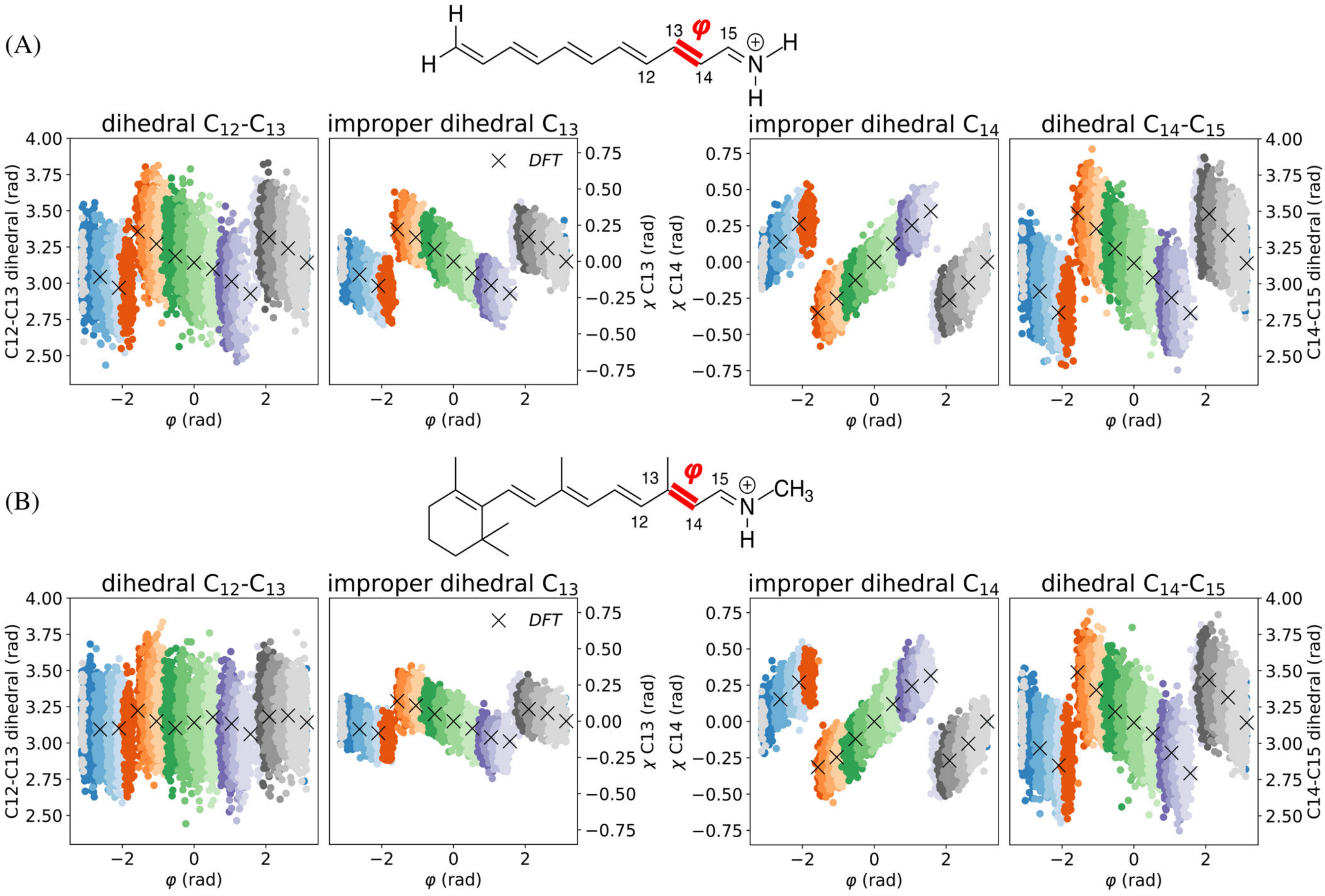

FIGURE 4 Correlations in pSb5 and pSb1. (A) Umbrella sampling simulations using DFTB3 (set US1) for pSb5 showing correlation between $C_{13}{=}C_{14}$ dihedral φ and dihedral C_{12}-C_{13}, the improper dihedral on C_{13}, the dihedral C_{14}-C_{15} and the improper dihedral on C_{14}. Different colors represent different umbrella windows. Black crosses represent constrained optimizations along φ using unrestricted DFT/B3LYP/6-31G*. (B) Same analysis for pSb1.

reaction and $1.99 \cdot 10^{-4}\,\mathrm{s}^{-1}$ for the reverse reaction. In pSb1, the lower energy barrier E_b leads to considerably faster rates, namely $1.42 \cdot 10^{-2}\,\mathrm{s}^{-1}$ for the trans→cis transition and $2.06 \cdot 10^{-1}\,\mathrm{s}^{-1}$ for the reverse reaction.

4.3.2 | High-temperature TST

The high-temperature approximation approximates the free energy contribution to the rates by neglecting the contribution due to the rotational degrees of freedom and by making a classical approximation for the harmonic vibrational partition function. Tables 2 and 3 show that for pSb5 and pSb1 the rotational contribution is less than 1 $\mathrm{kJ\,mol^{-1}}$, and thus neglecting this contribution is well justified. In our systems, the vibrational component contributes negatively to the free energy difference, thereby reducing the overall free energy difference $\Delta F^{\ddagger}$ in comparison to the potential energy barrier E_b. This effect is slightly underestimated in the classical approximation. Consequently, $\Delta F^{\ddagger,\mathrm{ht}}$ in high-temperature TST appears higher than $\Delta F^{\ddagger}$ in Eyring TST, and the high-temperature TST rates are slower than Eyring TST rates. The effect amounts to about 3 $\mathrm{kJ\,mol^{-1}}$ which lowers the rate by about a factor of two. Thus, the high-temperature approximation is suitable for our two systems.

4.3.3 | Infrequent metadynamics

The high-temperature approximation constitutes the link between a quantum partition function and the classical partition functions. Models based on classical partition functions can be sampled by MD simulations to obtain a statistical estimate of the rate. One method to do this is infrequent metadynamics, in which Gaussian bias function are deposited in the potential energy well of the reactant state, and the enhanced reaction rate constant is subsequently reweighted to the unbiased reaction rate constant. Rate constants for two different deposition paces of the Gaussian bias functions are shown in Tables 2 and 3. The obtained rate constants were insensitive with regards to doubling the pace of deposition (Table S1), indicating that the deposition rate is infrequent enough for rate constants to be reliable. The infrequent metadynamics simulations passed the Kolmogorov-Smirnoff test[25] which serves as indication whether the assumptions of TST are violated. The rate constants from infrequent metadynamics

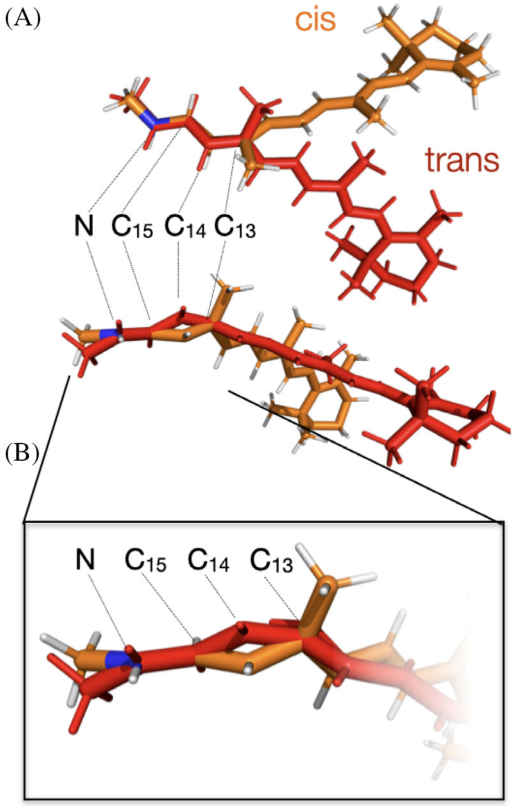

FIGURE 5 (A) Minimum energy structures from constrained optimizations using unrestricted DFT/B3LYP/6-31G* calculations on pSb1 at $\varphi = -60$ degrees (cis, orange structure) and $\varphi = -120$ degrees (trans, red structure). Structures are aligned along the N, C_{15} and C_{13} atoms. (B) Zoom on the reaction center.

are in very good agreement with the rate constants from high-temperature TST. Only in pSb1, the rate constant for the cis → trans reaction is slightly underestimated by infrequent metadynamics.

Infrequent metadynamics and high-temperature TST are based on very similar assumptions (Table 1). In this sense, infrequent metadynamics may be regarded as a sampling-based analogue to high-temperature TST. Because the results from infrequent metadynamics and high-temperature TST are in excellent agreement, we may conclude that sampling-based approaches are suitable for the calculation of reaction rates of chemical reaction and the required MD simulation times are accessible when using DFTB3 to calculate the PES.

4.3.4 | Reaction coordinate based rate theories

We calculated the rate constants from Kramers' (Equation 14) and Pontryagin's (Equation 15) rate theories using the free energy surfaces and diffusion profiles in Figure 2 (Tables 2 and 3). Values for the parameters in Equation (14) are reported in Tables S2 and S3 in the supplement. Surprisingly, these rates are orders of magnitude higher than rates from TST or from infrequent metadynamics. In pSb5, Kramers' rate constant is three orders of magnitude higher then the rate constant from high-temperature TST. This can be traced back to the low free energy barriers $F^{\ddagger}_{AB}$ in the FES compared to the energy difference $\Delta F^{\ddagger}$, as calculated within TST.

Kramers' rate theory can treat reactions that violate the TST assumptions. Therefore, differences between high-temperature TST and Kramers' rate theory might be explained by a complicated reactant state or by violations of the harmonic approximation. However, the choice of our test system, the slow convergence of the metadynamics simulations for the FES in pSb5, as well as the sensitivity of the FES to parameters collectively raise concerns about the optimality of the chosen reaction coordinate. With a sub-optimal reaction coordinate, the free-energy barriers are underestimated and thus Kramers' rate theory overestimates the rate constants. Although φ appears an intuitive choice for the reaction coordinate, the correlated motions in orthogonal degrees of freedom described above suggests that these motions need to be taken into account to construct a sufficiently accurate reaction coordinate.

On the other hand, while pSb1 exhibits the same correlated motions as pSb5, the discrepancy between $F^{\ddagger}_{AB}$ and $\Delta F^{\ddagger}$ is much smaller. Consequently Kramers' rate theory overestimates the rate constants from high-temperature TST for pSb1 only by a factor of 40 for the trans → cis reaction and by a factor of 17 for the reverse reaction. Additionally, the calculation of the FES converges quickly for pSb1. It is not obvious, why the $C_{13}{=}C_{14}$ dihedral angle φ would be a poor reaction coordinate for pSb5 but a reasonably accurate reaction coordinate in pSb1.

Pontryagin's rate theory yields even higher rate constants than Kramers' rate theory and this points to a second effect that might be at play. Pontryagin's rate theory assumes overdamped Langevin dynamics along the reaction coordinate and would overestimate the rates if the effective dynamics actually falls into the intermediate or weak friction regime. In the weak friction regime, also Kramers' rate theory for intermediate friction (Equation 14) would overestimate the rate constant. The friction regime is in part determined by the "sharpness" of the free energy barriers as measured by $\omega_{\ddagger}$, the angular frequency of the harmonic approximation of the FES maximum. Both systems in fact exhibit very sharp barriers and thus high values of $\omega_{\ddagger}$, which might shift the effective dynamics into the weak-to-intermediate friction regime.

4.4 | Comparison across different PES

Tables 2 and 3 compare the energy barriers and the rotational and vibrational contribution to the free energy differences at the level of DFTB3 to those at the unrestricted DFT/B3LYP/6-31G* level, abbreviated DFT/B3LYP in the following. The potential energy barriers E_b from DFT/B3LYP calculations closely aligning with literature-reported values.[2,20,21]

Compared to unrestricted DFT/B3LYP, DFTB3 tends to underestimate the barrier heights, as has been reported previously.[34,42,43] Energies of constrained optimizations along φ for DFT/B3LYP and DFTB3 are shown in Figure S2 in section III of the supplementary

TABLE 2 Rates for thermal cis-trans isomerization around the $C_{13}{=}C_{14}$ double bond in **pSb5** using **DFTB3** as well as DFT/B3LYP/6-31G* without (**DFT**) and with (**DFT-D3**) Grimme's dispersion correction.

		DFTB3		DFT		DFT-D3	
	Equation	**trans → cis**	**cis → trans**	**trans → cis**	**cis → trans**	**trans → cis**	**cis → trans**
Free energy difference between *A* and $AB^{\ddagger}$ in Eyring TST [kJ mol^{-1}]							
E_b		112.2	104.5	123.6	108.5	123.6	109.3
ΔF_{rot}	6a	−0.5	0.2	−0.4	0.1	−0.4	0.1
ΔF_{vib}	6a	−7.3	−8.3	−6.2	−6.5	−6.5	−6.6
$\Delta F^{\ddagger}$	5	104.4	96.5	117.0	102.2	116.8	102.8
Free energy differenece betweeen *A* and $AB^{\ddagger}$ in high-temperature TST [kJ mol^{-1}]							
E_b		112.2	104.5	123.6	108.5	123.6	109.3
$\Delta F_{\mathrm{vib}}^{\mathrm{ht}}$	8	−4.6	−5.2	−3.6	−3.6	−3.7	−3.7
$\Delta F^{\ddagger,\mathrm{ht}}$	8	107.6	99.3	120.0	104.8	119.9	105.6
Free energy barrier$F^{\ddagger}_{AB}$ [kJ mol^{-1}]							
$F^{\ddagger}_{AB}$		89.0	80.5	n/a	n/a	n/a	n/a
Rates [s^{-1}]							
Eyring TST	3	8.30×10^{-6}	1.99×10^{-4}	5.40×10^{-8}	2.04×10^{-5}	5.81×10^{-8}	1.56×10^{-5}
high *T* TST	7	2.28×10^{-6}	6.39×10^{-5}	1.62×10^{-8}	7.00×10^{-6}	1.65×10^{-8}	5.19×10^{-6}
InMetaD 1	11	1.94×10^{-6}	1.04×10^{-4}	n/a	n/a	n/a	n/a
InMetaD 2	11	2.63×10^{-6}	9.22×10^{-5}	n/a	n/a	n/a	n/a
Kramers	14	4.06×10^{-3}	1.74×10^{-1}	n/a	n/a	n/a	n/a
Pontryagin	15	1.14×10^{-2}	2.74×10^{-1}	n/a	n/a	n/a	n/a

material. The discrepancy between DFT/B3LYP and DFTB3 is larger for the trans → cis transitions than in the cis → trans transitions, with a discrepancy as high as 11.4 kJ mol^{-1} in pSb5. The exception to this trend is the cis → trans transition in pSb1, for which the DFT/B3LYP is 1 kJ mol^{-1} lower than the DFTB3 barrier.

The rotational contributions to total free energy difference are nearly identical at DFT/B3LYP and at DFTB3, which can be attributed to the rigid molecular scaffold. The vibrational motion lowers the total free energy barrier in all four reactions. However, the effect is smaller at the level of DFT/B3LYP than with DFTB3. The discrepancy between DFT/B3LYP and DFTB3 for the vibrational contribution can be as large as the discrepancy for the potential energy barrier E_b (see e.g., cis → trans reaction in pSb1). This highlights the need to consider not only the potential energy barrier but also the vibrational free energy of the reactant and transition state when comparing different PES.

Overall, we find that the total free energy difference $\Delta F^{\ddagger}$ is 6 to 13 kJ mol^{-1} larger in DFT/B3LYP than in DFTB3. Consequently, the Eyring TST rate constants at the level of DFT/B3LYP are one to two orders of magnitude lower than at the level of DFTB3. As with DFTB3, the high-temperature rate constant is slightly lower than the Eyring TST rate constant, because the reduction of the total free energy difference due to the vibrational contribution is underestimated when using the high-temperature limit. Rates from infrequent metadynamics or reaction-coordinate based methods are not available, because they require ab-initio MD simulations. The necessary simulation time to converge these rate estimates is challenging to attain at this level of theory.

The last two columns in Tables 2 and 3 report the influence of the the D3 dispersion correction for DFT[47] on the energy barriers and the free energy contributions to the rates. The effect is less than 1 kJ mol^{-1} (only exception: ΔF_{vib} for trans → cis in pSb1). The difference in the energies for constrained optimizations along φ (Figure S2 in the supplement) is equally small. As a result, there is a minimal difference in the rates when calculated with and without D3 correction. We suspect that the small influence of the D3 correction on the PES stems from the linear and rigid structure of the two molecules. Dispersion is a strongly distance-dependent pairwise interaction. Due to the linearity, the molecules likely have a small intramolecular dispersion overall. Due to the rigid polyene scaffold, most pairwise distances do not change during the reaction. Even though rotation from trans to cis shortens the distance between the Schiff base and the β-ionone ring, the distance remains so large that the two groups have minimal dispersion interaction.

5 | METHODS

Calculations for DFTB3 were carried out with the DFTB+ software package[48] using the 3ob-3-1 Slater-Koster parameter set.[49] Energy minimizations, constrained optimizations and Nudged Elastic Band

TABLE 3 Rates for thermal cis-trans isomerization around the $C_{13}{=}C_{14}$ double bond in **pSb1** using **DFTB3** as well as DFT/B3LYP/6-31G* without (**DFT**) and with (**DFT-D3**) Grimme's dispersion correction.

		DFTB3		DFT		DFT-D3	
	Equation	trans → cis	cis → trans	trans → cis	cis → trans	trans → cis	cis → trans
Free energy difference between *A* and $AB^\ddagger$ in Eyring TST [$\mathrm{kJ\,mol^{-1}}$]							
E_b		93.7	91.1	98.0	90.1	98.2	90.4
ΔF_{rot}	6a	−0.1	0.0	−0.1	−0.0	−0.1	−0.0
ΔF_{vib}	6a	−7.7	−12.0	−2.4	−3.8	−4.1	−3.7
$\Delta F^\ddagger$	5	85.8	79.2	95.4	86.2	94.0	86.7
Free energy difference$\Delta F^\ddagger$ between *A* and $AB^\ddagger$ in high-temperature TST [$\mathrm{kJ\,mol^{-1}}$]							
E_b		93.7	91.1	98.0	90.1	98.2	90.4
$\Delta F^{\mathrm{ht}}_{\mathrm{vib}}$	8	−5.1	−9.4	0.5	−1.1	−1.1	−0.9
$\Delta F^{\ddagger,\mathrm{ht}}$	8	88.5	81.7	98.4	89.0	97.0	89.5
Free energy barrier$F^\ddagger_{AB}$ [$\mathrm{kJ\,mol^{-1}}$]							
$F^\ddagger_{AB}$		78.9	75.0	n/a	n/a	n/a	n/a
Rates [$\mathrm{s^{-1}}$]							
Eyring TST	3	1.42×10^{-2}	2.06×10^{-1}	3.09×10^{-4}	1.24×10^{-2}	5.35×10^{-4}	9.92×10^{-3}
high *T* TST	7	4.81×10^{-3}	7.44×10^{-2}	9.21×10^{-5}	4.12×10^{-3}	1.58×10^{-4}	3.31×10^{-3}
InMetaD1	11	2.97×10^{-3}	9.30×10^{-3}	n/a	n/a	n/a	n/a
InMetaD2	11	3.09×10^{-3}	1.22×10^{-2}	n/a	n/a	n/a	n/a
Kramers	14	1.92×10^{-1}	1.30×10^{0}	n/a	n/a	n/a	n/a
Pontryagin	15	5.43×10^{-1}	2.07×10^{0}	n/a	n/a	n/a	n/a

(NEB) calculations were done by interfacing DFTB+ with the Atomic Simulation Environment (ASE)[50] and using the Broyden-Fletcher-Goldfarb-Shanno (BFGS) algorithm[51] for numerical optimization. Vibrational analysis of the optimized structures was done using DFTB+ to obtain the vibrational frequencies, while rotational moments of inertia were calculated by entering the optimized configuration into the Gaussian 16 software.[52] From these data we calculated rates for Eyring TST and high-temperature TST.

Ab-initio MD simulations were performed using DFTB+ using the velocity-Verlet integrator with a time step of 1 fs. Before simulations, energy minimization was done, followed by temperature equilibration at 300 K in two steps. In a first equilibration run, the Berendsen thermostat[53] with a coupling time of 2 ps is employed, while in a second equilibration run a Nosé-Hoover chain setup[54–56] of coupling time 2 ps and chain length 3 is used. For production runs, the same thermostat setup was used as for the second equilibration runs.

Well-tempered metadynamics[29] and umbrella sampling[44] were carried out by interfacing the PLUMED[57] software package with DFTB+. Parameter sets for metadynamics and umbrella sampling sets can be found in Tables 4 and 5 respectively. Sets of runs for infrequent metadynamics were set up by equilibrating in the reactant state, after which a metadynamics bias is applied until a transition is registered. The transition times were reweighted using the acceleration factor which was directly calculated by PLUMED. The set of reweighted transition times was fitted to the theoretical cumulative distribution function of a Poisson distribution (Equation 10) to obtain a mean first-passage time and corresponding rate.

Diffusion profiles were calculated using the method from Reference 8. Effective masses of the reactant states were calculated by measuring the average squared velocity along the dihedral angle and using the equipartition theorem. Frequencies of the harmonic approximations of the reactant wells and transition state barriers were calculated from spring constants obtained by harmonically fitting the corresponding wells or barriers. Free energy barriers $F^\ddagger_{AB}$ are measured from the FES directly. One-dimensional rate methods (Kramers and Pontryagin) can then be applied straightforwardly.

Calculations at the DFT level were performed using the Gaussian 16 software[52] using unrestricted DFT with the B3LYP functional[23,24] and the 6-31G* basis set.[58] Full geometry optimizations as well as constrained optimizations were done using the Berny optimization algorithm[59] as implemented in Gaussian. Transition state search was performed using the Synchronous Transit-guided Quasi-Newton (STQN) method[60,61] as implemented in Gaussian, where the reactant and product state input configurations were chosen to be the geometry optimized structures in the trans and cis states. Gaussian performs a full thermochemical analysis including calculation of the translational, rotational and

TABLE 4 Parameters for metadynamics and infrequent metadynamics simulations for pSb5 and pSb1 using DFTB3.

	Height [kJ mol^{-1}]	Width [rad]	Pace [ps]	Bias factor	Time [ns]	Runs
pSb5						
MetaD1	1.3	0.15	0.5	16	152	n/a
MetaD2	1.3	0.10	0.5	16	87	n/a
MetaD3	0.75	0.075	0.25	25	51	n/a
InMetaD1	1.3	0.05	5.0	16	n/a	25
InMetaD2	1.3	0.05	10.0	16	n/a	30
pSb1						
MetaD1	1.3	0.10	0.5	16	86	n/a
MetaD2	1.3	0.05	0.5	16	63	n/a
MetaD3	1.3	0.10	0.5	16	24	n/a
InMetaD1	1.3	0.05	5.0	16	n/a	25
InMetaD2	1.3	0.05	10.0	16	n/a	30

TABLE 5 Parameters for umbrella sampling using DFTB3.

Windows	Biased region [rad]	Interval [rad]	Force constant [kJ mol^{-1} rad^{-2}]
63	$[-3.1, +3.1]$	0.1	500
10	$[-1.95, -1.05]$	0.1	500
10	$[+1.05, +1.95]$	0.1	500

Note: Each umbrella sampling set was run with 83 windows positioned as shown here. In total, three sets were run for pSb5 and three for pSb1 (Figure 2).

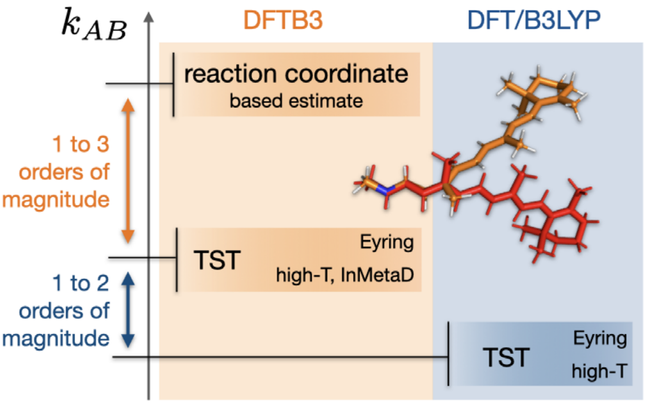

FIGURE 6 Effect of rate model and PES on the estimated reaction rate constant.

vibrational partition functions and corresponding energies and entropies.[62]

This allows for straightforward calculation of rates for Eyring TST. Vibrational frequencies were obtained from Gaussian separately[63] and used to calculate rates for high-temperature TST.

A complete overview of the computational details is given in section II of the supplementary information.

6 | CONCLUSIONS

We studied the thermal cis-trans isomerization in two retinal analogues at 300 K in the gas phase. This reaction falls well within the approximation of TST, and thus accurate values for the reaction rate constant can be obtained from this theoretical framework. However, reactions in molecules with numerous flexible degrees of freedom or reactions in complex environments may not be accurately modeled by TST. We therefore explored whether accurate estimates of the reaction rate constant can be obtained from MD simulations. The impact of changing the theoretical framework for modelling the reaction rate must be assessed relative to the error in the potential energy surface (PES), which is often considered to be the primary error source in rate modeling. To gauge the effect of changing the PES, we compared TST rate constants at the level of at the DFTB3 and the unrestricted DFT/B3LYP/6-31G* level. Figure 6 summarizes our results.

Reaction rate constants at DFTB3 are larger than those at DFT, with a difference of one to two orders magnitude. However only in pSb5 the increase in reaction rate can be mainly attributed to a lower potential energy barrier. In pSb1, the change of the vibrational free energy has an equally strong (trans → cis) or even larger (cis → trans) contribution to the increase of the reaction rate constant. Thus, reducing the comparison of different PES to the height of the potential energy barrier and neglecting entropic effects may be misleading.

It is important to note that we only compared PES that are ultimately derived from DFT. DFT and wavefunction-based methods tend to differ in delocalization of the conjugated π-electron system, with DFT typically overdelocalizing the π-electrons.[64] Overdelocalization reduces the double-bond character in the $C_{13}{=}C_{14}$ double bond, and thus decreases the reaction barrier. In fact, for cis-trans isomerization in polyene chains, DFT/B3LYP/6-31G* underestimates the torsional barrier compared to CASSCF[65] as well as compared to experimental data.[66–68] Thus, the true reaction rate constant might be even lower than our DFT estimates.

An important assumption when estimating reaction rate constants from MD simulations is that classical mechanics are used to model the dynamics of the nuclei and to approximate the partition functions. The classical limit is well justified for rugged potential energy landscapes with broad minima and relatively low energy barriers, but might not be appropriate for modelling a chemical reaction. In both of our molecules, the classical limit (high-temperature TST) yields a lower rate constant than Eyring TST, but the effect is less than an order of magnitude. Thus, the error due to the classical limit is small compared to the uncertainty due to the model of the PES.

Since the classical limit is justified for our systems, one should in principle be able to estimate reaction rate constants from MD simulations. Indeed, the infrequent metadynamics results are in excellent agreement with results from high-temperature TST. The length of the simulations (on a biased PES) were in the nanosecond regime, the mean-first passage times $\tau_{AB} = 1/k_{AB}$ are in the regime of hundreds to hundred thousands of seconds. This is a enormous speedup, with the largest acceleration factors being of the order of 10^{14}.

By contrast, our results from Kramers and Pontryagin's rate theory overestimate the rate constant by multiple orders of magnitude. These two methods rely on a reaction coordinate – in our case the $C_{13}{=}C_{14}$ torsion angle φ - but the FES can be very sensitive to the choice of this reaction coordinate. In fact, we found that the improper dihedrals of the substituents on the C_{13} and C_{14} atoms correlate with the reaction coordinate φ. We hypothesized that this was indicative of a isomerization mechanism consisting of a concerted motion where the C_{14} atom temporarily nods out of the polyene plain, before the isomerization is completed. Thus, even though the torsion angle φ is a very intuitive reaction coordinate, it might not be optimal enough to yield accurate results for Kramers and Pontryagin's rate theory.

This places us in a challenging position. Both MD based-approaches, infrequent metadynamics and reaction coordinate based rate models, come with a high computational cost. Our simulations required approximately 10 to 100 ns for each rate estimation. However, since infrequent metadynamics is derived from TST, it is particularly suitable for chemical reactions that align well with Eyring TST. By contrast, reaction coordinate based rate theories have the potential to model systems deviating from the harmonic approximation and the separation of timescales. However, their robustness is compromised due to sensitivity to the reaction coordinate and the friction regime.

Fortunately, several alternatives exist. Within reaction coordinate-based rate models, one can optimize the reaction coordinate,[69,70] and we will explore this approach in subsequent work.[71] Interestingly, neural networks[17,72] can be used to optimize reaction coordinates. Another avenue extends these models to encompass effective dynamics within multidimensional collective variable spaces.[73,74] Alternatively, one can opt for transition path sampling[75–77] and leverage dynamical reweighting techniques that are not based on TST.[5,78,79] In summary, while sampling chemical reactions in complex systems poses a formidable challenge, there is optimism that this wide variety of ideas will allow us to solve this task.

ACKNOWLEDGMENTS

This research has been funded by Deutsche Forschungsgemeinschaft (DFG) through grant SFB 1114 "Scaling Cascades in Complex Systems"–project number 235221301. Simon Ghysbrecht acknowledges funding by the Einstein Center of Catalysis/BIG-NSE. Open Access funding enabled and organized by Projekt DEAL.

DATA AVAILABILITY STATEMENT

The data that support the findings of this study are available from the corresponding author upon reasonable request.

ORCID

Simon Ghysbrecht https://orcid.org/0009-0003-7556-9592

REFERENCES

[1] H. Eyring, *J Chem Phys* **1935**, *3*, 107.
[2] B. Peters, *Reaction rate theory and rare events*, Elsevier, Amsterdam **2017**.
[3] D. Frenkel, B. Smit, *Understanding molecular simulation: from algorithms to applications*, Elsevier, Amsterdam **2023**.
[4] P. Hänggi, P. Talkner, M. Borkovec, *Rev. Mod. Phys.* **1990**, *62*, 251.
[5] S. Kieninger, L. Donati, B. G. Keller, *Curr. Opin. Struct. Biol.* **2020**, *61*, 124.
[6] B. Peters, *Annu. Rev. Phys. Chem.* **2016**, *67*, 669.
[7] J. Hénin, T. Lelièvre, M. Shirts, O. Valsson, L. Delemotte, *Living J Comput Mol Sci* **2022**, *4*, 1583.
[8] G. Hummer, *New J. Phys.* **2005**, *7*, 34.
[9] H. A. Kramers, *Physica* **1940**, *7*, 284.
[10] L. Pontryagin, A. Andronov, A. Vitt, *J. Exp. Theor. Phys.* **1933**, *3*, 165.
[11] P. Tiwary, M. Parrinello, *Phys. Rev. Lett.* **2013**, *111*, 230602.
[12] M. Gaus, Q. Cui, M. Elstner, *J. Chem. Theory Comput.* **2011**, *7*, 931.
[13] P. Pracht, F. Bohle, S. Grimme, *Phys. Chem. Chem. Phys.* **2020**, *22*, 7169.
[14] R. Schade, T. Kenter, H. Elgabarty, M. Lass, T. D. Kühne, C. Plessl, *Int J High Perform Comput Appl* **2023**, *37*, 530.
[15] H. M. Senn, W. Thiel, *Angew Chem Int Ed* **2009**, *48*, 1198.
[16] T. P. Senftle, S. Hong, M. M. Islam, S. B. Kylasa, Y. Zheng, Y. K. Shin, C. Junkermeier, R. Engel-Herbert, M. J. Janik, H. M. Aktulga, *Npj Comput. Mater.* **2016**, *2*, 1.
[17] P. Gkeka, G. Stoltz, A. Barati Farimani, Z. Belkacemi, M. Ceriotti, J. D. Chodera, A. R. Dinner, A. L. Ferguson, J.-B. Maillet, H. Minoux, *J. Chem. Theory Comput.* **2020**, *16*, 4757.
[18] A.-N. Bondar, M. Knapp-Mohammady, S. Suhai, S. Fischer, J. C. Smith, *Theor. Chem. Acc.* **2011**, *130*, 1169.
[19] P. Tavan, K. Schulten, D. Oesterhelt, *Biophys. J.* **1985**, *47*, 415.
[20] E. Tajkhorshid, S. Suhai, *J Phys Chem B* **1999**, *103*, 5581.
[21] S. Gozem, M. Huntress, I. Schapiro, R. Lindh, A. A. Granovsky, C. Angeli, M. Olivucci, *J. Chem. Theory Comput.* **2012**, *8*, 4069.
[22] M. Elstner, *Theor. Chem. Acc.* **2006**, *116*, 316.
[23] C. Lee, W. Yang, R. G. Parr, *Phys. Rev. B* **1988**, *37*, 785.
[24] A. D. Becke, *Phys. Rev. A* **1988**, *38*, 3098.
[25] M. Salvalaglio, P. Tiwary, M. Parrinello, *J. Chem. Theory Comput.* **2014**, *10*, 1420.
[26] H. Grubmüller, *Phys Rev E* **1995**, *52*, 2893.
[27] A. F. Voter, *Phys. Rev. Lett.* **1997**, *78*, 3908.
[28] S. A. Khan, B. M. Dickson, B. Peters, *J Chem Phys* **2020**, *153*, 054125.
[29] A. Barducci, G. Bussi, M. Parrinello, *Phys. Rev. Lett.* **2008**, *100*, 020603.
[30] J. Baudry, S. Crouzy, B. Roux, J. C. Smith, *J. Chem. Inf. Comput. Sci.* **1997**, *37*, 1018.
[31] J. Baudry, S. Crouzy, B. Roux, J. C. Smith, *Biophys. J.* **1999**, *76*, 1909.
[32] E. Tajkhorshid, S. Suhai, *Chem. Phys. Lett.* **1999**, *299*, 457.
[33] E. Tajkhorshid, B. Paizs, S. Suhai, *J Phys Chem B* **1999**, *103*, 4518.
[34] H. Zhou, E. Tajkhorshid, T. Frauenheim, S. Suhai, M. Elstner, *Chem. Phys.* **2002**, *277*, 91.
[35] L. De Vico, C. S. Page, M. Garavelli, F. Bernardi, R. Basosi, M. Olivucci, *J. Am. Chem. Soc.* **2002**, *124*, 4124.

[36] S. Gozem, H. L. Luk, I. Schapiro, M. Olivucci, *Chem. Rev.* **2017**, *117*, 13502.

[37] A. Zen, E. Coccia, S. Gozem, M. Olivucci, L. Guidoni, *J. Chem. Theory Comput.* **2015**, *11*, 992.

[38] B. Aradi, B. Hourahine, T. Frauenheim, *J Phys Chem A* **2007**, *111*, 5678.

[39] B. Hourahine, S. Sanna, B. Aradi, C. Köhler, T. Niehaus, T. Frauenheim, *J Phys Chem A* **2007**, *111*, 5671.

[40] P. Melix, A. F. Oliveira, R. Rüger, T. Heine, *Theor. Chem. Acc.* **2016**, *135*, 1.

[41] M. Sugihara, V. Buss, P. Entel, M. Elstner, T. Frauenheim, *Biochemistry* **2002**, *41*, 15259.

[42] A.-N. Bondar, M. Elstner, S. Suhai, J. C. Smith, S. Fischer, *Structure* **2004**, *12*, 1281.

[43] N. Elghobashi-Meinhardt, P. Phatak, A.-N. Bondar, M. Elstner, J. C. Smith, *J Membrane Biol* **2018**, *251*, 315.

[44] G. M. Torrie, J. P. Valleau, *J. Comput. Phys.* **1977**, *23*, 187.

[45] A. Laio, M. Parrinello, *Proc Natl Acad Sci* **2002**, *99*, 12562.

[46] G. Bussi, G. A. Tribello, in *Biomolecular Simulations. Methods in Molecular Biology* (Eds: M. Bonomi, C. Camilloni), Vol. 2022, Humana, New York, NY **2019**.

[47] S. Grimme, J. Antony, S. Ehrlich, H. Krieg, *J. Chem. Phys.* **2010**, *132*, 154104.

[48] B. Hourahine, B. Aradi, V. Blum, F. Bonafé, A. Buccheri, C. Camacho, C. Cevallos, M. Deshaye, T. Dumitrică, A. Dominguez, *J. Chem. Phys.* **2020**, *152*, 124101.

[49] M. Gaus, A. Goez, M. Elstner, *J. Chem. Theory Comput.* **2013**, *9*, 338.

[50] A. H. Larsen, J. J. Mortensen, J. Blomqvist, I. E. Castelli, R. Christensen, M. Dułak, J. Friis, M. N. Groves, B. Hammer, C. Hargus, *J. Phys: Condens. Matter* **2017**, *29*, 273002.

[51] R. Fletcher, *Practical methods of optimization*, John Wiley & Sons, Hoboken, NJ, USA **2000**.

[52] M. J. Frisch, G. W. Trucks, H. B. Schlegel, G. E. Scuseria, M. A. Robb, J. R. Cheeseman, G. Scalmani, V. Barone, G. A. Petersson, H. Nakatsuji, X. Li, M. Caricato, A. V. Marenich, J. Bloino, B. G. Janesko, R. Gomperts, B. Mennucci, H. P. Hratchian, J. V. Ortiz, A. F. Izmaylov, J. L. Sonnenberg, D. Williams-Young, F. Ding, F. Lipparini, F. Egidi, J. Goings, B. Peng, A. Petrone, T. Henderson, D. Ranasinghe, V. G. Zakrzewski, J. Gao, N. Rega, G. Zheng, W. Liang, M. Hada, M. Ehara, K. Toyota, R. Fukuda, J. Hasegawa, M. Ishida, T. Nakajima, Y. Honda, O. Kitao, H. Nakai, T. Vreven, K. Throssell, J. A. Montgomery Jr., J. E. Peralta, F. Ogliaro, M. J. Bearpark, J. J. Heyd, E. N. Brothers, K. N. Kudin, V. N. Staroverov, T. A. Keith, R. Kobayashi, J. Normand, K. Raghavachari, A. P. Rendell, J. C. Burant, S. S. Iyengar, J. Tomasi, M. Cossi, J. M. Millam, M. Klene, C. Adamo, R. Cammi, J. W. Ochterski, R. L. Martin, K. Morokuma, Gaussian 16 Revision C.01. **2016**.

[53] H. J. Berendsen, J. Postma, W. F. Van Gunsteren, A. DiNola, J. R. Haak, *J Chem Phys* **1984**, *81*, 3684.

[54] S. Nosé, *J Chem Phys* **1984**, *81*, 511.

[55] W. G. Hoover, *Phys. Rev. A* **1985**, *31*, 1695.

[56] G. J. Martyna, M. L. Klein, M. Tuckerman, *J Chem Phys* **1992**, *97*, 2635.

[57] G. A. Tribello, M. Bonomi, D. Branduardi, C. Camilloni, G. Bussi, *Comput. Phys. Commun.* **2014**, *185*, 604.

[58] W. J. Hehre, R. Ditchfield, J. A. Pople, *J. Chem. Phys.* **1972**, *56*, 2257.

[59] H. B. Schlegel, *J. Comput. Chem.* **1982**, *3*, 214.

[60] C. Peng, H. Bernhard Schlegel, *Isr. J. Chem.* **1993**, *33*, 449.

[61] C. Peng, P. Y. Ayala, H. B. Schlegel, M. J. Frisch, *J. Comput. Chem.* **1996**, *17*, 49.

[62] J. W. Ochterski, Gaussian Inc. **2000**.

[63] J. W. Ochterski, Gaussian Inc. **1999**.

[64] M. Wanko, M. Hoffmann, P. Strodel, A. Koslowski, W. Thiel, F. Neese, T. Frauenheim, M. Elstner, *J Phys Chem B* **2005**, *109*, 3606.

[65] B. Paizs, E. Tajkhorshid, S. Suhai, *J Phys Chem B* **1999**, *103*, 5388.

[66] T. Okada, M. Sugihara, A.-N. Bondar, M. Elstner, P. Entel, V. Buss, *J. Mol. Biol.* **2004**, *342*, 571.

[67] F. Buda, P. Giannozzi, F. Mauri, *J Phys Chem B* **2000**, *104*, 9048.

[68] A.-N. Bondar, J. C. Smith, M. Elstner, *Theor. Chem. Acc.* **2010**, *125*, 353.

[69] E. Vanden-Eijnden, *Annu. Rev. Phys. Chem.* **2010**, *61*, 391.

[70] B. Roux, *J Phys Chem A* **2021**, *125*, 7558.

[71] S. Ghysbrecht, L. Donati, B. G. Keller, arXiv preprint arXiv: 2312.12948. **2023**.

[72] H. Jung, R. Covino, A. Arjun, C. Leitold, C. Dellago, P. G. Bolhuis, G. Hummer, *Nat Comput Sci* **2023**, *3*, 334.

[73] H. C. Lie, K. Fackeldey, M. Weber, *SIAM J Matrix Anal Appl* **2013**, *34*, 738.

[74] L. Donati, M. Weber, B. G. Keller, *J. Phys: Condens. Matter* **2021**, *33*, 115902.

[75] P. G. Bolhuis, D. Chandler, C. Dellago, P. L. Geissler, *Annu. Rev. Phys. Chem.* **2002**, *53*, 291.

[76] D. M. Zuckerman, L. T. Chong, *Annu. Rev. Biophys.* **2017**, *46*, 43.

[77] K. Palacio-Rodriguez, F. Pietrucci, *J. Chem. Theory Comput.* **2022**, *18*, 4639.

[78] L. Donati, B. G. Keller, *J Chem Phys* **2018**, *149*, 072335.

[79] K. Shmilovich, A. L. Ferguson, *J. Phys. Chem. A* **2023**, *127*, 3497.

SUPPORTING INFORMATION

Additional supporting information can be found online in the Supporting Information section at the end of this article.

How to cite this article: S. Ghysbrecht, B. G. Keller, *J. Comput. Chem.* **2024**, *45*(16), 1390. https://doi.org/10.1002/jcc.27332

Supplementary Information: Thermal Isomerization Rates in Retinal Analogues using Ab-Initio Molecular Dynamics

Simon Ghysbrecht and Bettina G. Keller[a)]

(Dated: 16 February 2024)

I. TRANSITION STATE THEORIES

The introduction of activated complex theory introduced here largely follows the textbook by Mortimer[1]. Alternative derivations can be found in textbooks by Peters[2] or McQuarrie & Simon[3].

Eyring transition state theory

The cis-trans isomerization is a unimolecular reaction $A \rightarrow B$ which, according to the theory of the activated complex, is modeled as

$$A \rightleftharpoons AB^{\ddagger} \rightarrow B \tag{S1}$$

where the reactant A is the cis state, $AB^{\ddagger}$ is the activated complex, and B is the trans state. One assumes (1) that A and $AB^{\ddagger}$ are in equilibrium with equilibrium constant

$$K^{\ddagger} = \frac{[AB^{\ddagger}]}{[A]} \tag{S2}$$

where [...] denotes concentrations, and (2) that the rate-determining step in the reaction is the decay of $AB^{\ddagger}$ to the product state B. Then the reaction rate is

$$r_{AB} = -\frac{d[A]}{dt} = k_{AB}[A] = \nu_r[AB^{\ddagger}] = \nu_r K^{\ddagger}[A] \tag{S3}$$

where k_{AB} is the rate constant with units s^{-1}, ν_r is the rate at which the TS conformation decays, and the last equality arises from the definition of the equilibrium constant. Note that for a unimolecular reaction, equilibrium constant $K^{\ddagger}$ and dimensionless equilibrium constant $\widetilde{K}^{\ddagger}$ are identical, because

$$K^{\ddagger} = \frac{[AB^{\ddagger}]}{[A]} = \frac{[AB^{\ddagger}]/c^{\circ}}{[A]/c^{\circ}} = \widetilde{K}^{\ddagger}\,, \tag{S4}$$

where c° is the standard concentration.

The rate constant of the reaction then is

$$k_{AB}^{\mathrm{Eyr}} = \nu_r K^{\ddagger} = \nu_r \cdot \frac{q_{AB^{\ddagger}}}{q_A} \exp\left(-\frac{E_b}{RT}\right) \tag{S5}$$

where we related $K^{\ddagger}$ to its definition in terms of molecular partition functions $q_{AB^{\ddagger}}$ and q_A. q_A is calculated with respect to the energy E_A at the minimum energy conformation of A, whereas $\widetilde{q}_{AB^{\ddagger}}$ is calculated with respect to the energy at the saddle point of the Born-Oppenheimer potential energy surface $E_{AB^{\ddagger}}$, i.e. both energies are measured at a single point in conformational space. $E_b = E_{AB^{\ddagger}} - E_A$ accounts for the the difference in reference

---

[a)] Electronic mail: bettina.keller@fu-berlin.de energies and can be interpreted as the energetic barrier of the reaction. R is the ideal gas constant, and T is the temperature.

We calculate and report potential and free energies in units of $\mathrm{J\,mol^{-1}}$, correspondingly the thermal energy is also reported as a molar quantity: RT. Likewise masses and reduced masses are treated as molar masses: $\mathrm{kg\,mol^{-1}}$. If potential and free energies are treated with units of J, and masses with units of kg, R should be replaced by the Boltzmann constant $k_B = R/N_A$ in eq. S5 and all of the following equations. N_A is the Avogadro constant.

Assuming that the electronic, translational, rotational and vibrational degrees of freedom are sufficiently decoupled, one can decompose the molecular partition function

$$q_i = q_{i,\mathrm{el}} \cdot q_{i,\mathrm{tr}} \cdot q_{i,\mathrm{rot}} \cdot q_{i,\mathrm{vib}} \qquad i = A, AB^{\dagger} \tag{S6}$$

into electronic partition function $q_{i,\mathrm{el}}$, translational partition function $q_{i,\mathrm{tr}}$, rotational partition function $q_{i,\mathrm{rot}}$, and vibrational partition function $q_{i,\mathrm{vib}}$. The ratio of partition functions in eq. S5 then decomposes into factors

$$\frac{q_{AB^{\ddagger}}}{q_A} = \frac{q_{AB^{\ddagger},\mathrm{el}}}{q_{A,\mathrm{el}}} \cdot \frac{q_{AB^{\ddagger},\mathrm{tr}}}{q_{A,\mathrm{tr}}} \cdot \frac{q_{AB^{\ddagger},\mathrm{rot}}}{q_{A,\mathrm{rot}}} \cdot \frac{q_{AB^{\ddagger},\mathrm{vib}}}{q_{A,\mathrm{vib}}} \,. \tag{S7}$$

In retinal, the electronically excited states are only populated when the molecule is excited by light. At room temperature and without any external excitation, only the electronic ground state is populated. Therefore $q_{AB^{\ddagger},\mathrm{el}} = q_{A,\mathrm{el}} = 1$, and the electronic factor in eq. S7 equals 1. The translational partition function is modelled using the quantum mechanical treatment of a particle in a box. The translational factor then reduces to the ratio of masses $q_{AB^{\ddagger},\mathrm{tr}}/q_{A,\mathrm{tr}} = \left(M_{AB^{\ddagger}}/M_A\right)^{3/2} = 1$, since in a unimolecular reaction the molar mass of the reactant M_A and the molar mass of the activated complex $M_{AB^{\ddagger}}$ are equal. The rotational partition function is modelled using the quantum mechanical treatment of a rigid rotor

$$q_{i,rot} = \frac{\pi^2}{\sigma_i}\sqrt{\frac{8\pi\, I_{i,a}\, RT}{h^2}}\sqrt{\frac{8\pi\, I_{i,b}\, RT}{h^2}}\sqrt{\frac{8\pi\, I_{i,c}\, RT}{h^2}} \qquad i = A, AB^{\dagger} \tag{S8}$$

where $I_{i,a}$, $I_{i,b}$, and $I_{i,c}$ are the three moments of inertia in the two retinal conformations (measured at the minimum of the reactant state and at the saddle point of the transition state and in molar units), h is the molar Planck constant, and σ_i is the symmetry number which is 1 for both conformations. The rotational factor thus reduces to

$$\frac{q_{AB^{\ddagger},\mathrm{rot}}}{q_{A,\mathrm{rot}}} = \sqrt{\frac{I_{AB^{\ddagger},a}}{I_{A,a}} \cdot \frac{I_{AB^{\ddagger},b}}{I_{A,b}} \cdot \frac{I_{AB^{\ddagger},c}}{I_{A,c}}} \,. \tag{S9}$$

We assume that the dynamics of the remaining $3N-6$ vibrational degrees of freedom can be modelled by a multidimensional harmonic oscillators (harmonic approximation), where the frequencies $\nu_{i,k}$, with $i = A, AB^{\ddagger}$, along each direction are given by the square rooted eigenvalues of the mass-weighted Hessian matrices at the minimum of the reactant state for $q_{A,\mathrm{vib}}$, and at the saddle point for $q_{AB^{\ddagger},\mathrm{vib}}$[4,5]. We define $q_{A;\mathrm{vib}}$ and $q_{AB^{\ddagger};\mathrm{vib}}$ relative to the PES minimum at A and relative to the saddle point of the PES minimum at $AB^{\ddagger}$, i.e. the vibrational partition functions include the zero-point energies.

The vibrational partition function at the reactant state is

$$q_{A;\mathrm{vib}} = \prod_{k=1}^{3N-6} \frac{\exp\left(-\frac{h\nu_{A,k}}{2RT}\right)}{1-\exp\left(-\frac{h\nu_{A,k}}{RT}\right)} \,. \tag{S10}$$

Molar masses are used for the mass-weighted Hessian matrices, and the force-constant of the potential is given in molar units.

The mass-weighted Hessian matrix at the saddle point has one negative eigenvalue and accordingly one imaginary frequency $\nu^{*}_{AB^{\ddagger},r}$. This imaginary frequency cannot be properly treated as harmonic vibration, and one therefore defines a reduced vibrational partition function from which the imaginary frequency is excluded

$$\widetilde{q}_{AB^\ddagger;\mathrm{vib}} = \prod_{k=1,k\neq r}^{3N-6} \frac{\exp\left(-\frac{h\nu_{AB^\ddagger,k}}{2RT}\right)}{1-\exp\left(-\frac{h\nu_{AB^\ddagger,k}}{RT}\right)} \,. \tag{S11}$$

The reduced vibrational partition function $\widetilde{q}_{AB^\ddagger;\mathrm{vib}}$ is related to the vibrational partition function $q_{AB^\ddagger;\mathrm{vib}}$ by a multiplicative factor $q_{AB^\ddagger;\mathrm{vib}} = f_r \cdot \widetilde{q}_{AB^\ddagger;\mathrm{vib}}$, which is approximated as

$$f_r \approx \frac{RT}{h\nu_{AB^\ddagger,r}} = \frac{RT}{h\nu_r} \,. \tag{S12}$$

where the absolute value of the imaginary frequency is set equal to the decay rate of the activated complex: $|\nu^*_{AB^\ddagger,r}| = \nu_r$. The vibrational factor then is

$$\frac{q_{AB^\ddagger,\mathrm{vib}}}{q_{A,\mathrm{vib}}} = \frac{RT}{h\nu_r} \cdot \frac{\widetilde{q}_{AB^\ddagger,\mathrm{vib}}}{q_{A,\mathrm{vib}}} \,. \tag{S13}$$

With these models and approximations, the reaction rate in eq. S5 can be calculated as

$$\begin{aligned} k_{AB}^{\mathrm{Eyr}} &= \nu_r \cdot \frac{RT}{h\nu_r} \cdot \frac{\widetilde{q}_{AB^\ddagger,\mathrm{vib}}}{q_{A,\mathrm{vib}}} \cdot \frac{q_{AB^\ddagger,\mathrm{rot}}}{q_{A,\mathrm{rot}}} \cdot \exp\left(-\frac{E_b}{RT}\right) \\ &= \frac{RT}{h} \cdot \frac{\widetilde{q}_{AB^\ddagger,\mathrm{vib}}}{q_{A,\mathrm{vib}}} \cdot \frac{q_{AB^\ddagger,\mathrm{rot}}}{q_{A,\mathrm{rot}}} \cdot \exp\left(-\frac{E_b}{RT}\right) \end{aligned} \tag{S14}$$

where the frequency of the reactive mode ν_r cancels. This equation for the reaction rate is often called **Eyring TST** or **harmonic TST**. By setting

$$\Delta F^\ddagger = E_b - RT \ln\left[\frac{\widetilde{q}_{AB^\ddagger,\mathrm{vib}}}{q_{A,\mathrm{vib}}} \cdot \frac{q_{AB^\ddagger,\mathrm{rot}}}{q_{A,\mathrm{rot}}}\right] \tag{S15}$$

eq. S14 becomes consistent with eq. 3.

There are two ways to justify the treatment of the imaginary frequency[6]. In both derivations, one realizes that the eigenvector associated to ν^*_r corresponds to the direction of the reaction coordinate s at the saddle point. In the first derivation[1,6], one treats the motion along this coordinate as a vibrational motion with frequency ν^*_r. Applying the high-temperature approximation yields eq. S12. One further assumes that the TS decays with ν_r, i.e. there is no restoring force and with the first vibration along this coordinate the $AB^\ddagger$ falls apart.

In the second derivation[2,6], the frequency at which the $AB^\ddagger$ decays, ν_r, is modelled as the reactive flux across the transition state region. The reactive degree of freedom is then treated as a translational degree of freedom, rather than a vibrational degree of freedom. To obtain the reactive flux, one additionally calculates the expected value of the absolute velocity at TS in the classical approximation. This approach also leads to eq. S12.

High-temperature approximation

In the high-temperature approximation, one assumes that the rate is dominated by the energy barrier and the vibrational contribution, and thus

$$\frac{q_{AB^\ddagger,\mathrm{rot}}}{q_{A,\mathrm{rot}}} \approx 1 \,. \tag{S16}$$

Then

$$k_{AB}^{\mathrm{ht}} = \frac{RT}{h} \cdot \frac{\widetilde{q}_{AB^\ddagger,\mathrm{vib}}}{q_{A,\mathrm{vib}}} \cdot \exp\left(-\frac{E_b}{RT}\right) \,. \tag{S17}$$

Using eqs. S10 and S11, the ration of vibriational partition functions can be reformulated as

$$\frac{\widetilde{q}_{AB^\ddagger,\mathrm{vib}}}{q_{A,\mathrm{vib}}} = e^{-\frac{h\nu_{A,r}}{2RT}} \cdot \prod_{k=1,k\neq r}^{3N-6} \frac{\exp\left(-\frac{h\nu_{A,k}}{2RT}\right)}{\exp\left(-\frac{h\nu_{AB^\ddagger,k}}{2RT}\right)} \cdot \frac{\prod_{k=1,k\neq r}^{3N-6} 1-\exp\left(-\frac{h\nu_{AB^\dagger,k}}{RT}\right)}{\prod_{k=1}^{3N-6} 1-\exp\left(-\frac{h\nu_{A,k}}{RT}\right)} . \tag{S18}$$

The first factor is the contribution of the specific mode in A that corresponds to the reactive mode at $AB^\ddagger$. The second factor represents the contribution due to the zero-point energies of the vibrational modes (excluding the reactive mode). The third factor is the ratio the vibrational partition functions relative to the zero-point energies.

At high temperatures, the ratio in the first term can be approximated as

$$\begin{aligned}\prod_{k=1,k\neq r}^{3N-6} \frac{\exp\left(-\frac{h\nu_{A,k}}{2RT}\right)}{\exp\left(-\frac{h\nu_{AB^\ddagger,k}}{2RT}\right)} &= \prod_{k=1,k\neq r}^{3N-6} \exp\left(-\frac{h\,\Delta\nu_k}{2RT}\right) \\ &\approx 1 \end{aligned} \tag{S19}$$

where $\Delta\nu_k = \nu_{A,k} - \nu_{AB^\ddagger,k}$ is the frequency difference between A and $AB^\ddagger$ of the kth mode, We assumed that $h\Delta\nu_k \ll RT$, and hence $\exp\left(-\frac{h\,\Delta\nu_k}{2RT}\right) \approx \exp(0) = 1$. We furthermore assume that for the mode $\nu_{A,r}$ has a low frequency, such that $h\nu_{A,r} \ll RT$ and hence $e^{-\frac{h\nu_{A,r}}{2RT}} \approx \exp(0) = 1$. Then the entire first factor can be approximated by 1. In making this approximation we neglect the contribution of the zero-point energies to the free energy difference $\Delta F^\ddagger$.

For the high-temperature approximation of the second term, one uses a Maclaurin series expansion of the exponential function and truncates it after the linear term

$$1-\exp\left(-\frac{h\nu_{A,k}}{RT}\right) \approx 1 - 1 + \frac{h\nu_{A,k}}{RT} = \frac{h\nu_{A,k}}{RT} \tag{S20}$$

which is justified if $h\nu_{A,k} \ll RT$. Then

$$\begin{aligned}\frac{\prod_{k=1,k\neq r}^{3N-6} 1-\exp\left(-\frac{h\nu_{AB^\dagger,k}}{RT}\right)}{\prod_{k=1}^{3N-6} 1-\exp\left(-\frac{h\nu_{A,k}}{RT}\right)} &\approx \frac{\prod_{k=1,k\neq r}^{3N-6} \frac{RT}{h\nu_{AB^\ddagger,k}}}{\prod_{k=1}^{3N-6} \frac{RT}{h\nu_{A,k}}} \\ &= \frac{h}{RT} \cdot \frac{\prod_{k=1}^{3N-6} \nu_{A,k}}{\prod_{k=1,k\neq r}^{3N-6} \nu_{AB^\ddagger,k}} . \end{aligned} \tag{S21}$$

Inserting eq. S19 and S21 into eq. S17 yields the high-temperature approximation to the rate constant form Eyring TST

$$k_{AB}^{\mathrm{ht}} = \frac{\prod_{k=1}^{3N-6} \nu_{A,k}}{\prod_{k=1,k\neq r}^{3N-6} \nu_{AB^\ddagger,k}} \cdot \exp\left(-\frac{E_b}{RT}\right) . \tag{S22}$$

Classical harmonic approximation

Eq. S22 can also be obtained from the classical treatment of the vibrational partition function. The classical Hamilton function of a one-dimensional harmonic vibration is $\mathcal{H}(\mathbf{x},\mathbf{p}) = \frac{\kappa}{2}\mathbf{x}^2 + \frac{\mathbf{p}^2}{2M}$, where M is the reduced molar mass, $\mathbf{x}$ is the position, $\mathbf{p}$ is the momentum, and κ is the molar force constant for the harmonic approximation of the potential. The corresponding classical partition function is

$$
\begin{aligned}
q_{\text{classical,vib},1D} &= \frac{1}{h}\int_{-\infty}^{\infty} \mathrm{d}\mathbf{x} \int_{-\infty}^{\infty} \mathrm{d}\mathbf{p} \exp\left(-\frac{1}{RT}\mathcal{H}(\mathbf{x},\mathbf{p})\right) \\
&= \frac{1}{h}\int_{-\infty}^{\infty} \mathrm{d}\mathbf{x} \exp\left(-\frac{1}{RT}\frac{\kappa}{2}\mathbf{x}^2\right)\int_{-\infty}^{\infty} \mathrm{d}\mathbf{p} \exp\left(-\frac{1}{RT}\frac{\mathbf{p}^2}{2M}\right) \\
&= \frac{1}{h}\cdot\sqrt{\pi RT\frac{2}{\kappa}}\cdot\sqrt{\pi RT 2M} \\
&= \frac{RT}{h}\cdot 2\pi\cdot\sqrt{\frac{M}{\kappa}} \\
&= \frac{RT}{h\nu}
\end{aligned}
\tag{S23}
$$

where we used that the two integrals are Gaussian integrals, and that the frequency of a harmonic oscillator is $\nu = \frac{1}{2\pi}\cdot\sqrt{\kappa/M}$. The vibrational partition function of a system with N atoms then is

$$
q_{\text{classical,vib}} = \prod_{k=1}^{3N-6}\frac{RT}{h\nu_k}
\tag{S24}
$$

The ratio of classical vibrational partition functions then is

$$
\begin{aligned}
\frac{\widetilde{q}_{AB^\ddagger,\text{classical,vib}}}{q_{A,\text{classical,vib}}} &= \frac{\prod_{k=1,k\neq r}^{3N-6}\frac{RT}{h\nu_{AB^\ddagger,k}}}{\prod_{k=1}^{3N-6}\frac{RT}{h\nu_{A,k}}} \\
&= \frac{h}{RT}\cdot\frac{\prod_{k=1}^{3N-6}\nu_{A,k}}{\prod_{k=1,k\neq r}^{3N-6}\nu_{AB^\ddagger,k}}\,.
\end{aligned}
\tag{S25}
$$

Using this ratio in eq. S17 yields the high-temperature approximation for rate constant from Eyring TST (eq. S22). This result shows that, in the limit of high temperature, classical and quantum mechanical treatment of transition state theory coincide.

At $T = 300\,\mathrm{K}$, this is approximation is valid for $\nu \ll k_B T/h = 6.25\cdot 10^{12}\,\mathrm{s}^{-1}$ or $208.5\,\mathrm{cm}^{-1}$. Since many vibrational modes in our two compounds have higher frequencies, the high-temperature approximation does not yet strictly apply. However, the two molecular scaffolds are very rigid and most vibrational modes likely have similar frequencies in A and in $AB^\ddagger$. The corresponding factor for these modes in $\frac{\widetilde{q}_{AB^\ddagger,\text{vib}}}{q_{A,\text{vib}}}$ then is about 1 and its contribution to the free-energy difference $\Delta F^\ddagger$ is approximately zero. The one covalent bond that is altered during the reaction, the $C_{13}{=}C_{14}$ double bond, is represented by ν_r and is treated separately in the theory of the activated complex. Thus, the high-temperature approximation of the transition state rate can be a valid approximation, even if the high-temperature limit for the individual vibrational partition functions is not yet reached.

Sampling anharmonic vibrations

The dynamics of the a system with N atoms evolve in the $6N$-dimensional phase space $\mathbf{\Gamma} = (\mathbf{x},\mathbf{p}) \in \mathbb{R}^{6N}$, where $\mathbf{x} \in \mathbb{R}^{3N}$ are the atomic positions and $\mathbf{p} \in \mathbb{R}^{3N}$ are the atomic momenta. $V(\mathbf{x})$ is the molecular potential energy function and represents the Born-Oppenheimer surface. In the present study, these dynamics are simulated in the NVT ensemble at $T = 300\,\mathrm{K}$. The classical Hamilton function of such a system is $\mathcal{H}(\mathbf{x},\mathbf{p}) = V(\mathbf{x}) + \sum_{i=1}^{3N}\frac{p_j^2}{2M_j}$, where M_j is the molar mass associated to the jth degree of freedom.

The classical partition functions of the reactant state A and the activated complex $AB^\ddagger$ are

$$q_{\text{classical,i}} = q_{\text{classical},\,\mathbf{x},i} \cdot q_{\text{classical},\,\mathbf{p},i} \qquad i = A, AB^\ddagger \tag{S26}$$

with

$$\begin{aligned} q_{\text{classical},\,\mathbf{x},i} &= \frac{1}{h^{3N}} \int_{\mathbf{x}\in i} \mathrm{d}\mathbf{x} \exp\left(-\frac{1}{RT} V(\mathbf{x})\right) \\ q_{\text{classical},\,\mathbf{p},i} &= \int \mathrm{d}\mathbf{p} \exp\left(-\frac{1}{RT} \sum_{i=j}^{3N} \frac{p_j^2}{2M_i}\right) \\ & i = A, AB^\ddagger\,. \end{aligned} \tag{S27}$$

We assumed that all N atoms in the system are distinguishable, which is a reasonable assumption for a single molecule like retinal. It is a matter of convention whether the factor $\frac{1}{h^{3N}}$ is included in the configurational partition function $q_{\text{classical},\,\mathbf{x}}$ or not.

Using classical partition functions in eq. S5 yields

$$k_{AB}^{\text{Eyr}} = \nu_r \cdot K^\ddagger = \nu_r \cdot \frac{q_{\text{classical},AB^\ddagger}}{q_{\text{classical},A}}\,. \tag{S28}$$

Note that in the classical treatment of the partition function, A and $AB^\ddagger$ have the same reference energy and the factor E_b is absorbed into the partition function. The factor $\exp\left(-\frac{E_b}{RT}\right)$ arises when the integration for $q_{\text{classical},\,\mathbf{x},i}$ is carried out.

Classical partition functions and reaction rates can be estimated by sampling the dynamics of the molecule using MD simulations. In this sense, MD simulation is a numerical integration technique to solve the high-dimensional integrals that appear in the classical partition function, without resorting to a harmonic approximation. However, owing to the large barriers involved in chemical reactions, the numerical estimates converge poorly when the simulation is carried out at $V(\mathbf{x})$. Instead one uses importance sampling and reweighting.

Here, we discuss metadynamics[7–10] and infrequent metadynamics[11] as importance sampling methods to obtain the classical approximation of Eyring TST. In this method, one samples the dynamics at a biased potential

$$V^{\text{InMetaD}}(\mathbf{x}, t) = V(\mathbf{x}) + U(\mathbf{x}, t) \tag{S29}$$

where $U(\mathbf{x}, t)$ is a time-dependent bias. The bias is chosen such that the rate constant k_{AB}^{InMetaD} at $V^{\text{InMetaD}}(\mathbf{x})$ is increased to the rate constant k_{AB} at the molecular potential: $k_{AB}^{\text{InMetaD}} = \alpha k_{AB}$, where the acceleration factor is

$$\begin{aligned} \alpha &= \frac{k_{AB}^{\text{InMetaD}}}{k_{AB}} \\ &= \nu_r^{\text{InMetaD}} \frac{q_{\text{classical},AB^\ddagger}^{\text{InMetaD}}}{q_{\text{classical},A}^{\text{InMetaD}}} \cdot \frac{1}{\nu_r} \frac{q_{\text{classical},A}}{q_{\text{classical},AB^\ddagger}} \\ &\approx \frac{q_{\text{classical},A}}{q_{\text{classical},A}^{\text{InMetaD}}}\,, \end{aligned} \tag{S30}$$

where $q_{\text{classical},A}^{\text{InMetaD}}$ and $q_{\text{classical},AB^\ddagger}^{\text{InMetaD}}$ are the classical partition functions for A and $AB^\ddagger$ at the biased potential $V^{\text{InMetaD}}(\mathbf{x})$. In the last line in eq. S30, we assumed that $\nu_r \approx \nu_r^{\text{InMetaD}}$ and $q_{\text{classical},AB^\ddagger} \approx q_{\text{classical},AB^\ddagger}^{\text{InMetaD}}$. This is the case if the bias is only deposited in the reactant state, and the potential in the region around $AB^\ddagger$ remains unmodified.

At constant bias $U(\mathbf{x})$, this acceleration factor is essentially the free energy difference in the reactant state A and can be estimated as

$$\alpha = \frac{q_{\text{classical},A}}{q_{\text{classical},A}^{\text{InMetaD}}}$$

$$
\begin{aligned}
&= \frac{\frac{1}{h^{3N}} \int_{\mathbf{x}\in A} \mathrm{d}\mathbf{x} \exp\left(-\frac{1}{RT} V(\mathbf{x})\right)}{\frac{1}{h^{3N}} \int_{\mathbf{x}\in A} \mathrm{d}\mathbf{x} \exp\left(-\frac{1}{RT}\left[V(\mathbf{x}) + U(\mathbf{x})\right]\right)} \\
&= \frac{\int_{\mathbf{x}\in A} \mathrm{d}\mathbf{x} \exp\left(-\frac{1}{RT}\left[V(\mathbf{x}) + U(\mathbf{x})\right]\right) \cdot \exp\left(+\frac{1}{RT} U(\mathbf{x})\right)}{\int_{\mathbf{x}\in A} \mathrm{d}\mathbf{x} \exp\left(-\frac{1}{RT}\left[V(\mathbf{x}) + U(\mathbf{x})\right]\right)} \\
&= \left\langle \exp\left(+\frac{1}{RT} U(\mathbf{x})\right) \right\rangle_A
\end{aligned}
\tag{S31}
$$

where $\langle ... \rangle_A$ denotes an ensemble average restricted to the reactant state A and is measured at $V^{\text{InMetaD}}(\mathbf{x})$.

To estimate the rate from the simulation data, one uses that the rate is related to the dynamics via

$$
k_{AB} = \frac{1}{\tau_{AB}} = \frac{1}{\alpha}\, k_{AB}^{\text{InMetaD}} = \frac{1}{\alpha \tau_{AB}^{\text{InMetaD}}}
\tag{S32}
$$

where $\tau_{AB}^{\text{InMetaD}}$ is the mean first passage time at $V^{\text{InMetaD}}(\mathbf{x})$. The estimator for the mean first passage time is the arithmetic mean of the sampled first passage times $\tau_{AB,i}^{\text{InMetaD}}$

$$
\tau_{AB}^{\text{InMetaD}} = \lim_{N_{AB}\to\infty} \frac{1}{N_{AB}} \sum_{i=1}^{N_{AB}} \tau_{AB,i}^{\text{InMetaD}}
\tag{S33}
$$

where N_{AB} is the number of transition events observed during the simulation. Alternatively, one can estimate $\tau_{AB}^{\text{InMetaD}}$ by fitting the cumulative distribution function of the simulated first passage times to the cumulative distribution of a Poisson process.

In infrequent metadynamics[11], a time-dependent bias $U(\mathbf{x}, t)$ is used. One assumes $U(\mathbf{x}, t)$ changes slowly enough that at any time t the assumptions of Eyring TST are met, and that no bias is deposited in the transition state region. One starts a simulation $\mathbf{x}^{(i)}$ in reactant state A and stops the simulation as soon as it crosses $AB^{\ddagger}$. Because of the time-dependent bias, the first passage times at $V^{\text{InMetaD}}(\mathbf{x})$ and at $V(\mathbf{x})$ are not simply related by constant acceleration function, but by the following time integral

$$
\tau_{AB,i} = \int_{t=0}^{\tau_{AB,i}^{\text{InMetaD}}} \mathrm{d}t\, \exp\left(+\frac{1}{k_B T} U(\mathbf{x}_t^{(i)})\right) ,
\tag{S34}
$$

where we used the result from eq. S31 to approximate the instantaneous acceleration. Discretizing the integral yields[12,13]

$$
\tau_{AB,i} \approx \Delta t \sum_{t=1}^{N_{i,t}} \exp\left(+\frac{1}{k_B T} U(\mathbf{x}_t^{(i)})\right) ,
\tag{S35}
$$

where $\mathbf{x}_t^{(i)}$ is the tth time step in trajectory $\mathbf{x}^{(i)}$, Δt is the time difference between subsequent frames in the trajectory $U(\mathbf{x}_t^{(i)})$ is the bias at time $t\Delta t$ at position $\mathbf{x}_t^{(i)}$, and N_t is the number of frames in the trajectory. From these rescaled first passage times, one can estimate the mean first passage time τ_{AB} by fitting to a Poisson distribution.

Eq. S34 can be cast in terms of an acceleration factor by multiplying with $1 = \tau_{AB,i}^{\text{InMetaD}} / \tau_{AB,i}^{\text{InMetaD}}$

$$
\tau_{AB,i} = \tau_{AB,i}^{\text{InMetaD}} \cdot \alpha(\tau_{AB,i}^{\text{InMetaD}})
\tag{S36}
$$

where

$$
\alpha(\tau_{AB,i}^{\text{InMetaD}}) = \frac{1}{\tau_{AB,i}^{\text{InMetaD}}} \int_{t=0}^{\tau_{AB,i}^{\text{InMetaD}}} \mathrm{d}t\, \exp\left(+\frac{1}{k_B T} U(\mathbf{x}_t^{(i)})\right) .
\tag{S37}
$$

II. COMPUTATIONAL DETAILS

A. Geometry optimization on the DFTB3 PES

Starting structures of the cis and the trans conformation of pSb5 and pSb1 were generated using Gaussian's graphical interface, GaussView 6[14], and converted to *.xyz* file format. These structures were energy minimized on the level of the self-consistent-charge density-functional tight-binding method including the third order correction (DFTB3) and using the 3ob-3-1 Slater–Koster parameter set[15]. Applicability of self-consistent charge DFTB to the retinal cofactor has been extensively documented[16,17]. Energy minimizations and constrained optimizations were carried out by interfacing DFTB+ software package[18] with the Atomic Simulation Environment (ASE)[19], and using the Broyden–Fletcher–Goldfarb–Shanno (BFGS) algorithm[20] with a maximum force of $10^{-5}\,\mathrm{eV\,\AA^{-1}}$ as convergence criterion. Transition states were optimized using the Nudged Elastic Band (NEB) method[21] with climbing image[22] using 22 nodes starting from the optimized reactant and product states (trans and cis respectively) in combination with BFGS for numerical optimization. For pSb5, the spring constants of the bands were chosen to be $0.8\,\mathrm{eV\,\AA^{-2}}$, while a maximal force of $0.02\,\mathrm{eV\,\AA^{-1}}$ was used as convergence criterion. For pSb1, the transition state search was considerably more sensitive to the parameters used. Here, a two-step optimization was performed, first using NEB without climbing image with spring constants of $0.3\,\mathrm{eV\,\AA^{-2}}$ and a maximum force of $0.01\,\mathrm{eV\,\AA^{-1}}$, followed by a second NEB optimization with climbing image using the same spring constants and maximum force.

Moments of inertia for the reactant states (cis or trans) as well as for transition states were obtained by entering the configurations into the Gaussian 16 software[23], which calculates rotational temperatures $\Theta_{\mathrm{rot},i,k} = h^2/8\pi^2 k_B I_{i,k}$, where i designates the configuration (A or $AB^{\ddagger}$) and k designates the axis of inertia (a, b or c, see section I of this supplement). These were used to calculate the ratio of rotational partition functions $q_{AB^{\ddagger},\mathrm{rot}}/q_{A,\mathrm{rot}}$ as in eq. S9, from which the rotational contributions ΔF_{rot} (eq. 6a) to the free energy difference $\Delta F^{\ddagger}$ (eq. 5) was computed, see Tables II and III.

Vibrational mode analyses were carried out for the reactant states (cis or trans) as well as for transition states using DFTB+. The smallest six frequencies correspond to the translational and rotational degrees of freedom, and were excluded from the subsequent calculations. After removing these frequencies, reactant state configurations did not have imaginary frequencies, and transition state configurations only had one imaginary frequency, as is expected for optimized structures. For pSb5, the imaginary frequency was $-2347.45\,\mathrm{cm^{-1}}$ and the lowest real frequency was $35.0\,\mathrm{cm^{-1}}$. For pSb1, the imaginary frequency was $-690.5\,\mathrm{cm^{-1}}$ and the lowest real frequency was $15.3\,\mathrm{cm^{-1}}$. From the vibrational frequencies, the vibrational contributions ΔF_{vib} (eq. 6b) to the free energy differences for Eyring TST ($\Delta F^{\ddagger}$, eq. 5) and $\Delta F_{\mathrm{vib}}^{\mathrm{ht}}$ for the high-temperature limit ($\Delta F^{\ddagger,\mathrm{ht}}$, eq. 8) were calculated. From the free energy differences $\Delta F^{\ddagger}$ and $\Delta F^{\ddagger,\mathrm{ht}}$, Eyring TST rate constants and high-temperature TST rate constants were calculated using eqs. 3 and 7, respectively.

To obtain the energy scan in Fig. S2, twelve constrained geometry optimizations were carried out for each compound, where the dihedral angle φ was constrained at values in 30 degree intervals over the whole 360 degree range, that is at -150, -120, -90, -60, -30, 0, 30, 60, 90, 120, 150 and 180 degrees.

B. Well-tempered metadynamics with DFTB3

Starting structures of the cis and the trans conformation of pSb5 and pSb1 were generated as described in section II A of the supplement.

MD simulations (equilibration and production) were carried out using the DFTB+ software package[18]. The potential energy and the resulting forces were calculated with the self-consistent-charge density-functional tight-binding method including the third order correction (DFTB3) in combination with the 3ob-3-1 Slater–Koster parameter set[15]. The equations of motions were integrated using the velocity-Verlet integrator with a time step of $\Delta t = 1\,\text{fs}$. The 1 fs time step was validated by comparison to the periods of the fastest vibrational components obtained from vibrational mode analysis. These were 9.7 fs and 10.0 fs in the reactant states, and 9.6 and 10.0 fs in the transition states, for pSb5 and pSb1 respectively. Thus, our time step is about an order of magnitude smaller then the fastest vibrational mode.

The system was equilibrated for 50 ps using Berendsen thermostat[24] at $T = 300\,\text{K}$ with a coupling strength of $\Delta t/\tau = 5 \times 10^{-4}$, corresponding to a the coupling time of $\tau = 2\,\text{ps}$. This was followed by a second equilibration of 50 ps at $T = 300\,\text{K}$ using a Nosé-Hoover thermostat[25–27] of chain length three and coupling frequency of 0.5 THz, corresponding to a the coupling time of $\tau = 2\,\text{ps}$.

Well-tempered metadynamics[28] were carried out by plugging the PLUMED software package[29–31] with the DFTB+ package[18]. Potential energy, integrator settings and settings of the Nosé-Hoover thermostat were the same as in the second equilibration run. For each of the two systems, we carried out three different well-tempered metadynamics simulations (MetaD1, MetaD2, MetaD3). As biased collective variable, we used the C_{12}-C_{13}=C_{14}-C_{15} dihedral angle φ. Height and width of the Gaussian bias potentials, deposition rate, and bias factor, as well as simulation time are reported in Table IV. Sporadically, the self-consistent charge calculation of the DFTB3 force evaluation would fail to converge for a specific configuration along a longer metadynamics run. In that case, a small perturbation was enforced to the velocities of the corresponding configuration, after which the metadynamics simulation was resumed. Unbiasing weights for the trajectory were calculated using the bias potential obtained at the end as described in Ref. 32. Free energy surfaces were calculated after building a weighted histogram from the trajectory starting at a simulation time where the bias can be considered converged.

C. Error estimates for metadynamics FES

Error estimates for free energy profiles obtained from metadynamics reweighting can be determined using the block analysis technique[33] on the reweighted trajectory. Block analysis was carried out using the example code on the PLUMED website.

The free energy difference at a certain simulation time is calculated by determining the FES corresponding to the bias at that time (i.e. from the scaled upside-down bias, see Refs. 32–34). This FES is used to calculate the relative probabilities of being in cis versus being in trans. Using eq. 12:

$$\pi_{\text{cis}} = \int_{-\pi/2}^{\pi/2} \mathrm{d}\varphi\, \pi(\varphi) = \int_{-\pi/2}^{\pi/2} \mathrm{d}\varphi\, \exp\left(-\frac{F(\varphi)}{k_B T}\right) \tag{S38}$$

and equivalent for trans in $\varphi < -\pi/2$ and $\varphi > \pi/2$. The free energy of a state can then be calculated using $F_{\text{cis}} = -k_B T \ln \pi_{\text{cis}}$ and equivalent for trans, and the free energy difference

$$\Delta F = F_{\text{cis}} - F_{\text{trans}} = -k_B T \ln \frac{\pi_{\text{cis}}}{\pi_{\text{trans}}}\,. \tag{S39}$$

D. Umbrella Sampling

Umbrella Sampling[35] has been run for thermal isomerization over the C_{13}=C_{14} double bond for both pSb5 and pSb1, constraining the C_{12}-C_{13}=C_{14}-C_{15} dihedral angle φ. Biasing of the CV was carried out by plugging the PLUMED software package[29–31] with the DFTB+ package[36].

For both pSb5 and pSb1, three sets of umbrella sampling simulations have been performed, i.e. sets US1, US2 and US3. Each set has the same parameter setup and consisted of 83 trajectories. The parameters (number of windows, the region of φ in which they are distributed at a regular interval, and the force constant of the umbrella potential) are reported in Table V.

Each window was initialized starting from the structure obtained from constrained optimization at the φ-value closest to the position of the window. For every window, an initial equilibration of 25 ps was performed from the respective starting structure using a Berendsen thermostat of coupling strength 5×10^{-4}. The initial velocities were generated randomly from an initial Maxwell-Boltzmann distribution of atomic velocities. This is followed by a second equilibration run of 25 ps using the same Nosé-Hoover chain setup that is used during production runs. Every production trajectory was 2 ns making for a total simulation time of 166 ns per set. Binless WHAM[33,37] was used to establish the free energy profile from the trajectory data.

Error estimates for the free energy profiles obtained from umbrella sampling can be computed using the bootstrapping method[38]. For each umbrella, the trajectory was split in 20 blocks of equal length. A 'new' trajectory of the same length as the original is then constructed by taking combinations of these 20 blocks with the possibility of repetition. After doing this for all umbrellas, the free energy surface is recalculated using WHAM. This procedure is repeated 200 times, producing 200 free energy surfaces which allows calculation of standard deviations which can be shown to be good estimates of standard errors on the free energy surface[39]. Notice the standard errors might be underestimated because of correlations between blocks within each trajectory[40]. Because of important correlated motion in orthogonal degrees of freedom, we expect this to be the case for US of pSb5.

E. Unbiased MD simulations with DFTB3

Separate unbiased ab-initio MD simulations were performed in the cis and the trans state for both pSb5 and pSb1, i.e. generating a total of four unbiased trajectories. Dynamics were simulated using the DFTB+ software package[36] at the DFTB3 level, with starting structures of the cis and the trans conformation of pSb5 and pSb1 generated similarly as before (section II A of the supplement). For each simulation, first a 25 ps equilibration using the Berendsen thermostat[24] at 300 K with a coupling time of 2 ps was performed, followed by a second equilibration of 25 ps at 300 K using a Nosé-Hoover thermostat[25–27] with chain length 3 and a coupling time of 2 ps. Once equilibrated, production runs of 2 ns were performed.

F. Infrequent metadynamics with DFTB3

Infrequent metadynamics[11,41] was used to study a total of four transitions: cis → trans and trans → cis for both pSb5 and pSb1. For each of these four transitions, two separate sets of infrequent metadynamics (InMetaD1 and InMetaD2) were carried out, giving rise to a total of eight sets and eight corresponding rates (four for pSb5 in Table II and four for pSb1 in Table III). Each set consists of a number of trajectories (also referred to as 'runs' i) starting in the reactant state and ending in the product state.

Trajectories were generated by plugging the PLUMED software package[30] with the DFTB+ package[36]. Potential energy, integrator settings and settings of the Nosé-Hoover thermostat were the same as in the metadynamics simulations described above. As biased collective variable, we used the C_{12}-C_{13}=C_{14}-C_{15} dihedral angle φ. Height and width of the Gaussian bias potentials, deposition rate, and bias factor, number of simulations are reported in Table IV.

Notice that, because DFTB+ implements deterministic dynamics (velocity-Verlet + Nosé-Hoover), additional care needs to be taken in generating the correct initial conditions, i.e. to start each run from uncorrelated starting configurations and velocities according to

Molecule	**Set**	**pace** [ps]	**runs**	$k_{t\to c}$ [s^{-1}] (p-value)	$k_{c\to t}$ [s^{-1}] (p-value)	$\min_i \tau^{\mathrm{InMetaD}}_{\mathrm{t}\to\mathrm{c},i}$ [ns]	$\max_i \tau^{\mathrm{InMetaD}}_{\mathrm{t}\to\mathrm{c},i}$ [ns]	$\min_i \tau^{\mathrm{InMetaD}}_{\mathrm{c}\to\mathrm{t},i}$ [ns]	$\max_i \tau^{\mathrm{InMetaD}}_{\mathrm{c}\to\mathrm{t},i}$ [ns]
pSb5	InMetaD1	5	25	1.94×10^{-6} (0.58)	1.04×10^{-4} (0.77)	10.8	18.2	8.4	15.4
pSb5	InMetaD2	10	30	2.63×10^{-6} (0.93)	9.22×10^{-5} (0.78)	22.0	32.6	18.2	28.0
pSb1	InMetaD1	5	25	2.97×10^{-3} (0.77)	9.30×10^{-3} (0.56)	5.6	11.8	6.7	10.6
pSb1	InMetaD2	10	30	3.09×10^{-3} (0.75)	1.22×10^{-2} (0.44)	13.6	20.1	11.8	19.9

TABLE S1. Parameters and rates for infrequent metadynamics simulations of thermal cis-trans isomerization around the C_{13}=C_{14} double bond in pSb5 and pSb1. Parameters of the metadynamics biasing can be found in Table IV. Rates are repeated from Tables II and III. The pace and the amount of runs used to fit the TCDF are given. Additionally, the minimum and maximum biased transition times are given for each set. For each rate calculation, the p-value is shown as well.

local equilibrium in the reactant state. Generating good initial starting states was taken care of in the equilibration phase of each separate run. To obtain uncorrelated starting configurations for the infrequent metadynamics runs, we equilibrated the starting reactant state configuration with randomized velocities before each run. Additionally, the total equilibration time of each run was randomized to be anywhere between 10 and 100 ps.

Trajectories for runs from trans to cis were terminated once a value of $\varphi \in [-\pi/5, \pi/5]$ was reached, where the molecule is definitely in the cis state. The biased transition time $\tau^{\mathrm{InMetaD}}_{\mathrm{t}\to\mathrm{c},i}$ was then taken to be the time of the last trajectory point where the configuration can still be considered at the trans side, i.e. the last trajectory point where $\varphi < -\pi/2$ or $\varphi > \pi/2$. The unbiased transition times $\tau_{\mathrm{t}\to\mathrm{c},i}$ can then be calculated from eq. 11. Trajectories for runs from cis to trans were stopped once a value of $\varphi < -4\pi/5$ or $\varphi > 4\pi/5$ was reached, where the molecule is definitely in the trans state. The biased transition time $\tau^{\mathrm{InMetaD}}_{\mathrm{c}\to\mathrm{t},i}$ was then taken to be the time of the last trajectory point where the configuration can still be considered at the cis side, i.e. the last trajectory point where $\varphi \in [-\pi/2, \pi/2]$, and unbiased transition times $\tau_{\mathrm{c}\to\mathrm{t},i}$ can be calculated from eq. 11. To get an idea of the actual simulation times, the minimum and maximum biased transition times for each set are given in Table S1. Notice that acceleration factors α were very large for our particular application of infrequent metadynamics, with numbers up to the order of $\alpha\left(\tau^{\mathrm{InMetaD}}_{\mathrm{t}\to\mathrm{c},i}\right) \sim 10^{14}$ in set InMetaD1 for trans to cis runs for pSb5.

The estimated mean first-passage times can then be obtained by fitting the reweighted transition times of all runs within a set to a Poisson distribution (eq. 10), and rates can be calculated directly using eq. 9. Parameters for the infrequent metadynamics simulations, p-values of the Kolmogorov-Smirnoff test, as well as ranges of the simulated first-passage times are reported in Table S1.

G. Pontryagin and Kramers Rate Calculations

Rates from Pontryagin and Kramers' rate equations (eqs. 15 and 14 respectively) were calculated using free energy surfaces MetaD1 for both pSb5 and pSb1, see Fig. 2. Diffusion profiles for both pSb5 and pSb1 were taken from the umbrella windows of the corresponding US3 set.

Calculation of rates from the Pontryagin equation in eq. 15 entails a nested integration over the free energy profile $F(\varphi)$ and the position-dependent diffusion $D(\varphi)$. The integrals were calculated numerically, where the inner integral was carried out starting from the barrier peak on the other side of the reactant state. Rates were initially calculated separately in the two possible direction, i.e. going clockwise or counterclockwise, for both trans-to-cis as cis-to-trans isomerizations. The actual rates are then obtained by summing:

$$k_{\text{trans}\to\text{cis}} = k_{\text{t}\to\text{c,left}} + k_{\text{t}\to\text{c,right}} \tag{S40a}$$

$$k_{\text{cis}\to\text{trans}} = k_{\text{c}\to\text{t,left}} + k_{\text{c}\to\text{t,right}} \tag{S40b}$$

where $k_{\text{t}\to\text{c,left}}$ indicates trans-to-cis isomerization over the left free energy barrier, and analogous for $k_{\text{t}\to\text{c,right}}$, $k_{\text{c}\to\text{t,left}}$ and $k_{\text{c}\to\text{t,right}}$.

For calculation of Kramers' rate equation (eq. 14), free energy barriers $F^{\ddagger}$ were determined directly from the free energy profile by subtracting the maximum free energy value at the corresponding peak (left or right) by the minimum value at the reactant side under consideration. In this way, four energy barriers per free energy surface $F^{\ddagger}_{\text{t}\to\text{c,left}}$, $F^{\ddagger}_{\text{t}\to\text{c,right}}$, $F^{\ddagger}_{\text{c}\to\text{t,left}}$ and $F^{\ddagger}_{\text{c}\to\text{t,right}}$ are obtained. Masses in reduced dimensions for reactant states μ_{trans} and μ_{cis} were calculated by running unbiased 2 ns runs in the corresponding states, calculating the average kinetic energy in the reduced dimension (i.e. the dihedral angle) and comparing to the temperature using the equipartition theorem:

$$\mu_A = \frac{k_B T}{\langle v_{\varphi}^2 \rangle_A}. \tag{S41}$$

The reactant state dihedral velocities ω_A (where A denotes cis or trans) can then be calculating using

$$\omega_A = \sqrt{\frac{\kappa_A}{\mu_A}} \tag{S42}$$

where spring constant κ_A is obtained by fitting the free energy surface to a harmonic potential $\frac{1}{2}\kappa_A(\varphi - \varphi_A)^2$ where φ_A corresponds to the free energy minimum at the corresponding reactant state A. Fits for the trans and cis free energy wells show close agreement with harmonic potentials at the bottom, which validates the harmonic assumptions of the reactant and product states in the formulations for Kramers' equation. The friction coefficient ξ in eq. 14 was taken to be the friction coefficient $\xi^{\ddagger}$ at the barrier top, which can be calculated directly from the diffusion profile using the Einstein-Stokes relation:

$$\xi^{\ddagger} = \frac{k_B T}{\mu^{\ddagger} D^{\ddagger}} \tag{S43}$$

where $D^{\ddagger}$ is the value of the diffusion coefficient at the barrier top and $\mu^{\ddagger}$ has been approximated by averaging μ_{cis} and μ_{trans}. The angular frequency at the barrier top $\omega^{\ddagger}$ has been calculated in a similar way as at the reactant states using:

$$\omega^{\ddagger} = \sqrt{\frac{\kappa^{\ddagger}}{\mu^{\ddagger}}} \tag{S44}$$

where $\kappa^{\ddagger}$ was obtained using a parabolic fit to the free energy surface at the barrier top. Again, total rates are obtained by summing rates for both barriers as in eqs. S40.

The resulting parameters for Kramers' rate constant are reported in Tables S2 and S3.

H. Geometry Optimization using unrestricted DFT and DFT-D3

All calculations for pSb5 and pSb1 at the DFT level were performed with the Gaussian 16 software[23] using unrestricted DFT with the B3LYP functional[42,43] and 6-31G* basis set[44], same as in Refs. 17,45,46. Gaussian's default settings were used for the integration grid, i.e. for the grid size used for numerical integration of the functional, as well as for the convergence settings of the self-consistent field (SCF) iterations. This proved sufficient for reactant and transition state optimization and vibrational analysis as described below.

		trans→cis		cis→trans	
	units	TS	TS'	TS	TS'
μ_A	[kg.m^2.rad^{-2}]	7.03×10^{-47}	7.03×10^{-47}	2.35×10^{-47}	2.35×10^{-47}
$D^\ddagger$	[rad^2.ps^{-1}]	0.68	0.67	0.68	0.67
$\xi^\ddagger$	[ps^{-1}]	1.31×10^2	1.31×10^2	1.31×10^2	1.31×10^2
ω_A	[ps^{-1}]	4.67×10^1	4.67×10^1	6.68×10^1	6.68×10^1
$\omega^\ddagger$	[ps^{-1}]	3.08×10^2	2.80×10^2	3.08×10^2	2.80×10^2
$F^\ddagger$	[kJ.mol^{-1}]	89.0	88.7	80.5	80.2

TABLE S2. Parameters for one-dimensional rate theories calculated for $F(\varphi)$ for pSb5 using metadynamics (MetaD1) for trans→cis and cis→trans transitions. Values are given separately for transitions over the left (TS) and right (TS') torsional barrier.

		trans→cis		cis→trans	
	units	TS	TS'	TS	TS'
μ_A	[kg.m^2.rad^{-2}]	6.80×10^{-47}	6.80×10^{-47}	2.49×10^{-47}	2.49×10^{-47}
$D^\ddagger$	[rad^2.ps^{-1}]	0.62	0.64	0.62	0.64
$\xi^\ddagger$	[ps^{-1}]	1.45×10^2	1.39×10^2	1.45×10^2	1.39×10^2
ω_A	[ps^{-1}]	4.34×10^1	4.34×10^1	6.24×10^1	6.24×10^1
$\omega^\ddagger$	[ps^{-1}]	2.08×10^2	2.26×10^2	2.08×10^2	2.26×10^2
$F^\ddagger$	[kJ.mol^{-1}]	78.7	78.9	74.8	75.0

TABLE S3. Parameters for one-dimensional rate theories calculated for $F(\varphi)$ for pSb1 using metadynamics (MetaD1) for trans→cis and cis→trans transitions. Values are given separately for transitions over the left (TS) and right (TS') torsional barrier.

All calculations were done in parallel with and without Grimme's empirical dispersion corrections with the D3 damping function[47], while using the same functional and basis functions. Adding D3 corrections in Gaussian was done by including the *EmpiricalDispersion=GD3* keyword. Calculations including D3 corrections are designated as DFT-D3 calculations.

First, full geometry optimizations were performed in the cis and trans states, where the *opt=tight* keyword was used to control the convergence criterion. Furthermore, geometry optimizations with constrained dihedral angle φ were performed using the *ModRedundant* keyword with default cutoffs for the convergence criterions of the optimization algorithm. Gaussian uses the Berny optimization algorithm[48] as default for both minimizations and optimizations.

Transition state search was performed using the Synchronous Transit-guided Quasi-Newton (STQN) method[49,50] with the *opt=qst3* keyword, where the reactant and product state input configurations were chosen to be the geometry optimized structures in the trans and cis states. Separate transition states were optimized for different directions of trans-cis rotation, i.e. clockwise or counterclockwise. This was done by providing an approximate transition state configuration with dihedral angle of $\varphi = 90°$ or $\varphi = -90°$ respectively.

Gaussian performs a full thermochemical analysis including calculation of the translational, rotational and vibrational partition functions and corresponding energies and entropies[5]. This allows for straightforward calculation of rates using Eyring's equation (eq. 3).

Rotational characteristic temperatures were calculated by Gaussian by default, and can be used to calculate the rotational contributions ΔF_rot (eq. 6a) to the free energy difference ($\Delta F^\ddagger$, eq. 5), similar as was done for DFTB3.

Vibrational mode analyses were performed on the reactant and transition state structures using the *freq* keyword in Gaussian. Notice Gaussian automatically disregards the frequencies associated with the translational and rotational degrees of freedom. The structures optimized to a minimum did not have any imaginary frequencies, while the structures optimized to transition states had only one imaginary frequency, as is expected. For pSb5, the imaginary frequency was $-882.9\,\mathrm{cm}^{-1}$ and the lowest real frequency was $28.4\,\mathrm{cm}^{-1}$. For pSb1, the imaginary frequency was $-428.0\,\mathrm{cm}^{-1}$ and the lowest real frequency was $16.1\,\mathrm{cm}^{-1}$.

The vibrational frequencies can be used to calculate the vibrational contributions to the free energy differences, both fully quantum mechanical (ΔF_{vib} and $\Delta F^{\ddagger}$, eqs. 6b and 5) as in the high-temperature limit ($\Delta F_{\mathrm{vib}}^{\mathrm{ht}}$ and $\Delta F^{\ddagger,\mathrm{ht}}$, eq. 8), same as was done for DFTB3. Subsequently, rates for high-temperature TST can be calculated according to eq. 7. Rotational and vibrational contributions to the free energy differences as well as rates can be found in Tables II and III.

III. SUPPLEMENTARY FIGURES

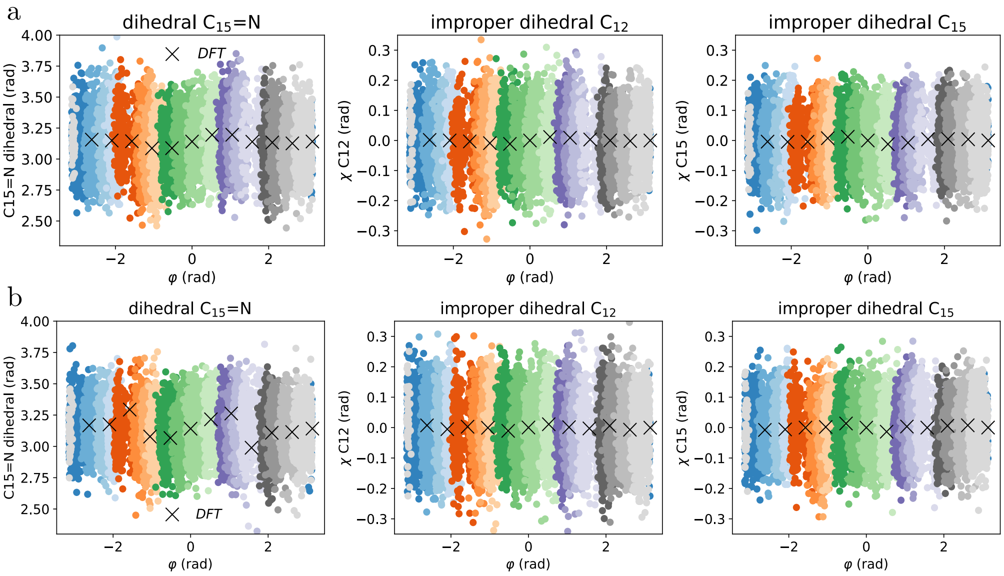

FIG. S1. **a:** Sampling using DFTB3 set US3 for **pSb5** showing correlation between C_{13}=C_{14} dihedral φ and improper dihedrals of substituents on C_{13}, C_{14}, C_{12} and C_{15} atoms. Configurations taken from 83 trajectories from harmonic restraints at different values of φ, with configurations of each trajectory colored with a different color. Black crosses correspond to configurations obtained from geometry optimization using unrestricted DFT/B3LYP/6-31G* with constrained dihedral φ. **b:** Sampling using DFTB3 set US1 for **pSb1** showing correlation between C_{13}=C_{14} dihedral φ and improper dihedrals of substituents on C_{13}, C_{14}, C_{12} and C_{15} atoms. Configurations taken from 83 trajectories from harmonic restraints at different values of φ, with configurations of each trajectory colored with a different color. Black crosses correspond to configurations obtained from geometry optimization using unrestricted DFT/B3LYP/6-31G* with constrained dihedral φ.

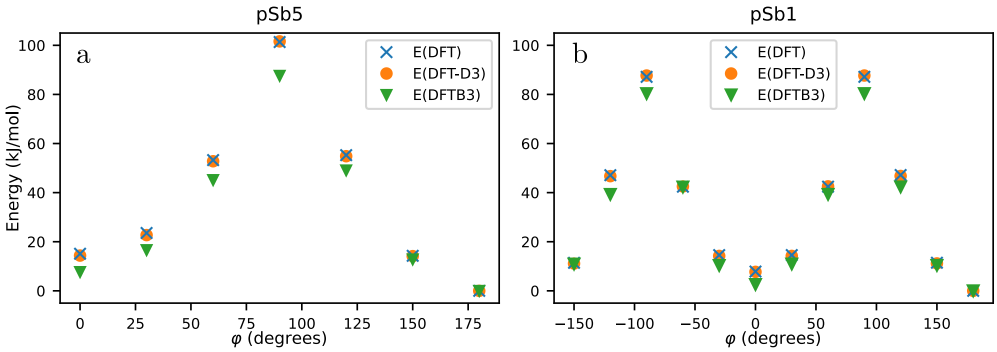

FIG. S2. Electronic energies from constrained optimization calculations using DFTB3 ($E(\mathrm{DFTB3})$) as well as unrestricted DFT/B3LYP/6-31G* with ($E(\mathrm{DFT}-\mathrm{D3})$) and without ($E(\mathrm{DFT})$) Grimme's D3 correction for **a:** pSb5 and **b:** pSb1. Energies have been taken relative to the trans structure (180 degrees) within the respective level of theory.

IV. REFERENCES

[1] Mortimer, R. G., Physical chemistry, Academic Press, 2000.

[2] Peters, B., Reaction rate theory and rare events, Elsevier, 2017.

[3] McQuarrie, D. A. and Simon, J. D., Physical chemistry: a molecular approach, Vol. 1, University Science Books Sausalito, CA, 1997.

[4] Ochterski, J. W., Gaussian Inc., 1999.

[5] Ochterski, J. W., Gaussian Inc., 2000.

[6] Laidler, K. J., Chemical Kinetics, Pearson Education Inc., 1987.

[7] Grubmüller, H., Physical Review E, 1995, **52**(3), 2893.

[8] Voter, A. F., Physical Review Letters, 1997, **78**(20), 3908.

[9] Huber, T.; Torda, A. E. and Van Gunsteren, W. F., Journal of Computer-Aided Molecular Design, 1994, **8**(6), 695–708.

[10] Laio, A. and Parrinello, M., Proceedings of the National Academy of Sciences, 2002, **99**(20), 12562–12566.

[11] Tiwary, P. and Parrinello, M., Physical Review Letters, 2013, **111**(23), 230602.

[12] Khan, S. A.; Dickson, B. M. and Peters, B., The Journal of Chemical Physics, 2020, **153**(5), 054125.

[13] Palacio-Rodriguez, K. and Pietrucci, F., Journal of Chemical Theory and Computation, 2022, **18**(8), 4639–4648.

[14] Dennington, R.; Keith, T. A. and Millam, J. M., GaussView Version 6, 2019.

[15] Gaus, M.; Goez, A. and Elstner, M., Journal of Chemical Theory and Computation, 2013, **9**(1), 338–354.

[16] Zhou, H.; Tajkhorshid, E.; Frauenheim, T.; Suhai, S. and Elstner, M., Chemical Physics, 2002, **277**(2), 91–103.

[17] Bondar, A.-N.; Knapp-Mohammady, M.; Suhai, S.; Fischer, S. and Smith, J. C., Theoretical Chemistry Accounts, 2011, **130**, 1169–1183.

[18] Hourahine, B.; Aradi, B.; Blum, V.; Bonafé, F.; Buccheri, A.; Camacho, C.; Cevallos, C.; Deshaye, M.; Dumitrică, T.; Dominguez, A. and others, , The Journal of Chemical Physics, 2020, **152**(12).

[19] Larsen, A. H.; Mortensen, J. J.; Blomqvist, J.; Castelli, I. E.; Christensen, R.; Dułak, M.; Friis, J.; Groves, M. N.; Hammer, B.; Hargus, C. and others, , Journal of Physics: Condensed Matter, 2017, **29**(27), 273002.

[20] Fletcher, R., Practical methods of optimization, John Wiley & Sons, 2000.

[21] Henkelman, G. and Jónsson, H., The Journal of Chemical Physics, 2000, **113**(22), 9978–9985.

[22] Henkelman, G.; Uberuaga, B. P. and Jónsson, H., The Journal of Chemical Physics, 2000, **113**(22), 9901–9904.

[23] Frisch, M. J.; Trucks, G. W.; Schlegel, H. B.; Scuseria, G. E.; Robb, M. A.; Cheeseman, J. R.; Scalmani, G.; Barone, V.; Petersson, G. A.; Nakatsuji, H.; Li, X.; Caricato, M.; Marenich, A. V.; Bloino, J.; Janesko, B. G.; Gomperts, R.; Mennucci, B.; Hratchian, H. P.; Ortiz, J. V.; Izmaylov, A. F.; Sonnenberg, J. L.; Williams-Young, D.; Ding, F.; Lipparini, F.; Egidi, F.; Goings, J.; Peng, B.; Petrone, A.; Henderson, T.; Ranasinghe, D.; Zakrzewski, V. G.; Gao, J.; Rega, N.; Zheng, G.; Liang, W.; Hada, M.; Ehara, M.; Toyota, K.; Fukuda, R.; Hasegawa, J.; Ishida, M.; Nakajima, T.; Honda, Y.; Kitao, O.; Nakai, H.; Vreven, T.; Throssell, K.; Montgomery, Jr., J. A.; Peralta, J. E.; Ogliaro, F.; Bearpark, M. J.; Heyd, J. J.; Brothers, E. N.; Kudin, K. N.; Staroverov, V. N.; Keith, T. A.; Kobayashi, R.; Normand, J.; Raghavachari, K.; Rendell, A. P.; Burant, J. C.; Iyengar, S. S.; Tomasi, J.; Cossi, M.; Millam, J. M.; Klene, M.; Adamo, C.; Cammi, R.; Ochterski, J. W.; Martin, R. L.; Morokuma, K.; Farkas, O.; Foresman, J. B. and Fox, D. J., Gaussian 16 Revision C.01, 2016.

[24] Berendsen, H. J.; Postma, J. v.; Van Gunsteren, W. F.; DiNola, A. and Haak, J. R., The Journal of Chemical Physics, 1984, **81**(8), 3684–3690.

[25] Nosé, S., The Journal of Chemical Physics, 1984, **81**(1), 511–519.

[26] Hoover, W. G., Physical Review A, 1985, **31**(3), 1695.

[27] Martyna, G. J.; Klein, M. L. and Tuckerman, M., The Journal of Chemical Physics, 1992, **97**(4), 2635–2643.

[28] Barducci, A.; Bussi, G. and Parrinello, M., Physical Review Letters, 2008, **100**(2), 020603.

[29] Bonomi, M.; Branduardi, D.; Bussi, G.; Camilloni, C.; Provasi, D.; Raiteri, P.; Donadio, D.; Marinelli, F.; Pietrucci, F.; Broglia, R. A. and others, , Computer Physics Communications, 2009, **180**(10), 1961–1972.

[30] Tribello, G. A.; Bonomi, M.; Branduardi, D.; Camilloni, C. and Bussi, G., Computer physics communications, 2014, **185**(2), 604–613.

[31] The PLUMED consortium, , Nature methods, 2019, **16**(8), 670–673.

[32] Branduardi, D.; Bussi, G. and Parrinello, M., Journal of Chemical Theory and Computation, 2012, **8**(7), 2247–2254.

[33] Bussi, G. and Tribello, G. A. In Biomolecular Simulations; Springer, 2019; pages 529–578.

[34] Bussi, G. and Laio, A., Nature Reviews Physics, 2020, **2**(4), 200–212.

[35] Torrie, G. M. and Valleau, J. P., Journal of Computational Physics, 1977, **23**(2), 187–199.

[36] Hourahine, B.; Sanna, S.; Aradi, B.; Köhler, C.; Niehaus, T. and Frauenheim, T., The Journal of Physical Chemistry A, 2007, **111**(26), 5671–5677.

[37] Tan, Z.; Gallicchio, E.; Lapelosa, M. and Levy, R. M., The Journal of Chemical Physics, 2012, **136**(14), 04B608.

[38] Efron, B., The jackknife, the bootstrap and other resampling plans, SIAM, 1982.

[39] Gatz, D. F. and Smith, L., Atmospheric Environment, 1995, **29**(11), 1185–1193.
[40] Hub, J. S.; De Groot, B. L. and Van Der Spoel, D., Journal of Chemical Theory and Computation, 2010, **6**(12), 3713–3720.
[41] Salvalaglio, M.; Tiwary, P. and Parrinello, M., Journal of Chemical Theory and Computation, 2014, **10**(4), 1420–1425.
[42] Becke, A. D., Physical Review A, 1988, **38**(6), 3098.
[43] Lee, C.; Yang, W. and Parr, R. G., Physical Review B, 1988, **37**(2), 785.
[44] Hehre, W. J.; Ditchfield, R. and Pople, J. A., J. Chem. Phys., 1972, **56**, 2257–2261.
[45] Tajkhorshid, E. and Suhai, S., The Journal of Physical Chemistry B, 1999, **103**(26), 5581–5590.
[46] Tajkhorshid, E.; Paizs, B. and Suhai, S., The Journal of Physical Chemistry B, 1999, **103**(21), 4518–4527.
[47] Grimme, S.; Antony, J.; Ehrlich, S. and Krieg, H., The Journal of Chemical Physics, 2010, **132**(15).
[48] Schlegel, H. B., Journal of Computational Chemistry, 1982, **3**(2), 214–218.
[49] Peng, C. and Bernhard Schlegel, H., Israel Journal of Chemistry, 1993, **33**(4), 449–454.
[50] Peng, C.; Ayala, P. Y.; Schlegel, H. B. and Frisch, M. J., Journal of Computational Chemistry, 1996, **17**(1), 49–56.

3.2 Paper A2

"Accuracy of reaction coordinate based rate theories for modeling chemical reactions: insights from the thermal isomerization in retinal"

S. Ghysbrecht, L. Donati, B. G. Keller
J. Comput. Chem., **2024**

Accepted manuscript
Preprint: https://doi.org/10.48550/arXiv.2312.12948

This is the pre-peer reviewed version of the following article:
S. Ghysbrecht, L. Donati, B. G. Keller, "Accuracy of reaction coordinate based rate theories for modelling chemical reactions: insights from the thermal isomerization in retinal" *J. Comput. Chem. 46.1* **(2025)**: e27529,
which has been published in final form at https://doi.org/10.1002/jcc.27529. This article may be used for non-commercial purposes in accordance with Wiley Terms and Conditions for Use of Self-Archived Versions.

Contributions:
Simon Ghysbrecht, Luca Donati and Bettina Keller conceived the project and wrote the manuscript. L.D. performed the computational work for the one-dimensional model systems. S.G. performed the computational work for the atomistic model of retinal. All authors contributed to the the final version of the manuscript.

Summary

Rate theories enable estimation of rate constants for chemical reactions from molecular dynamics (MD) simulations. However, vastly different results can be obtained from different methods. In the previous section, different rare event methods were used to calculate rate constants for thermal cis-trans isomerization in two retinal analogues using density functional tight-binding (DFTB) to model the potential energy surface (PES). While numerical sampling of transitions through infrequent metadynamics produced rates that were in good agreement with values obtained from Eyring transition state theory, methods from effective dynamics along a one-dimensional reaction coordinate yielded rates which were up to three orders of magnitude higher. In this paper, the source of this discrepancy is examined, and alternative methods and reaction coordinates as well as multidimensional extensions are evaluated. The following research questions are investigated:

1. How do rates from effective dynamics compare to rates from numerical sampling in one-dimensional model potentials?
2. How do rates from effective dynamics compare to rates from numerical sampling for thermal cis-trans isomerization in a retinal system modeled by a force field?
3. What is the influence of the choice of reaction coordinate?

First, the rate theories are compared for one-dimensional model systems characterized by analytical free energy profiles. In one dimension, effective dynamics evidently corresponds to the explicit dynamics, and thus consistency of these rate equations is tested directly against numerical sampling. Effective dynamics-based methods assessed here are Kramers', which takes on different formulations for different friction regimes, and Pontryagin and grid-based methods, which are derived for the high friction regime. For all examined free energy profiles, these methods yield results which, in their appropriate friction regime, are consistent with results from numerical simulation of transitions, carried out either by unbiased simulations or by infrequent metadynamics. This underscores that these methods accurately reproduce rates as long as the effective dynamics are reliable. As a consequence, the discrepancies in the retinal analogues likely arise from unreliable representation of the full-dimensional dynamics by the one-dimensional reaction coordinate.

Second, we conduct MD simulations to explore cis-trans isomerization in a retinal model system using a force field[135]. Although utilizing force fields extends simulation times to microseconds, it remains insufficient for directly sampling transitions. In a first approach and similarly as in the previous section, infrequent metadynamics are used, biasing the $C_{13}{=}C_{14}$ dihedral angle φ and reweighting transition times to estimate rate constants ($2 \times 10^{-5}\,\mathrm{s}^{-1}$).[2]

---

[2] Rates between brackets are given for cis-to-trans isomerization. Similar trends are seen in trans-to-cis rates, see Tab. 2 in the paper.

Subsequently, metadynamics and umbrella sampling (US) are used to generate free energy and diffusion profiles in φ, just as was done in the previous study. Free energy barriers from metadynamics are found to be overestimated compared to those from US, an effect attributed to correlated motion orthogonal to the biased dihedral angle around the transition state[136]. Consistent with DFTB results, application of effective dynamics-based methods to US free energy profiles along φ as reaction coordinate result in rates ($6 \times 10^{-3}\,\mathrm{s}^{-1}$ for Kramers) orders of magnitude higher than those from infrequent metadynamics.

Third, the effect of the reaction coordinate is investigated. Similar to our observations with DFTB in the preceding section, we note correlations between neighboring dihedral angles and φ. Particularly notable are contributions from out-of-plane wagging of the substituents on the C_{13} and C_{14} atoms, gauged through the corresponding improper dihedral angles χ_1 and χ_2. In a first approach, path reaction coordinates are optimized through path adaptive sampling, taking into account the two improper dihedrals in addition to φ. Free energy profiles along these path reaction coordinates reveal barriers approximately 9 kJ/mol higher than those along φ. Correspondingly, rates derived from effective dynamics-based methods are substantially lower ($5 \times 10^{-5}\,\mathrm{s}^{-1}$ for Kramers, $4 \times 10^{-5}\,\mathrm{s}^{-1}$ for Pontryagin and grid-based) and are closer to those obtained from infrequent metadynamics. Metadynamics along the path reaction coordinate again produce free energy barriers higher than those obtained from US, suggesting that certain correlated motions remain unaccounted for. In a second approach, grid-based models are applied to three-dimensional free energy surfaces spanned by φ, χ_1 and χ_2, obtained from multidimensional metadynamics or US. This approach corresponds to modeling effective dynamics in a three-dimensional subspace, and yields rates ($1 \times 10^{-5}\,\mathrm{s}^{-1}$) in good agreement to those obtained from infrequent metadynamics. In this case, rates from three-dimensional free energy surfaces generated from metadynamics and US are very close.

Accuracy of reaction coordinate based rate theories for modelling chemical reactions: insights from the thermal isomerization in retinal

Simon Ghysbrecht and Bettina G. Keller*
Freie Universität Berlin, Department of Biology,
Chemistry and Pharmacy, Arnimallee 22, 14195 Berlin

Luca Donati
Freie Universität Berlin, Department of Mathematics and Computer Science, Arnimallee 22, 14195 Berlin and
Zuse Institute Berlin, Takustraße 7, 14195 Berlin

(Dated: November 8, 2024)

Modern potential energy surfaces have shifted attention to molecular simulations of chemical reactions. While various methods can estimate rate constants for conformational transitions in molecular dynamics simulations, their applicability to studying chemical reactions remains uncertain due to the high and sharp energy barriers and complex reaction coordinates involved. This study focuses on the thermal cis-trans isomerization in retinal, employing molecular simulations and comparing rate constant estimates based on one-dimensional rate theories with those based on sampling transitions and grid-based models for low-dimensional collective variable spaces. Even though each individual method to estimate the rate passes its quality tests, the rate constant estimates exhibit considerable disparities. Rate constant estimates based on one-dimensional reaction coordinates prove challenging to converge, even if the reaction coordinate is optimized. However, consistent estimates of the rate constant are achieved by sampling transitions and by multi-dimensional grid-based models.

I. INTRODUCTION

Elucidating chemical reaction mechanisms and rates is a central goal in computational chemistry. Yet, calculating this type of dynamical properties remains significantly more challenging than obtaining structural or thermodynamic information. Making precise predictions of reaction rates is particularly difficult.

The difficulties arise from two main sources: inaccuracies in the model of the potential energy surface (PES) [1], and inaccuracies in the method to calculate the rate on this PES [2]. Modelling a chemical reaction often requires a highly accurate PES based on explicitly evaluating the electronic structure at each nuclear configuration. Until recently, the computational cost of electronic structure methods has been so large that their use has been confined to single-point calculations [3] or short simulations of small systems [4]. Only few rate theories can work with so little information. Among them Eyring transition state theory [5] remains the most frequently used method. However, several extensions of Eyring transition state theory, such as variational transition state theory[6, 7] and Grote-Hynes theory [8], have been introduced to account for recrossing and the influence of the solvent.

With recent advances in electronic structure methods [9, 10] and the advent of neural network potentials [11, 12], molecular dynamics (MD) simulations of chemical reactions in complex environments become possible, allowing for the explicit treatment of solvent effects and entropic effects. A wide variety of methods to estimate rates[13, 14], that have been developed in the context of MD simulations of soft-matter systems, can now be applied to chemical reactions in complex environments. Soft-matter systems are characterized by rugged PES with multiple minima connected by energy barriers that are in the same range as the thermal energy. Examples are peptide[15] and protein dynamics[16], molecular binding[17] or crystal nucleation[18]. The accuracy of simulation-based rate estimates in the context of chemical reactions, which usually feature a single high and sharp barrier, is still a matter of debate.

It is important to acknowledge that simulation-based rate estimates are founded on classical mechanics and therefore do not account for quantum tunneling or energy quantization. While quantum tunneling is significant in proton transfer reactions, its rate diminishes exponentially with the square root of the reactant's mass and the barrier height. As a result, for reactions involving carbon or other medium-mass atoms, quantum tunneling is observable only when the reactant molecule is highly strained and consequently the reaction barrier is low [19]. However, energy quantization of the vibrational degrees of freedom does have a noticeable effect in most reactions, in particular, if the reactant molecule is rigid. For the thermal isomerization of protonated Schiff bases, which are closely related to retinal, neglecting the energy quantization incurs an error in the reaction rate of about a factor of three at room temperature [2]. It is worth noting that one can incorporate the effect of energy quantization into the potential energy and thereby achieve quantum-corrected classical dynamics [20].

Simulation-based rate estimates broadly fall into two distinct categories. The first approach is based on counting transitions across the reaction barrier. Since for most chemical reactions, the mean first passage time exceeds

---

* bettina.keller@fu-berlin.de

the accessible simulation time by far, one employs dynamical reweighting techniques, in which the sampling is enhanced and the transition count is subsequently reweighted [21–23]. Infrequent metadynamics[24] falls into this category.

The second approach is based on assuming an effective dynamics along a one-dimensional reaction coordinate, which requires the free energy surface and diffusion constant or diffusion profile as a function of this reaction coordinate. The influence of the neglected degrees of freedom and the curvature of the reaction coordinate on the system's dynamics are captured by these two functions, which can be readily estimated from atomistic simulations of the full molecular system[25–27]. From the effective dynamics, one may then derive analytical expressions for the rate constants. Kramers' rate theory [28, 29] falls into this second category.

The advantage of Kramers' theory is that, given a reaction coordinate, the individual steps of this approach are well-established and straight-forward. However, both the free energy surface and the diffusion constant depend on the reaction coordinate and thus the accuracy of the rate estimate hinges on the quality of this coordinate.

Furthermore, Kramers' analytical expressions for the rate fall into three limiting cases (friction regimes), and it is essential to ensure the correct friction regime is applied. Both the barrier height and the "sharpness" of the barrier, represented by the barrier frequency, determine the friction regime. The high friction regime is induced by high barriers (compared to thermal energy) and broad barriers (barrier frequency compared to friction due to the implicit degrees of freedom). The low and intermediate friction regimes are induced by low and sharp barriers. Chemical reactions with high and sharp barriers fall into a middle ground, where it is not a priori clear whether the high friction regime applies.

To investigate how these effects play out in a chemical reaction, we study the thermal cis-trans isomerization around the C_{13}=C_{14} double bond of retinal coupled to a lysine in vacuum [30, 31]. As PES, we use an empirical force field, whose computational efficiency permits a broad comparison of rate estimates. For a cis-trans isomerization one may use an empirical force field, because the molecule's sigma bonds stay intact. Our goal is to explore whether classical MD in combination with Kramers' rate theory can model this reaction with quantitatively accurate reaction rates and mechanism (on a given PES). As comparison, we include rate estimates for overdamped Langevin dynamics along a one-dimensional reaction coordinate (Pontryagin's rate theory [32]), grid-based models [33, 34] of an effective dynamics in a multidimensional collective variable space, and infrequent metadynamics[24].

II. THEORY

A. Definitions

The cis-trans isomerization of retinal is a unimolecular reaction

$$A \xrightarrow{\mathrm{k_{AB}}} B\,, \tag{1}$$

where A is the cis isomer, B is the trans isomer, and k_{AB} is the reaction rate constant. The rate constant is related to the mean first-passage time (MFPT) τ_{AB} by

$$k_{AB} = \frac{1}{\tau_{AB}}\,. \tag{2}$$

The configuration of the molecule is given by the positions of its N atoms in Cartesian space: $\mathbf{x} \in \Gamma_x \subset \mathbb{R}^{3N}$, where Γ_x is called configuration space. We model the dynamics within the Born-Oppenheimer approximation, where $V(\mathbf{x})$ represents the Born-Oppenheimer potential energy of the electronic ground state. Reactant state $A \subset \Gamma_x$ and the product state $B \subset \Gamma_x$ are regions around minima in $V(\mathbf{x})$, whereas the transition state (TS) corresponds to a saddle point in $V(\mathbf{x})$.

Collective variables are low-dimensional representations of the $3N$-dimensional atomic positions. A collective variable vector is a (possibly non-linear) function

$$\mathbf{q} : \Gamma_x \to \mathbb{R}^m \tag{3}$$

which maps each position $\mathbf{x} \in \Gamma_x$ onto a low-dimensional vector $\mathbf{q} \in \mathbb{R}^m$, where $m \ll 3N$.

The free energy along $\mathbf{q}$ is defined as:

$$F(\mathbf{q}) = -RT \ln \pi(\mathbf{q}) \tag{4}$$

where $\pi(\mathbf{q})$ is the configurational Boltzmann density marginalized to the collective variable space

$$\pi(\mathbf{q}) = Z_{\mathrm{conf}}^{-1} \int_{\Gamma_x} \mathrm{d}\mathbf{x}\, \exp\left(-\frac{V(\mathbf{x})}{RT}\right) \delta\left[\mathbf{q}(\mathbf{x}) - \mathbf{q}\right]\,. \tag{5}$$

Here, $\delta\left[\mathbf{q}(\mathbf{x}) - \mathbf{q}\right]$ is the Dirac delta function and Z_{conf} is the configurational part of the classical partition function $Z_{\mathrm{conf}} = \int_{\Gamma_x} \mathrm{d}\mathbf{x}\, \exp\left(-V(\mathbf{x})/RT\right)$.

A reaction coordinate is a one-dimensional collective variable that scales monotonously between reactant state A and product state B:

$$q : \Gamma_x \to [0, 1]\,. \tag{6}$$

q is zero for the reactant state A and one for product state B. In this manner, q represents the progress of the reaction. Other intervals are also possible, but can be rescaled to $[0, 1]$. The free energy $F(q)$ along the reaction coordinate is defined analogous to eqs. 4 and 5.

In eqs. 4 and 5, R is the ideal gas constant and T is the temperature. We calculate and report potential and free energies in units of J/mol, correspondingly the thermal energy is also reported as a molar quantity: RT. If units of energy are used for potential and free energies, R should be replaced by the Boltzmann constant $k_B = R/N_A$ in eqs. 4 and 5 and all of the following equations. N_A is the Avogadro constant.

Equations of motion for the effective dynamics for q and $\mathbf{q}$ (underdamped Langevin dynamics, overdamped Langevin dynamics with and without position dependent diffusion), as well as the associated Fokker-Planck operators are reported in section I of the SI.

The equations of motion for the effective dynamics require an effective mass (molar) μ_q, which can be estimated from the equipartition theorem[26]

$$\langle E_{\mathrm{kin}} \rangle = \frac{1}{2}\mu_q \langle v^2 \rangle = \frac{1}{2}RT \tag{7}$$

where $\langle v^2 \rangle$ is the average squared velocity along q.

The rate theories introduced in the following, with the exception of the grid-based models, all assume separation of time scales. That is, on average, the system should fully sample the local equilibrium distribution within A, before it escapes over the transition state TS. This is only the case if the free energy barrier $F^{\ddagger}_{AB}$ of the reaction is much larger than the thermal energy: $F^{\ddagger}_{AB} \gg RT$.

B. Simple transition state theory

In simple TST [13, 29] (or equivalently: harmonic TST or Vineyard TST), one uses a one-dimensional reaction coordinate q and the free energy $F(q)$ along this reaction coordinate. A then corresponds to the region around a minimum on the one-dimensional free energy surface, whereas TS is a point q_{TS} along the reaction coordinate that separates reactant state A ($q < q_{TS}$) and product state B ($q > q_{TS}$). Usually TS is positioned at the maximum of the free energy barrier. The rate is derived by considering the probability flux across TS (see SI section I)

$$k_{AB} = \kappa \cdot \frac{\omega_A}{2\pi} \exp\left(-\frac{F^{\ddagger}_{AB}}{RT}\right) . \tag{8}$$

The free energy barrier is

$$\begin{aligned} F^{\ddagger}_{AB} &= F(q_{TS}) - F(q_A) \\ F^{\ddagger}_{BA} &= F(q_{TS}) - F(q_B) \end{aligned} \tag{9}$$

where $F^{\ddagger}_{AB}$ is measured from the free energy minimum of A to TS, and, analogously, $F^{\ddagger}_{BA}$ is measured from the free energy minimum of B to TS. ω_A in eq. 8 is the angular frequency of the harmonic approximation of the reactant state minimum. $\kappa \in [0, 1]$ is the transmission factor, which accounts for the fraction of molecules that proceed from TS to the product state B. Molecules, that revert to A after they have already passed TS, recross the transition state region. At this point, κ is an ad-hoc correction to the rate constant. In this contribution, we will set $\kappa = 1$ when applying eq. 8, meaning that all molecules that reach TS complete the reaction, and recrossing can be neglected.

C. Kramers' rate theory

In Kramers' rate theory[28, 29], one uses a one-dimensional reaction coordinate q. One models the effective dynamics along q by underdamped Langevin dynamics, where the free energy $F(q)$ takes the role of the potential energy governing the drift and the neglected degrees act as a thermal bath. The interaction with this thermal bath is modelled by a friction and a random force, where the friction force can be scaled by a friction coefficient or collision rate ξ (with units time^{-1}). Thus, two thermal parameters enter Kramers' model: ξ and T.

One models $F(q)$ as a double well function, where the minima correspond to reactant (A) and product (B) state, and the barrier corresponds to the transition state (TS). Around each of the three states, $F(q)$ is approximated by a harmonic function

$$F(q) = \begin{cases} F(q_A) + \frac{1}{2}\mu_q \, \omega_A^2 \, (q - q_A)^2 & \text{if } \; q \approx q_A \\ F(q_{TS}) - \frac{1}{2}\mu_q \, \omega_{TS}^2 \, (q - q_{TS})^2 & \text{if } \; q \approx q_{TS} \\ F(q_B) + \frac{1}{2}\mu_q \, \omega_B^2 \, (q - q_B)^2 & \text{if } \; q \approx q_B \, , \end{cases} \tag{10}$$

where q_A, q_B and q_{TS} are positions of the extrema, ω_A, ω_B and ω_{TS} are the angular frequencies of the harmonic approximation around the extrema. Fig. 1.a, c, e show the harmonic approximation for double wells on a circular coordinate.

In total, five parameters originating from the free energy surface govern Kramers' model: ω_A, ω_B, ω_{TS}, $F^{\ddagger}_{AB}$ and $F^{\ddagger}_{BA}$. To obtain the rate constant, the thermal parameters are compared to the free energy parameters. Three limiting cases are classified according to the thermal energy $RT/F^{\ddagger}_{AB}$ and the friction ξ/ω_{TS} (See Fig. 15 in Ref. 29).

The weak friction limit (or sometimes: diffusion limited regime) is defined by $\xi/\omega_{TS} < RT/F^{\ddagger}_{AB}$. In this regime, the deterministic forces (due to the free energy) dominate the diffusive forces (friction and the thermal noise terms). Thus, the underdamped Langevin dynamics is quasi-Hamiltonian. The rare interactions with the heat bath cause the total energy of the system to slowly oscillate and the rate constant is derived by considering the time evolution for the energy probability density [29]. One obtains

$$k_{AB} = \frac{I(F^{\ddagger}_{BA})}{I(F^{\ddagger}_{AB}) + I(F^{\ddagger}_{BA})} \cdot \xi \frac{I(F^{\ddagger}_{AB})}{RT} \cdot \frac{\omega_A}{2\pi} \exp\left(-\frac{F^{\ddagger}_{AB}}{RT}\right) \tag{11}$$

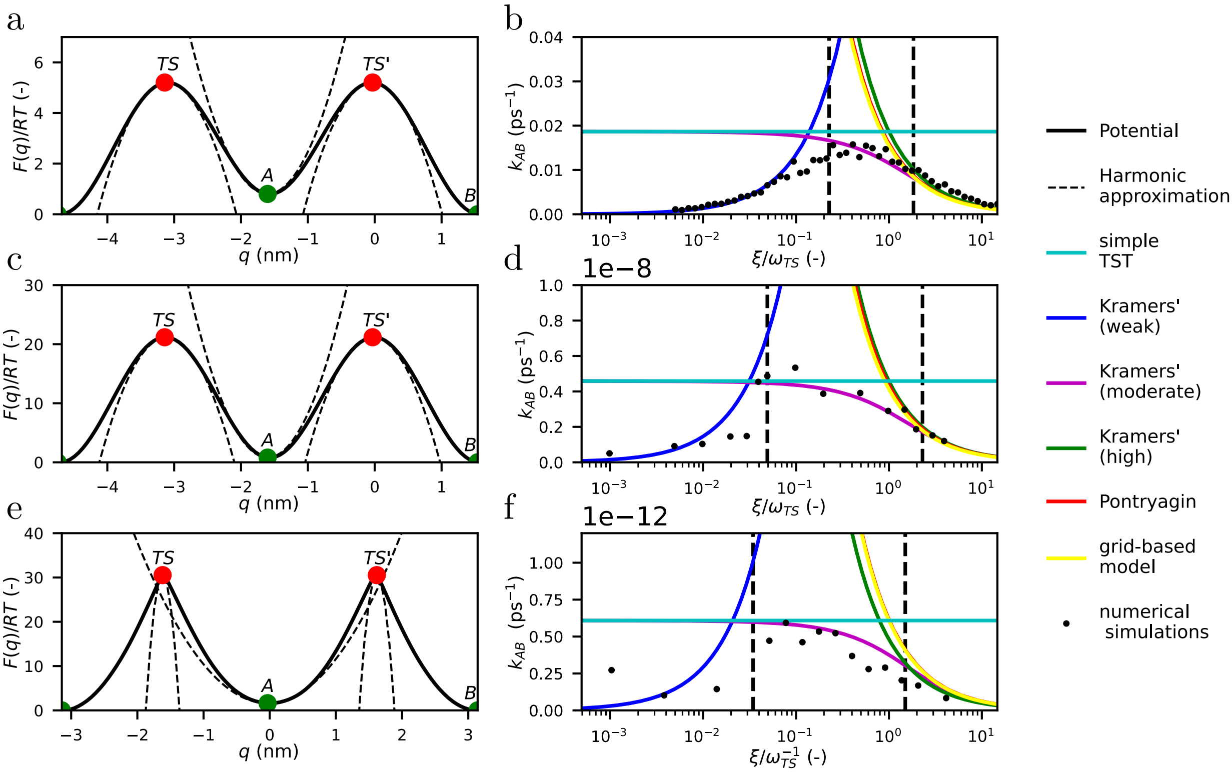

FIG. 1: One-dimensional model systems and corresponding rate constants from A to B as a function of ξ/ω_{TS}: **a, b:** low barriers; **c, d:** high and broad barriers; **e, f:** high and sharp barriers. Rates have been calculated by simple TST (eq. 8), Kramers' weak friction (eq. 11), Kramers' moderate friction (eq. 13), Kramers' high friction (eq. 14), Pontryagin (eq. 16), grid-based model (eq. 18), and from numerical simulations. Threshold between weak and moderate friction is $\xi/\omega_{TS} = RT/F^\ddagger_{AB}$. Threshold between moderate and high friction is at the value of ξ/ω_{TS} where eq. 13 and eq. 14 deviate less than five percent.

where

$$\begin{aligned} I(F^\ddagger_{AB}) &= \oint_{H(q,p)=F^\ddagger_{AB}} p \, \mathrm{d}q \\ &= 2\int_{q^-_{AB}}^{q^+_{AB}} \sqrt{2\mu_q \left(F^\ddagger_{AB} - F(q)\right)} \, \mathrm{d}q \\ &= \frac{2\pi F^\ddagger_{AB}}{\omega_A} \end{aligned} \tag{12}$$

is an integral over closed orbits of the phase space corresponding respectively to the total energy $F^\ddagger_{AB}$. $I(F^\ddagger_{BA})$ is defined analogously. The limits of the integrals are obtained by setting $p = 0$ in the Hamiltonian function: $q^\pm_{AB} = q_A \pm \sqrt{2F^\ddagger_{AB}/\mu_q\omega_A^2}$ (and equivalent $q^\pm_{BA} = q_B \pm \sqrt{2F^\ddagger_{BA}/\mu_q\omega_B^2}$). The resulting formula is the reduced action of the harmonic oscillator at an energy $F^\ddagger_{AB}$ (and equivalent for $F^\ddagger_{BA}$). A sharp peak at the transition state corresponds to a large value of ω_{TS}, and thus might induce the weak friction limit.

The moderate-to-high friction limit is defined by $\xi/\omega_{TS} > RT/F^\ddagger_{AB}$. The diffusive forces are stronger than the deterministic forces, but not by orders of magnitude. In this regime, one assumes a steady state probability flux from state A across the a transition state region [29]. This assumption replaces the requirement for thermal equilibrium between reactant and transition state in transition state theory. This yields

$$k_{AB} = \frac{\xi}{\omega_{TS}}\left(\sqrt{\frac{1}{4}+\frac{\omega_{TS}^2}{\xi^2}} - \frac{1}{2}\right) \cdot \frac{\omega_A}{2\pi} \exp\left(-\frac{F^\ddagger_{AB}}{RT}\right) . \tag{13}$$

The high friction limit is defined by $\xi/\omega_{TS} \gg RT/F^\ddagger_{AB}$. The diffusive forces dominate the deterministic forces. At high values of ξ, the prefactor in eq. 13 can be approximated as ω_{TS}/ξ (see SI section I), yielding

$$k_{AB} = \frac{\omega_{TS}}{\xi} \cdot \frac{\omega_A}{2\pi} \exp\left(-\frac{F^\ddagger_{AB}}{RT}\right) . \tag{14}$$

This regime is also called the spatial diffusion limited

regime, or the diffusive regime.
The rate constants for the three friction regimes (eqs. 11, 13, 14) have the same functional form as in simple TST (eq. 8), but in addition they provide explicit expressions for the transmission factor κ. Kramers' rate theory provides a model for recrossing in terms of the shape of the free energy surface, the temperature and the strength of the heat bath.

D. Pontryagin's rate theory

The following rate model is often quite generically introduced as a means to calculate the mean first-passage time (MFPT) τ_{AB} or escape rate k_{AB} for diffusion over a barrier. It is derived from the Fokker-Planck equation for overdamped Langevin dynamics (Smoluchowski equation). Here, we will refer to it as the Pontryagin's rate theory [32].
In Pontryagin's rate theory [29, 32], one uses a one-dimensional reaction coordinate q and models the effective dynamics along q by overdamped Langevin dynamics, which is the high friction limit of underdamped Langevin dynamics. In this rate theory, the friction coefficient $\xi(q)$ may vary along the reaction coordinate q. This generalization is important because the fluctuations of the neglected degrees of freedom may vary along q [27], and additionally the curvature of q may give rise to a position dependent friction. Conventionally, Pontryagin's rate constant is not formulated in terms of $\xi(q)$ but in terms of the closely related position dependent diffusion profile

$$D(q) = \frac{RT}{\mu_q \xi(q)} \tag{15}$$

where μ_q is a molar mass. The rate constant is then given by the following nested integral

$$k_{AB} = \left\{ \int_{q_A}^{q_B} \mathrm{d}q' \left[\frac{1}{D(q')} e^{\beta F(q')} \int_{-\infty}^{q'} \mathrm{d}q''\, e^{-\beta F(q'')} \right] \right\}^{-1} \tag{16}$$

with $\beta = 1/RT$. A closed-form version is not available, but computing the nested integral numerically is straightforward.
This expression for the rate constant does not make any assumptions on the shape of the reactant state and transition barrier and includes the full position dependent diffusion profile. Inserting the harmonic approximation and assuming constant diffusion in eq. 16 yields Kramers' rate equations in the high friction limit (eq. 14).

E. Grid-based models

In grid-based models[33, 34], one uses a multidimensional collective variable $\mathbf{q} \in \mathbb{R}^m$ and models the effective dynamics in this collective variable space by overdamped Langevin dynamics with position dependent diffusion. The collective variable space is discretized into n disjoint cells. The cells are divided into three sets $\mathcal{A}$, $\mathcal{B}$, and $\mathcal{I}$, where $\mathcal{A}$ represents the reactant state A, $\mathcal{B}$ represents the product state B, and $\mathcal{I}$ the intermediate region. Independent of the assignment to the three sets, the transition rate Q_{ij} from cell i to cell j is

$$Q_{ij} = \begin{cases} Q_{ij} & \text{if } i \neq j \text{ and cells adjacent} \\ 0 & \text{if } i \neq j \text{ and cells not adjacent}\,. \\ -\sum_{l=1, l\neq i}^{n} Q_{il} & \text{if } i = j \end{cases} \tag{17}$$

Eq. 17 defines a $n \times n$ row-normalized rate matrix $\mathbf{Q}$ with elements Q_{ij}. $\mathbf{Q}$ is a discretization of the Fokker-Planck operator for overdamped Langevin dynamics, where we assumed that the free energy is constant within each grid cell.

Q_{ij} between adjacent cells can be calculated as[33–35]

$$Q_{ij} = D_{ij} \frac{\mathcal{S}_{ij}}{\mathcal{V}_i h_{ij}} \cdot \frac{\sqrt{\pi(\mathbf{q}_j)\pi(\mathbf{q}_i)}}{\pi(\mathbf{q}_i)} \tag{18}$$

where $\mathbf{q}_i$ and $\mathbf{q}_j$ are the centers of the adjacent grid cells, $\pi(\mathbf{q})$ is given by eq. 5, $h_{ij} = \|\mathbf{q}_j - \mathbf{q}_i\|$ is the Euclidean distance between the centers of the cells, $\mathcal{S}_{ij}$ is the area of the intersecting surface between cells i and j, $\mathcal{V}_i$ is the volume of the Voronoi cell i, and D_{ij} is the diffusion on the boundary between cells i and j, which we approximate as $D_{ij} = \frac{1}{2}\left(D(\mathbf{q}_i) + D(\mathbf{q}_j)\right)$. Because of the square root in eq. 18, the approach is called Square Root Approximation of the Fokker-Planck equation (FP-SqRA) [33, 34].
In eq. 18, the probability density at the cell boundary between adjacent cells is approximated by the geometric mean of the Boltzmann weights of the cells[33, 34]. Using a harmonic mean instead leads to the Harmonic Averaging Approximation of the Fokker-Planck equation (FP-HAA):

$$Q_{ij} = D_{ij} \frac{\mathcal{S}_{ij}}{\mathcal{V}_i h_{ij}} \cdot \frac{1}{\pi(\mathbf{q}_j)} \frac{2\pi(\mathbf{q}_j)\pi(\mathbf{q}_i)}{\pi(\mathbf{q}_i) + \pi(\mathbf{q}_j)} \tag{19}$$

and has improved convergence properties [36].

Mean first-passage times $\tau_{i\to B}$ from any cell i to the to the product state B can be computed by solving[37]

$$\mathbf{Q}\, \boldsymbol{\tau}_B = -\mathbf{1} \tag{20}$$

for $\boldsymbol{\tau}_B = \left[\tau_{1\to B}, \ldots, \tau_{n\to B}\right]^T$. This vector contains MFPTs for all cells i to the product state B. To enforce this, eq. 20 must be solved while imposing the boundary condition that $\tau_{k\to B} = 0$ for all $k \in \mathcal{B}$. The MFPT from A to B is then obtained by averaging over the state-wise MFPTs

$$\tau_{AB} = \sum_{i \in \mathcal{A}} \pi_{A,i} \tau_{i\to B} \tag{21}$$

where $\pi_{A,i} = \pi_i / \sum_{i\in\mathcal{A}} \pi_i$ and $\pi_i = \int_{\mathbf{q}\in\,\mathrm{cell}\,i} \mathrm{d}\mathbf{q}\, \pi(\mathbf{q})$. The rate constant is the inverse of this MFPT (eq. 2).

F. Rates from sampling transitions

The system is simulated on $V(\mathbf{x})$, and the reaction rate k_{AB} is obtained as a statistical estimate of the observed transitions between A and B. It is sufficient to define $A \subset \Gamma_x$ and $B \subset \Gamma_x$ as regions in the configurational space, a transition state does not need to be defined. The first-passage times from A to B are recorded in a series of n simulations, whose initial states are located in A and which are terminated once they reach B. This yields a series of first-passage times $(\tau_{AB,1}, \tau_{AB,2} \dots \tau_{AB,n})$.

The MFPT τ_{AB} can be calculated as the arithmetic mean of these first-passage times, or – with better statistical accuracy – by fitting the cumulative distribution function of a Poisson process[15]

$$P(\tau_{AB,i}) = 1 - \exp\left(-\frac{\tau_{AB,i}}{\tau_{AB}}\right) \tag{22}$$

to the cumulative distribution histogram of these fist passage times. In eq. 22, τ_{AB} is the MFPT and acts as a fitting parameter, which is inserted into eq. 2 to obtain the reaction rate.

For reactions with high energy barriers the transition times are orders of magnitude longer than the accessible simulation times. Therefore in infrequent metadynamics simulations [24, 38], a time dependent bias function $U(\mathbf{x}, t)$ is introduced that increases in strength as the simulation proceeds and pushes the system over the barrier into state B. Each accelerated first-passage time is then reweighted to the corresponding physical first-passage time by a discretized time-integral over the length of the trajectory [24, 39, 40]

$$\tau_{AB,i} = \Delta t \sum_{k=1}^{T_i} \exp\left(\frac{U(\mathbf{x}_{i,k}, k\Delta t)}{RT}\right) \tag{23}$$

where Δt is the time step of the trajectory, T_i is the total number of time steps in the ith trajectory, $\mathbf{x}_{i,k}$ is the kth configuration in this trajectory, and $t = k\Delta t$ is the corresponding time. This reweighting assumes that no bias has been deposited on the transition state, which is approximately ensured by the slow deposition of the infrequent metadynamics protocol.

III. RESULTS

A. Friction regimes

To study the effect of the curvature of the free energy surface on the friction regime independently from the choice of the reaction coordinate, we devised one-dimensional model systems with a circular reaction coordinate $q \in [-\pi, +\pi]$. As in the actual retinal molecule, the free energy functions $F(q)$ for these models exhibits two energy barriers and two minima. The models differ in the height and the "sharpness" of the barriers, where the first model has low and broad free energy barriers, the second model has high and broad free energy barriers. The third model is the actual free energy function along the C_{13}=C_{14} torsion angle of retinal and exhibits sharp and high free energy barriers. Figs. 1.a, c, e show the free energy functions along with the harmonic approximations for the minima and the barriers. Tab. I reports the corresponding parameters. We set $T = 300\,\mathrm{K}$, and thus the thermal energy is $RT = 2.49\,\mathrm{kJ\,mol^{-1}}$.

With increasing barrier height the rate constant due to simple TST drops by orders of magnitude from $k_{AB} \sim 10^{-2}\,\mathrm{ps}$ to $k_{AB} \sim 10^{-9}\,\mathrm{ps}$ and $k_{AB} \sim 10^{-13}\,\mathrm{ps}$ (cyan lines in Fig. 1.b, d, f). However, comparison to the numerical simulations (black dots in Fig. 1.b, d, f) shows that simple TST is a crude approximation and severely overestimates the rate constants in the low and high friction regimes.

The numerical simulations reproduce Kramers' turnover[29, 41], i.e. the bell curve characterized by low rates in the weak friction regime, high rates in the moderate friction region, and low rates again in the high friction region (see SI Tab. S.7 for representative numerical values). Kramers' rate theory models this turnover by devising a seperate rate equation for each of the three friction regimes (eqs. 11, 13, and 14). The theory requires that $F^{\ddagger}_{AB} \gg RT$, which is well fulfilled for the second ($F^{\ddagger}_{AB} = 20.4\,RT$) and the third model ($F^{\ddagger}_{AB} = 29.0\,RT$) and to a lesser extent for the first model ($F^{\ddagger}_{AB} = 4.4\,RT$).

The friction regime is determined by the relative sizes of the ratios $RT/F^{\ddagger}_{AB}$ and ξ/ω_{TS}. The ratio $RT/F^{\ddagger}_{AB}$ compares the thermal energy to the free energy barrier. Within the assumptions of Kramers' theory, $RT/F^{\ddagger}_{AB} \ll 1$. The ratio ξ/ω_{TS} compares the time it takes to cross the transition state region, $1/\omega_{TS}$, to the average time between two interactions with the thermal bath. $\xi/\omega_{TS} > 1$ means that, on average, several interactions with the thermal bath occur while the system crosses the transition state region, implying a high friction regime. $\xi/\omega_{TS} < 1$ means that, on average, no interaction with the thermal bath occurs while the system crosses the transition state region, implying a weak friction regime. For $\xi/\omega_{TS} \approx 1$, transition time and interaction with the thermal bath occur on the same timescale.

All other parameters being equal, an increase in the curvature of the free energy barrier leads to an increase in ω_{TS} and thus might shift the effective dynamics into the weak or intermediate friction regime. In our model systems, the ω_{TS} increases across the models from $\omega_{TS} \approx 5\,\mathrm{ps^{-1}}$ to $\omega_{TS} \approx 10\,\mathrm{ps^{-1}}$ and finally reaching $\omega_{TS} = 48.38\,\mathrm{ps^{-1}}$, and $\omega_{TS'} = 46.21\,\mathrm{ps^{-1}}$ for the model representing the actual retinal. Simultaneously, the free energy barrier increases across the models. The result-

		Small barrier	**High barrier**	**Inter-polated** TS	TS'
RT	[kJ mol^{-1}]	2.49	2.49	2.49	
$F^{\ddagger}_{AB}$	[kJ mol^{-1}]	10.98	50.84	72.11	72.10
$F^{\ddagger}_{BA}$	[kJ mol^{-1}]	12.96	52.74	76.15	76.14
ω_A	[ps^{-1}]	4.78	10.13	6.83	
ω_B	[ps^{-1}]	4.98	10.21	7.60	
ω_{TS}	[ps^{-1}]	4.89	10.17	48.38	46.21
energy ratio					
$RT/F^{\ddagger}_{AB}$	[-]	0.23	0.05	0.03	0.03
threshold between weak and moderate friction					
ξ/ω_{TS}	[-]	0.23	0.05	0.03	0.03
ξ	[ps^{-1}]	1.12	0.51	1.45	1.39
threshold between moderate and high friction					
ξ/ω_{TS}	[-]	1.90	2.30	1.50	1.57
ξ	[ps^{-1}]	9.29	23.39	72.57	72.55

TABLE I: Parameters for one-dimensional rate theories calculated for the one-dimensional systems.

ing boundaries between the friction regimes are shown as vertical dashed lines in Fig. 1.b, d, f.

Kramers' rate constants k_{AB} as a function of ξ/ω_{TS} are represented as blue, purple and green lines for the three friction limits (Fig. 1.b, d, f). Each of the three rate equations agrees well with the numerical results when applied within the appropriate friction regime. Outside of their respective friction regime, the three rate equations yield very inaccurate results. In particular, the rate equation for the high friction regime vastly overestimates the rates in the weak and moderate friction regime.

Additionally, we report the results from Pontryagin's rate theory (red line, eq. 16) and the grid-based model (yellow line, eq. 18), which both assume overdamped Langevin dynamics. For a position independent friction coefficient ξ, these models closely align with the high friction regime of Kramers' rate theory, and equally overestimate the rate constant in the weak and moderate friction regime. These results underlines the importance of determining the system's friction regime and choosing the appropriate rate model.

For the free energy function of retinal (third model system), the moderate friction regime ranges from $\xi = 1.45\,\text{ps}^{-1}$ to $\xi = 72.57\,\text{ps}^{-1}$. The friction coefficient ξ of the effective dynamics along q is not a parameter that can be chosen freely, but it is determined by the influence of the neglected degrees of freedom and is calculated from the diffusion constant $D(q)$ (eq. 15) and the effective mass μ_p (eq. 7). This is explored in the following section.

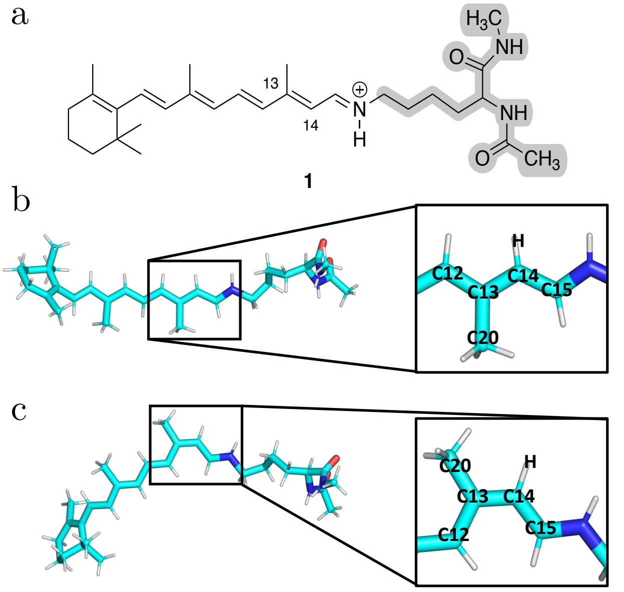

FIG. 2: **a:** Retinal covalently linked to a capped lysine residue. Position restraints have been applied to heavy atoms highlighted in gray. **b:** trans-configuration. **c:** cis-configuration.

B. Atomistic model of retinal

Our model of retinal (Fig. 2.a) consists of the retinal molecule, which is covalently bound to a capped lysine residue via a protonated Schiff base [42]. This corresponds to the chemical structure of retinal in a protein environment. Since the lysine residue cannot move freely in a protein environment, we placed position restraints on all heavy atoms of lysine (backbone and side chain) as well as on the atoms in the caps. All atoms in retinal including the cyclohexene ring were allowed to move freely. As potential energy function of this molecule we use an empirical atomistic force field. Our goal is to calculate the reaction rate constants of the thermal cis-trans isomerization around the C_{13}=C_{14} double bond (Fig. 2.b-c), where the cis-configuration is the reactant state A and the trans-configuration is the product state B.

C. C_{13}=C_{14}-torsion angle as reaction coordinate

As initial reaction coordinate for the one-dimensional rate models, we choose the torsion angle φ constituted by the chain of carbon atoms C_{12}-C_{13}=C_{14}-C_{15} (Fig. 2). Fig. 3 shows two free energy functions along this reaction coordinate, which were numerically calculated by well-tempered metadynamics simulations[38] (blue line) and by umbrella sampling simulations[43] combined with weighted histogram analysis[44] (orange line). The statistical uncertainty of the free energy profiles are shown

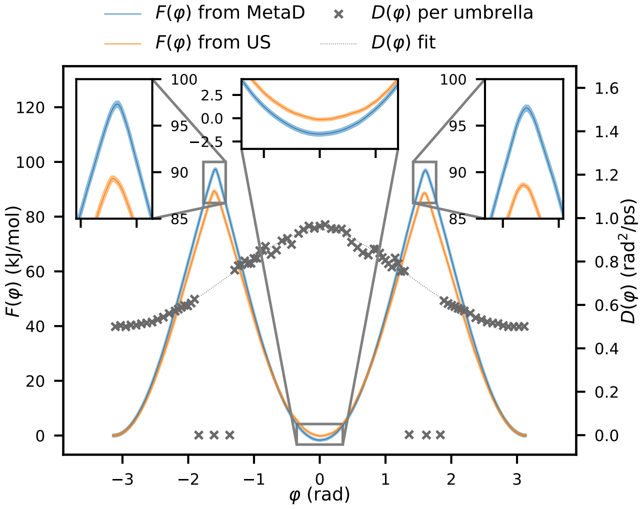

FIG. 3: Free energy surfaces $F(\varphi)$ and diffusion profiles $D(\varphi)$ estimated from umbrella sampling (US) and metadynamics (MetaD) by biasing the $C_{13}{=}C_{14}$ torsion angle φ. Statistical standard errors given by the thickness of the curves.

as shaded areas in Fig. 3, but they are only about as large as the linewidth. The figure also shows the position dependent diffusion $D(\varphi)$ obtained from umbrella sampling simulations following Ref. 27. Because of the sharp barriers, the diffusion profile could not be estimated in the transition regions, and we relied on the interpolation (dotted line in Fig. 3) in these regions.

Both $F(\varphi)$ have minima at the cis-configuration ($\varphi = 0\,\mathrm{rad}$) and at the trans-configuration ($\varphi = \pm\pi\,\mathrm{rad}$), where we set the trans state to $F(\varphi) = F(\pi) = 0$. Cis- and trans-configuration have the same free energy in $F(\varphi)$ from umbrella sampling, whereas, in $F(\varphi)$ from metadynamics, the cis-configuration is about $1.6\,\mathrm{kJ\,mol^{-1}}$ lower than the trans-configuration. The minima are separated by two free energy barriers TS and TS' corresponding to rotating clockwise and counterclockwise around φ, respectively. Both methods, umbrella sampling and metadynamics, predict that the barriers TS and TS' are equal in height. Umbrella sampling yields a barrier height of $F^{\ddagger}_{\mathrm{cis}\to\mathrm{trans}} = 89\,\mathrm{kJ\,mol^{-1}}$, whereas metadynamics yields barriers that are about $10\,\mathrm{kJ\,mol^{-1}}$ higher ($F^{\ddagger}_{\mathrm{cis}\to\mathrm{trans}} = 99\,\mathrm{kJ\,mol^{-1}}$).

Even though we monitored the convergence of the two free energy methods carefully, the difference in the predicted free energy barrier is sizeable. At room temperature, the difference corresponds to about four times the thermal energy of $RT = 2.49\,\mathrm{kJ\,mol^{-1}}$, and in absolute terms it is well above the limit for chemical accuracy of $1\,\mathrm{kcal\,mol^{-1}} = 4.2\,\mathrm{kJ\,mol^{-1}}$. Because the free energy difference enters exponentially in each of the rate models, this difference strongly affects the predicted rate. We return to this discussion in section III F, but for now will discuss rates based on the umbrella sampling $F(\varphi)$.

The parameters for the one-dimensional rate theories for $F(\varphi)$ from umbrella sampling and from metadyamics are reported in SI Tabs. S.1 and S.2.

Next, we determine the friction regime by comparing the energy ratio is $RT/F^{\ddagger}_{\mathrm{cis}\to\mathrm{trans}} = 0.028$ to the friction ratio ξ_{TS}/ω_{TS}. The friction coefficient of the effective dynamics along φ is $\xi_{TS} = 132\,\mathrm{ps^{-1}}$ for transitions via TS (determined via eqs. 15 and 7). The curvature of TS is $\omega_{TS} = 244\,\mathrm{ps^{-1}}$, yielding the friction ratio $\xi_{TS}/\omega_{TS} = 0.54$. The corresponding ratio for the other barrier is $\xi_{TS'}/\omega_{TS'} = 0.50$. Both friction ratios are much higher than the energy ratio, and therefore the effective dynamics along φ fall into the moderate-to-high or even high friction regime.

Tab. II shows the rate constants derived from one-dimensional rate theories for the moderate and high friction regime. Methods that assume high friction (Kramers' (high friction), Pontryagin, grid-based) all yield a rate constant of $k_{\mathrm{cis}\to\mathrm{trans}} \approx 0.009 - 0.015\,\mathrm{s^{-1}}$ for the cis-trans transition. The two methods that are based on overdamped Langevin dynamics (Pontryagin and grid-based models) yield indistinguishable rate constants ($k_{\mathrm{cis}\to\mathrm{trans}} \approx 0.009\,\mathrm{s^{-1}}$), which is slightly lower than the high friction limit of Kramers' rate theory ($k_{\mathrm{cis}\to\mathrm{trans}} \approx 0.015\,\mathrm{s^{-1}}$).

The high friction Kramers' rate constant ($k_{\mathrm{cis}\to\mathrm{trans}} \approx 0.015\,\mathrm{s^{-1}}$) is higher than the one form the moderate friction regime ($k_{\mathrm{cis}\to\mathrm{trans}} \approx 0.006\,\mathrm{s^{-1}}$). Since the two methods would coincide in the high friction region, this indicates, that the effective dynamics along φ fall into the moderate friction regime and are best described by Kramers' rate theory for moderate friction.

Simple TST is a reasonable approximation in the moderate friction regime and yields a rate constant of $k_{\mathrm{cis}\to\mathrm{trans}} \approx 0.008\,\mathrm{s^{-1}}$, only slightly overestimating Kramers' rate constant for moderate friction. The rate constant of the reverse reaction, $k_{\mathrm{trans}\to\mathrm{cis}}$, are reported in Tab. II and show the same effects.

D. Comparison to infrequent metadynamics

Even though the results from one-dimensional rate theories (using φ as reaction coordinate) seem consistent, they deviate drastically from rate constants estimated from molecular simulations (Tab. II). We used infrequent metadynamics and biased along φ to simulate the cis-trans isomerization. The resulting rate constant, $k_{\mathrm{cis}\to\mathrm{trans}} = 2.23 \cdot 10^{-5}\,\mathrm{s^{-1}}$, is more than two orders of magnitude smaller than the most appropriate one-dimensional rate theory $k_{\mathrm{cis}\to\mathrm{trans}} = 5.83 \cdot 10^{-3}\,\mathrm{s^{-1}}$ (Kramers' with moderate friction). By moving from a one-dimensional system (Fig. 1) to a high-dimensional system (Fig. 2) we have lost the agreement between one-dimensional rate theories and numerical simulations.

The deviation between Kramers' rate theory and numerical simulation for retinal is in stark contrast to the good agreement between the two approaches for the one-dimensional systems. It is, however, in line with the results from Ref. 2, where we found a similar disparity between simulated rate constants and the moderate friction limit of Kramers' rate theory.

Two known error sources of infrequent metadynamics are (*i*) slow processes that occur orthogonal to the biased coordinate, e.g. due to sub-minima in the reactant state [45, 46], and (*ii*) perturbation of the transitions state region because bias is deposited there[15, 24]. Retinal is a very rigid molecule and does not exhibit sub-minima within the cis- or within the trans-configuration, making the first error source unlikely. Our rate constants are insensitive to the variations in the bias deposition rate, which confirms that the transition state region is unperturbed (Fig. S.4). Thus, for this specific system the limitations of infrequent dynamics metadynamics do not explain the deviation results of one-dimensional rate theories.

A second error source might be a wrong choice of the friction regime. However, the analysis in section III C shows that, for this system, the difference between the high friction and the intermediate friction results are small and do not explain the discrepancy with the simulation results. Specifically, high friction: $k_{\mathrm{cis}\to\mathrm{trans}} = 1.45 \cdot 10^{-2}\,\mathrm{s}^{-1}$, moderate friction: $k_{\mathrm{cis}\to\mathrm{trans}} = 5.83 \cdot 10^{-3}\,\mathrm{s}^{-1}$, simulation: $k_{\mathrm{cis}\to\mathrm{trans}} = 2.23 \cdot 10^{-5}\,\mathrm{s}^{-1}$.

We conclude that the disparity between Kramers rate constant for moderate friction and the simulated results is based in the high-dimensionality of the system. One-dimensional rate theories are sensitive to the choice of reaction coordinate[47]. To explain the gap between the simulated rate constant and Kramers' rate constant, we will next optimize the reaction coordinate.

E. Optimized reaction coordinate

The reaction coordinate $q = \varphi$ cleanly separates the reactant and the product state and thus fulfills an important criterion for a good reaction coordinate. However, closer inspections shows that other degrees of freedom besides the torsion angle participate in the cis-trans isomerization. The bonding environments around C_{13} and C_{14} are planar when retinal is in the cis- or trans-configuration, but both C_{13} and C_{14} bend out of plane in the vicinity of the transition state [2, 48]. The out-of-plane motion around C_{13} is captured by the improper dihedral χ_1 defined by $\{C_{13}, C_{14}, C_{12}, C_{20}\}$. Likewise, the out-of-plane motion around C_{14} is captured by the improper dihedral χ_2 defined by $\{C_{14}, C_{15}, C_{13}, H\}$. The correlation between φ and the two improper dihedrals has been demonstrated at the levels of DFT/B3LYP and DFTB[2, 48], and is also captured by our umbrella sampling simulations using an empirical force field.

Fig. 4.a shows the configurations of a series of umbrella sampling simulations projected into the two-dimensional space spanned by φ and χ_1. These distributions seem to "jump" at the transition states ($\varphi = \pm\frac{\pi}{2}$). The projection into the space spanned by φ and χ_2 shows a similar behaviour (Fig. 4.b). Note that the amplitude of the "jump" is not very large, only $\pm 0.4\,\mathrm{rad}$, compared to the range of φ itself. (In SI Fig. S.5 the zoom on χ_1 and χ_2 has been removed to give a more realistic impression of the amplitude.)

We optimized nonlinear reaction paths $\mathbf{s}\,(\sigma_s)$ in the space spanned by φ, χ_1 and χ_2 using the path finding algorithm from Ref. 49. The paths are parametrized by a path progression parameter σ_s which can be used as a reaction coordinate in rate theories: $q = \sigma_s$. In total, we optimized four reaction paths: two reaction paths for the transition from cis to trans, each rotating in a different direction, and similarly two reaction paths for the transition from trans to cis (Fig. 4.c,d). The progress of the optimization is shown in SI Fig. S.6. The optimized reaction coordinates are correlated to χ_1 and χ_2 but do not exhibit any sudden jumps in the two-dimensional distributions (SI Fig. S.7 and S.8).

To employ one-dimensional rate theories on these optimized reaction coordinates, we calculated free energy functions $F(\sigma_s)$, using umbrella sampling and metadynamics, as well as diffusion profiles (see Fig. 4.e for paths from cis to trans and Fig. S.9 in the SI for paths from trans to cis). We will discuss the rate constant derived from the umbrella sampling for the reaction cis → trans in detail. The rate constants for the reverse reaction have similar values and show the same trends (see Tab. II).

For the optimized reaction coordinate umbrella sampling yields a barrier height of $F^{\ddagger}_{\mathrm{cis}\to\mathrm{trans}} = 98\,\mathrm{kJ\,mol}^{-1}$, which is $9\,\mathrm{kJ\,mol}^{-1}$ higher than the free energy barrier for φ. Due to this higher free energy barrier, all one-dimensional rate theories yield lower rates for σ_s than for φ and therefore are in much better agreement with the numerical results. Nonetheless, a discussion of the friction regime is worthwhile.

Despite the increase in the free energy barrier, the energy ratio is only slightly lower than for φ: $RT/F^{\ddagger}_{\mathrm{cis}\to\mathrm{trans}} = 0.025$. By contrast the friction ratio for σ_s is about ten times higher than for φ: namely $\xi_{TS}/\omega_{TS} = 5.09$ (for path *cis_trans1*). This is caused by an increased friction coefficient of the effective dynamics and a broader free energy barrier ($\xi_{TS} = 785\,\mathrm{ps}^{-1}$ and $\omega_{TS} = 154\,\mathrm{ps}^{-1}$ for path *cis_trans1*). Consequently, the effective dynamics along $q = \sigma_s$ fall into the high friction regime.

This is also reflected by the values for Kramers' rate constants for moderate friction regime and for the high friction regime. For $q = \sigma_s$, these two equation yield almost the same value ($k_{\mathrm{cis}\to\mathrm{trans}} = 4.81 \cdot 10^{-5}\,\mathrm{s}^{-1}$ and $k_{\mathrm{cis}\to\mathrm{trans}} = 4.98 \cdot 10^{-5}\,\mathrm{s}^{-1}$, see Tab. II), which is only the case in the high friction regime. Another consequence of the higher friction regime is that simple TST considerably overestimates the rate constant ($k_{\mathrm{cis}\to\mathrm{trans}} = 2.57 \cdot 10^{-4}\,\mathrm{s}^{-1}$). Pontryagin's rate theory and the grid-based model yield the same rate constant ($k_{\mathrm{cis}\to\mathrm{trans}} = 3.66 \cdot 10^{-5}\,\mathrm{s}^{-1}$), which is lower than the result from Kramers' rate theory. Since the effective dynamics fall into the high friction regime, this deviation

method	**eq.**	**CV**	$F(\mathbf{q})$ **via US** $k_{\text{trans}\to\text{cis}}$ [s^{-1}]	 $k_{\text{cis}\to\text{trans}}$ [s^{-1}]	$F(\mathbf{q})$ **via MetaD** $k_{\text{trans}\to\text{cis}}$ [s^{-1}]	 $k_{\text{cis}\to\text{trans}}$ [s^{-1}]
C_{13}=C_{14}-torsion angle as reaction coordinate						
Simple TST	8	φ	5.17×10^{-3}	7.55×10^{-3}	2.05×10^{-4}	1.60×10^{-4}
Kramers (moderate friction)	13	φ	3.99×10^{-3}	5.83×10^{-3}	1.67×10^{-4}	1.30×10^{-4}
Kramers (high friction)	14	φ	9.90×10^{-3}	1.45×10^{-2}	4.96×10^{-4}	3.86×10^{-4}
Pontryagin	16	φ	1.08×10^{-2}	8.93×10^{-3}	4.68×10^{-4}	2.17×10^{-4}
Grid-based	19	φ	1.07×10^{-2}	8.95×10^{-3}	4.67×10^{-4}	2.17×10^{-4}
Optimized reaction coordinate σ_s						
Simple TST	8	path	2.41×10^{-4}	2.57×10^{-4}	9.56×10^{-6}	1.19×10^{-5}
Kramers (moderate friction)	13	path	4.45×10^{-5}	4.81×10^{-5}	1.85×10^{-6}	2.26×10^{-6}
Kramers (high friction)	14	path	4.61×10^{-5}	4.98×10^{-5}	1.92×10^{-6}	2.34×10^{-6}
Pontryagin	16	path	5.80×10^{-5}	3.66×10^{-5}	2.51×10^{-6}	1.73×10^{-6}
Grid-based	19	path	5.78×10^{-5}	3.66×10^{-5}	2.53×10^{-6}	1.75×10^{-6}
Grid-based model for multidimensional collective variables						
Grid-based (diffusion *grid1*)	19	φ, χ_1, χ_2	(5.66×10^{-6})	(7.05×10^{-6})	8.13×10^{-6}	1.23×10^{-5}
Grid-based (averaged *grid1*)	19	φ, χ_1, χ_2	(1.14×10^{-5})	(1.44×10^{-5})	1.58×10^{-5}	2.40×10^{-5}
Grid-based (diffusion *grid2*)	19	φ, χ_1, χ_2	(7.14×10^{-6})	(9.05×10^{-6})	1.03×10^{-5}	1.56×10^{-5}
Grid-based (averaged *grid2*)	19	φ, χ_1, χ_2	(1.02×10^{-5})	(1.35×10^{-5})	1.40×10^{-5}	2.13×10^{-5}

Sampling

method	**eq.**	**CV**	$k_{\text{trans}\to\text{cis}}$ [s^{-1}]	$k_{\text{cis}\to\text{trans}}$ [s^{-1}]
InMetaD	23	φ	2.18×10^{-5}	2.23×10^{-5}
InMetaD	23	φ, χ_1, χ_2	2.22×10^{-5}	2.60×10^{-5}

TABLE II: Rate constants determined through different methodologies for the thermal cis-trans isomerization over the C_{13}=C_{14} double bond in retinal. (...): results sensitive to the grid.

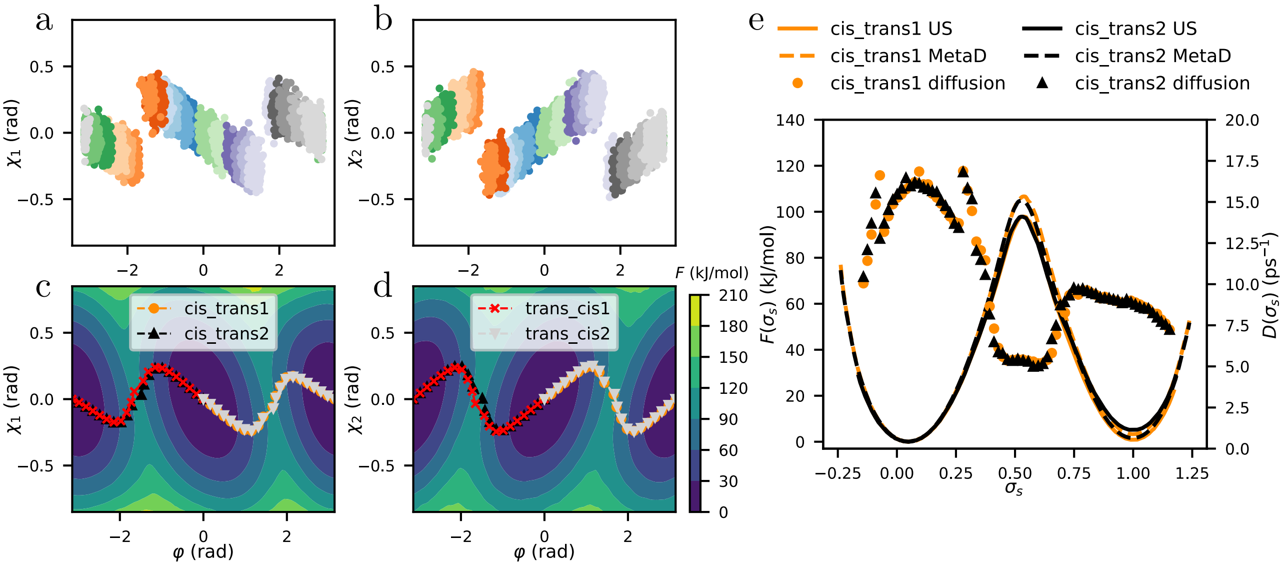

FIG. 4: **a:** Scatter plots of the umbrella sampling simulations (one color per umbrella) for dihedral φ vs. improper dihedral χ_1. **b:** The same for dihedral φ vs. improper dihedral χ_2. **c:** 3-dimensional free energy surface $F(\varphi, \chi_1, \chi_2)$ from metadynamics projected into the (φ, χ_1)-space. Lines show optimized reaction coordinates. **d:** The same but projected into (φ, χ_2)-space **e:** Free energy profiles from metadynamics and umbrella sampling as well as diffusion profiles for optimized reaction coordinate for the cis-to-trans isomerization.

is not likely caused by the assumption of overdamped Langevin dynamics in these theories. The more likely cause is that Kramers' rate theory assumes a position independent diffusion constant, whereas both Pontryagin and grid-based models account for variations in the diffusion constant along the reaction coordinate.

In summary, optimizing the reaction coordinate had two effects on the one-dimensional rate models: the free energy barrier increased, and the friction ratio ξ_{TS}/ω_{TS} increased. Both effects lower the estimate of the rate constant and thus improve the agreement with the simulation results.

F. Umbrella sampling vs metadynamics

For both reaction coordinates, $q = \varphi$ and $q = \sigma_s$, we find that the free energy barriers from metadynamics are consistently 7 to 10 $\mathrm{kJ\,mol^{-1}}$ higher than the free energy barriers from umbrella sampling (SI Tab. S.3 and S.4). Consequently, the rate constants based on metadynamics are about an order of magnitude lower than those based on umbrella sampling.

The sampling for both methods is generous, such that the statistical uncertainty is negligible (Fig. 3 and 4.e). The free energy functions do not change noticeably when we vary the parameters of the method (force constant and positioning of the umbrella potentials, width of the Gaussian bias potentials in metadynamics, SI Fig. S.11). However, in metadynamics, the error estimated by block analysis[50] as well as the free energy difference between the cis- and the trans-configuration converged only slowly for both reaction coordinates (SI Fig. S.10).

Fig. 4 indicates that the optimal reaction coordinate follows a Z-shaped curve embedded in multiple collective variables. If the metadynamics bias does not account for all of these relevant collective variables, the system can be pushed into a position parallel to the transition state. However, from this position, the system is unable to transition into state B. As a result, repeated failed crossing attempts lead to a buildup of bias in basin A, overfilling this minimum. Once the system escapes the local minimum due to the excessive bias, it might not adequately sample the transition state or other important configurations, especially if the metadynamics bias does not account for the slow collective variables necessary for proper exploration. This may ultimately cause an overestimation of the free energy barrier. For a detailed discussion of this effect see Ref. [51], especially Fig. 2 therein.

The slow convergence of the error estimates as well as the free energy difference could therefore indicate that further degrees of freedom are relevant to the optimal reaction coordinate. Candidates are the torsion around the neighboring single bonds, i.e. C_{12}-C_{13} and C_{14}-C_{15}. Projecting the configurations into the space spanned by these torsion angles and φ, we find similar "jumps" as in Fig. 4, albeit less pronounced (SI Fig. S.12). The optimized reaction coordinate σ_s is still correlated with the torsion around these single bonds, but does not exhibit any sudden jumps in the two-dimensional distributions (SI Fig. S.7), even though these torsion angles were not explicitly part of the optimization process. By comparing SI Fig. S.7 and S.8, we observe that for metadynamics along σ_s, the sampling in the transition state region is clearly reduced compared to umbrella sampling. This supports the conclusion that transitions are more challenging, leading to an overestimation of the free energy barriers.

G. Multidimensional collective variables

An alternative to one-dimensional rate theories are grid-based models in multidimensional collective variable spaces. We calculated the three-dimensional free energy function $F(\varphi, \chi_1, \chi_2)$ using metadynamics with three-dimensional Gaussian bias functions, as well as using umbrella sampling with three-dimensional harmonic constraints. The position dependent diffusion profile for the diffusion in each of the three directions were calculated using umbrella sampling with three-dimensional harmonic restraining potentials on a coarse grid (*grid1*) and a fine grid (*grid2*). See SI Figs. S.13 and S.14.

The projection of $F(\varphi, \chi_1, \chi_2)$ into the two-dimensional spaces (φ, χ_1) and (φ, χ_2) are shown in Fig. 4.c and d, and explain the sudden "jumps" in the two-dimensional distributions in Fig. 4.a and b. The free energy minima of the cis- and the trans-configuration are slanted in the two-dimensional space. Specifically, the configurations overlap for values of φ near the barrier, and thus φ does not cleanly discriminate between cis- and the trans-configuration. In Fig. 4.c, when going form negative values of φ to positive values across the cis-minimum, χ_1 steadily decreases from +0.3 rad to -0.3 rad. At the transition state, the value of χ_1 is restored to $\chi_1 = +0.3\,\mathrm{rad}$ within a short interval of φ, giving rise to "jumps" in the two-dimensional distribution. The correlation of φ to χ_2 shows a similar behaviour (Fig. 4.D). The optimized path follows this sudden change in χ_1 and χ_2 by zigzagging through the three-dimensional space.

To obtain our grid-based rate model, we discretized the three-dimensional space $(\varphi, \chi_1, \chi_2)$, and calculated the rate matrix $\mathbf{Q}$ from the free energy surface and the diffusion profiles using eq. 19, which then yielded the reaction rate constants via eq. 20 and 21. Convergence of the rates with respect to different discretizations of $(\varphi, \chi_1, \chi_2)$ is better for metadynamics than for umbrella sampling. (SI Fig. S.1). The rate constants of the three-dimensional models are in good agreement with the rate constants from the simulations (Tab. II).

Most importantly, in the three-dimensional models, the results from metadynamics and from umbrella sampling are in excellent agreement. The rate estimates are somewhat sensitive to the model of the diffusion profile. In particular, using a uniform diffusion profile along each of the three collective variables (averaged *grid1* and *grid2*) yields rate constants that are slightly closer to the simulated results than when estimating a fully position dependent diffusion profile (diffusion *grid1* and *grid2*). This might be caused by numerical effects when using the fully position dependent diffusion profile.

We additionally repeated the infrequent metadynamics simulations using three-dimensional Gaussian bias functions in the space spanned by φ, χ_1 and χ_2. The resulting rate constants are very close to those obtained from infrequent metadynamics with one-dimensional biasing (Tab. II).

Method	**Reaction Coordinate**	**simulation time**		**time step**
		MetaD $[10^{-6}\,\mathrm{s}]$	US $[10^{-6}\,\mathrm{s}]$	$[10^{-15}\,\mathrm{s}]$
1D FES	dihedral φ	2.0	0.996	2.0
1D FES	path σ	8.0	9.6	1.0
3D FES	dihedrals φ, χ_1, χ_2	1.0	3.92	2.0
InMetaD		12.0		2.0

TABLE III: Aggregated MD simulation times to calculate rates for both isomerization directions ($k_{\mathrm{cis}\to\mathrm{trans}}$ and $k_{\mathrm{trans}\to\mathrm{cis}}$).

H. Computational Cost

The main computational costs for one-dimensional rate theories (simple TST, Kramers' rate, Pontryagin's rate, grid-based models) comes from the enhanced sampling MD simulations (metadynamics or umbrella sampling), while reweighting to obtain the free energy surface from these simulation data and evaluation of the rate equations exerts a negligible computational cost. Pontryagin's rate and grid-based models additionally require a diffusion profile. When using umbrellas sampling, FES and diffusion profile[27] can be obtained from the same set of simulations. In this case the diffusion profile has negligble computational cost. If metadynamics is used to generate the FES, additional simulations might be required to estimate the diffusion profiles.

To compare the computational cost of one-dimensional rate theories and grid-based models (Tab. III), we therefore focus on the computational cost of MD simulations for generating the FES. For the path-based FES, this cost estimate includes the simulation time for optimizing the four paths (clockwise and counter-clockwise rotation for both $k_{\mathrm{cis}\to\mathrm{trans}}$ and $k_{\mathrm{trans}\to\mathrm{cis}}$, total), as well as the simulation time for generating the FES along the optimized paths. We additionally include the computational cost of the MD simulations for infrequent metadynamics, where again the cost of reweighting these trajectories is negligible (Tab. III).

Across all methods the required simulation time ranges between 1 μs and 12 μs. Considering that the mean-first passage time of the cis-trans isomerization (at the present force field) is $\tau = k^{-1} \sim 5 \times 10^4\,\mathrm{s}$, this is a remarkably short simulation time. Using enhanced sampling, reweighting and appropriate rate models, we bridged ten orders of magnitude in time scales from microseconds of total simulation time to hours in molecular process. However, relative to modern computational capabilities, the cost remains significant. At a time step of 2 fs, a simulation time of 1 μs amounts to 500 million force calls, which is currently only feasible for computationally very efficient energy functions.

Since MD simulations for a small molecule in vacuum with an atomistic force field are relatively inexpensive, we sampled generously without optimizing the simulation times. Therefore, the computational costs presented in Tab. III are not a quantitative benchmark, but should be considered as representative examples.

IV. COMPUTATIONAL METHODS

A. One-dimensional model systems

The model free energy functions on the circular reaction coordinate $q \in [-\pi, \pi]$ in Fig. 1.a and 1.b are defined by

$$F(q) = a \cos 2q - b \sin q\,, \tag{24}$$

in units $\mathrm{kJ\,mol^{-1}}$. We set $a = 2.4RT$ and $b = -1\,\mathrm{kJ\,mol^{-1}}$ for Fig. 1.a, and $a = 10.4\,\beta^{-1}\,\mathrm{kJ\,mol^{-1}}$ and $b = -1\,\mathrm{kJ\,mol^{-1}}$ for Fig. 1.b. The free energy function in Fig. 1.c was prescribed by a spline interpolation of a metadynamics profile measured along φ of the retinal system studied in this work.

Numerical simulation was carried out by implementing the ISP integrator[52] for underdamped Langevin dynamics (SI eq. S.7) for a particle with effective mass $m = 1\,\mathrm{amu} \cdot \mathrm{nm}^2 \cdot \mathrm{rad}^{-2}$ and using a time step of $\Delta t = 0.001\,\mathrm{ps}$. The temperature of the system was $T = 300\,\mathrm{K}$, and the gas constant $R = 8.314463\,\mathrm{J\,mol^{-1}\,K^{-1}}$ for all simulations. We varied the value of the friction coefficient ξ in ranges that matched the free energy barrier of the model potentials: Fig. 1.a: $\xi = 0.002\,\mathrm{ps}^{-1}$ to $\xi = 72\,\mathrm{ps}^{-1}$; Fig. 1.b: $\xi = 0.005\,\mathrm{ps}^{-1}$ to $\xi = 150\,\mathrm{ps}^{-1}$; Fig. 1.c: $\xi = 0.02\,\mathrm{ps}^{-1}$ to $\xi = 713\,\mathrm{ps}^{-1}$.

For the model systems in Fig. 1.b and Fig. 1.c, we used infrequent metadynamics [24] to enhance the sampling. For Fig. 1.b, Gaussian bias functions of height $0.1\,\mathrm{kJ\,mol^{-1}}$ and width $0.6\,\mathrm{rad}$ were deposited every 300 time steps (weak friction regime); $0.05\,\mathrm{kJ\,mol^{-1}}$ and width $0.4\,\mathrm{rad}$ every 150 time steps (moderate and high friction regime). For Fig. 1.c, Gaussian bias functions of height $0.8\,\mathrm{kJ\,mol^{-1}}$ and width $0.1\,\mathrm{rad}$ were deposited every 100 time steps (weak friction regime); and of height $0.5\,\mathrm{kJ\,mol^{-1}}$ and width $0.1\,\mathrm{rad}$ every 100 time steps (moderate and high friction regime). Well-tempering has been enforced using a biasing factor of 100. Forces were

calculated by adding the gradient of the free energy profile to the gradient of the biasing potential $U(q,t)$.
The transition rates in Fig. 1.a and Fig. 1.b were estimated by realizing 100 simulations starting at the left minimum $q_A = -1.6\,\text{rad}$ and measuring the first-passage time to reach the barrier at $q_{TS} = 0\,\text{rad}$ or $q_{TS'} = -\pi\,\text{rad}$. The reciprocal of the mean and standard deviation of the first-passage times gives the escape rate with its uncertainty. The transition rates in Fig. 1.b were estimated by the same procedure, but simulations started at $q_A = 0\,\text{rad}$ and stopped at $q_{TS} = 1.6\,\text{rad}$ or $q_{TS'} = -1.6\,\text{rad}$. Transition rates for simple TST formula and Kramers' rate theory in the moderate and high friction limit were calculated by applying of eqs. 8, 13, 14, where ω_A, ω_B or ω_{TS} were calculated from the second derivative of the free energy profile. The integrals in Kramers' rate theory in the weak friction regime (eq. 11) and Pontryagin's rate theory (eq. 16) were evaluated by discretizing the interval $[-\pi, +\pi]$ in 100 subsets of equal length and employing the trapezoidal rule. The same discretization was used for grid-based model (eq. 18).

B. Atomistic model of retinal

Retinal parameters for atomistic force field calculations were taken from DFT studies on the protonated Schiff base[30], adapted to GROMACS format[31], while the connecting amino acid was modelled using the AMBER99SB*-ILDN forcefield[53]. The starting structure was obtained by cutting out the lysine amino acid and retinal cofactor from a recent crystal structure[54]. All simulations are carried out at 300 K in vacuum using stochastic dynamics with GROMACS[55] version 2019.4 built in Langevin integrator with a 2 fs step size and an inverse friction coefficient of 2 ps. For the path collective variables occasionally lower time steps were used. Position restraints of $10000\,\text{kJ}\,\text{mol}^{-1}\text{nm}^{-2}$ were put on all heavy atoms of the peptide chain as well as on the lysine chain carbon atoms (Fig. 2), while the LINCS constraint algorithm[56] was applied to all hydrogen bonds. Before all simulations, energy minimization and NVT equilibration were performed. Metadynamics [39, 40, 57, 58] and umbrella sampling [43] simulations were carried out by plugging PLUMED[25] with GROMACS. Diffusion profiles were calculated by following Ref 27. The reaction coordinate was optimized using the PLUMED implementation of the adaptive path CV method in Ref. 49 in combination with metadynamics. Effective masses of the reactant states were calculated by measuring the average squared velocity along the reaction coordinate and applying eq. 7. Frequencies ω_A, ω_B, ω_{TS} and $\omega_{TS'}$ were calculated from spring constants obtained by harmonically fitting the corresponding wells or barriers. Free energy barriers are measured from the FES directly. One-dimensional rate methods (simple TST, Kramers', Pontryagin) can then be applied straightforwardly. For grid-based methods, 500 cells were used for one-dimensional discretizations, while a discretization of (31,23,23) was used in the 3D CV space (φ,χ_1,χ_2), with χ_1 and χ_2 being discretized in the region between -1 and 1 radians for metadynamics and -0.7 and 0.7 radians for umbrella sampling. Rates from direct numerical simulation were obtained from infrequent metadynamics runs, where acceleration factors were calculated directly by PLUMED. See SI section II A for a complete description of the computational details.

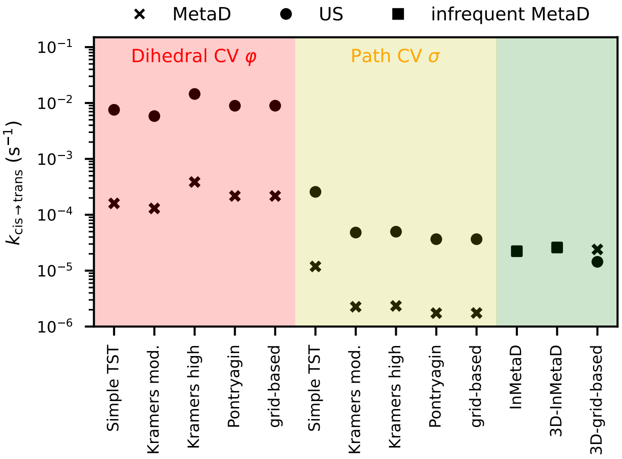

FIG. 5: Rate constants determined through different methodologies for the thermal cis-trans isomerization over the C_{13}=C_{14} double bond in retinal.

V. DISCUSSION AND CONCLUSION

Fig. 5 summarizes the results of this study. For the thermal cis-trans isomerization in retinal, different methods to calculate the rate constant yield drastically different results. Specifically, reaction-coordinate based rate estimates using the torsion angle $q = \varphi$ as an intuitive reaction coordinate differ by about two orders of magnitude from the infrequent metadynamics results, which is based on counting transitions. Furthermore within the reaction-coordinate based estimates, the results are very sensitive to the method of calculating the free energy profile: the results with an umbrella sampling FES differ systematically form those with a metadynamic FES.
These deviations are not primarily caused by a poor choice of the friction regime in the Kramers' rate estimates. For $q = \varphi$ the effective dynamics falls into the intermediate friction regime, but using rate equations for overdamped friction instead changes the rate constant only by about a factor of 2. Thus, for particular choice for calculating $F(q)$, all one-dimensional rate theories yield similar results. The same is true for the optimized reaction coordinate, whose effective dynamics falls into the high friction regime. However, it remains crucial to confirm the friction regime and use the appropriate formula,

because Kramers' rate for high friction scenarios may significantly overestimate the rate constant when applied in the wrong friction regime (Fig. 1).

Optimizing the reaction coordinate lowered the rate estimates of the one-dimensional rate theories by two orders of magnitude compared to $q = \varphi$. These lower rate constants are likely more accurate, since the free energy function of a poor reaction coordinate underestimates the true reaction barrier.

It is surprising at first that, for the cis-trans isomerization, an improved reaction coordinate has such a massive effect on the accuracy of the rate constant. Cis and trans configuration are defined by the torsion angle φ and therefore $q = \varphi$ cleanly separates reactant and product state [22], which is a crucial criterion for an optimal reaction coordinate. However, the optimization of q revealed that the intuitive reaction coordinate fails another important criterion. In the transition state, the optimized reaction coordinate forms a large angle to the intuitive reaction coordinate $q = \varphi$ (Fig. 4.c and d). Consequently, the probability flux across the barrier is nearly orthogonal to $q = \varphi$, rather than parallel as expected for an optimal reaction coordinate[22].

This curvature of the optimal reaction coordinate arises, because at the transition state the C_{13} and C_{14} slightly bend out of plane and thus the reaction coordinate takes a short detour into otherwise rigid degrees of freedoms, namely the improper dihedral angles χ_1 and χ_2. This detour is possible because, at the transition state, the electronic structure changes. In this case, the *p*-orbitals of C_{13} and C_{14} do no longer overlap. This effect is captured by DFT-calculations [2] and reproduced by the empirical force field used in this study.

Since a change in the electronic structure a the transition state is a hallmark of chemical reactions, we suspect that such short detours into orthogonal degrees of freedom (with respect to an intuitive reaction coordinate) will be the rule rather than the exception when modelling chemical reactions. However, finding such a curved optimal reaction coordinate is not trivial, even if an initial reaction coordinate and candidates for further correlated degrees of freedom are known, as in the case of retinal [2, 48]. Besides the path-based method [49] we used in our study, a wide range of other methods to identify optimal reaction coordinates have been proposed [59–61], including recent approaches based on neural networks [62, 63].

An alternative to optimizing the reaction coordinate is to improve the estimate of the rate constant for a sub-optimal reaction coordinate q by including non-Markovian effects into the effective dynamics along q. The corresponding equations are based on the generalized Langevin equation (GLE). Here, non-Markovian behaviour arises from the memory kernel, which is a time-integral over the time-dependent friction coefficient [64–66]. Memory kernels are notoriously hard to predict, but recently multiple methods have emerged to model them[67–69]. In addition, Grote-Hynes theory provides an equation for the memory kernel[8]. The resulting rate equation has the same functional form as Kramers rate equation for the moderate friction regime (eq. 13), where the Markovian friction ξ is replaced by the Laplace transform of the time-dependent friction coefficient[13]. In general, the closer the reaction coordinate follows the probability flux of the reaction, the smaller are the non-Markovian effects[65]. Although non-Markovian rate theories provide accurate rate estimates even for imperfect reaction coordinates, using these suboptimal reaction coordinates risks obscuring important mechanistic details needed for understanding the reaction. For example in retinal, the out-of-plane bending of C_{13} and C_{14} near the transition state is not captured by the initial reaction coordinate $q = \varphi$.

For our system, despite using an optimized reaction coordinate, metadynamics and umbrella sampling produced different free energy barriers, leading to significantly different rate estimates, as shown in Fig. 5. This is likely caused by the strong curvature of the optimized reaction coordinate and might indicate that $q = \sigma_s$ is not yet fully optimal.

Grid-based models in a multidimensional collective variable space offer an alternative to optimizing the one-dimensional reaction coordinate or including memory effects. Using the torsion angle φ and two improper torsion angles at C_{13} and C_{14} as collective variables, we obtained rate estimates that are in very good agreement with the simulation results (Fig. 5). Moreover, for these multidimensional models, the free energy functions derived from metadynamics and umbrella sampling agree, leading to similar rate constants. Multidimensional models have additional advantages: they can be applied to multistate dynamics, do not assume timescale separation, and they yield information on all of the slow processes in the system[33, 34]. The trade-off is the need to estimate a multidimensional free energy surface.

Furthermore, methods that model the reaction rate by envisioning a flux over a dividing surface[70] rather than a maximum in an energy landscape can be considered. In variational transition state theory (VTST), different approaches are used to optimize the dividing surface and minimize the TST reaction rate[6, 7, 71]. The reactive flux method[72], links the flux across a dividing surface to a correlation function which can be estimated from molecular simulations. Modern methods based on this framework include transition path sampling[22, 73], transition interface sampling[74] and forward flux sampling[75].

Our results show that rate constants for chemical reactions can be determined with high accuracy (within the classical approximation) from molecular simulations. The caveat is that the methods need to be carefully chosen for the system at hand. Of the various parameters that influence the rate constant, the curvature of the reaction coordinate at the transition state emerges as the most critical one.

VI. ACKNOWLEDGEMENTS

This research has been funded by Deutsche Forschungsgemeinschaft (DFG) through grant SFB 1114 "Scaling Cascades in Complex Systems" - project number 235221301, as well as by the Cluster of Excellence MATH+, project AA1-15 “Math-powered drug-design”. S.G. acknowledges funding by the Einstein Center of Catalysis/BIG-NSE.

VII. REFERENCES

---

[1] Vitalini, F.; Mey, A. S.; Noé, F. and Keller, B. G., *J. Chem. Phys.*, 2015, **142**(8).
[2] Ghysbrecht, S. and Keller, B. G., *J. Comput. Chem.*, 2024, **45**(16), 1390–1403.
[3] Harvey, J. N.; Himo, F.; Maseras, F. and Perrin, L., *ACS Catal.*, 2019, **9**(8), 6803–6813.
[4] Marx, D. and Hutter, J., *NIC series*, 2000, **1**, 301–449.
[5] Eyring, H., *J. Chem. Phys.*, 1935, **3**(2), 107–115.
[6] Keck, J. C., *J. Chem. Phys.*, 1960, **32**(4), 1035–1050.
[7] Truhlar, D. G. and Garrett, B. C., *Acc. Chem. Res.*, 1980, **13**(12), 440–448.
[8] Grote, R. F. and Hynes, J. T., *J. Chem. Phys.*, 1980, **73**(6), 2715–2732.
[9] Schade, R.; Kenter, T.; Elgabarty, H.; Lass, M.; Kühne, T. D. and Plessl, C., *Int. J. High Perform. Comput. Appl.*, 2023, **37**(5), 530–538.
[10] Gaus, M.; Cui, Q. and Elstner, M., *J. Chem. Theory Comput.*, 2011, **7**(4), 931–948.
[11] Kocer, E.; Ko, T. W. and Behler, J., *Annu. Rev. Phys. Chem.*, 2022, **73**, 163–186.
[12] Noé, F.; Tkatchenko, A.; Müller, K.-R. and Clementi, C., *Annu. Rev. Phys. Chem.*, 2020, **71**, 361–390.
[13] Peters, B., *Reaction Rate Theory and Rare Events*, Elsevier, 1st ed., 2017.
[14] Pietrucci, F., *REVIP*, 2017, **2**, 32–45.
[15] Salvalaglio, M.; Tiwary, P. and Parrinello, M., *J. Chem. Theory Comput.*, 2014, **10**(4), 1420–1425.
[16] Lane, T. J.; Shukla, D.; Beauchamp, K. A. and Pande, V. S., *Curr. Opin. Struct. Biol.*, 2013, **23**(1), 58–65.
[17] Ahmad, K.; Rizzi, A.; Capelli, R.; Mandelli, D.; Lyu, W. and Carloni, P., *Front. mol. biosci.*, 2022, **9**.
[18] Arjun, A. and Bolhuis, P., *J. Phys. Chem. B*, 2020, **125**(1), 338–349.
[19] Borden, W. T., *Wiley Interdiscip. Rev. Comput. Mol. Sci.*, 2016, **6**(1), 20–46.
[20] Zhang, Y.; Wang, Y.; Xu, X.; Chen, Z. and Yang, Y., *J. Chem. Theory Comput.*, 2023, **19**(24), 9358–9368.
[21] Kieninger, S.; Donati, L. and Keller, B. G., *Curr. Opin. Struct. Biol.*, 2020, **61**, 124–131.
[22] Bolhuis, P. G.; Chandler, D.; Dellago, C. and Geissler, P. L., *Annu. Rev. Phys. Chem.*, 2002, **53**(1), 291–318.
[23] Zuckerman, D. M. and Chong, L. T., *Annu. Rev. Biophys.*, 2017, **46**, 43–57.
[24] Tiwary, P. and Parrinello, M., *Phys. Rev. Lett.*, 2013, **111**(23), 230602.
[25] Tribello, G. A.; Bonomi, M.; Branduardi, D.; Camilloni, C. and Bussi, G., *Comput. Phys. Commun.*, 2014, **185**(2), 604–613.
[26] Daldrop, J. O.; Kappler, J.; Brünig, F. N. and Netz, R. R., *PNAS*, 2018, **115**(20), 5169–5174.
[27] Hummer, G., *New J. Phys.*, 2005, **7**(1), 34.
[28] Kramers, H. A., *Physica*, 1940, **7**(4), 284–304.
[29] Hänggi, P.; Talkner, P. and Borkovec, M., *Rev. Mod. Phys.*, 1990, **62**, 251–341.
[30] Hayashi, S.; Tajkhorshid, E. and Schulten, K., *Biophys. J.*, 2002, **83**(3), 1281–1297.
[31] Malmerberg, E.; Omran, Z.; Hub, J. S.; Li, X.; Katona, G.; Westenhoff, S.; Johansson, L. C.; Andersson, M.; Cammarata, M.; Wulff, M. and others, , *Biophys. J.*, 2011, **101**(6), 1345–1353.
[32] Pontryagin, L.; Andronov, A. and Vitt, A., *Zh. Eksp. Teor. Fiz*, 1933, **3**, 165.
[33] Lie, H. C.; Fackeldey, K. and Weber, M., *SIAM. J. Matrix Anal. Appl.*, 2013, **34**, 738–756.
[34] Donati, L.; Weber, M. and Keller, B. G., *J. Phys. Condens. Matter*, 2021, **33**(11), 115902.
[35] Bicout, D. J. and Szabo, A., *J. Chem. Phys.*, 1998, **109**, 10.1063/1.476800.
[36] Heida, M.; Kantner, M. and Stephan, A., *ESAIM: Math. Model. Numer. Anal.*, 2021, **55**(6), 3017–3042.
[37] Berezhkovskii, A. M. and Szabo, A., *J. Chem. Phys.*, 2019, **150**(5), 054106.
[38] Barducci, A.; Bussi, G. and Parrinello, M., *Phys. Rev. Lett.*, 2008, **100**(2), 020603.
[39] Grubmüller, H., *Phys. Rev. E*, 1995, **52**(3), 2893.
[40] Voter, A. F., *Phys. Rev. Lett.*, 1997, **78**(20), 3908.
[41] Tiwary, P. and Berne, B., *J. Chem. Phys.*, 2016, **144**(13), 134103.
[42] Schulten, K. and Hayashi, S. In *Quantum Effects in Biology;* Cambridge University Press, 2014; pages 237–263.
[43] Torrie, G. M. and Valleau, J. P., *J. Comput. Phys.*, 1977, **23**(2), 187–199.
[44] Kumar, S.; Rosenberg, J. M.; Bouzida, D.; Swendsen, R. H. and Kollman, P. A., *J. Comput. Chem.*, 1992, **13**(8), 1011–1021.
[45] Dickson, B. M., *J. Chem. Theory Comput.*, 2018, **15**(1), 78–83.
[46] Khan, S. A.; Dickson, B. M. and Peters, B., *J. Chem. Phys.*, 2020, **153**(5).
[47] Peters, B., *Annu. Rev. Phys. Chem.*, 2016, **67**, 669–690.
[48] Bondar, A.-N.; Knapp-Mohammady, M.; Suhai, S.; Fischer, S. and Smith, J. C., *Theor. Chem. Acc.*, 2011, **130**, 1169–1183.
[49] Leines, G. D. and Ensing, B., *Phys. Rev. Lett.*, 2012, **109**(2), 020601.
[50] Bussi, G. and Tribello, G. A. In *Biomolecular Simulations;* Springer, 2019; pages 529–578.
[51] Laio, A. and Gervasio, F. L., *Rep. Prog. Phys.*, 2008, **71**(12), 126601.
[52] Izaguirre, J. A. .; Schweet, C. R. and Pande, V., *Pac. Symp. Biocomput.*, 2010, **15**, 240–251.
[53] Lindorff-Larsen, K.; Piana, S.; Palmo, K.; Maragakis, P.; Klepeis, J. L.; Dror, R. O. and Shaw, D. E., *Proteins: Struct., Funct., Bioinf.*, 2010, **78**(8), 1950–1958.

[54] Volkov, O.; Kovalev, K.; Polovinkin, V.; Borshchevskiy, V.; Bamann, C.; Astashkin, R.; Marin, E.; Popov, A.; Balandin, T.; Willbold, D. and others, , *Science*, 2017, **358**(6366).

[55] Abraham, M. J.; Murtola, T.; Schulz, R.; Páll, S.; Smith, J. C.; Hess, B. and Lindahl, E., *SoftwareX*, 2015, **1**, 19–25.

[56] Hess, B.; Bekker, H.; Berendsen, H. J. and Fraaije, J. G., *J. Comput. Chem.*, 1997, **18**(12), 1463–1472.

[57] Huber, T.; Torda, A. E. and Van Gunsteren, W. F., *J. Comput. Aided Mol. Des.*, 1994, **8**, 695–708.

[58] Laio, A. and Parrinello, M., *PNAS*, 2002, **99**(20), 12562–12566.

[59] Vanden-Eijnden, E. and others, , *Annu. Rev. Phys. Chem.*, 2010, **61**, 391–420.

[60] Roux, B., *J. Phys. Chem. A*, 2021, **125**(34), 7558–7571.

[61] Palacio-Rodriguez, K. and Pietrucci, F., *J. Chem. Theory Comput.*, 2022, **18**(8), 4639–4648.

[62] Shmilovich, K. and Ferguson, A. L., *J. Phys. Chem. A*, 2023, **127**(15), 3497–3517.

[63] Jung, H.; Covino, R.; Arjun, A.; Leitold, C.; Dellago, C.; Bolhuis, P. G. and Hummer, G., *Nat. Comput. Sci.*, 2023, pages 1–12.

[64] Mori, H., *Prog. Theor. Phys.*, 1965, **33**(3), 423–455.

[65] Zwanzig, R., *Phys. Rev.*, 1961, **124**(4), 983.

[66] Zwanzig, R., *Nonequilibrium statistical mechanics*, Oxford university press, 2001.

[67] Dominic III, A. J.; Cao, S.; Montoya-Castillo, A. and Huang, X., *J. Am. Chem. Soc.*, 2023, **145**(18), 9916–9927.

[68] Vroylandt, H.; Goudenège, L.; Monmarché, P.; Pietrucci, F. and Rotenberg, B., *PNAS*, 2022, **119**(13), e2117586119.

[69] Ayaz, C.; Tepper, L.; Brünig, F. N.; Kappler, J.; Daldrop, J. O. and Netz, R. R., *PNAS*, 2021, **118**(31), e2023856118.

[70] Wigner, E., *Trans. Faraday Soc.*, 1938, **34**, 29–41.

[71] Bao, J. L. and Truhlar, D. G., *Chem. Soc. Rev.*, 2017, **46**(24), 7548–7596.

[72] Chandler, D., *J. Chem. Phys.*, 1978, **68**(6), 2959–2970.

[73] Dellago, C.; Bolhuis, P. G. and Chandler, D., *J. Chem. Phys.*, 1999, **110**(14), 6617–6625.

[74] Van Erp, T. S.; Moroni, D. and Bolhuis, P. G., *J. Chem. Phys.*, 2003, **118**(17), 7762–7774.

[75] Allen, R. J.; Frenkel, D. and Ten Wolde, P. R., *J. Chem. Phys.*, 2006, **124**(19).

Supplementary Information: Accuracy of reaction coordinate based rate theories for modelling chemical reactions: insights from the thermal isomerization in retinal

Simon Ghysbrecht, Luca Donati, and Bettina G. Keller

(Dated: 10 November 2024)

I. EXTENSIONS TO THEORY

A. Effective dynamics

1. One-dimensional reaction coordinates

The effective dynamics of the system along a one-dimensional reaction coordinate q can be modelled by underdamped Langevin dynamics[1]

$$\begin{cases} \dot{q}_t &= \frac{1}{\mu_q} p_t \\ \dot{p}_t &= -\frac{d}{dq} F(q) - \xi p_t + \sqrt{2RT\xi\mu_q}\, \eta_t \, , \end{cases} \tag{S1}$$

where $q_t = q(x_t)$ denotes the position of the system along the reaction coordinate at time t, p_t is the conjugate momentum, μ_q is an effective mass, ξ is the effective friction coefficient or collision frequency (units: [time^{-1}]), and $F(q)$ is the free energy profile defined in eq. 4. As in the main part of the manuscript, the free energies has units of J/mol, and correspondingly the thermal energy is also formulated as a molar quantity RT, where T us the temperature and R is the ideal gas constant. The last term in eq. S1 is the random force, where η_t is a Gaussian white noise with $\langle \eta_t \rangle = 0$ and $\langle \eta_0, \eta_t \rangle = \delta_t$.

Eq. S1 samples the Boltzmann distribution

$$\pi(q, p) = Z_{\mathrm{conf}}^{-1} \exp\left(-\frac{F(q)}{RT}\right) \cdot \sqrt{\frac{1}{2\pi\mu_q RT}} \exp\left(-\frac{1}{2\mu_q RT} p^2\right) . \tag{S2}$$

The first factor is the configurational Boltzmann distribution

$$\pi(q) = Z_{\mathrm{conf}}^{-1} \exp\left(-\frac{F(q)}{RT}\right) \tag{S3}$$

where Z_{conf} the configurational partition function, which normalizes the configurational Boltzmann distribution.

Let us now consider the Langevin equation defined in eq. S1 and assume to have a trajectory realised with a very fine time discretization in Δt timesteps. If we counted the number of collisions between the molecular system and the solvent molecules, whose action is represented by the friction term and the noise term, we would observe few collisions in the time unit Δt. Imagine now to enlarge the time unit Δt by a unitless factor $g > 1$, we would observe more collisions and the time-averaged acceleration over the timestep $g \cdot \Delta t$ would be zero. In other words, by increasing the number of collisions in the unit time, the velocity reaches a steady-state. Then, by coarse-graining the time, the term $\dot{p}_t$ on the left-hand side of the Langevin equation can be deleted. Instead of enlarging the time unit, to increase the number of observed collisions in the unit time, we can act on the parameter ξ, i.e. the friction coefficient. Increasing $\xi \to g \cdot \xi$ is in fact equivalent to increasing the number of collisions in the unit time Δt. This allows us, in a completely equivalent manner, to delete the term on the left-hand side of eq. S1 and write the so-called Langevin equation for the high friction regime:

$$\dot{q}_t = -\frac{1}{\mu_q \xi}\frac{d}{dq}F(q_t) + \sqrt{\frac{2RT}{\xi\mu_q}}\,\eta_t\,. \tag{S4}$$

When modelling rare events and transitions across large free energy barriers, the constant friction ξ is often replaced by a position dependent friction coefficient $\xi(q)$. Eq. S4 can then be written as

$$\dot{q}_t = -\frac{D(q_t)}{RT}\frac{d}{dq}F(q_t) + \frac{d}{dq}D(q_t) + \sqrt{2D(q_t)}\,\eta_t \tag{S5}$$

where we introduced the position dependent diffusion profile $D(q)$ which is defined via the Einstein relation

$$D(q) = \frac{RT}{\mu_q \xi(q)}\,. \tag{S6}$$

Eq. S5 can be derived by applying Ito's formula to a higher-dimensional Langevin equation with constant diffusion. Both eq. S4 and eq. S5 sample the same configurational equilibrium density (eq. S3).

Numerical simulations of the eq. S1 can be realized using the ISP algorithm[2]

$$\begin{cases} v_{k+1} = \exp\left(-\xi\,\Delta t\right)\, v_k \\ \qquad\qquad - \left[1 - \exp\left(-\xi\,\Delta t\right)\right]\dfrac{\nabla F(q_k)}{\xi m} \\ \qquad\qquad + \sqrt{\dfrac{RT}{m}\left[1 - \exp\left(-2\xi\,\Delta t\right)\right]}\,\eta_k \\ q_{k+1} = q_k + v_{k+1}\Delta t \end{cases} \tag{S7}$$

where q_k and v_k denote respectively the position and the velocity of the particle at time t_k, $\Delta t = t_{k+1} - t_k = 0.001\,\mathrm{ps}^{-1}$ is the integrator time step, and η_k are independent and uncorrelated random numbers drawn from a standard Gaussian distribution.

2. Multidimensional collective variables

The effective dynamics in this m-dimensional collective variable space can be modelled as overdamped Langevin dynamics with position dependent diffusion.

$$\dot{\mathbf{q}}_t = -\frac{1}{RT}D(\mathbf{q}_t)\nabla F(\mathbf{q}_t) + \nabla \cdot D(\mathbf{q}_t) + \sqrt{2D(\mathbf{q}_t)}\boldsymbol{\eta}_t\,, \tag{S8}$$

where $\nabla = (\partial/\partial q_1, \ldots \partial/\partial q_m)^\top$ is the gradient with respect to $\mathbf{q}$, $\boldsymbol{\eta}_t$ is a m-dimensional Gaussian white noise with $\langle \boldsymbol{\eta}_t \rangle = \mathbf{0}$ and $\langle \boldsymbol{\eta}_0,\, \boldsymbol{\eta}_t \rangle = \delta_t$. $D(\mathbf{q})$ is a $m \times m$ diagonal matrix whose ith element represents the diffusion profile along the ith collective variable.

3. White noise vs. Wiener process

Eq. S1 contains η_t as a symbol for a Gaussian white noise. The use of a white noise process is problematic, because it does not have a clear physical interpretation. Formally, one can define η as the time derivative of a Wiener process W_t, i.e. $\eta_t = \dot{W}_t$. Unfortunately, the Wiener process is not differentiable and the derivative is only defined in a finite difference sense $\dot{W}_t \approx (W_{t+h} - W_t)/h$, for small time increments h. A mathematically more rigorous way to formulate eq. S1 is to use increments of the Wiener process rather than time derivatives:

$$\begin{cases} dq_t &= \frac{1}{\mu_p} p_t dt \\ dp_t &= -\frac{d}{dq} F(q) dt - \xi p_t dt + \sqrt{2RT\xi\mu_p}\, dW_t \,. \end{cases} \tag{S9}$$

The same discussion applies to eqs. S4, S5 and S8.

4. Fokker-Planck equations

Associated to each of the stochastic equations of motion (eqs. S1, S4, S5 and S8) there exists a Fokker-Planck equation. The Fokker-Planck equation is a deterministic partial differential equation which describes how the probability density $\rho(p, q, t)$, for eq. S1, or $\rho(q, t)$, for eqs. S4 and S5, or $\rho(\mathbf{q}, t)$ for eq. S8 evolves with time:

$$\frac{\partial}{\partial t}\rho(t) = \mathcal{Q}\rho(t) \,. \tag{S10}$$

$\mathcal{Q}$ is Fokker-Planck operator.

The Fokker-Planck equation for underdamped Langevin dynamics (eq. S1) is called Klein-Kramers equation and $\mathcal{Q}$ is given as

$$\mathcal{Q} = -\frac{p}{m}\frac{\partial}{\partial q} + \xi m \frac{\partial}{\partial p}\left(\frac{p}{m} + RT\frac{\partial}{\partial p}\right) + \frac{\partial F(q)}{\partial q}\frac{\partial}{\partial p} \tag{S11}$$

The Fokker-Planck equation for overdamped Langevin dynamics (eq. S4) is called Smoluchowski equation. $\mathcal{Q}$ given as

$$\mathcal{Q} = D\frac{\partial^2}{\partial q^2} + \xi^{-1} m^{-1} \frac{\partial}{\partial q}\frac{\partial F(q)}{\partial q} \tag{S12}$$

The Fokker-Planck operator for overdamped Langevin dynamics with position dependent diffusion (eq. S4) is

$$\mathcal{Q} = \frac{\partial^2}{\partial q^2} D(q) + \frac{\partial}{\partial q}\left(\beta D(q)\frac{\partial F(q)}{\partial q} - \frac{\partial D(q)}{\partial q}\right) \tag{S13}$$

$$= \frac{\partial}{\partial q} D(q) e^{-\beta F(q)} \frac{\partial}{\partial q} e^{\beta F(q)} \,. \tag{S14}$$

The Fokker-Planck equation for overdamped Langevin dynamics with position dependent diffusion in a multidimensional space (eq. S8) is given as

$$\mathcal{Q} = \nabla \cdot D(\mathbf{q}) e^{-\beta F(\mathbf{q})} \nabla e^{\beta F(\mathbf{q})} \tag{S15}$$

(if $D(\mathbf{q})$ is a diagonal matrix).

We used the following convention to denote differential operators: derivatives written as operators ($\frac{\partial}{\partial q}, \frac{\partial}{\partial p}, \frac{\partial^2}{\partial q^2}$ and ∇) should be applied to anything that follows behind it, while derivatives written as functions ($\frac{\partial F(q)}{\partial q}$ and $\frac{\partial D(q)}{\partial q}$) should be considered stand-alone functions, i.e. the derivative only applies to the function ($F(q)$ or $D(q)$ respectively) directly and not what comes after it.

B. Simple transition state theory

In simple TST[3,4] one defines the transition state TS as a point q_{TS} along the reaction coordinate that separates reactant state A ($q < q_{TS}$) and product state B ($q > q_{TS}$). In the full dimensional configurational space Γ_x, this point corresponds to an isosurface on which the value of the reaction coordinate is constant. Using the Dirac delta function, the surface is defined by $\delta\left(q(\mathbf{x}) - q_{TS}\right)$ and separates the reactant configurations from the product configurations. The TST rate constant is derived from the one-directional flux across the dividing surface assuming the reactant and transition state are in equilibrium[4,5]:

$$k_{AB} = \kappa \cdot \frac{1}{2}\left\langle |\dot{q}| \right\rangle_{TS} \cdot l_q^{-1} \exp\left(-\frac{F(q_{TS}) - F_A}{RT}\right) . \tag{S16}$$

The variable

$$F_A = -RT \ln\left(l_q^{-1} \int_A \mathrm{d}q \exp\left(\frac{-F(q)}{RT}\right)\right) \tag{S17}$$

denotes the free energy of the entire reactant state, not just its minimum. The factor $l_q^{-1} \exp\left(-\frac{F(q_{TS})-F_A}{RT}\right)$ in eq. S16 is the relative probability density of finding the system at the transition state, where l_q is the unit of length along coordinate q. The factor $\langle |\dot{q}| \rangle_{TS}$ is the averaged absolute velocity along q at the transition state TS. The factor $1/2$ accounts for the fact that only half of all systems in an ensemble move in the forward direction. κ is again the transmission factor to correct for the fact that in reality not all systems that cross the dividing surface proceed to state B, but instead revert to A (recrossing).

Since transition state theory assumes the transition state to be in thermal equilibrium with the reactant state, the absolute velocity $|\dot{q}|$ can be averaged using the Maxwell-Boltzmann distribution, giving $\langle |\dot{q}| \rangle_{TS} = \sqrt{\frac{2RT}{\pi \mu_q}}$, where μ_q is the effective mass. Furthermore, the reactant state A can be approximated by a harmonic potential around the reactant state minimum q_A,

$$F(q) = F(q_A) + \frac{1}{2}\mu_q \omega_A^2 (q - q_A)^2 \quad \text{if} \quad q \approx q_A\,, \tag{S18}$$

where ω_A is the angular frequency associated to harmonic approximation, μ_q the reduced mass, and $F(q_A)$ is the free energy at the minimum of the reactant state. Carrying out the integral in eq. S17 for eq. S18 and inserting the and the result for $\langle |\dot{q}| \rangle_{TS}$ into eq. S16 yields

$$k_{AB} = \kappa \cdot \frac{\omega_A}{2\pi} \exp\left(-\frac{F_{AB}^{\ddagger}}{RT}\right) . \tag{S19}$$

In Ref. 4, eq. S16 is called the generalized TST approach, and eq. S19 is called one-dimensional Vineyard TST[6]. In this work, we follow Ref. 3 where the result in eq. S19 is called simple transition state theory.

C. Kramers' rate theory: from moderate to high friction

In the main part of the article, eq. 14 is derived from eq. 13 as follows:

$$\begin{aligned}
\frac{\xi}{\omega_{TS}}\left(\sqrt{\frac{1}{4} + \frac{\omega_{TS}^2}{\xi^2}} - \frac{1}{2}\right) &= \frac{\xi}{\omega_{TS}}\left(\sqrt{\frac{1}{4}}\sqrt{1 + 4\frac{\omega_{TS}^2}{\xi^2}} - \frac{1}{2}\right) \\
&\approx \frac{\xi}{\omega_{TS}}\left(\frac{1}{2}\left(1 + \frac{1}{2}4\frac{\omega_{TS}^2}{\xi^2}\right) - \frac{1}{2}\right) \\
&= \frac{\xi}{\omega_{TS}}\left(\frac{1}{2} + \frac{\omega_{TS}^2}{\xi^2} - \frac{1}{2}\right) \\
&= \frac{\omega_{TS}}{\xi}\,,
\end{aligned} \tag{S20}$$

where in the second line, we approximated the square-root by a power series

$$\sqrt{1+a} = 1 + \frac{1}{2}a - \frac{1}{8}a^2 + \frac{1}{16}a^3 - \frac{5}{128}a^4 + \dots \qquad |a| \leq 1 \tag{S21}$$

with $a = 4\omega_{TS}^2/\xi^2$, and truncated after the second term.

II. COMPUTATIONAL DETAILS

A. Classical MD with atomistic force field

1. Dynamics

Retinal parameters for atomistic force field calculations were taken from DFT studies on the protonated Schiff base[7–9], adapted to GROMACS format[10], while the connecting amino acid was modelled using the AMBER99SB*-ILDN forcefield[11]. The starting structure was obtained by cutting out the lysine amino acid and retinal cofactor from a recent crystal structure[12], while the ends of the lysine were capped with methyl groups as shown in Fig. 2.

All simulations are carried out at 300 K in vacuum and are done using stochastic dynamics with GROMACS[13,14] version 2019.4 built in Langevin integrator with a 2 fs timestep and an inverse friction coefficient of 2 ps, except when using path collective variables, where, when explicitly mentioned, lower time steps were used. Strong position restraints of 10000 kJ mol^{-1}nm^{-2} were put on all heavy atoms of the peptide chain as well as on the lysine chain carbon atoms (Fig. 2), while the LINCS constraint algorithm was applied to all hydrogen bonds. Before all simulations, energy minimization and NVT equilibration were performed.

2. Free energy and diffusion constant calculation along φ

As initial reaction coordinate for the one-dimensional rate models, we choose the dihedral angle φ constituted by the retinal chain atoms C$_{12}$-C$_{13}$=C$_{14}$-C$_{15}$. For four atoms with indices i, j, k and l, the vectors connecting the atoms are $\mathbf{r}_{ji} = \mathbf{r}_j - \mathbf{r}_i$, $\mathbf{r}_{kj} = \mathbf{r}_k - \mathbf{r}_j$ and $\mathbf{r}_{lk} = \mathbf{r}_l - \mathbf{r}_k$. The general dihedral angle φ is then defined[15,16] by the angle between two planes, one constituted by vectors $\mathbf{r}_{ji}$ and $\mathbf{r}_{kj}$ and the other constituted by vectors $\mathbf{r}_{kj}$ and $\mathbf{r}_{lk}$:

$$\cos\varphi = \frac{(\mathbf{r}_{ji} \times \mathbf{r}_{kj}) \cdot (\mathbf{r}_{kj} \times \mathbf{r}_{lk})}{|\mathbf{r}_{ji} \times \mathbf{r}_{kj}|\, |\mathbf{r}_{kj} \times \mathbf{r}_{lk}|} \tag{S22a}$$

$$\sin\varphi = \frac{[(\mathbf{r}_{ji} \times \mathbf{r}_{kj}) \times (\mathbf{r}_{kj} \times \mathbf{r}_{lk})] \cdot \mathbf{r}_{kj}}{|\mathbf{r}_{kj}|\, |\mathbf{r}_{ji} \times \mathbf{r}_{kj}|\, |\mathbf{r}_{kj} \times \mathbf{r}_{lk}|}\,. \tag{S22b}$$

The torsion angle can be obtained using the atan2 function[17]:

$$\begin{aligned}\varphi = \operatorname{atan2}\big(&- [(\mathbf{r}_{kj} \times \mathbf{r}_{ji}) \times (\mathbf{r}_{lk} \times \mathbf{r}_{kj})] \cdot \mathbf{r}_{kj}\,, \\ &|\mathbf{r}_{kj}|\, (\mathbf{r}_{ji} \times \mathbf{r}_{kj}) \cdot (\mathbf{r}_{kj} \times \mathbf{r}_{lk})\big)\,.\end{aligned} \tag{S23}$$

This implies a certain convention with regards to the sign and phase of φ. In general, φ is zero for the case where the the dihedral corresponds to a cis/syn state, and $\pm\pi$ when the dihedral corresponds to a anti/trans state. Increasing values of φ correspond to a clockwise rotation of the plane constituted by vectors $\mathbf{r}_{kj}$ and $\mathbf{r}_{lk}$ with regards to the plane constituted by vectors $\mathbf{r}_{ji}$ and $\mathbf{r}_{kj}$ when looking along the $\mathbf{r}_{kj}$ vector, i.e. similar to conventions in stereochemistry[15]. For the case of retinal in Fig. 2, the dihedral angle φ is defined by matching indices i, j, k and l with atoms C$_{12}$, C$_{13}$, C$_{14}$ and C$_{15}$ respectively.

Metadynamics (MetaD) and umbrella sampling (US) were carried out by plugging PLUMED[18–20] with the GROMACS software package[13,14]. Before production runs, the model system was energy minimized and NVT equilibrated over 400 ps. Subsequently, 2 μs of well-tempered metadynamics[21] were run biasing φ at a pace of 1 ps using Gaussians with a height of 1.2 kJ mol^{-1}, a standard deviation of 0.05 radians while the bias factor was 10. Unbiasing weights for the trajectory were calculated using the bias potential obtained at the end as described in Ref. 22. Free energy surfaces can then be calculated after building a weighted histogram from the trajectory starting at a simulation time where the bias can be considered converged. On account of the large simulation time, there is no significant change in the free energy profile depending on whether we build the histogram on the full trajectory or only after a certain time at which we consider the bias converged. There was also no considerable difference when calculating FES after reweighting with a time-dependent bias as in Refs. 23 and 24, and FES from reweighted trajectories were always close to the free energy estimated from the upside-down bias potential $F(\varphi) = -\frac{\gamma}{\gamma-1}V_b(\varphi)$, where $V_b(\varphi)$ is the biasing potential at the end of the well-tempered metadynamics simulation[21], and γ is the bias factor[25,26].

Monitoring the evolution of the metadynamics simulations can be done by following the free energy difference ΔF between the trans and cis state as estimated from the upside-down bias potential as a function of simulation time as in Fig. S.10.a. See SI section III B below for more details. It is apparent from the oscillating free energy differences that the biasing potentials are still undergoing changes with time. Consequently, dynamics along the dihedral angle do not reach a point of being completely diffusive, which is a first indication of hidden motion not being included in the collective variable used here, i.e. the dihedral angle φ.

To test the sensitivity of metadynamics to the width of the deposited Gaussians, additional sets of simulations were performed using the same simulation and metadynamics parameters as before but changing the standard deviation of the deposited Gaussians. The resulting free energy profiles can be seen in Fig. S.11.b. The free energy surfaces appear to have a small dependency on the width of the Gaussians used, which can in part be explained by the biasing potentials still evolving due to hidden motion as explained above. That being said, Gaussians of standard deviation 0.17 radians seem too wide for accurately reweighting the shapes of barrier peaks and reactant wells.

Error estimates for free energy profiles obtained from metadynamics reweighting can be determined using the block analysis technique[27] on the reweighted trajectory. To check convergence of the free energy profile, one commonly plots the average error as a function of block size. Because data from an MD trajectory are generally correlated, the average error will be underestimated for small block sizes in which case the error analysis of the free energy profile will not represent an accurate evaluation of the quality of the free energy surface. When sufficiently large blocks are used, the average error will converge to a plateau value suggesting the data has decorrelated and indicating the error analysis can now be trusted. In cases where the average error does not converge even for very large block sizes, correlated effects should be considered too strong and the trajectory too short to truthfully capture them, and thus the accuracy of the computed free energy surface and its error analysis can be questioned. Block analysis was carried out using the example code on the PLUMED website[27]. Average errors of the energy profile as a function of block size are shown for different metadynamics simulations in Fig. S.10.a. The average errors appear to be converging for large block sizes. Notice that FES could still depend on the parameters chosen for the metadynamics simulations, and errors are only estimated within a certain parameter set.

Umbrella sampling was carried out by running 83 trajectories of 12 ns for a total of 996 ns of simulation time. Each trajectory was restrained with a harmonic potential of spring constant $400\,\mathrm{kJ\,mol^{-1}\,rad^{-2}}$ at different values of φ:

- 63 umbrellas were positioned at regular 0.1 radian intervals between -3.1 and 3.1 radians
- 10 umbrellas were positioned at regular 0.1 radian intervals between -1.95 and -1.05 radians
- 10 umbrellas were positioned at regular 0.1 radian intervals between 1.05 and 1.95 radians.

For each trajectory, a two step equilibration procedure was carried out before each production runs. First, a 20 ps NVT equilibration was carried out at a lower spring constant of $100\,\mathrm{kJ\,mol^{-1}\,rad^{-2}}$ starting from an energy minimized structure. Second, another 20 ps NVT equilibration was carried out at the same spring constant of the production runs, i.e. at $400\,\mathrm{kJ\,mol^{-1}\,rad^{-2}}$. In this way, the production runs start from configurations which can be considered equilibrated within their respective umbrella sampling restraints.

From the umbrella sampling trajectories, binless WHAM[27,28] was used to reconstruct the free energy profile. For each trajectory, a value for the diffusion coefficient was calculated using Hummer's formulation of position dependent diffusion coefficients[29]:

$$D(\varphi = \langle\varphi\rangle) = \frac{\mathrm{var}(\varphi)}{\tau_\varphi} \tag{S24}$$

where $\tau_\varphi = \int_0^\infty \langle\delta\varphi(t)\delta\varphi(0)\rangle\,\mathrm{d}t/\mathrm{var}(\varphi)$ with $\delta\varphi(t) = \varphi(t) - \langle\varphi\rangle$. The diffusion coefficient as a continuous function of φ was obtained using cubic spline interpolation on all resulting diffusion data points excluding data points near the transition state where Hummer's formula cannot be applied directly and the diffusion coefficient is underestimated. Accordingly, all data points with values under $0.4\,\mathrm{rad^2/ps}$ were ignored for interpolation. The corresponding profiles can be found in Fig. 3 as well as in Fig. S.11.c under the label *set1*. Additional sets have been run and are also shown:

- *set2* has the same parameter setup as *set1*.
- For *set3*, 125 trajectories of 12 ns were run with harmonic spring constant $750\,\mathrm{kJ\,mol^{-1}rad^{-2}}$ positioned in 0.05 rad intervals between -3.1 and 3.1 rad.

Computation of the reweighted histograms was done applying kernel density estimation (KDE) with Gaussian kernels of bandwidth 0.01 radians for all metadynamics runs as well as for umbrella sampling sets *set1* and *set2*. For umbrella sampling set *set3*, it turned out to be challenging to find a good choice of bandwidth for KDE, and therefore conventional discrete histograms were utilized instead.

Error estimates for the free energy profiles obtained from umbrella sampling can be computed using the bootstrapping method[30]. For each umbrella, the trajectory was split in 20 blocks of equal length. A 'new' trajectory of the same length as the original is then constructed by taking combinations of these 20 blocks with the possibility of repetition. After doing this for all umbrellas, the free energy surface is recalculated using WHAM. This procedure is repeated 200 times, producing 200 free energy surfaces which allows calculation of standard deviations which can be shown to be good estimates of standard errors on the free energy surface[31]. Notice the standard errors might be underestimated because of correlations between blocks within each trajectory[32]. Free energy and diffusion profiles including error estimates for all umbrella sampling sets can be found in Fig. S.11.c.

3. Rate calculations along dihedral reaction coordinate

Rates along the φ reaction coordinate were calculated using the free energy profiles in Fig. 3, both for metadynamics ($\sigma = 0.05$ rad and umbrella sampling (*set1*), see Tab. II. Diffusion coefficients were taken from the diffusion profile from umbrella sampling *set1*.

Free energy barriers $F^\ddagger$ were measured directly from the free energy profile by subtracting the minimum free energy value at the reactant side of the isomerization under consideration from the maximum value at the corresponding peak. Notice we denote the peak at negative φ as TS and the peak at positive φ as TS', similar as in Fig. 1.e. In this fashion, four energy barriers per free energy surface $F^\ddagger_{\mathrm{t}\to\mathrm{c},TS}$, $F^\ddagger_{\mathrm{t}\to\mathrm{c},TS'}$, $F^\ddagger_{\mathrm{c}\to\mathrm{t},TS}$ and $F^\ddagger_{\mathrm{c}\to\mathrm{t},TS'}$ are obtained. Masses in reduced dimensions for reactant states μ_{trans} and μ_{cis} were calculated by running unbiased 12 ns runs in the corresponding states, calculating the average kinetic energy in the reduced dimension (i.e. the dihedral angle) and comparing to temperature using the equipartition theorem

$$\mu_A = \frac{k_B T}{\langle v_\varphi^2\rangle_A} \tag{S25}$$

similar as in Ref. 33. In principle, applying the equipartition theorem here is an approximation, since it cannot be used for collective variables obtained from nonlinear transformations of Cartesian coordinates. Since the free energy surface is nearly harmonic at the reactants states, however, we expect it to be a good approximation. The reactant state dihedral velocities ω_A (where A denotes cis or trans) can then be calculating using

$$\omega_A = \sqrt{\frac{\kappa_A}{\mu_A}} \tag{S26}$$

where spring constant κ_A is obtained by fitting the free energy surface to a harmonic potential $\frac{1}{2}\kappa_A(\varphi - \varphi_A)^2$ where φ_A corresponds to the free energy minimum at the corresponding reactant state A. Fits for the trans and cis free energy wells show close agreement with harmonic potentials at the bottom, which validates the harmonic assumptions of the reactant and product states in the formulations for simple TST and Kramers' equations (eqs. 8, 11, 13 and 14). Alternatively, one can calculate a period T_A from the unbiased trajectories by choosing two cutoff values for φ above and below its value for minimal free energy (e.g. above and below approximately zero radians for the cis state) and by counting transitions of the trajectory dihedral angle between these cutoffs as a function of time. Angular velocities calculated from this period $\omega_A = 2\pi/T_A$ gave similar results to the ones obtained from the harmonic fit in combination with the equipartition theorem above. Given the free energy barrier heights and the reactant state angular frequency, simple TST rates can be calculated directly for each barrier using eq. 8. Notice that calculating reaction constants for full processes requires taking into account transitions over both peaks:

$$k_{\text{trans}\to\text{cis}} = k_{\text{t}\to\text{c},TS} + k_{\text{t}\to\text{c},TS'} \tag{S27a}$$

$$k_{\text{cis}\to\text{trans}} = k_{\text{c}\to\text{t},TS} + k_{\text{c}\to\text{t},TS'}\,. \tag{S27b}$$

In order to calculate Kramers' rate in the moderate-to-high friction limit as in eq. 13 or in the high friction limit as in eq. 14, the friction coefficient at the barrier top can be calculated directly from the diffusion profile using:

$$\xi_{TS} = \frac{k_B T}{\mu_{TS} D_{TS}} \tag{S28}$$

where $D_{TS} = D(\varphi_{TS})$ is the value of the diffusion coefficient at the barrier top taken from the spline interpolation and μ_{TS} has been approximated by averaging μ_{cis} and μ_{trans}. The angular frequency at the barrier top ω_{TS} has been calculated in a similar way as at the reactant states using:

$$\omega_{TS} = \sqrt{\frac{\kappa_{TS}}{\mu_{TS}}} \tag{S29}$$

where κ_{TS} was obtained using a parabolic fit to the free energy surface at the barrier top. An identical analysis can be done to obtain the friction coefficient $\xi_{TS'}$ at the other barrier TS'. Again, total rates are obtained by summing rates for both barriers as in eqs. S27.

Calculating isomerization rates over a specific barrier using the Pontryagin equation (eq. 16) was done by nested integration using the calculated free energy profile from MetaD or US as well as the position dependent diffusion from eq. S24. Here, the inner integral was carried out from the barrier peak on the other side of the reactant state. Again, rates over individual barriers were combined to describe full thermal isomerization rates using eqs. S27.

Rates from grid-based models were calculated by discretizing the dihedral CV φ in 500 cells of equal size and building the rate matrix according to eq. 19. For each cell i with cell middle φ_i, the population $\pi_i = \pi(\varphi_i)$ was determined by using spline interpolation of the free energy surface as obtained from metadynamics or US, evaluating at $\varphi = \varphi_i$ and applying eq. 5. In principle, populations π_i need not be normalized since only ratios appear in eq. 19. The values for the diffusion coefficient $D(\varphi_i)$ were similarly obtained by spline interpolation of the results from application of eq. S24 to the US trajectories and evaluating at the cell middles. For the very high barriers we are dealing with, populations π_i in cells near the barrier can get very small, and high precision numbers need to be used in the construction of the rate matrix. The mpmath[34] python package was used to administer arbitrary precision in building the rate matrix, and the FLINT[35] python package was used to solve for the mean first-passage times in eq. 20. A precision of 50 digits was used for these calculations. The initial conditions are enforced by setting $\mathbf{1}[j] = 0$ and adapting the rate matrix $\mathbf{Q}[j,:] = 0$ and $\mathbf{Q}[j,j] = -1$ for all $j \in B$.

4. Infrequent Metadynamics

Infrequent metadynamics (InMetaD) were run for both the trans-cis and cis-trans transition in sets of 30 runs and fitted to a Poisson distributions[36] as described in the Theory section (eq. 22). Biasing was done on the $C_{13}{=}C_{14}$ dihedral CV φ at a pace of 100 ps with a Gaussian height of $1.2\,\mathrm{kJ\,mol^{-1}}$, standard deviation of 0.05 rad and bias factor of 16. Trajectories for runs from trans to cis were terminated once a value (in radians) of $\varphi \in [-\pi/5, \pi/5]$ was reached, where the molecule is definitely in the cis state. The biased transition time $\tau^{\mathrm{InMetaD}}_{\mathrm{t}\to\mathrm{c},i}$ was then taken to be the time of the last trajectory point where the configuration can still be considered at the trans side, i.e. the last trajectory point where $\varphi < -\pi/2$ or $\varphi > \pi/2$. The unbiased transition times $\tau_{\mathrm{t}\to\mathrm{c},i}$ can then be calculated from eq. 23. Trajectories for runs from cis to trans were stopped once a value of $\varphi < -1.9$ rad or $\varphi > 1.9$ rad was reached, where the molecule is definitely in the trans state. The biased transition time $\tau^{\mathrm{InMetaD}}_{\mathrm{c}\to\mathrm{t},i}$ was then taken to be the time of the last trajectory point where the configuration can still be considered at the cis side, i.e. the last trajectory point where $\varphi \in [-\pi/2, \pi/2]$, and unbiased transition times $\tau_{\mathrm{c}\to\mathrm{t},i}$ can be calculated from eq. 23.

KS tests were done using using a million randomly generated points according to the corresponding TCDF (eq. 22) for both trans-cis and cis-trans transitions, yielding a p-value of 0.95 and 0.74 respectively, which is well above the proposed cutoff of 0.05. A graphical representation of the TCDF fit and KS test as well as the biased potential at the moment of the transitioning for example runs can be found in Fig. S.4. Average transition times, standard errors, Poisson fitted transition times and corresponding p-values can be found in Tab. S.5.

5. Multidimensional Free Energy and Diffusion surfaces

Multidimensional free energy surfaces were calculated from multidimensional metadynamics simulations implemented using a similar setup as for the one-dimensional case. Well-tempered metadynamics were run biasing the three-dimensional space spanned by the following collective variables:

- φ: $C_{13}{=}C_{14}$ dihedral angle
- χ_1: improper dihedral constituting the out of plane bending of the carbon atom of the methyl group on the C_{13} atom
- χ_2: improper dihedral constituting the out of plane bending of the hydrogen on the C_{14} atom.

See eqs. S22-S23 for a mathematical definition. Three-dimensional Gaussians of width 0.07 rad in each CV were deposited at a pace of 1 ps and with a bias factor of 12. In this case, metadynamics were only carried out for 1 μs because the retinal cofactor was noticed to collapse upon the lysine backbone for larger simulation times. Since such configurations were not observed during one-dimensional metadynamics or umbrella sampling, and we are not interested in them from a conceptual point of view, the trajectory was cut before they appear, i.e. after 1 μs. The three-dimensional free energy surface $F(\varphi, \chi_1, \chi_2)$ was calculated by building a three-dimensional histogram from trajectory data and reweighting using the bias obtained at the end of the metadynamics simulation. Equivalently, two-dimensional free energy surfaces $F(\varphi, \chi_1)$ and $F(\varphi, \chi_2)$ (Fig. 4.b and d) and one-dimensional free energy surface $F(\varphi)$ (Fig. 3) can be computed by reweighting two- and one-dimensional histograms respectively, using the same trajectory data and bias. Convergence of the bias and block error analysis are shown in Fig. S.10.b.

Multidimensional diffusion surfaces D_φ, D_{χ_1} and D_{χ_2} were computed by applying a multidimensional generalization of Hummer's formulation in eq. S24. In our three-dimensional case, a series of trajectories are run with three-dimensional harmonic restraints positioned on a regular grid in collective variable space. For each trajectory, one value for each of the diffusion coefficients D_φ, D_{χ_1} and D_{χ_2} can then be calculated by computing correlation functions in each direction (eq. S24). Additionally their corresponding average positions $\langle\varphi\rangle$, $\langle\chi_1\rangle$ and $\langle\chi_2\rangle$ are computed, yielding a three-dimensional 'grid' (which now might be irregular) in collective variable space, with for each point an associated value for D_φ, D_{χ_1} and D_{χ_2}. Diffusion surfaces $D_\varphi(\varphi, \chi_1, \chi_2)$, $D_{\chi_1}(\varphi, \chi_1, \chi_2)$ and $D_{\chi_2}(\varphi, \chi_1, \chi_2)$ can then be obtained by three-dimensional interpolation.

In this fashion, two sets of diffusion profiles in each direction were calculated using different grids and different spring constants for the harmonic restraints. We will refer to the sets as *grid1* and *grid2*.

For *grid1*, 200 trajectories of 5 ns were run employing three-dimensional harmonic restraints with 400 $\mathrm{kJ\,mol^{-1}\,rad^{-2}}$ spring constants in each direction, positioned on a regular $8 \times 5 \times 5$ grid in CV space as follows:

- φ varies over 8 steps in regular intervals from $-\pi$ to π
- χ_1 varies over 5 steps in regular intervals from -0.5 to 0.5
- χ_2 varies over 5 steps in regular intervals from -0.5 to 0.5.

Two-dimensional cuts of the resulting three-dimensional diffusion surfaces are shown in Fig. S.13.

For *grid2*, 729 trajectories of 2 ns were run employing three-dimensional harmonic restraints with 600 $\mathrm{kJ\,mol^{-1}\,rad^{-2}}$ spring constants in each direction, positioned on a regular $9 \times 9 \times 9$ grid in CV space as follows:

- φ varies over 9 steps in regular intervals from $-\pi$ to π
- χ_1 varies over 9 steps in regular intervals from -1 to 1
- χ_2 varies over 9 steps in regular intervals from -1 to 1.

Two-dimensional cuts of the resulting three-dimensional diffusion surfaces are shown in Fig. S.14.

Multidimensional US simulations were performed by running 5 ns trajectories on a total of 784 three-dimensional harmonic restraints, positioned on a three-dimensional grid in $(\varphi, \chi_1, \chi_2)$. The harmonic restraints had spring constants of 400 $\mathrm{kJ\,mol^{-1}}$ in φ directions and 300 $\mathrm{kJ\,mol^{-1}}$ in both χ_1 and χ_2 directions, and were positioned as follows:

- φ varies over 16 steps in regular intervals from $-\pi$ to π
- χ_1 varies over 7 steps in regular intervals from -1 to 1
- χ_2 varies over 7 steps in regular intervals from -1 to 1.

We will refer to this grid as *grid3*. While *grid1* and *grid2* were exclusively used for calculations of position dependent diffusion profiles, *grid3* was exclusively used for construction of a three-dimensional free energy surface $F(\varphi, \chi_1, \chi_2)$. This was done employing binless WHAM[27,28].

6. Adaptive Path Collective Variables

For a more accurate description of the dynamics, we aim to find a path CV description of the thermal isomerization in the space spanned by the φ, χ_1 and χ_2 CVs. Paths have been optimized using the adaptive path collective variable method[37,38] implemented in PLUMED under the ADAPTIVE_PATH module in combination with well-tempered metadynamics. In order to correctly handle the periodicity of φ, the sine and cosine were used rather than including the angle directly. In order to avoid differences in scale of the CVs[38,39], we have also taken the sines of the improper dihedrals. Notice that in this case we do not have to include the corresponding cosines as the range of interest of the improper dihedrals doesn't warrant it. Thus, in practice, the adaptive path CV algorithm was performed in four dimensions:

- sin_phi: sine of φ
- cos_phi: cosine of φ
- sin_improper1: sine of χ_1
- sin_improper2: sine of χ_2.

Although in principle cyclic paths can be handled with the adaptive path CV scheme[39], we have chosen to study each transition separately, i.e. we optimized the *cis_trans1*, *cis_trans2*, *trans_cis1* and *trans_cis2* paths in separate runs.

- *trans_cis1* describes trans-cis isomerization in counterclockwise direction (increasing torsion angle)
- *trans_cis2* describes trans-cis isomerization in clockwise direction (decreasing torsion angle).
- *cis_trans1* describes cis-trans isomerization in counterclockwise direction (increasing torsion angle)
- *cis_trans2* describes cis-trans isomerization in clockwise direction (decreasing torsion angle)

The initial and final states for each path, which are kept fixed during the adaptive path CV algorithm, have been chosen as 0 or $\pm\pi$ rad depending on the transition under consideration. As initial guess paths, linear interpolations of φ between the initial and final state values were used, while χ_1 and χ_2 were simply set to zero over the full initial guess paths.

The adaptive path CV for each transition was run using 21 path nodes over the course of a 1 μs well-tempered metadynamics trajectory. Notice that one of the path CV components, χ_2, encompasses out of plane bending of a hydrogen atom. Since LINCS constraints were applied, a smaller time step of 1 fs was chosen for all dynamics where an (adaptive) path CV is being biased. Additionally, the actual biasing was done in a more gentle way, decreasing the height of the initial Gaussians to $0.2\,\mathrm{kJ\,mol^{-1}}$ while the width was set at 0.05 normalized path units and the pace was 0.5 ps. We also intended to limit the bias factor. For adaptive path CVs, however, the bias factor is generally preferred to be chosen higher than for general well-tempered metadynamics runs as to optimize the convergence of the path[38]. A factor of 12 turned out to be a good compromise for all transitions except for *trans_cis2*, where a smaller factor of 10 was used. During metadynamics sampling we used a tube restraint of $200\,\mathrm{kJ\,mol^{-1}}$ per normalized units squared to avoid bifurcations[37,38], e.g. isomerizations in the wrong direction, and a half life of 5×10^5 steps to allow sufficient flexibility in the path adaptive algorithm[38]. Furthermore, harmonic walls of $500\,\mathrm{kJ\,mol^{-1}}$ per normalized units squared have been put on the path parameter σ_s before the reactant state and behind the product state, that is at $\sigma_s = -0.4$ and $\sigma_s = 1.4$.

7. Free Energy and Rate Calculations on Path Collective Variables

Free energy profiles on each of the four paths were calculated using metadynamics and umbrella sampling biasing the path collective variable optimized during the adaptive path sampling described above. All dynamics were done using 1 fs time steps.

Well-tempered metadynamics were run for $1\,\mu$s for each path depositing Gaussians of standard deviation of $0.5/21 = 0.0238$ normalized path units, a height of $1.4\,\mathrm{kJ\,mol^{-1}}$, a pace of 0.5 ps and a bias factor of 12. Tube restraints of $200\,\mathrm{kJ\,mol^{-1}}$ per normalized units squared were used for all profiles. Furthermore, harmonic walls with a spring constant of $500\,\mathrm{kJ\,mol^{-1}}$ per path units squared were employed before the reactant state at $\sigma_s = -5/21 = 0.238$ and after the product state at $\sigma_s = 26/21 = 1.238$ to avoid isomerization along different paths from the one being investigated. Unbiasing weights were calculated using the bias potential at the end of the trajectories, and FES were composed from the accompanying weighted histograms. Notice it is also necessary to reweight the tube restraints; we noticed a difference in barrier height of about $2\,\mathrm{kJ\,mol^{-1}}$ if this restraint was not included in the reweighting. Construction of weighted histograms was done with kernel density estimation (KDE) with Gaussian kernels of bandwidth $0.1/21 = 0.00476$ for all metadynamics runs. Error estimation and convergence of the free energy difference are shown for metadynamics simulations for each path in Fig. S.10.c.

Umbrella sampling simulations were carried out using 70 umbrellas of 20 ns, restraint along the path collective variable using harmonic restraints of spring constant $100\,\mathrm{kJ\,mol^{-1}}$ per normalized path units squared, located at regular intervals between $-3.2/21 = -0.152$ and $24.4/21 = 1.162$ normalized path units. This makes for a total of $1.4\,\mu$s simulation time per path. Again, tube restraints and harmonic walls before reactant and behind product states were used for all profiles, with the same spring constants and positions as for metadynamics on the path CV described above. For some trajectories restrained near the barrier top, LINCS errors occurred. This could generally be helped by choosing a more suitable starting configuration or by reducing the time step to 0.5 fs for these cases. Notice that sampling along σ_s is smoother than sampling along φ, as there is no 'jump' at the barrier, see Fig. S.7. For all umbrella sampling sets, conventional discrete grids were utilized to construct weighted histograms. Diffusion profiles were calculated by applying Hummer's method (eq. S24) to trajectories of each of the umbrellas.

Rates were calculated similarly as for the C_{13}=C_{14} dihedral angle CV described in Section. II A 3. Since we have calculated free energies for all paths separately, we are only interested in rates from left to right for each path, i.e. for increasing value of the path CV σ_s. Reduced masses μ_A and μ_B in reactant state A and product state B were calculated from 10 ns unbiased simulations in the reactant and product states respectively, and subsequent application of eq. S25 monitoring the kinetic energy in the path CV σ_s instead of in φ. Similarly ω_A was obtained using the path CV equivalent of eq. S26 where the spring constant κ_A is obtained by fitting the free energy surface along σ_s in the reactant state A to a harmonic potential. Angular frequencies ω_A obtained this way were compared to frequencies obtained from measuring oscillation periods T_A in the reactant states, with both corresponding very well. Similarly, ξ_{TS} and ω_{TS} were calculated in the same way as we did for the dihedral CV, i.e. trough eqs. S28 and S29, where κ_{TS} was obtained by a parabolic fit and μ_{TS} by averaging μ_A and μ_B. The obtained values are shown in Tabs. S.4 and S.3. Coefficients for evaluating the friction limit can be found in the same tables. These constants can be used to calculate the TST and Kramers' rates. Pontryagin rate was computed carrying out the nested integration using the free energy and diffusion profile as a function of σ_s. Grid-based models were carried out by discretizing the path CV in 500 bins and using high precision libraries[34,35] with 50 digits to build and solve the rate matrix as in eqs. 19 and 20, similarly as for the dihedral CV case.

An overview of all resulting rates from free energy profiles from metadynamics and umbrella sampling along the path CVs can be found in Tab. II.

		trans→cis		cis→trans	
	units	*TS*	*TS′*	*TS*	*TS′*
μ_A	[kg.m^2 rad^{-2}]	6.81×10^{-47}	6.81×10^{-47}	2.41×10^{-47}	2.41×10^{-47}
D_{TS}	[rad^2.ps^{-1}]	0.680	0.687	0.680	0.687
ξ_{TS}	[ps^{-1}]	1.32×10^2	1.31×10^2	1.32×10^2	1.31×10^2
ω_A	[ps^{-1}]	4.99×10^1	4.99×10^1	7.72×10^1	7.72×10^1
ω_{TS}	[ps^{-1}]	2.44×10^2	2.63×10^2	2.44×10^2	2.63×10^2
$F^\ddagger$	[kJ mol^{-1}]	88.6	89.3	88.8	89.5
ξ_{TS}/ω_{TS}	[-]	0.54	0.50	0.54	0.50
$RT/F^\ddagger$	[-]	0.028	0.028	0.028	0.028

TABLE S.1. Retinal: parameters for one-dimensional rate theories calculated for $F(\varphi)$ obtained by umbrella sampling.

		trans→cis		cis→trans	
	units	*TS*	*TS′*	*TS*	*TS′*
μ_A	[kg.m^2 rad^{-2}]	6.81×10^{-47}	6.81×10^{-47}	2.41×10^{-47}	2.41×10^{-47}
D_{TS}	[rad^2.ps^{-1}]	0.680	0.687	0.680	0.687
ξ_{TS}	[ps^{-1}]	1.32×10^2	1.31×10^2	1.32×10^2	1.31×10^2
ω_A	[ps^{-1}]	5.17×10^1	5.17×10^1	7.99×10^1	7.99×10^1
ω_{TS}	[ps^{-1}]	2.97×10^2	3.42×10^2	2.97×10^2	3.42×10^2
$F^\ddagger$	[kJ mol^{-1}]	96.9	97.3	98.6	99.0
ξ_{TS}/ω_{TS}	[-]	0.45	0.38	0.45	0.38
$RT/F^\ddagger$	[-]	0.026	0.026	0.025	0.025

TABLE S.2. Retinal: parameters for one-dimensional rate theories calculated for $F(\varphi)$ obtained by metadynamics.

	units	*trans_cis1*	*trans_cis2*	*cis_trans1*	*cis_trans2*
μ_A	[kg.m^2]	1.42×10^{-48}	1.44×10^{-48}	5.18×10^{-49}	5.10×10^{-49}
D_{TS}	[ps^{-1}]	5.413	5.552	5.449	5.421
ξ_{TS}	[ps^{-1}]	7.92×10^2	7.65×10^2	7.85×10^2	7.90×10^2
ω_A	[ps^{-1}]	5.89×10^1	5.86×10^1	8.86×10^1	8.91×10^1
ω_{TS}	[ps^{-1}]	1.46×10^2	1.52×10^2	1.54×10^2	1.52×10^2
$F^\ddagger$	[kJ mol^{-1}]	96.9	97.1	97.9	97.8
ξ_{TS}/ω_{TS}	[-]	5.41	5.05	5.09	5.21
$RT/F^\ddagger$	[-]	0.026	0.026	0.025	0.025

TABLE S.3. Retinal: parameters for one-dimensional rate theories calculated for $F(\sigma_s)$ obtained by umbrella sampling.

	units	*trans_cis1*	*trans_cis2*	*cis_trans1*	*cis_trans2*
μ_A	[kg.m^2]	1.42×10^{-48}	1.44×10^{-48}	5.18×10^{-49}	5.10×10^{-49}
D_{TS}	[ps^{-1}]	5.396	5.565	5.403	5.440
ξ_{TS}	[ps^{-1}]	7.94×10^2	7.63×10^2	7.92×10^2	7.87×10^2
ω_A	[ps^{-1}]	5.91×10^1	5.86×10^1	8.88×10^1	8.94×10^1
ω_{TS}	[ps^{-1}]	1.54×10^2	1.58×10^2	1.55×10^2	1.55×10^2
$F^\ddagger$	[kJ mol^{-1}]	105.2	104.9	106.7	104.8
ξ_{TS}/ω_{TS}	[-]	5.16	4.82	5.12	5.08
$RT/F^\ddagger$	[-]	0.024	0.024	0.023	0.024

TABLE S.4. Retinal: parameters for one-dimensional rate theories calculated for $F(\sigma_s)$ obtained by metadynamics.

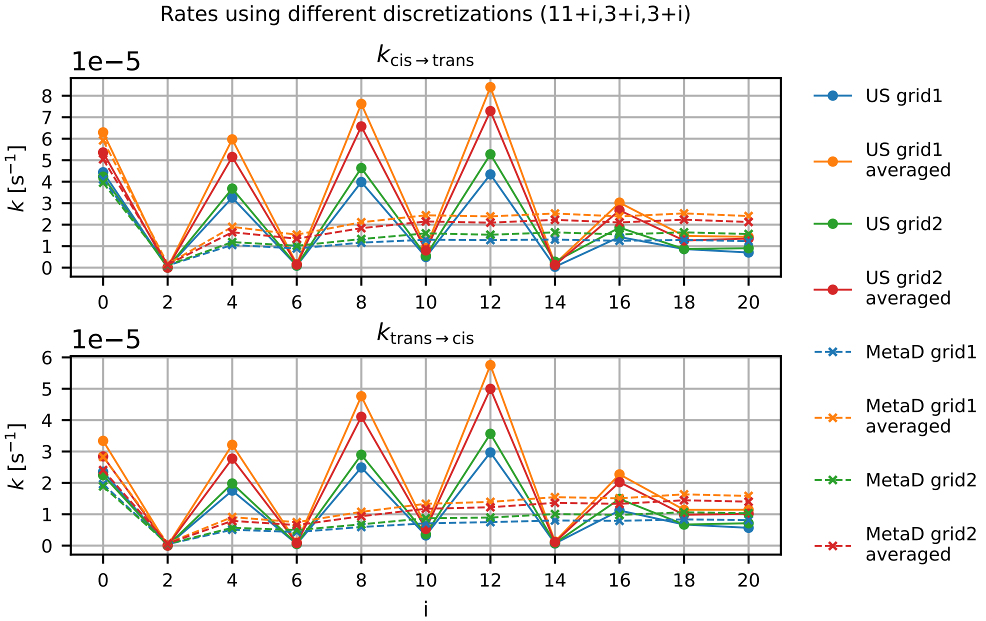

FIG. S.1. Isomerization rates as a function of discretization for 3D grid-based models applied to 3D FES from metadynamics and umbrella sampling (*grid3*) and with averaged and position dependent diffusion for two diffusion schemes *grid1* (Fig. S.13) and *grid2* (Fig. S.14).

8. Multidimensional Discretization of the Fokker-Planck Operator

Similarly as for the one-dimensional cases, grid-based models can be implemented by discretizing the three-dimensional CV space spanned by φ, χ_1 and χ_2 and building the rate matrix according to eq. 19. This was done for the free energy surface obtained from three-dimensional metadynamics (see above) as well as for the free energy surface obtained from three-dimensional umbrella sampling (see above, *grid3*). The χ_1 and χ_2 CVs where discretized between -1 and 1 rad for the metadynamics surface and -0.7 and 0.7 rad for the US surface, and were treated as non-periodic. For both surfaces, φ was discretized between $-\pi$ and π rad and treated as periodic just as was done for the one-dimensional case. Within a choice of discretization, all cells had the same shape and size, i.e. each CV was discretized in cells of the same length.

The free energy and diffusion surfaces calculated as detailed above were interpolated using radial basis function (RBF) interpolation as implemented in scipy, and evaluated at the cell middles q_i for each cell i to yield the free energy and diffusion values π_i and D_i necessary to build the rate matrix according to eq. 19. High precision libraries[34,35] were used to handle the high barriers, just as for the one-dimensional case. 50 digits were used for all calculations. Notice that working with high-precision numbers makes calculations much slower and therefore severely limits the discretization which can be used. The discretization used in this work divided the CV space in (31,23,23) blocks in φ, χ_1 and χ_2 collective variables respectively, yielding a total of 16399 cells. Rates from the three-dimensional grid-based models for different diffusion surfaces can be found in Tab. II.

While the discretization is fine enough to yield converged rates for the 3D FES from metadynamics, the rates from 3D US do not converge as quickly (Fig. S.1). Therefore, rates calculated from the 3D US FES are given between brackets in Tab. II, and have to be interpreted with care. We stress that discretizations could be significantly increased for application to barrier heights that do not necessitate high precision numbers.

InMetaD

biased CV	**trans→cis**			**cis→trans**		
	$\mu \pm$ S.E. [s]	τ [s]	p-value	$\mu \pm$ S.E. [s]	τ [s]	p-value
φ	$4.45 \times 10^4 \pm 7.70 \times 10^3$	4.58×10^4	0.95	$4.16 \times 10^4 \pm 6.39 \times 10^3$	4.48×10^4	0.74
φ, χ_1, χ_2	$4.06 \times 10^4 \pm 6.07 \times 10^3$	4.51×10^4	0.52	$4.27 \times 10^4 \pm 8.98 \times 10^3$	3.85×10^4	0.98

TABLE S.5. Average transition times (μ), corresponding standard errors (S.E.) and transition times from Poisson fit (τ) from infrequent metadynamics for classical model system with 1D biasing using φ as collective variable and with 3D biasing in the CV space spanned by φ, χ_1 and χ_2. Rates mentioned in Tab. II correspond to $1/\tau$.

9. Three-dimensional Infrequent Metadynamics

Three-dimensional infrequent metadynamics were run for both trans-cis and cis-trans transitions in sets of 30 runs for each. Biasing was done using three-dimensional Gaussians of height $0.75\,\mathrm{kJ\,mol^{-1}}$ with a standard deviation of 0.07 rad in all three dimensions, that is, along φ, χ_1 and χ_2. The deposition pace was 20 ps while a bias factor of 20 was used. Determining the biased transition time for trans-to-cis and cis-to-trans simulation was done based on the φ value alone in the same way as for one-dimensional infrequent metadynamics described above.

The reweighted transition times were fitted to a Poisson distribution and a KS test was done using a million randomly generated points according to the TCDF from the corresponding fits, as described in Ref. 36. The corresponding rates can be found in Tab. II. Average transition times, standard errors, Poisson fitted transition times and corresponding p-values can be found in Tab. S.5.

10. Transition State Search

Since GROMACS does not have a method for transition state (i.e. first-order saddle point) search implemented, transition state configurations were estimated using relaxed scans along one of the path CVs. From the umbrella sampling simulations along the *cis_trans1* path (SI section II A 7), seventeen candidate configurations were selected for which $\varphi \in [\pi/2 - 0.001, \pi/2 + 0.001]$, $\chi_1 \in [-0.01, 0.01]$ and $\chi_2 \in [-0.01, 0.01]$. For each of the candidates, a relaxed scan along the *cis_trans1* path CV was performed. More specifically, a series of constrained optimizations was carried out, restraining the path parameter σ_s at specific values near the transition state in addition to the backbone restraints that were already used in all dynamics simulations. For each candidate, 41 constrained optimizations were performed, with restraints on σ_s carried out between 11.20/21 and 11.28/21 in steps of 0.002/21 normalized path units, each time with a spring constant of $1500\,\mathrm{kJ\,mol^{-1}}$ per normalized path units squared. The optimizations were performed using GROMACS' limited-memory Broyden-Fletcher-Goldfarb-Shanno quasi-Newtonian[40] minimizer (l-bfgs). For each of the seventeen candidates, the optimized configuration in the scan at the σ_s-value with the highest potential energy was chosen to represent the transition state configuration (see Fig. S.2.a for candidates TS0 and TS8).

Hessian matrices and the corresponding eigenvalues were calculated on the obtained transition state structures using GROMACS' normal-mode analysis functionalities. The path parameter restraints used in the constrained optimization were not included for the Hessian calculations. Additionally, and contrary to the molecular dynamics simulations performed before, the constrained optimization as well as the normal-mode analysis were performed without inclusion of LINCS constraints, as these cannot be handled in GROMACS' normal-mode analysis functionalities. All structures obtained from the relaxed scans (labeled TS0 to TS16) roughly corresponded to first-order saddle points, where one eigenvalue was large and negative and the subsequent six eigenvalues corresponding to translational and rota-

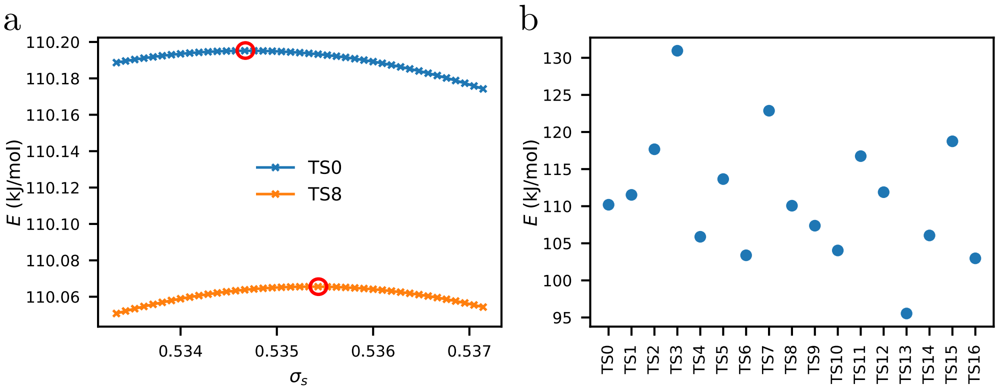

FIG. S.2. **a:** Potential energies of relaxed scan along the *cis_trans1* path collective variable for two example candidates (TS0 and TS8). The configurations at the potential energy maxima are circled in red and are chosen to represent the transition state in further analysis (Eyring and high-temperature TST).
b: Potential energies of the transition state configurations obtained from relaxed scan for seventeen candidates (TS0-TS16) in reference to the potential energy of the optimized structure in the trans state. Transition states differ up to 35 kJ mol^{-1} in potential energy.

tional degrees of freedom were small (corresponding to wavenumbers under 40 cm^{-1}).

In parallel with the transition states, structures were energy minimized using the same minimizer and without LINCS constraints in the trans and the cis state as representations of the reactant states. Equivalent as for the transition states, Hessian matrices and corresponding eigenvalues were calculated, with all eigenvalues found to be positive and the six smallest eigenvalues found to be small. Potential energies of the transition states (i.e. at the potential energy maxima of the relaxed scan) in reference to the potential energy of the optimized structure in the trans state are shown in Fig. S.2.b for all seventeen candidates (TS0-TS16). Notice the potential energies of the obtained maxima of the candidates still vary quite a bit (up to 35 kJ mol^{-1}), indicating the relaxed PES scan is not an optimal tool for finding the lowest-lying transition state.

11. Eyring Transition State Theory and the High-Temperature Limit

When configurations for the reactant (minimum on the PES) and transition state (first-order saddle point on the PES) are available, rates can be estimated by Eyring's transition state theory:

$$k_{AB}^{\mathrm{Eyr}} = \frac{RT}{h}\frac{\widetilde{q}_{\mathrm{AB}^{\ddagger}}}{q_A}\exp\left(-\frac{E_b}{RT}\right) \tag{S30}$$

where E_b is the potential energy difference between reactant state A and transition state $AB^{\ddagger}$ and q_A and $\widetilde{q}^{\ddagger}_{AB}$ are the partition functions of the reactant and transition states respectively. The tilde over the transition state partition function indicates that the degree of freedom associate with the negative eigenvalue of the first-order saddle point should be excluded. Partition functions are commonly factorized in their translational, rotational, vibrational and electronic contributions. For unimolecular reactions such as cis-trans isomerization, the translational contribution to the partition function remains unchanged, and thus cancels in eq. S30. Rotational contributions to the partition function are also expected to not change much between reactant and transition states, as strong positional restraints keep the backbone in place and the molecule remains relatively linear over the course of

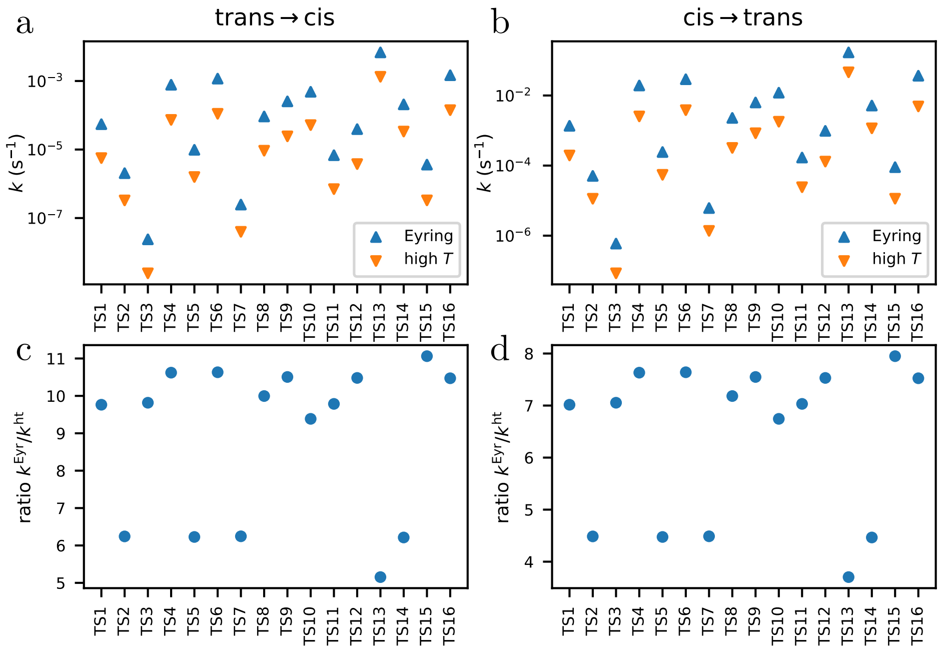

FIG. S.3. **a,b**: Rates from Eyring TST and the high temperature (high T) approximation for trans→cis (**a**) and cis→trans (**b**) isomerization. Rates for different transition states vary over multiple orders of magnitude. **c,d**: ratio of rate from Eyring (k^{Eyr}) over rate from the high temperature approximation (k^{ht}) for trans→cis (**c**) and cis→trans (**d**) isomerization. Eyring and high T rates approximately differ by a factor between 4 and 11.

isomerization. Therefore, rotational contributions to $\widetilde{q}_{\mathrm{AB}^\ddagger}/q_A$ and thus k^{Eyr}_{AB} are neglected in our analysis. Furthermore, we assume only the electronic ground state is involved during thermal cis-trans isomerization, and thus also electronic contributions are ignored. Consequently, only vibrational contributions to the partition functions in eq. S30 are considered here.

The quantum mechanical partition functions for vibrational degrees of freedom are given by

$$q_{A;\mathrm{vib}} = \prod_{k=1}^{3N-6} \frac{\exp\left(-\frac{h\nu_{A,k}}{2RT}\right)}{1-\exp\left(-\frac{h\nu_{A,k}}{RT}\right)} \quad \text{and} \quad \widetilde{q}_{AB^\ddagger;\mathrm{vib}} \prod_{k=1,k\neq r}^{3N-6} \frac{\exp\left(-\frac{h\nu_{AB^\ddagger,k}}{2RT}\right)}{1-\exp\left(-\frac{h\nu_{AB^\ddagger,k}}{RT}\right)} \tag{S31}$$

where N is the amount of atoms in the system. Frequencies $\nu_{A,k}$ and $\nu_{AB^\ddagger,k}$ are obtained from the square-rooted eigenvalues of the mass-weighted Hessian of the reactant and transition states respectively[41,42]. Rates calculated by combining eqs. S30 and S31 are given in Fig. S.3.a and b in blue.

Instead of using the quantum mechanical partition function, one can also use classical partition functions for the vibrational degrees of freedom in a so-called high-temperature approximation. The high-temperature equivalents of eq. S31 are given by[41]

$$q_{A;\mathrm{ht,vib}} = \prod_{k=1}^{3N-6} \frac{RT}{h\nu_{A,k}} \quad \text{and} \quad \widetilde{q}_{AB^\ddagger;\mathrm{ht,vib}} = \prod_{k=1,k\neq r}^{3N-6} \frac{RT}{h\nu_{AB^\ddagger,k}} \tag{S32}$$

and the corresponding high-temperature approximation of Eyring's TST

$$k_{AB}^{\mathrm{ht}} = \frac{RT}{h}\frac{\widetilde{q}_{\mathrm{AB}^{\ddagger};\mathrm{ht,vib}}}{q_{A;\mathrm{ht,vib}}}\exp\left(-\frac{E_b}{RT}\right) \tag{S33}$$

$$= \frac{\prod_{k=1}^{3N-6}\nu_{A,k}}{\prod_{k=1,k\neq r}^{3N-6}\nu_{AB^{\ddagger},k}}\exp\left(-\frac{E_b}{RT}\right)\,. \tag{S34}$$

Rates from eq. S34 are given in Fig. S.3.a and b in orange.

The high-temperature limit estimates the rate corresponding to sampling from a fully classical dynamics on the potential energy surface given by the force field. This is the same rate as estimated by the rate methods used above, as all of these are based in classical MD simulations, i.e. calculated from simulations integrating Newton's laws of motion. When using the quantum partition functions in eq. S31, however, quantization of the vibrational degrees of freedom is taken into account. Comparing rates from Eyring's TST to rates using the high-temperature limit thus gives us an idea of the impact of this quantization. From Fig. S.3.c and d, quantization is expected to increase rates by a factor between 4 to 11.

III. ADDITIONAL TABLES AND FIGURES

method	equation	Moderate friction		High friction	
		Small barrier			
		k_{AB} [ps^{-1}]	k_{BA} [ps^{-1}]	k_{AB} [ps^{-1}]	k_{BA} [ps^{-1}]
Simple TST	(8)	1.86×10^{-2}	1.94×10^{-2}	1.86×10^{-2}	1.94×10^{-2}
Kramers (weak friction)	(11)	6.55×10^{-2}	3.53×10^{-2}	2.09×10^{-1}	1.13×10^{-1}
Kramers (moderate friction)	(13)	1.44×10^{-2}	6.77×10^{-3}	8.84×10^{-3}	4.13×10^{-3}
Kramers (high friction)	(14)	3.11×10^{-2}	1.48×10^{-2}	9.73×10^{-3}	4.63×10^{-3}
Grid-based	(18)	3.03×10^{-2}	1.43×10^{-2}	9.47×10^{-3}	4.49×10^{-3}
Direct simulation		1.48×10^{-2} ± 1.53×10^{-2}	6.52×10^{-3} ± 6.59×10^{-3}	1.05×10^{-2} ± 9.72×10^{-3}	5.04×10^{-3} ± 4.95×10^{-3}
		High barrier			
Simple TST	(8)	4.58×10^{-9}	4.63×10^{-9}	4.58×10^{-9}	4.63×10^{-9}
Kramers (weak friction)	(11)	7.10×10^{-9}	3.32×10^{-9}	4.26×10^{-7}	1.99×10^{-7}
Kramers (moderate friction)	(13)	4.47×10^{-9}	2.02×10^{-9}	1.40×10^{-9}	6.38×10^{-10}
Kramers (high friction)	(14)	9.33×10^{-8}	4.22×10^{-8}	1.55×10^{-9}	7.04×10^{-10}
Grid-based	(18)	8.40×10^{-8}	3.80×10^{-8}	1.40×10^{-9}	6.34×10^{-10}
Infrequent metadynamics	(23)	4.60×10^{-9} ± 4.26×10^{-9}	1.84×10^{-9} ± 1.37×10^{-9}	1.24×10^{-9} ± 4.05×10^{-10}	6.29×10^{-10} ± 6.72×10^{-10}
		Interpolated potential			
Simple TST	(8)	6.08×10^{-13}	1.58×10^{-13}	6.08×10^{-13}	1.58×10^{-13}
Kramers (weak friction)	(11)	1.47×10^{-12}	4.11×10^{-13}	5.91×10^{-11}	1.64×10^{-11}
Kramers (moderate friction)	(13)	5.92×10^{-13}	1.55×10^{-13}	2.46×10^{-13}	6.59×10^{-14}
Kramers (high friction)	(14)	9.31×10^{-12}	2.20×10^{-12}	2.32×10^{-13}	5.50×10^{-14}
Grid-based	(18)	1.17×10^{-11}	3.18×10^{-12}	2.94×10^{-13}	7.95×10^{-14}
Infrequent metadynamics	(23)	5.21×10^{-13} ± 6.39×10^{-13}	1.76×10^{-13} ± 2.18×10^{-13}	2.07×10^{-13} ± 1.98×10^{-13}	5.28×10^{-14} ± 4.95×10^{-14}

TABLE S.6. One-dimensional potential. Kinetic rates estimated at specific friction values: $\xi = 2.5\,\mathrm{ps}^{-1}$ (moderate friction - small barrier); $\xi = 8\,\mathrm{ps}^{-1}$ (high friction - small barrier); $\xi = 0.5\,\mathrm{ps}^{-1}$ (moderate friction - high barrier); $\xi = 30\,\mathrm{ps}^{-1}$ (high friction - high barrier); $\xi = 2.5\,\mathrm{ps}^{-1}$ (moderate friction - interpolated potential); $\xi = 100\,\mathrm{ps}^{-1}$ (high friction - interpolated potential).

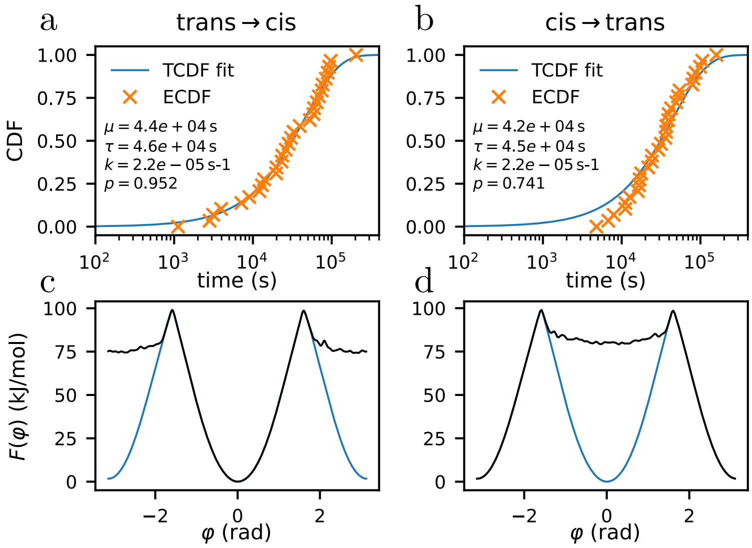

FIG. S.4. **a, b:** TCDF fit to results of 30 InMetaD runs for trans-cis (a) and cis-trans (b) transitions. μ is the transition time averaged over 30 runs, τ is the transition time as obtained from fitting and $k = 1/\tau$ the corresponding rate. p is the calculated p-value of the KS test. **c, d:** Free energy profiles obtained from metadynamics simulation (as in Fig. 3) with the biasing potential at the moment of transitioning for an example run of InMetaD for trans-cis (c) and cis-trans (d) isomerization added on top in black.

A. Optimized reaction coordinate

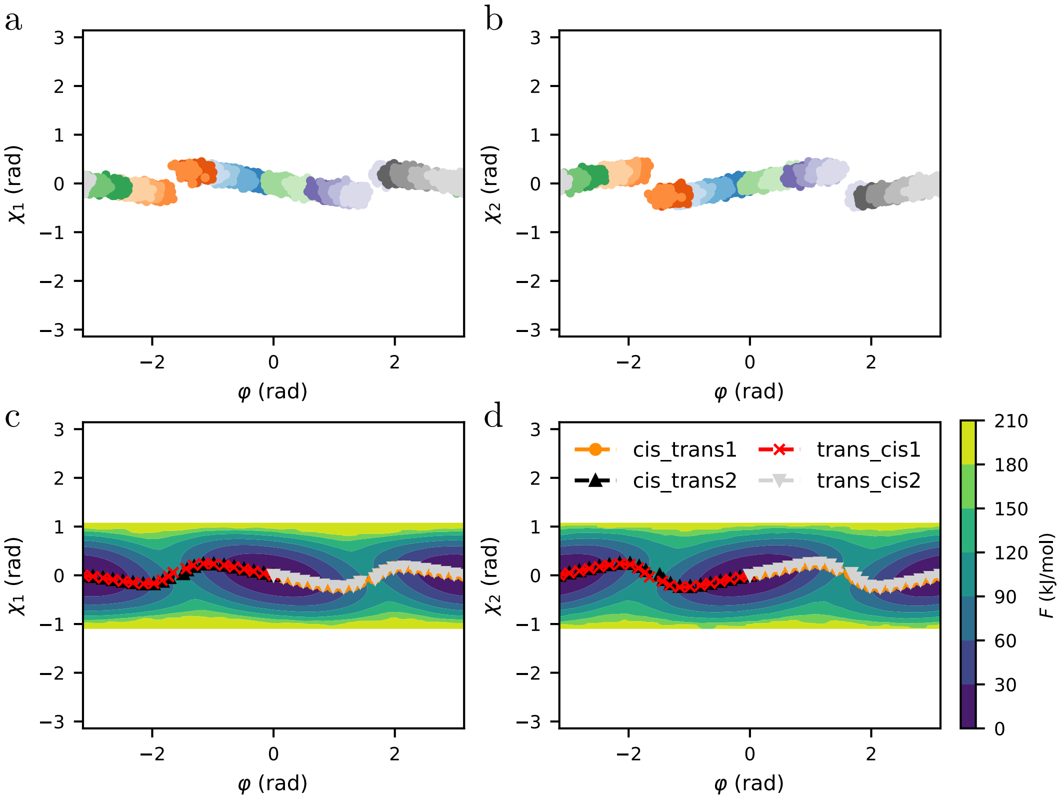

FIG. S.5. Unscaled version of Fig. 4 to indicate how small the out of plane bending of the improper dihedral substituents really are.

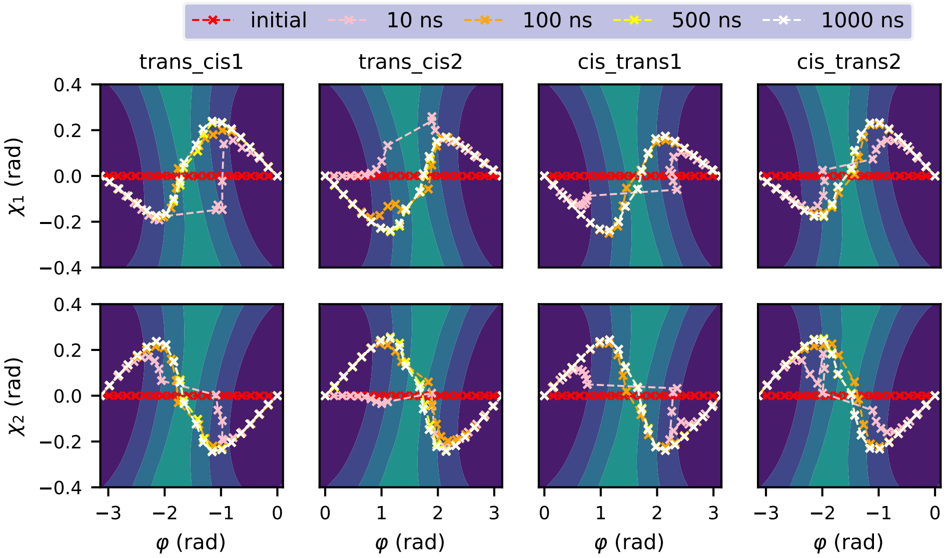

FIG. S.6. Time evolution of 21 nodes of path collective variables for four trajectories of 1 μs of metadynamics, each trajectory representing one transition: *cis_trans1*, *cis_trans2*, *trans_cis1* and *trans_cis2*. **Top row:** path evolution represented in 2D space spanned by φ and χ_1. Underlying contour plot taken from 2D-reweighted free energy surface from 3D metadynamics simulation (see also Fig. 4 left). **Bottom row:** path evolution represented in 2D space spanned by φ and χ_2. Underlying contour plot taken from 2D-reweighted free energy surface from 3D metadynamics simulation (see also Fig. 4 right).

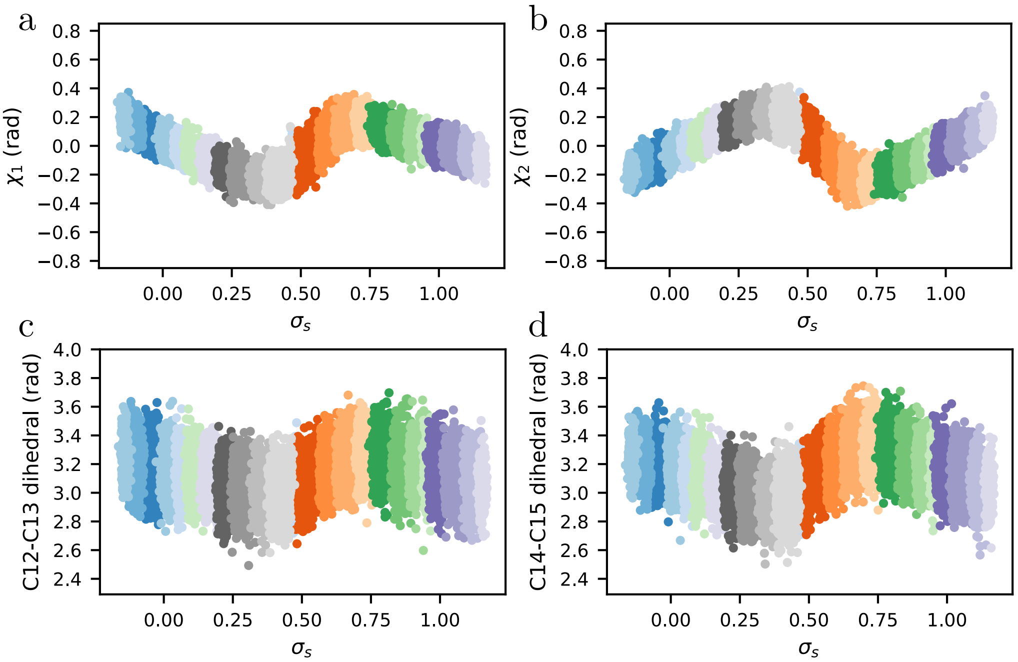

FIG. S.7. **a, b, c, d:** Scatter plot of improper dihedrals χ_1 (a) and χ_2 (b) as well as proper dihedrals C_{11}=C_{12}-C_{13}=C_{14} (c) and C_{13}=C_{14}-C_{15}=NH (d) versus the path CV for umbrella sampling along the path CV of path *cis_trans1*. Clearly the correlation of the improper dihedrals χ_1 and χ_2 is handled more smoothly as compared to umbrella sampling along the dihedral CV φ, as the sampling doesn't 'jump' at the peaks anymore (compare to Fig. 4). Interestingly, also the correlation of the proper dihedrals (C_{12}-C_{13} and C_{14}-C_{15}) is handled more smoothly as the sampling doesn't 'jump' at the peaks anymore either (compare to Fig. S.12).

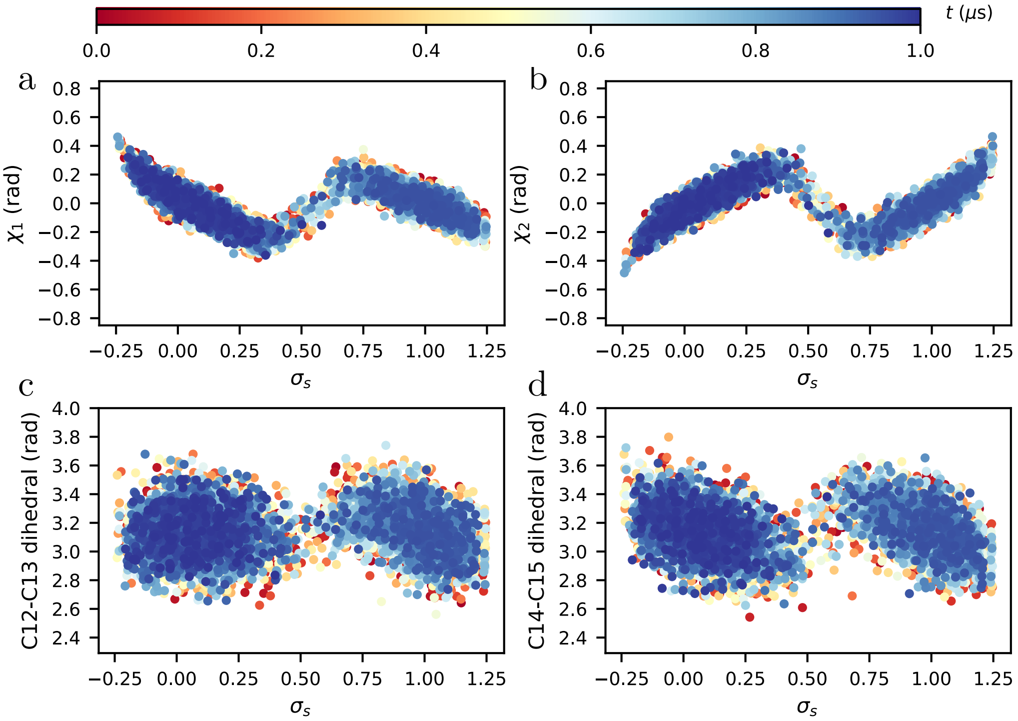

FIG. S.8. **a, b, c, d:** Scatter plot of improper dihedrals χ_1 (a) and χ_2 (b) as well as proper dihedrals $C_{11}{=}C_{12}$-$C_{13}{=}C_{14}$ (c) and $C_{13}{=}C_{14}$-$C_{15}{=}NH$ (d) versus the path CV for metadynamics along the path CV of path *cis_trans1*. The color of the markers indicates the simulation time at which the corresponding configuration was generated.

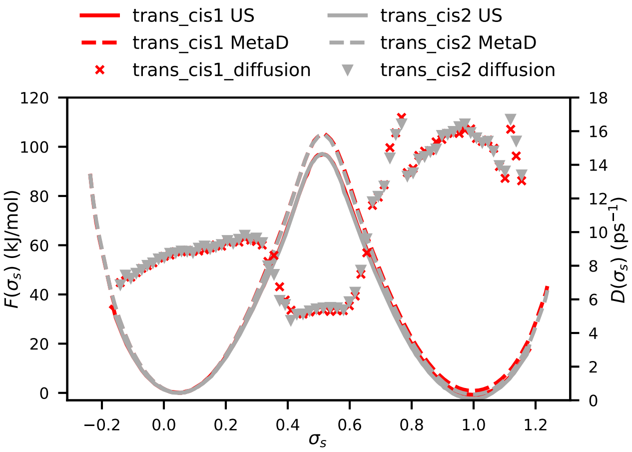

FIG. S.9. Free energy profiles from metadynamics and umbrella sampling as well as diffusion profiles for optimized trans to cis path collective variable.

B. Umbrella sampling vs. metadynamics

Convergence of the free energy difference between the cis and trans state $\Delta F = F_{\text{cis}} - F_{\text{trans}}$ in the metadynamics biases are given in Fig. S.10 for different metadynamics runs. For the corresponding details about parameter sets, see SI section II A. For the final free energy surfaces, see Figs. 3 and 4.

The free energy difference at a certain simulation time is calculated by determining the FES corresponding to the bias at that time (i.e. from the scaled upside-down bias, see Refs. 22,25,27). This FES is used to calculate the relative probabilities of being in cis versus being in trans. Using eq. S3:

$$\pi_{\text{cis}} = \int_{-\pi/2}^{\pi/2} \mathrm{d}\varphi \, \pi(\varphi) = \int_{-\pi/2}^{\pi/2} \mathrm{d}\varphi \, \exp\left(-\frac{F(\varphi)}{RT}\right) \tag{S35}$$

and equivalent for trans in $\varphi < -\pi/2$ and $\varphi > \pi/2$. For the 3D FES, the integration is additionally carried out over χ_1 and χ_2 over their full range. The free energy of a state can then be calculated using $F_{\text{cis}} = -RT \ln \pi_{\text{cis}}$ and equivalent for trans, and the free energy difference

$$\Delta F = F_{\text{cis}} - F_{\text{trans}} = -RT \ln \frac{\pi_{\text{cis}}}{\pi_{\text{trans}}} \, . \tag{S36}$$

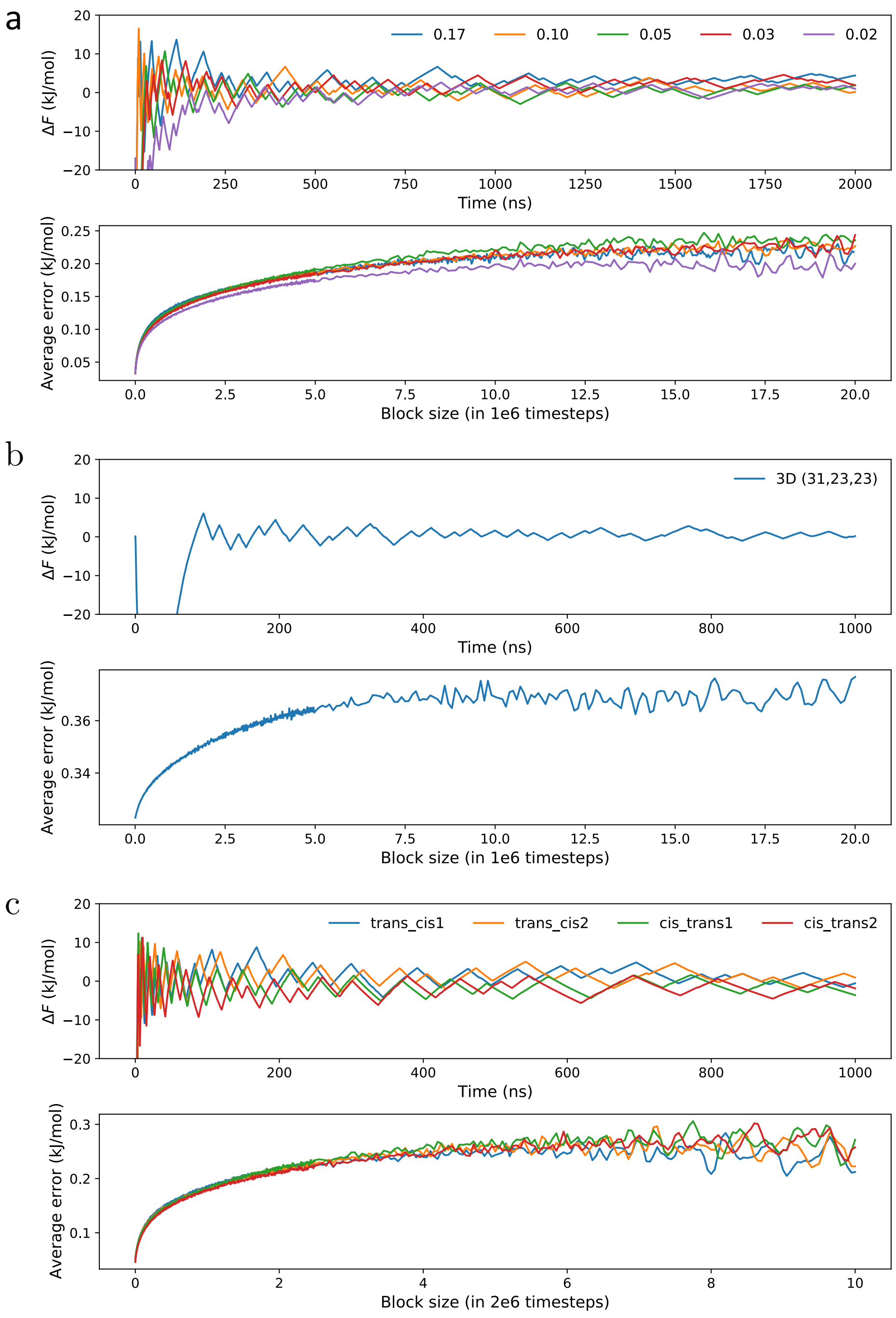

FIG. S.10. **Convergence of the metadynamics bias** Convergence of free energy difference between trans and cis for metadynamics bias and error convergence from block analysis for: **a:** MetaD simulations biasing the $C_{13}{=}C_{14}$ dihedral angle φ for different Gaussian standard deviations (in radians). All these simulations were run for 2 μs with a deposition pace of 1 ps and a biasing factor of 10. **b:** 3D MetaD simulation. Error convergence from block analysis for 3D free energy surface was done using discretization (31,23,23). Simulation was run for 1 μs with a deposition pace of 1 ps and a biasing factor of 12. **c:** MetaD simulations along path CVs. Simulation was run for 1 μs with a deposition pace of 0.5 ps and a biasing factor of 12.

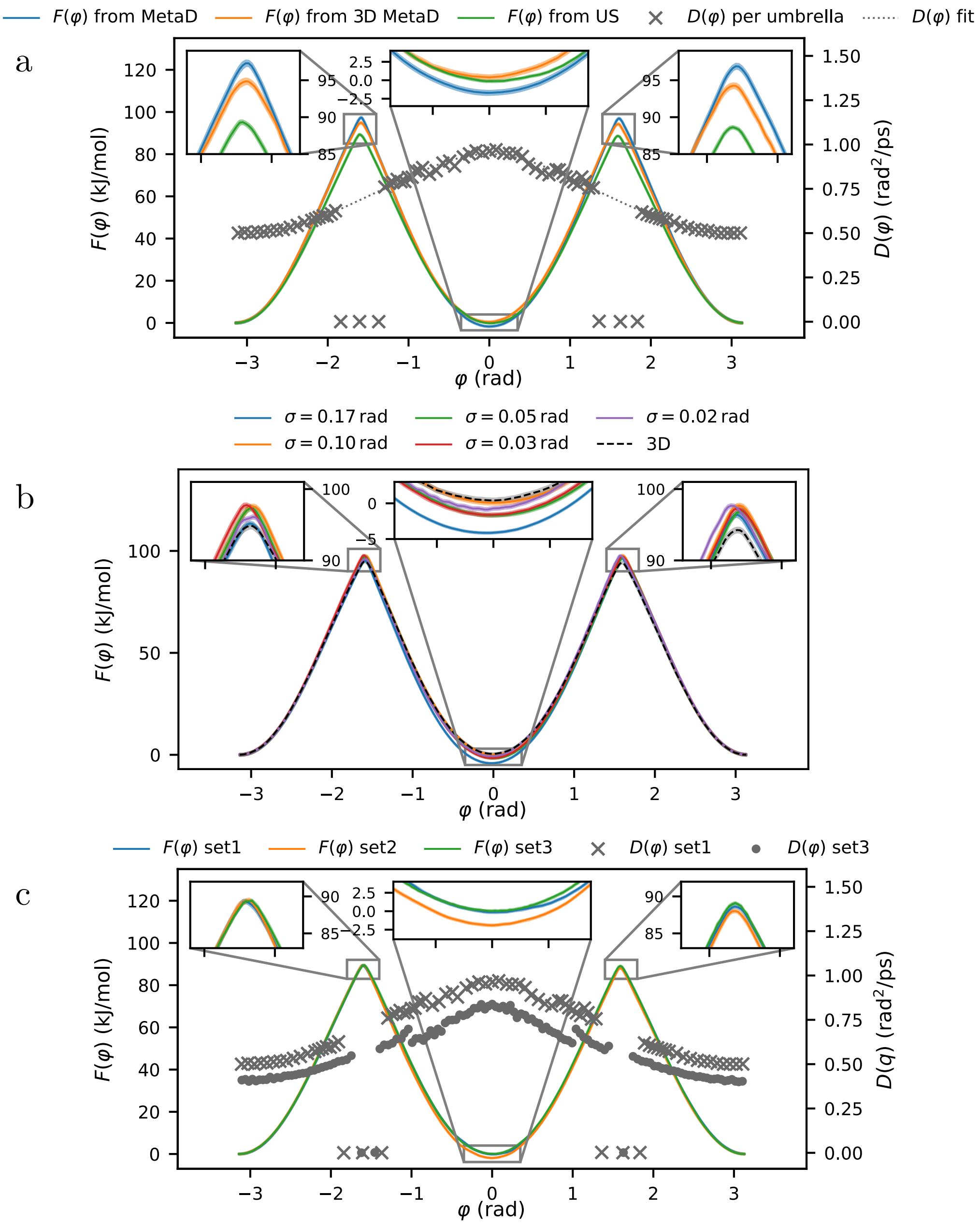

FIG. S.11. **a:** Free energy surfaces $F(\varphi)$ and diffusion profiles $D(\varphi)$ estimated from MetaD and US biasing $C_{13}{=}C_{14}$ torsion angle φ including standard errors.
b: Free energy profiles for metadynamics simulations biasing the $C_{13}{=}C_{14}$ dihedral angle φ for different Gaussian standard deviations (in radians), as well as profile reweighted from 3D metadynamics. One-dimensional metadynamics simulations (colored) were run for 2 μs with a deposition pace of 1 ps using Gaussians with a height of 1.2 kJ mol^{-1} and a biasing factor of 10. 3D metadynamics simulation (black, dashed) was run for 1 μs with a deposition pace of 1 ps using Gaussians with a height of 1.2 kJ mol^{-1} and a width of 0.07 rad in each dimension and a biasing factor of 12.
c: Free energy profiles for US simulations biasing the $C_{13}{=}C_{14}$ dihedral angle φ. The statistical uncertainty of the free energy profiles are shown as shaded areas, but they are so small, that they are hardly discernible.

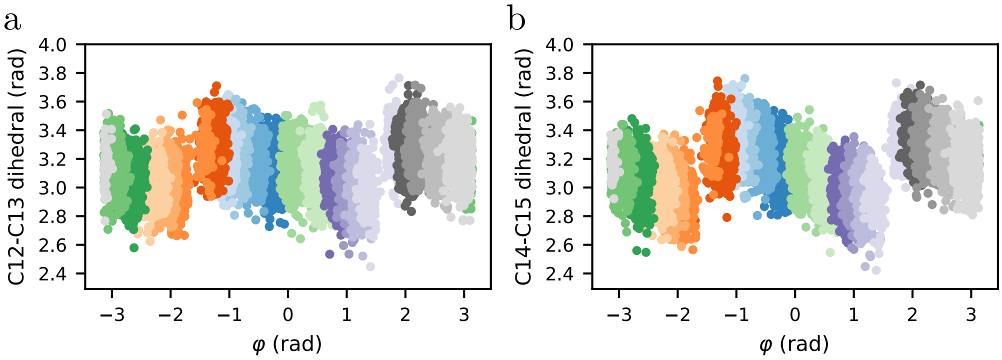

FIG. S.12. **a, b:** Scatter plot of proper dihedrals C_{11}=C_{12}-C_{13}=C_{14} (a) and C_{13}=C_{14}-C_{15}=NH (b) versus φ for umbrella sampling along φ (US *set2*). These proper dihedrals are also correlated and also cause hysteresis when using φ as a reaction coordinate (compare to Fig. 4).

C. Multidimensional models

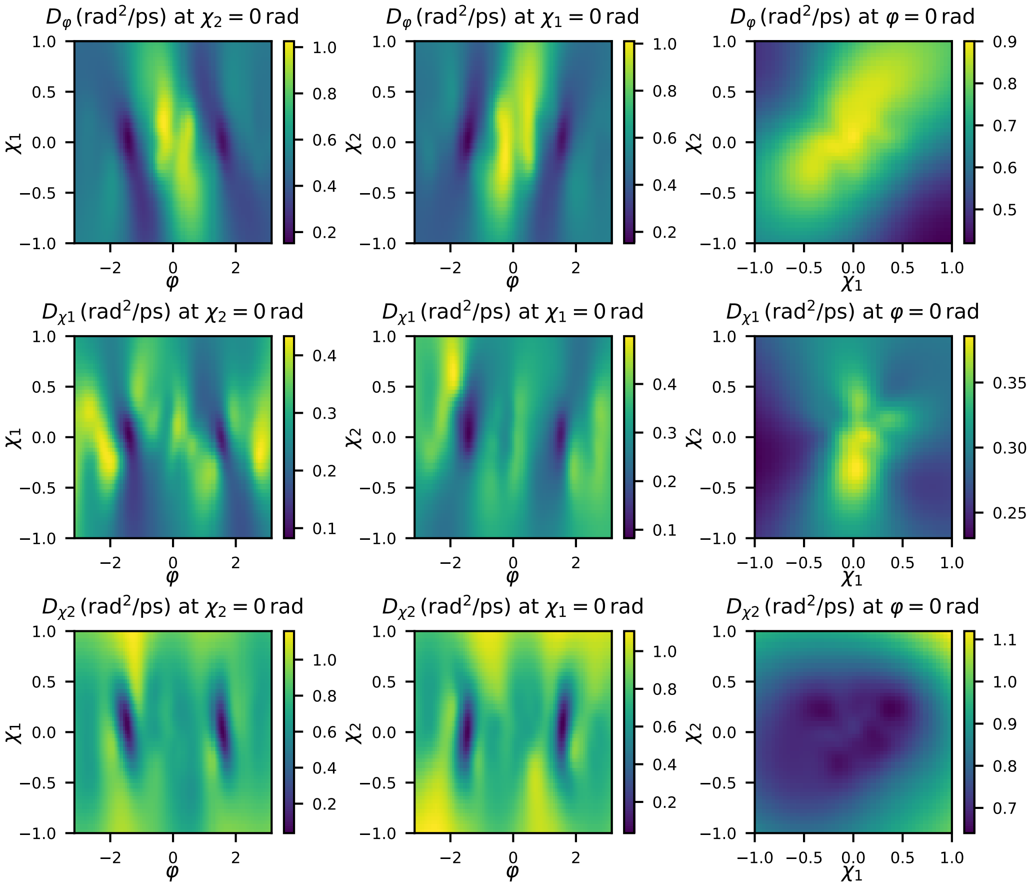

FIG. S.13. Interpolated three-dimensional diffusion surfaces D_φ, D_{χ_1} and D_{χ_2} obtained from *grid1* of three-dimensional harmonic restraints.

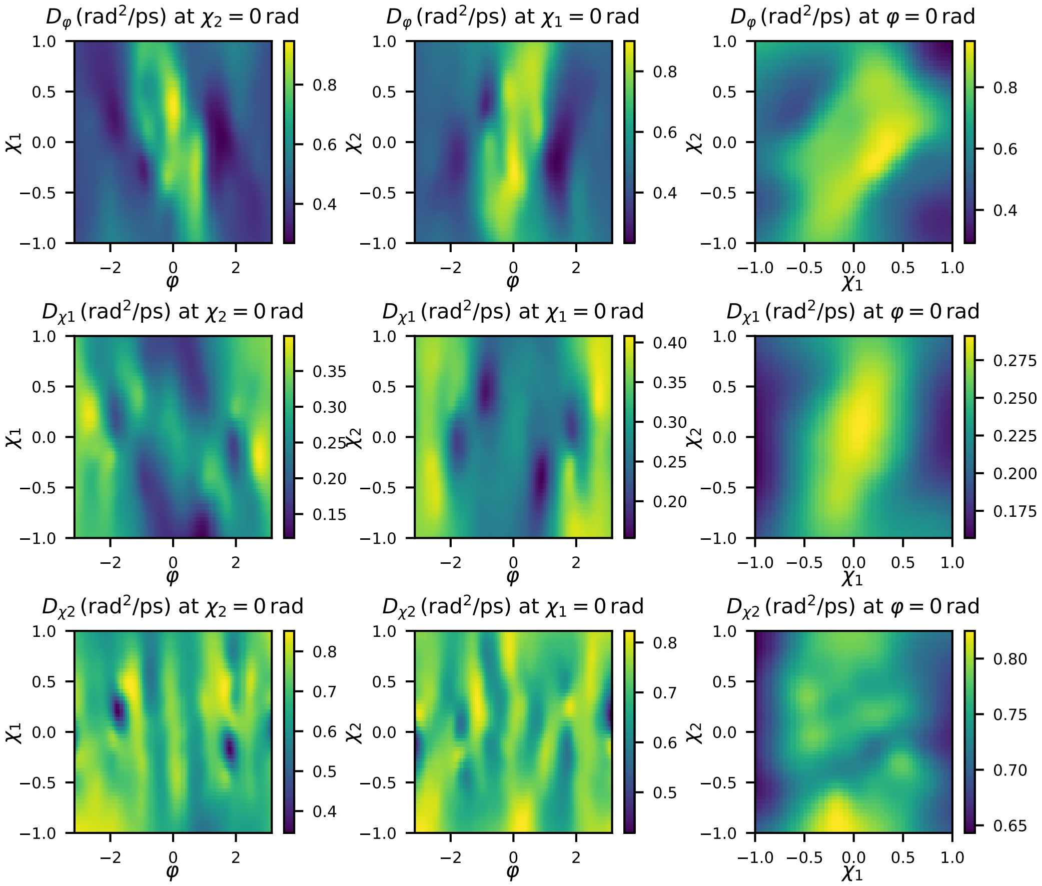

FIG. S.14. Interpolated three-dimensional diffusion surfaces D_φ, D_{χ_1} and D_{χ_2} obtained from *grid2* of three-dimensional harmonic restraints.

IV. REFERENCES

[1] Hannes Risken and Hannes Risken. Fokker-Planck equation. Springer, 1996.

[2] J. A . Izaguirre, C. R. Schweet, and V.S. Pande. Multiscale dynamics of macromolecules using normal mode Langevin. Pac. Symp. Biocomput., 15:240–251, 2010.

[3] Peter Hänggi, Peter Talkner, and Michal Borkovec. Reaction-rate theory: fifty years after kramers. Rev. Mod. Phys., 62:251–341, 1990.

[4] Baron Peters. Reaction Rate Theory and Rare Events. Elsevier, 1st edition, 2017.

[5] H Pelzer and E Wigner. The speed constansts of the exchange reactions. Z. Phys. Chem. B, 15:445–552, 1932.

[6] George H Vineyard. Frequency factors and isotope effects in solid state rate processes. J. Phys. Chem. Solids., 3(1-2):121–127, 1957.

[7] Emadeddin Tajkhorshid, Béla Paizs, and Sandor Suhai. Role of isomerization barriers in the pKa control of the retinal Schiff base: a density functional study. J. Phys. Chem. B, 103(21):4518–4527, 1999.

[8] Shigehiko Hayashi, Emad Tajkhorshid, and Klaus Schulten. Structural changes during the formation of early intermediates in the bacteriorhodopsin photocycle. Biophys. J., 83(3):1281–1297, 2002.

[9] Emadeddin Tajkhorshid, Jérôme Baudry, Klaus Schulten, and Sandor Suhai. Molecular dynamics study of the nature and origin of retinal's twisted structure in bacteriorhodopsin. Biophys. J., 78(2):683–693, 2000.

[10] Erik Malmerberg, Ziad Omran, Jochen S Hub, Xuewen Li, Gergely Katona, Sebastian Westenhoff, Linda C Johansson, Magnus Andersson, Marco Cammarata, Michael Wulff, et al. Time-resolved WAXS reveals accelerated conformational changes in iodoretinal-substituted proteorhodopsin. Biophys. J., 101(6):1345–1353, 2011.

[11] Kresten Lindorff-Larsen, Stefano Piana, Kim Palmo, Paul Maragakis, John L Klepeis, Ron O Dror, and David E Shaw. Improved side-chain torsion potentials for the Amber ff99SB protein force field. Proteins: Struct., Funct., Bioinf., 78(8):1950–1958, 2010.

[12] Oleksandr Volkov, Kirill Kovalev, Vitaly Polovinkin, Valentin Borshchevskiy, Christian Bamann, Roman Astashkin, Egor Marin, Alexander Popov, Taras Balandin, Dieter Willbold, et al. Structural insights into ion conduction by Channelrhodopsin 2. Science, 358(6366), 2017.

[13] David Van Der Spoel, Erik Lindahl, Berk Hess, Gerrit Groenhof, Alan E Mark, and Herman JC Berendsen. GROMACS: fast, flexible, and free. J. Comput. Chem., 26(16):1701–1718, 2005.

[14] Mark James Abraham, Teemu Murtola, Roland Schulz, Szilárd Páll, Jeremy C Smith, Berk Hess, and Erik Lindahl. GROMACS: High performance molecular simulations through multi-level parallelism from laptops to supercomputers. SoftwareX, 1:19–25, 2015.

[15] Wikipedia. Dihedral angle — Wikipedia, The Free Encyclopedia. `http://en.wikipedia.org/w/index.php?title=Dihedral%20angle&oldid=1155191517`, 2023. [Online; accessed 08-June-2023].

[16] The PLUMED consortium. Plumed2. `https://github.com/plumed/plumed2`, 2019.

[17] Wikipedia. Atan2 — Wikipedia, The Free Encyclopedia. `http://en.wikipedia.org/w/index.php?title=Atan2&oldid=1156958741`, 2023. [Online; accessed 08-June-2023].

[18] Massimiliano Bonomi, Davide Branduardi, Giovanni Bussi, Carlo Camilloni, Davide Provasi, Paolo Raiteri, Davide Donadio, Fabrizio Marinelli, Fabio Pietrucci, Ricardo A Broglia, et al. PLUMED: A portable plugin for free-energy calculations with molecular dynamics. Comput. Phys. Commun., 180(10):1961–1972, 2009.

[19] Gareth A Tribello, Massimiliano Bonomi, Davide Branduardi, Carlo Camilloni, and Giovanni Bussi. PLUMED 2: New feathers for an old bird. Comput. Phys. Commun., 185(2):604–613, 2014.

[20] The PLUMED consortium. Promoting transparency and reproducibility in enhanced molecular simulations. Nat. Methods, 16(8):670–673, 2019.

[21] Alessandro Barducci, Giovanni Bussi, and Michele Parrinello. Well-tempered metadynamics: a smoothly converging and tunable free-energy method. Phys. Rev. Lett., 100(2):020603, 2008.

[22] Davide Branduardi, Giovanni Bussi, and Michele Parrinello. Metadynamics with adaptive Gaussians. J. Chem. Theory Comput., 8(7):2247–2254, 2012.

[23] Massimiliano Bonomi, Alessandro Barducci, and Michele Parrinello. Reconstructing the equilibrium Boltzmann distribution from well-tempered metadynamics. J. Comput. Chem., 30(11):1615–1621, 2009.

[24] Pratyush Tiwary and Michele Parrinello. A time-independent free energy estimator for metadynamics. J. Phys. Chem. B, 119(3):736–742, 2015.

[25] Giovanni Bussi and Alessandro Laio. Using metadynamics to explore complex free-energy landscapes. Nat. Rev. Phys., 2(4):200–212, 2020.

[26] Jérôme Hénin, Tony Lelièvre, Michael R Shirts, Omar Valsson, and Lucie Delemotte. Enhanced sampling methods for molecular dynamics simulations. arXiv preprint arXiv:2202.04164, 2022.

[27] Giovanni Bussi and Gareth A Tribello. Analyzing and biasing simulations with PLUMED. In Biomolecular Simulations, pages 529–578. Springer, 2019.

[28] Zhiqiang Tan, Emilio Gallicchio, Mauro Lapelosa, and Ronald M Levy. Theory of binless multi-state free energy estimation with applications to protein-ligand binding. J. Chem. Phys., 136(14):04B608, 2012.

[29] Gerhard Hummer. Position-dependent diffusion coefficients and free energies from Bayesian analysis of equilibrium and replica molecular dynamics simulations. New J. Phys., 7(1):34, 2005.

[30] Bradley Efron. The jackknife, the bootstrap and other resampling plans. SIAM, 1982.

[31] Donald F Gatz and Luther Smith. The standard error of a weighted mean concentration—-I. Bootstrapping vs other methods. Atmos. Environ., 29(11):1185–1193, 1995.

[32] Jochen S Hub, Bert L De Groot, and David Van Der Spoel. g_wham a free weighted histogram analysis implementation including robust error and autocorrelation estimates. J. Chem. Theory Comput., 6(12):3713–3720, 2010.

[33] Jan O Daldrop, Julian Kappler, Florian N Brünig, and Roland R Netz. Butane dihedral angle dynamics in water is dominated by internal friction. PNAS, 115(20):5169–5174, 2018.

[34] Fredrik Johansson. mpmath. `https://github.com/fredrik-johansson/mpmath`.

[35] Fredrik Johansson. python-flint. `https://github.com/fredrik-johansson/python-flint`.

[36] Matteo Salvalaglio, Pratyush Tiwary, and Michele Parrinello. Assessing the reliability of the dynamics reconstructed from metadynamics. J. Chem. Theory Comput., 10(4):1420–1425, 2014.

[37] Grisell Díaz Leines and Bernd Ensing. Path finding on high-dimensional free energy landscapes. Phys. Rev. Lett., 109(2):020601, 2012.

[38] Alberto Pérez de Alba Ortíz, Jocelyne Vreede, and Bernd Ensing. The adaptive path collective variable: a versatile biasing approach to compute the average transition path and free energy of molecular transitions. In Biomolecular Simulations, pages 255–290. Springer, 2019.

[39] Alberto Pérez de Alba Ortíz and Bernd Ensing. Simultaneous sampling of multiple transition channels using adaptive paths of collective variables. arXiv preprint arXiv:2112.04061, 2021.

[40] Richard H Byrd, Peihuang Lu, Jorge Nocedal, and Ciyou Zhu. A limited memory algorithm for bound constrained optimization. SIAM J. Sci. Comput., 16(5):1190–1208, 1995.

[41] Simon Ghysbrecht and Bettina G Keller. Thermal isomerization rates in retinal analogues using ab-initio molecular dynamics. J. Comput. Chem., 45(16):1390–1403, 2024.

[42] Joseph W Ochterski. Vibrational analysis in Gaussian. Gaussian Inc, 1999.

3.3 Paper B1

“Girsanov reweighting for simulations of underdamped Langevin dynamics. Theory”

S. Kieninger, S. Ghysbrecht, B. G. Keller
arXiv preprint arXiv:2303.14696, **2023**

Preprint: https://doi.org/10.48550/arXiv.2303.14696

Contributions:
Bettina Keller and Stefanie Kieninger conceived the project. Stefanie Kieninger and Simon Ghysbrecht investigated the integrators for the symmetric splitting methods and derived the expressions for the random number differences in the relative path probabilities of the reweighting scheme. B.K. introduced and designed the graphical representation of Langevin integrators. All authors contributed to the manuscript, with B.K. realizing the final version.

Summary

Girsanov reweighting enables the estimation of dynamical properties at a target potential $\widetilde{V}_{\mathrm{tar}}$ from trajectories simulated at a simulation potential V_{sim} by reweighting path probabilities of discretized trajectories at time step resolution (Section 2.4.2). When the path ensemble is sufficiently sampled, the path probability distribution at the target potential can be estimated and used to calculate dynamical properties. A strategic choice of perturbation potential U (Eq. 2.88) accelerates transitions in otherwise slow processes, and path reweighting subsequently facilitates the computation of rate constants at the unbiased target potential.

The relative path probabilities $\widetilde{\mathcal{P}}\left[\mathrm{x}\right]/\mathcal{P}\left[\mathrm{x}\right]$ depend on the integrator used to generate discrete trajectories x. For overdamped Langevin dynamics, the Girsanov theorem[23] ensures that as long as the biasing forces do not approach infinity, the relative path probability does not violate absolute continuity, meaning any path possible at the target potential is also possible at the simulation potential. The expression for the relative path probability for paths generated by the Euler-Maruyama algorithm is well known[26]. However, most molecular dynamics (MD) use underdamped Langevin dynamics, where absolute continuity is not guaranteed. Here, reweighting is contingent on the specific integrator, with relative path probabilities for some integrators already available[27]. In other words, integrators for underdamped Langevin dynamics must be individually studied, with no guarantee that reweighting for any specific one is achievable.

In this study, path reweighting is investigated with a focus on integrators from splitting methods[3] for underdamped Langevin dynamics. Single integration steps are constructed by applying a sequence of partial updates, each corresponding to an exact solve of a piece of the Langevin equation (Eq. 2.2). For the integrators considered here, the Langevin equation is separated into two deterministic parts $\mathcal{A}$ and $\mathcal{B}$, updating the position and momentum respectively, and a stochastic part $\mathcal{O}$. By carrying out the partial steps sequentially, a full single-step transition $(\mathbf{q}_k, \mathbf{p}_k) \rightarrow (\mathbf{q}_{k+1}, \mathbf{p}_{k+1})$ is approximated. Notice that different sequences of the partial steps yield disparate updates $(\mathbf{q}_{k+1}, \mathbf{p}_{k+1})$. More specifically, distinct integrators characterized by different arrangements of partial steps show differing performances in terms of errors on the computed positions and momenta as well as convergence to accurate configurational ensembles. Performance of distinct integrators is subject of intense investigation[137–140]. We are prompted to put forward the following research question:

1. Can we formulate a general approach to predict whether the relative path probability for Langevin integrators from splitting methods obeys absolute continuity?
2. Can we formulate a general approach to derive the associated relative path probability?

To address the first question, we examine the image of the update operators for various integrators. The image of an update operator represents all attainable values of $(\mathbf{q}_{k+1}, \mathbf{p}_{k+1})$

that can be reached from an initial point $(\mathbf{q}_k, \mathbf{p}_k)$, based on the random number used in stochastic step of the algorithm. The probability of generating this point does not affect the image definition; it only indicates if the point can be reached. We examined for each integrator whether the image of the update operator depends on the potential energy, i.e., if the images at the target and the simulation potential correspond (Figs. 1 and 2 in the paper). This ensures that all single-step transitions possible at the simulation potential are also possible at the target potential. This is a strict condition for absolute continuity and guarantees the Girsanov reweighting in full phase space is possible. Graphical representations decomposing the partial steps of each integrator (Figs. 3 and 4 in the paper) show which parts of the integration algorithm are affected by a change in the potential energy function and contribute in understanding why some integrators have potential independent images while others do not.

Formulating the relative path probability requires determining the probabilities of generating $(\mathbf{q}_{k+1}, \mathbf{p}_{k+1})$ at both the target and simulation potential, rather than just examining the images of the update operators. Computable expressions for the probability ratios are derived using the reweighting-on-the-fly approach[26, 27]. In this approach, relative path probabilities are expressed in terms of random numbers η_k generated during simulation, and random number differences $\Delta\eta_k$, which indicate the differences in random numbers necessary to reach the same point $(\mathbf{q}_{k+1}, \mathbf{p}_{k+1})$ at the target versus the simulation potential. When absolute continuity is fulfilled, these random number differences can effectively be expressed in terms of the gradient of the bias ∇U. An overview of expressions for random number differences for various integrators is provided in Tab. 1 of the paper, with detailed derivations in the Appendix. These can be employed to calculate the relative path probabilities directly using Eqs. 2.89-2.91 in Section 2.4.2.

In the Supporting Information (Section 3.4) to this Section, the reweighting formulations for different integrators are tested numerically for a model molecular system.

Girsanov reweighting for simulations of underdamped Langevin dynamics. Theory.

Stefanie Kieninger,[a] Simon Ghysbrecht,[a] and Bettina G. Keller[b]
Freie Universität Berlin, Department of Biology, Chemistry and Pharmacy, Arnimallee 22, 14195 Berlin

(Dated: 28 March 2023)

The critical step in a molecular process is often a rare-event and has to be simulated by an enhanced sampling protocol. Recovering accurate dynamical estimates from such biased simulation is challenging. Girsanov reweighting is a method to reweight dynamic properties formulated as path expected values. The path probability is calculated at the time-step resolution of the molecular-dynamics integrator. But the theory is largely limited to overdamped Langevin dynamics. For underdamped Langevin dynamics, the absolute continuity of the path probability ratio for the biased and unbiased potential is not guaranteed, but it depends on the Langevin integrator. We develop a general approach to derive the path probability ratio for Langevin integrators and to analyze whether absolute continuity is fulfilled. We demonstrate our approach on symmetric splitting methods for underdamped Langevin dynamics. For methods that obey absolute continuity, and thus can be used for Girsanov reweighting, we provide an expression for the relative path probability.

I. INTRODUCTION

Understanding rare events in molecular systems on an atomistic resolution would have great impact in many areas, such as the binding of drug molecules to receptors, protein-protein interactions in molecular machines, aggregation processes in biomolecular systems or artificial materials, phase transitions and chemical reactions. In principle, these processes can be studied by molecular dynamics (MD) simulations[1–3]. However, the timescale of molecular rare events are often well beyond the timescales that can be reached by direct MD simulations. Even if occasional rare-event transitions can be observed in the course of a direct MD simulation, the estimates of thermodynamic or kinetic properties are often not statistically meaningful. This is because passage times across a barrier into a target state are long-tailed distributed, and the tail contributes to the rare-event estimate. Furthermore, the dynamics in the fast degrees of freedom influence the free-energy surface and the diffusion constant of the rare-event transition in ways that are hard to predict, and any rare event can consist of multiple separate transition paths with different intermediate states and transition states. In short: it is important to sample the full path ensemble that contributes to a rare-event.

One approach to speed up the sampling of rare events is to add a bias to the molecular interaction potential. Enhanced sampling methods like metadynamics[4–8] and umbrella sampling[9,10] add energy to the system in order to steer the simulation away from states which have already sufficiently been explored. Since enhanced sampling changes the dynamics of the system, estimates of thermodynamics and dynamic properties are distorted and need to be unbiased. For thermodynamic properties, estimators that accurately reweight the enhanced sampling simulations, such as weighted histogram analysis method[11,12], are available. With these reweighting techniques, the statistical certainty of thermodynamic properties is drastically increased compared to direct simulations. As a result, the field

---

[a] equal contribution

[b] Electronic mail: bettina.keller@fu-berlin.de

is moving from direct simulations to combining enhanced sampling with thermodynamic reweighting techniques.

For dynamic properties, on the other hand, one cannot yet routinely use enhanced sampling simulations. In fact, dynamic reweighting techniques are currently a very active field of research[13]. Dynamic properties are path expected values weighted by the path probability density which depends on the potential energy function. Suppose, the system has been simulated at a potential V, and one would like to know a dynamic property at a target potential $\widetilde{V} = V + U$. To reweight the corresponding path expected value, one needs the relative path probability, i.e the ratio of the path probabilities at $\widetilde{V}$ and at V. Furthermore, the relative path probability needs to obey absolute continuity, i.e. any path that is possible the target potential $\widetilde{V}$ also needs to be possible at the simulation potential V.

Several methods to reweight simulations with bias potentials have been proposed in recent years. Usually an effective model of the dynamics is assumed, either a two-state dynamics in which transition state theory or Kramers' rate theory holds[14–18] or a Markov state model on a discretized state space[19–24]. Since the validity of these effective models changes with the potential energy function, they cannot be equally valid at V and at $\widetilde{V}$. It is difficult to judge how this affects the accuracy of the reweighted estimate. We argue that a more accurate approach is to consider the calculation of the path probability ratio as part of the enhanced sampling simulation. In the subsequent analysis, one would use the simulated paths along with the time-series of the relative path probability to reweight the desired dynamic property. For this the relative path probability ratio needs to be calculated at the time-step resolution of the MD simulation, and the corresponding equations need to match the MD integrator. Additionally, at this high time-resolution, the question of absolute continuity needs to be addressed.

Based on works by L. Onsager and S. Machlup[25] and, independently, by I.V. Girsanov[26], one can derive an exact reweighting technique, in which the path probability ratio is calculated at the time-step resolution of the MD simulation. For overdamped Langevin dynamics, the Girsanov theorem guarantees that the relative path probability does not violate absolute continuity, as long as the biasing forces do not approach infinity. This guarantee holds even for continuous solutions of the stochastic differential equation[26,27]. Additionally, the expression for the relative path probability for time-discretized paths generated by the Euler-Maruyama algorithm is well established[27,28]. Since the late 1990s, it has been shown several times that Girsanov reweighting or, equivalently, dynamic importance sampling can be used to unbias overdamped Langevin dynamics, both for model potentials[29–33] and for small molecular systems[34–36]. But the use of overdamped Langevin dynamics to model molecular rare events is limited. It can be used in the mesoscopic molecular regime, in which molecules are (partly) treated as rigid bodies, to study molecular crowding effects, association processes between large molecules, and even the dynamics of coarse-grained polymers[37,38] But because overdamped Langevin dynamics suppresses the fast intramolecular fluctuations, it cannot be used to model conformational transitions at atomistic resolutions.

By contrast, underdamped Langevin dynamics, often under the name ,,Langevin thermostats", is an accurate and frequently used equation of motion for atomistic MD[39]. For continuous solutions of underdamped Langevin dynamics, the path probability can be formulated[40], but one cannot guarantee that the relative path probability obeys absolute continuity. This, at first, seems like an impasse in the attempt to unbias dynamic estimates: one needs to sample the molecular rare events by underdamped Langevin dynamics, but for underdamped Langevin dynamics the relative path probability might not exist. Fortunately, when reweighting a MD simulation, the path expected value is not calculated for time-continuous paths but for time-discretized paths. As explained above, an accurate reweighting method needs to calculate the relative path probability at the time resolution at which the path is produced. Thus, depending on the integrator used to propagate the underdamped Langevin dynamics, the relative path probability density may exist after all, and Girsanov reweighting may become possible. Our approach is therefore not to discretize the continuous path integral.[33]. Instead we start from already existing algorithms to propagate the equation of motion for underdamped Langevin dynamics and derive the relative path probability for the resulting time-discretized paths.

Girsanov reweighting for underdamped Langevin dynamics has first been reported in Refs. 41 and 42. In Ref. 43 we introduced a formulation of the path probability ratio as a function of the random numbers generated during the simulation potential at V and a random number difference to $\widetilde{V}$, which we called reweighting on-the-fly. This allowed us on the one hand to efficiently calculate part of the relative path probability already during the simulation. On the under hand, it allowed us to approximate the relative path probability for underdamped Langevin dynamics. With this approximation, we could reweight metadynamics simulations of the folding equilibrium of β-hairpin peptide[44]. In Ref. 45 we analyzed this approximation and derived the path probability ratio for a simple Langevin integrator.

The goal of this contribution is to develop a general approach to derive the path probability for Langevin integrators and to analyze whether the relative path probability obeys absolute continuity. We focus on symmetric splitting methods for underdamped Langevin dynamics[46–49], and additionally include a closely related[50] variant[51,52] which is used as default Langevin thermostat in several MD simulation programs[53–55]. For methods that obey absolute continuity, and thus can be used for Girsanov reweighting, we provide an expression for the relative path probability.

We chose symmetric splitting methods, because their derivation is documented in great detail[46–49,56], which provides an easy entry point for our analysis. Additionally, the convergence properties of this class of integrators are well-understood[48,57–59]. However, the development of integrators for underdamped Langevin dynamics has been a very active field for decades and many other algorithms have been proposed[60–75]. We believe our approach to derive the path probability ratio can be applied to these Langevin integrators, too.

The article is structured as follows: In sections II and III we review the theory of Girsanov reweighting and of symmetric splitting algorithms. Sections IV and V contain our analysis of these integrators and the derivation of the relative path probabilities. In section VI we introduce a graphical representation of Langevin integrators that helped us to visualize and classify the effects of changeing the potential energy on the behaviour of the Langevin integrator. Section VII contains a short discussion and outlook.

II. GIRSANOV REWEIGHTING

A. Equation of motion, path probability density, and path integral

Consider a particle with mass m that moves in a one-dimensional position space $q \in \mathbb{R}$ according to underdamped Langevin dynamics

$$\begin{aligned}\dot{q} &= \frac{p}{m} \\ \dot{p} &= -\nabla_q V(q) - \xi p + \sqrt{2\xi k_B T m}\,\eta(t)\,,\end{aligned} \tag{1}$$

In eq. 1, $V(q)$ is the potential energy function, $\nabla_q = \partial/\partial q$ denotes the gradient with respect to the position coordinate, ξ is a collision or friction rate (in units of s^{-1}), T is the temperature and k_B is the Boltzmann constant. $\eta \in \mathbb{R}$ is an uncorrelated Gaussian white noise with unit variance centered at zero $\langle \eta(t)\eta(t')\rangle = \delta(t-t')$, where $\delta(t-t')$ is the Dirac delta-function. We use the dot-notation for derivatives with respect to time: $\dot{q} = \partial q/\partial t$. $x(t) = (q(t), p(t)) \in \Gamma \subset \mathbb{R}^2$ denotes the state of the system at time t, which consists of positions $q(t)$ and conjugated momenta $p(t) = m\dot{q}(t)$. Γ is called state space or phase space of the system.

A Langevin integrator yields a time-discretised solution of eq. 1: $\mathbf{x} = (x_0, x_1, x_2, \dots x_n)$. The path $\mathbf{x}$ is a sequence of $n+1$ states $x_k = (q_k, p_k) \in \Gamma$, where consecutive states x_k and x_{k+1} are separated by a (small) time step Δt, q_k is the position at time $k\Delta t$, and p_k is the momentum at time $k\Delta t$. $x_0 = (q_0, p_0)$ is the initial state of the path, and $\tau = n\Delta t$ is the path length.

A time-discretized path $\mathbf{x}$ is an element of the space $\mathcal{S} = \Gamma^{n+1}$. Its path probability density is $\mathcal{P}[\mathbf{x}] = p(x_0) \cdot \mathcal{P}[x_1 \dots x_n | x_0]$, where we wrote the path probability as a product of the probability density of the intial state $p(x_0)$ and the conditional probability of the path $\mathcal{P}[x_1 \dots x_n | x_0]$, given that the path starts in x_0. The Langevin integrators considered in this contribution implement a Markov process. That is, the probability to observe the state x_{k+1} at time $t = (k+1)\Delta t$ depends only on the previous state x_k at time $t = k\Delta t$ and not on any of the states before that, i.e. $p(x_{k+1}|x_k, x_{k-1} \dots x_0) = p(x_{k+1}|x_k)$. The path probability density to observe a particular path $\mathbf{x}$ can then be written as a product of the single-step transition probabilities $p(x_{k+1}|x_k)$

$$P[\mathbf{x}] = p(x_0) \cdot P[x_1 \dots x_n | x_0] = p(x_0) \cdot \prod_{k=0}^{n-1} p(x_{k+1}|x_k)\,. \tag{2}$$

The probability density of the initial state depends on the setup of the computational experiment. Here, we assume that the path $\mathbf{x}$ is a short snippet of a long equilibrium trajectory. Then we can assume that $p(x_0)$ is distributed according to the Boltzmann distribution

$$p(x_0) = p(q_0, p_0) = \frac{1}{Z} \exp\left(-\frac{V(q_0)}{k_B T}\right) \cdot \frac{1}{\sqrt{2\pi k_B T m}} \exp\left(-\frac{1}{k_B T}\frac{p_0^2}{2m}\right)\,, \tag{3}$$

where $Z = \int_{-\infty}^{\infty} \mathrm{d}q_0 \, \exp\left(-\frac{V(q_0)}{k_B T}\right)$ is the classical partition function. The functional form of the single-step transition probability depends on the Langevin integrator, and it is the aim of this contribution to analyze $p(x_{k+1}|x_k)$ for various integrators.

The path probability density $P[\mathbf{x}]$ is normalised as

$$\int_{\mathcal{S}} \mathcal{D}\mathbf{x}\, \mathcal{P}[\mathbf{x}] = \int_{x_0\in\Gamma} \int_{x_1\in\Gamma} \cdots \int_{x_n\in\Gamma} \mathrm{d}x_0 \mathrm{d}x_1 \dots \mathrm{d}x_n \; \mathcal{P}[\mathbf{x}] = 1\,, \tag{4}$$

where the first equality defines the path integral $\int_{\mathcal{S}} \mathcal{D}\mathbf{x} \dots$.

Let $s : \mathcal{S} \to \mathbb{R}$ be a path observable, i.e. a function that maps a time-discretised path to a number. The path expected value of this observable is

$$\langle s \rangle = \int \mathcal{D}\mathbf{x}\, \mathcal{P}[\mathbf{x}] s[\mathbf{x}] = \int_{x_0\in\Gamma} \int_{x_1\in\Gamma} \cdots \int_{x_n\in\Gamma} \mathrm{d}x_0 \mathrm{d}x_1 \dots \mathrm{d}x_n \; \mathcal{P}[\mathbf{x}] s[\mathbf{x}]\,, \tag{5}$$

Assuming ergodicity, this path expected value can be estimated from a set of N paths $(\mathbf{x}_1, \mathbf{x}_2 \dots \mathbf{x}_N)$ that has been sampled according to $\mathcal{P}[\mathbf{x}]$

$$\langle s \rangle = \lim_{N\to\infty} \frac{1}{N} \sum_{i=1}^{N} s[\mathbf{x}_i]\,. \tag{6}$$

A short comment on notation: we denote functions of paths $\mathbf{x}$ with square brackets around the argument, and functions of states $x = (q, p)$ with round brackets.

B. Girsanov reweighting

In Girsanov reweighting, one samples paths at a simulation potential $V(q)$, and from this sample one estimates path expected values at a target potential

$$\widetilde{V}(q) = V(q) + U(q)\,, \tag{7}$$

where $U(q)$ is called bias or perturbation potential. Let us point out the sign convention. In eq. 7, we add the perturbation U to the simulation potential V, which is the convention used in the literature on path reweighting. The literature on enhanced sampling simulations uses the opposite sign convention, i.e. the bias is subtracted from the simulation potential to obtain to the true (target) potential: $\widetilde{V} = V - U_{\mathrm{enh.\,samp.}}$. Thus, if Girsanov reweighting is used to unbias enhanced sampling simulations, the bias in eq. 7 is $U = -U_{\mathrm{enh.\,samp.}}$.

We assume that $\widetilde{V}$ represents a typical molecular potential, i.e. a function that has infinite discontinuities whenever two atoms occupy the same position, but is continuous and differentiable everywhere else. We further assume that $U(q)$ respects these discontinuities and does not introduce any new discontinuities. In practice this means that one cannot use soft-core potentials[76,77] to construct $U(q)$.

Formally, one can reweight the path expected value at the target potential as

$$\widetilde{\langle s\rangle} = \int \mathcal{D}\mathbf{x}\, \widetilde{\mathcal{P}}[\mathbf{x}]s[\mathbf{x}] = \int \mathcal{D}\mathbf{x}\, g(x_0)M[\mathbf{x}|x_0]\,\mathcal{P}[\mathbf{x}]s[\mathbf{x}]\,, \tag{8}$$

where $\widetilde{\mathcal{P}}[\mathbf{x}]$ is the path probability density at $\widetilde{V}$, and

$$g(x_0)\cdot M[\mathbf{x}|x_0] = \frac{\widetilde{p}(x_0)}{p(x_0)}\cdot\frac{\widetilde{\mathcal{P}}[x_1\dots x_n|x_0]}{\mathcal{P}[x_1\dots x_n|x_0]} \tag{9}$$

is the path reweighting factor. If $\widetilde{p}(x_0)$ and $p(x_0)$ are given by eq. 3 (for $\widetilde{V}$ and V, respectively), then the relative weight of the initial state is

$$g(x_0) = \frac{\widetilde{p}(x_0)}{p(x_0)} = \frac{Z}{\widetilde{Z}}\exp\left(-\frac{1}{k_BT}U(q_0)\right)\,. \tag{10}$$

If $M[\mathbf{x}|x_0]$ exists and one can find a computable expression for it, then one can estimate the path expected value at the target potential, $\widetilde{\langle s\rangle}$ from paths sampled at the simulation potential $(\mathbf{x}_1, \mathbf{x}_2\dots\mathbf{x}_N)$ by reweighting their contribution to the estimator

$$\widetilde{\langle s\rangle} = \lim_{N\to\infty}\frac{1}{N}\sum_{i=1}^{N} g(x_{i,0})M[\mathbf{x}_i|x_{i,0}]\cdot s[\mathbf{x}_i]\,. \tag{11}$$

where $g(x_{i,0})M[\mathbf{x}_i|x_{i,0}]$ is the relative weight of path $\mathbf{x}_i$ a the target potential $\widetilde{V}$. Whether $M[\mathbf{x}|x_0]$ exists, depends on the underlying dynamics, specifically on the condition of absolute continuity.

C. Absolute continuity

The path probability density $\widetilde{\mathcal{P}}[\mathbf{x}]$ at the target potential and the path probability density $\mathcal{P}[\mathbf{x}]$ at the simulation potential are absolutely continuous with respect to each other[26,27,43,78] if

$$\widetilde{\mathcal{P}}[S] = \int_{S\subset\mathcal{S}}\mathcal{D}\mathbf{x}\,\widetilde{\mathcal{P}}[\mathbf{x}] = 0 \Leftrightarrow \mathcal{P}[S] = \int_{S\subset\mathcal{S}}\mathcal{D}\mathbf{x}\,\mathcal{P}[\mathbf{x}] = 0\,, \tag{12}$$

where $S = S_0\times S_1\times\dots\times S_n$ is a small subset of the path space $\mathcal{S}$, a and S_i is a small region in phase space Γ in which x_i may be found. That is, any region of the path space $\mathcal{S}$ that is sampled by the dynamics at $\widetilde{V}(x)$ also needs to be sampled by the dynamics at $V(x)$, and vice versa. Otherwise the relative path probability density in eq. 9 is not defined.

(Strictly speaking only $\widetilde{\mathcal{P}}$ needs to be absolutely continuous with respect to $\mathcal{P}$. But since this almost surely implies[27] that also $\mathcal{P}$ is absolutely continuous with respect to $\widetilde{\mathcal{P}}$, we here omit this distinction.)

If $P[\mathbf{x}]$ and $\widetilde{P}[\mathbf{x}]$ can be decomposed as in eq. 2, absolute continuity is fulfilled if

$$\widetilde{p}(S_0) = \int_{S_0}\mathrm{d}x_0\,\widetilde{p}(x_0) = 0 \Leftrightarrow p(S_0) = \int_{S_0}\mathrm{d}x_0\,p(x_0) = 0 \tag{13}$$

and if

$$\widetilde{p}(S_{k+1}|x_k) = \int_{S_{k+1}} \mathrm{d}x_{k+1}\, \widetilde{p}(x_{k+1}|x_k) \ = 0 \Leftrightarrow p(S_{k+1}|x_k) = \int_{S_{k+1}} \mathrm{d}x_{k+1}\, p(x_{k+1}|x_k) \ = 0 \tag{14}$$

for all k with $k = 0, 1 \ldots, n-1$. Eq. 13 is fulfilled if $\widetilde{p}(x_0)$ and $p(x_0)$ are given by eq. 3 (for $\widetilde{V}$ and V, respectively), but other choices are also possible. For overdamped Langevin dynamics, the Girsanov theorem guarantees that - for sensible choices of $U(q)$ (see section II B) - eq. 14 is fulfilled. Thus for overdamped Langevin dynamics, $M[\mathbf{x}|x_0]$ exists, and for overdamped time-discretized paths generated by the Euler-Maruyama scheme[27,28], the computable expression for $M[\mathbf{x}|x_0]$ is well-established[27,31,33,35,42–44]. By contrast, the existence of $M[\mathbf{x}|x_0]$ cannot be guaranteed for underdamped Langevin dynamics (eq. 1). It may however exist for time-discretized paths of underdamped Langevin dynamics. In sections IV and V, we will discuss the existence of $M[\mathbf{x}|x_0]$ for symmetric splitting schemes[46–49] for underdamped Langevin dynamics.

D. Reweighting on-the-fly

To derive $M[\mathbf{x}|x_0]$, we use reweighting on-the-fly (proposed in Ref. 43 and discussed in more detail in Ref. 45). In this approach, the reweighting factor is formulated in terms of the random numbers η_k, which are generated during the simulation at V, and a random number difference $\Delta\eta_k$, which depends on the gradient of the bias ∇U. Both properties are easily accessible during the simulation, and part of the reweighting factor can be precalculated on-the-fly during the simulation. This makes the actual reweighting (eq. 11) computationally simple and efficient.

A stochastic integrator generates a sequence of random numbers $\boldsymbol{\eta} = (\eta_0, \eta_1, \ldots, \eta_{n-1})$ to represent the random force in a stochastic equation of motion (e.g. eq. 1). The random numbers η_k are usually drawn from a Gaussian normal distribution with zero mean and unit variance

$$P(\eta_k) = \sqrt{\frac{1}{2\pi}} \exp\left(-\frac{1}{2}\eta_k^2\right) . \tag{15}$$

If the initial state x_0 has been set and $\boldsymbol{\eta}$ has been generated, the path $\mathbf{x}|x_0 = (x_1 \ldots x_n|x_0)$ is fully determined. Thus, the stochastic integrators can be viewed as a map from a random number sequence $\boldsymbol{\eta}$ to a path $\mathbf{x}|x_0$. If the map is bijective (one-to-one mapping between random number sequence and path), the conditional path probability density is equal to the probability of drawing the corresponding sequence of random numbers:

$$\mathcal{P}[\mathbf{x}|x_0] = \mathcal{P}[\boldsymbol{\eta}] = \frac{1}{\sqrt[n]{2\pi}} \exp\left(-\frac{1}{2}\sum_{k=0}^{n-1}\eta_k^2\right) . \tag{16}$$

The stochastic integrator evaluates the gradient of the potential V, and therefore the map depends on V. If the potential is modified from V to the target potential $\widetilde{V}$, the map changes accordingly, and a different random number sequence $\widetilde{\boldsymbol{\eta}}$ is needed to generate the same path $\mathbf{x}|x_0$. The conditional path probability density at $\widetilde{V}$ is then equal to the probability of drawing $\widetilde{\boldsymbol{\eta}}$: $\widetilde{\mathcal{P}}[\mathbf{x}|x_0] = \mathcal{P}[\widetilde{\boldsymbol{\eta}}]$.

At each integration step k, the random numbers η_k and $\tilde{\eta}_k$ differ by $\Delta\eta_k$:

$$\tilde{\eta}_k = \eta_k + \Delta\eta_k \, . \tag{17}$$

This allows us to write the relative conditional path probability density as[45]

$$M[\mathbf{x}|x_0] = \frac{\widetilde{\mathcal{P}}[\mathbf{x}|x_0]}{\mathcal{P}[\mathbf{x}|x_0]} = \frac{\mathcal{P}[\widetilde{\boldsymbol{\eta}}]}{\mathcal{P}[\boldsymbol{\eta}]} = \exp\left(-\sum_{k=0}^{n-1}\eta_k \cdot \Delta\eta_k\right) \cdot \exp\left(-\frac{1}{2}\sum_{k=0}^{n-1}(\Delta\eta_k)^2\right) . \tag{18}$$

The random numbers η_k are recorded during the simulation at V; the expression for $\Delta\eta_k$ depends on the stochastic integrator.

The discussion so far applies to stochastic integrators that generate one random number η_k per integration step and degree of freedom. Some symmetric splitting methods for underdamped Langevin dynamics however generate two random numbers $(\eta_k^{(1)}, \eta_k^{(2)})$ per integration step and degree of freedom. The two random numbers are drawn independently from a Gaussian normal distribution with zero mean and unit variance, i.e. $P(\eta_k^{(1)}, \eta_k^{(2)}) = P(\eta_k^{(1)})P(\eta_k^{(2)})$, and $P(\eta_k^{(1)})$ and $P(\eta_k^{(2)})$ are given by eq. 15. Thus, an integrator with two random numbers per integration step can be viewed as a map from two sequences of random numbers $(\boldsymbol{\eta}^{(1)}, \boldsymbol{\eta}^{(2)})$ to a path $\mathbf{x}|x_0$, where $\boldsymbol{\eta}^{(1)} = (\eta_0^{(1)}, \eta_1^{(1)}, \dots, \eta_{n-1}^{(1)})$ and $\boldsymbol{\eta}^{(2)} = (\eta_0^{(2)}, \eta_1^{(2)}, \dots, \eta_{n-1}^{(2)})$. If the map is bijective, the conditional path probability density is equal to the probability of drawing the two random number sequences:

$$\mathcal{P}[\mathbf{x}|x_0] = \mathcal{P}[\boldsymbol{\eta}^{(1)}, \boldsymbol{\eta}^{(2)}] = \frac{1}{\sqrt[n]{2\pi}} \exp\left(-\frac{1}{2}\sum_{k=0}^{n-1}\left(\eta_k^{(1)}\right)^2\right) \cdot \frac{1}{\sqrt[n]{2\pi}} \exp\left(-\frac{1}{2}\sum_{k=0}^{n-1}\left(\eta_k^{(2)}\right)^2\right) \tag{19}$$

At the target potential $\widetilde{V}$, two different random number sequences $\widetilde{\boldsymbol{\eta}}^{(1)} = (\widetilde{\eta}_0^{(1)}, \widetilde{\eta}_1^{(1)}, \dots, \widetilde{\eta}_{n-1}^{(1)})$ and $\widetilde{\boldsymbol{\eta}}^{(2)} = (\widetilde{\eta}_0^{(2)}, \widetilde{\eta}_1^{(2)}, \dots, \widetilde{\eta}_{n-1}^{(2)})$ are needed to generate the same path $\mathbf{x}$. At each integration step k, the random numbers differ by $\Delta\eta_k^{(1)}$ and $\Delta\eta_k^{(2)}$:

$$\begin{aligned} \widetilde{\eta}_k^{(1)} &= \eta_k^{(1)} + \Delta\eta_k^{(1)} \\ \widetilde{\eta}_k^{(2)} &= \eta_k^{(2)} + \Delta\eta_k^{(2)} \,. \end{aligned} \tag{20}$$

The relative conditional path probability density can then be written as

$$\begin{aligned} M[\mathbf{x}|x_0] &= \frac{\widetilde{\mathcal{P}}[\mathbf{x}\,|\,x_0]}{\mathcal{P}[\mathbf{x}\,|\,x_0]} = \frac{P[\widetilde{\boldsymbol{\eta}}^{(1)}, \widetilde{\boldsymbol{\eta}}^{(2)}]}{P[\boldsymbol{\eta}^{(1)}, \boldsymbol{\eta}^{(2)}]} \\ &= \exp\left(-\sum_{k=0}^{n-1}\eta_k^{(1)}\cdot\Delta\eta_k^{(1)}\right)\cdot\exp\left(-\frac{1}{2}\sum_{k=0}^{n-1}(\Delta\eta_k^{(1)})^2\right)\cdot \\ &\quad \exp\left(-\sum_{k=0}^{n-1}\eta_k^{(2)}\cdot\Delta\eta_k^{(2)}\right)\cdot\exp\left(-\frac{1}{2}\sum_{k=0}^{n-1}(\Delta\eta_k^{(2)})^2\right)\,. \end{aligned} \tag{21}$$

As in eq. 18, the random numbers $\eta_k^{(1)}$ and $\eta_k^{(2)}$ are recorded during the simulation at V, and the expressions for $\Delta\eta_k^{(1)}$ and $\Delta\eta_k^{(2)}$ depend on the integrator.

At this point the obstacle in constructing path reweighting factors for underdamped Langevin dynamics becomes noticeable. In underdamped Langevin dynamics, the state $x_k = (q_k, p_k)$ is a two-dimensional vector. Thus, integrators with two random numbers per integration step map two real numbers to a two-dimensional state space, whereas integrators with one random number map a single real number to a two-dimensional state space. In both cases, $P[\mathbf{x}|x_0]$ can be derived from the integrator equations (see section III and supplementary material), but $M[\mathbf{x}|x_0]$ does not exist for all integrators (see sections IV and V).

III. LANGEVIN INTEGRATORS

A. Equation of motion and splitting methods

Eq. 1 can be reformulated as a vector field

$$\begin{pmatrix} \dot{q} \\ \dot{p} \end{pmatrix} = \underbrace{\begin{pmatrix} p/m \\ 0 \end{pmatrix}}_{A} + \underbrace{\begin{pmatrix} 0 \\ -\nabla_q V(q) \end{pmatrix}}_{B} + \underbrace{\begin{pmatrix} 0 \\ -\xi p + \sqrt{2\xi k_B T m}\,\eta(t) \end{pmatrix}}_{O} \,. \tag{22}$$

Each of the three terms, A, B and O, can be integrated separately to yield the following time-discretized update operators

$$\mathcal{A}\begin{pmatrix} q_k \\ p_k \end{pmatrix} = \begin{pmatrix} q_k + \Delta t \frac{1}{m} p_k \\ p_k \end{pmatrix} = \begin{pmatrix} q_k + a p_k \\ p_k \end{pmatrix} \tag{23a}$$

$$\mathcal{B}\begin{pmatrix} q_k \\ p_k \end{pmatrix} = \begin{pmatrix} q_k \\ p_k - \Delta t \nabla V(q_k) \end{pmatrix} = \begin{pmatrix} q_k \\ p_k + b(q_k) \end{pmatrix} \tag{23b}$$

$$\mathcal{O}\begin{pmatrix} q_k \\ p_k \end{pmatrix} = \begin{pmatrix} q_k \\ e^{-\xi \Delta t} p_k + \sqrt{k_B T m (1 - e^{-2\xi \Delta t})}\, \eta_k \end{pmatrix} = \begin{pmatrix} q_k \\ d\, p_k + f\, \eta_k \end{pmatrix}, \tag{23c}$$

with time step Δt and random number $\eta_k \sim \mathcal{N}(0,1)$, where $\mathcal{N}(\mu, \sigma^2)$ denotes the Gaussian normal distribution with mean μ and variance σ^2. Eqs. 23a – 23c are the time-discretized solutions of their respective parts in the differential equation (eq. 22), where 23c is the result known from the Ornstein-Uhlenbeck process (see Chapter 7.3.1. in Ref. 56). The second equality introduces the following abbreviations to keep the notation manageable

$$a = \Delta t \frac{1}{m} \tag{24a}$$

$$b(q_k) = -\Delta t \nabla V(q_k) \tag{24b}$$

$$d = e^{-\xi \Delta t} \tag{24c}$$

$$f = \sqrt{k_B T m (1 - e^{-2\xi \Delta t})} \tag{24d}$$

where d stands for dissipation and f for the thermal fluctuation.

Particularly accurate Langevin integration schemes can be derived using the (symmetric) operator splitting method, or Strang splitting[70,79]. In these algorithms, some of the update operators (eqs. 23a, 23b, and 23c) are carried out twice during an integration step, but each time with only half a time step $\frac{\Delta t}{2}$. If a step is carried out for only half a time step $\frac{\Delta t}{2}$, we denote the corresponding operator with a prime, e.g.

$$\mathcal{A}'\begin{pmatrix} q_k \\ p_k \end{pmatrix} = \begin{pmatrix} q_k + \frac{\Delta t}{2} \frac{1}{m} p_k \\ p_k \end{pmatrix} = \begin{pmatrix} q_k + a' p_k \\ p_k \end{pmatrix}. \tag{25}$$

Correspondingly, a', b', d' and f' are obtained by replacing Δt with $\Delta t/2$ in eqs. A1a-A1d. For an in-depth discussion on the theory of splitting operators we refer to Refs. 47, 48, 70, 79, and 80 and Chapter 7 in Ref. 81.

In this contribution, we will use the ABO method to illustrate our approach, and we will apply the approach to the following integrators based on eq. 22: ABOBA, BAOAB, OABAO, AOBOA, OBABO (Bussi-Parrinello thermostat), and BOAOB[46–49,58]. These algorithsm are implemented in OpenMM[53] via the package OpenMMTools[59]. We additionally include BAOA[51], because it is implemented in several MD simulations packages[53–55], where it is sometimes called Verlet-Middle integrator[73]. GROMACS implements the GROMACS stochastic dynamics (GSD) method[52], which is equivalent to BAOA[50].

B. Example: ABO method

The Langevin integrator that is constructed by carrying out eqs. 23a, 23b and 23c consecutively is called ABO method (sequential splitting[70,79]). The ABO algorithm yields a less accurate approximation to the actual dynamics than symmetric splitting methods (or equivalently: a small time step Δt is needed to obtain a given accuracy). Here, we use it to illustrate concepts.

The integrator equations of the ABO algorithm are

$$q_{k+1} = q_k + a p_k \tag{26a}$$

$$p_{k+1/2} = p_k + b(q_{k+1}) \tag{26b}$$

$$p_{k+1} = d p_{k+1/2} + f \eta_k \,. \tag{26c}$$

$p_{k+1/2}$ should not be interpreted as an integration by half a time step, but rather as 50% progress in the update of the momenta. Namely, in eq. 26b the momentum is updated according to the forces due to the potential energy function, and in eq. 26c the momentum update due to friction and random forces is carried out. The contributions of these two steps to the total momentum update are by no means equal.

The joint update of the position and momentum, i.e. the update operator of the ABO method $\mathcal{U}_{\mathrm{ABO}}$, is obtained by sequentially applying operators $\mathcal{A}$, $\mathcal{B}$, and $\mathcal{O}$ to the current state $(q_k, p_k)^\top$.

$$\begin{aligned}\begin{pmatrix} q_{k+1} \\ p_{k+1} \end{pmatrix} &= \mathcal{U}_{\mathrm{ABO}} \begin{pmatrix} q_k \\ p_k \end{pmatrix} \\ &= \mathcal{O}\mathcal{B}\mathcal{A} \begin{pmatrix} q_k \\ p_k \end{pmatrix} \\ &= \mathcal{O}\mathcal{B} \begin{pmatrix} q_k + a p_k \\ p_k \end{pmatrix} \\ &= \mathcal{O} \begin{pmatrix} q_k + a p_k \\ p_k + b(q_k + a p_k) \end{pmatrix} \\ &= \begin{pmatrix} q_k + a p_k \\ d p_k + d b(q_k + a p_k) + f \eta_k \end{pmatrix} . \end{aligned} \tag{27}$$

As usual the operators are applied from right to left, and hence the order of the operators in eq. 27 is reversed compared to the name.

The algorithms for each of the integrators in Tab. I as well as their update operators are reported in the supplementary material.

IV. THE IMAGES OF LANGEVIN UPDATE FUNCTIONS

The update operator $\mathcal{U}$ of a Langevin integrator depends parametrically on the random number η_k: when η_k is varied, the updated state (q_{k+1}, p_{k+1}) changes. One can thus interpret the update operator in eq. 27 as a function $\mathcal{U}$ that maps a random number $\eta_k \in \mathbb{R}$ to a point in state space $x_{k+1} = (q_{k+1}, p_{k+1})^\top \in \Gamma$. The current state (q_k, p_k) is treated as a parameter of $\mathcal{U}$. The image of the update function $\mathcal{U}$, i.e. "the set of all output values it may produce.", is the set of all points in state space that can theoretically be reached from (q_k, p_k) within a single integration time step. Note that the image only reflects whether or not a certain point can be reached. The probability with which this point would be generated during an integration time step does not play a role when discussing the image of $\mathcal{U}$. Besides η_k and (q_k, p_k), the update function $\mathcal{U}$ also depends on the potential energy function V. Thus the image of $\mathcal{U}$ might change if V is varied.

A. One random number per integration time step

First, we consider Langevin integrators that use a single random number per integration step, i.e. one $\mathcal{O}$-step (eq. 23c) per integration step k. In Tab. I, these are ABO, ABOBA, BAOAB and BAOA/GSD.

The following realization is crucial: given an initial state x_k, the image of $\mathcal{U}$ is not the entire state space Γ, but a one-dimensional curve C_{1d} within Γ. This one-dimensional curve is parametrized by η_k. Formally, we can characterize the function $\mathcal{U}$ as

$$\begin{aligned} \mathcal{U} :&\ \mathbb{R} \to C_{1d} \subset \Gamma \\ \mathcal{U} :&\ \eta_k \mapsto x_{k+1} . \end{aligned} \tag{28}$$

See Ref. 82 for an overview of parametrized curves and parametric equations.

Mathematically, it is not surprising that the image is one-dimensional, since it is impossible to map the one-dimensional number line $\mathbb{R}$ to a two-dimensional space. Algorithmically

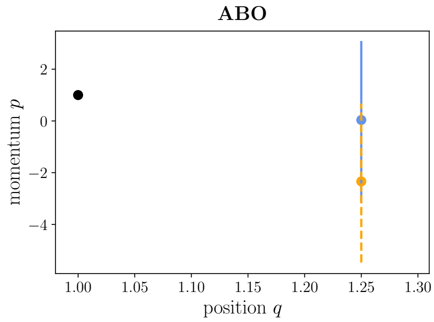

FIG. 1. Initial state $(q_k, p_k)^\top$ (black dot) and image of the update function $\mathcal{U}_{\mathrm{ABO}}(\eta_k; x_k, V)$ for an unscaled potential (blue line) and a scaled potential (orange line) for the ABO method. The image of the update function contains all possible states $(q_{k+1}, p_{k+1})^\top$ that can be reached from $(q_k, p_k)^\top$ within one integration time step Δt.
Parameters: $k_B, m, T, \xi = 1$, $\Delta t = 0.25$, $(q_k, p_k)^\top = (1, 1)^\top$, $V(q) = (q^2 - 1)^2 + q$, $\widetilde{V}(q) = 4.2 \cdot (q^2 - 1)^2 + q$ and $\eta \in [-5, 5]$.

this means that, given an initial state x_k, not all states in state space Γ can be reached by a single iteration of the integrator. Rather, the accessible states lie on C_{1d}, and which precise point on this line is obtained depends on η_k.

For the ABO method, this parametrization of C_{1d} by η_k can be made explicit by reformulating eq. 27 as

$$\begin{pmatrix} q_{k+1} \\ p_{k+1} \end{pmatrix} = \mathcal{U}_{\mathrm{ABO}}(\eta_k; x_k, V) = \begin{pmatrix} q_{k+1} \\ \bar{p}_{k+1} \end{pmatrix} + \begin{pmatrix} 0 \\ f \end{pmatrix} \eta_k \tag{29}$$

with $q_{k+1} = q_k + ap_k$ and $\bar{p}_{k+1} = dp_k + db(q_k + ap_k)$. That is, the algorithm first moves the system to $(q_{k+1}, \bar{p}_{k+1})^\top$ and then adjusts the momenta by $(0, f)^\top \eta_k$. Consequently, all accessible states of $\mathcal{U}_{\mathrm{ABO}}(\eta_k; x_k, V)$ lie on a vertical through $(q_{k+1}, \bar{p}_{k+1})^\top$.

Fig. 1 illustrates the image of $\mathcal{U}_{\mathrm{ABO}}(\eta_k; x_k, V)$. The initial point $(q_k, p_k) = (1, 1)$ is marked as a black dot. The point $(q_{k+1}, \bar{p}_{k+1})^\top$ for the potential $V(q) = (q^2 - 1)^2 + q$ is shown as a blue dot and acts as the support point for the image of $\mathcal{U}_{\mathrm{ABO}}(\eta_k; x_k, V)$. Varying η_k from -5 to +5 then yields the blue line, i.e. the image of $\mathcal{U}_{\mathrm{ABO}}(\eta_k; x_k, V)$ for $\eta_k \in [-5, 5]$. When the potential is changed to $\widetilde{V}(q) = 4.2 \cdot (q^2 - 1)^2 + q$, the point $(q_{k+1}, \bar{p}_{k+1})^\top$ shifts to the orange point. Varying η_k from -5 to +5 yields the image of $\mathcal{U}_{\mathrm{ABO}}(\eta_k; x_k, \widetilde{V})$ for $\eta_k \in [-5, 5]$, shown as the dashed orange line in Fig. 1. For arbitrary values of η_k, the images of the two functions coincide. Thus, the image of the update function of the ABO method, i.e. the set of possible updated states (q_{k+1}, p_{k+1}), does not depend on the potential V.

The update functions for ABOBA, BAOAB and BAOA/GSD are derived in the supplementary material. Their images are summarized in the second column of Tab. I and illustrated in Fig. 2. As in Fig. 1, the current state (q_k, p_k) is shown as a black dot, the support points for the image for two different potentials are shown as blue and orange dots, and the corresponding images for $\eta_k \in [-5, +5]$ are shown as blue and orange lines. Fig. 2 also contains the diagram for a Langevin integrator with two random numbers, AOBOA, which will be discussed in the following section.

Two aspects of the images of the update functions in Fig. 2 are important to point out. First, for ABOBA, BAOA/GSD and AOBOA, the possible updated states depend linearly on η_k, and thus the image is a line L_{1d} in the state space Γ. By contrast, the possible updated states of BAOAB depend non-linearly on η_k, and the image is a curve C_{1d}. Second, in ABOBA and AOBOA the image does not depend on the potential, whereas in BAOAB and BAOA/GSD the image changes if V is varied.

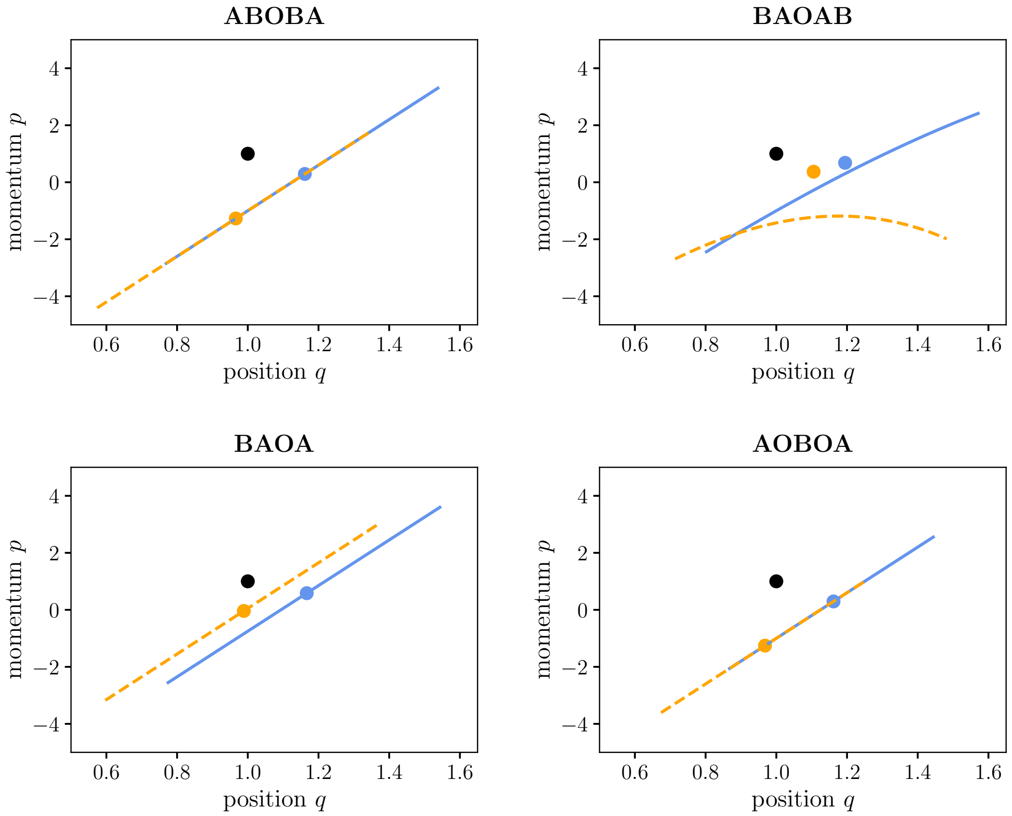

FIG. 2. Initial state $(q_k, p_k)^\top$ (black dot) and image of the update function $\mathcal{U}(\eta_k; x_k, V)$ for an unscaled potential (blue line) and a scaled potential (orange line) for the ABOBA, BAOAB, BAOA/GSD and AOBOA method. The image of the update function contains all possible states $(q_{k+1}, p_{k+1})^\top$ that can be reached from $(q_k, p_k)^\top$ within one integration time step Δt.
Parameters: $k_B, m, T, \xi = 1$, $\Delta t = 0.25$, $(q_k, p_k)^\top = (1, 1)^\top$, $V(q) = (x^2-1)^2 + x$, $\widetilde{V}(q) = 4.2 \cdot (x^2-1)^2 + x$, $\eta \in [-5, 5]$, or $\eta^{\mathrm{comb}} \in [-5, 5]$.

B. Two random numbers per integration time step

Next, we consider Langevin integrators that generate two random numbers per integration step, i.e. two $\mathcal{O}$-half-steps (eq. 23c with $\Delta t/2$ instead of Δt) per integration step k. In Tab. I, these are AOBOA, BOAOB, OBABO/BP, and OABAO. Their update functions are derived in the supplementary material.

The image of update functions of Langevin integrators with two random numbers can be the entire phase space Γ. That is, given an initial state (q_k, p_k), any point in phase space can be reached within a single integration time step, albeit mostly with very low probability. For BOAOB and OBABO/BP this is indeed the case. Both of their update functions have the following form

$$\begin{pmatrix} q_{k+1} \\ p_{k+1} \end{pmatrix} = \begin{pmatrix} \bar{q}_{k+1} \\ \bar{p}_{k+1} \end{pmatrix} + \begin{pmatrix} 0 \\ c \cdot b'(\bar{q}_{k+1} + af'\eta_k^{(1)}) \end{pmatrix} + \begin{pmatrix} af' \\ d'f' \end{pmatrix} \eta_k^{(1)} + \begin{pmatrix} 0 \\ f' \end{pmatrix} \eta_k^{(2)}\,, \tag{30}$$

where $\eta_k^{(1)}$ and $\eta_k^{(2)}$ are the two random numbers, and $c = 1$ for BOAOB, and $c = d'$ for OBABO/BP. The functions first move the system deterministically to a support point $(\bar{q}_{k+1}, \bar{p}_{k+1})$. BOAOB and OBABO/BP differ in the way this deterministic update is calculated (see supplementary material), but have analogous subsequent terms in the update function. (BOAOB: $\bar{q}_{k+1} = q_k + ad'p_k + ad'b'(q_k)$ and $\bar{p}_{k+1} = d'd'p_k + d'd'b'(q_k)$. OBABO/BP: $\bar{q}_{k+1} = q_k + ad'p_k + ab'(q_k)$ and $\bar{p}_{k+1} = d'd'p_k + d'b'(q_k)$.) From the support point, the momentum is slightly adjusted in the second term eq. 30, which however depends on the random number $\eta_k^{(1)}$ and thus represents a partly randomized update of the momentum. The last two terms in eq. 30 randomize the position and the momentum. Note that by scaling $\eta_k^{(1)}$ between $-\infty$ and $+\infty$, one can access any position, and by scaling $\eta_k^{(2)}$ one can access any momentum. Thus, the image of the update functions of BOAOB and OBABO/BP is the entire phase space Γ (Tab. I).

The update function of OABAO differs in a crucial point from eq. 30: in the second term both position and the momentum get a partly randomized update. This partly randomized update depends on the potential energy function via $b(q)$. One can construct cases, in which the update of the positions in the second term and the update in the third term compensate each other, and the images collapses from Γ to a line (see supplementary material). Thus, the image of the update function of OABAO depends on the potential, and the existence of $M[\mathbf{x}|x_0]$ and analytical expressions for $\Delta\eta_k^{(1)}$ and $\Delta\eta_k^{(2)}$ need to be discussed in the context of specific potentials V and $\widetilde{V}$. We will therefore exclude OABAO from the subsequent analysis.

AOBOA generates two random numbers $\eta_k^{(1)}$ and $\eta_k^{(2)}$ per integration time step. But $\eta_k^{(1)}$ and $\eta_k^{(2)}$ do not affect the position and the momentum independently as in eq. 30, and several combinations of $\eta_k^{(1)}$ and $\eta_k^{(2)}$ lead to the same updated state (q_{k+1}, p_{k+1}). In fact, one can combine $\eta_k^{(1)}$ and $\eta_k^{(2)}$ into an effective random number

$$\eta_k^{\mathrm{comb}} = d'\eta_k^{(1)} + \eta_k^{(2)} \sim \mathcal{N}(0, d'^2 + 1)\,. \tag{31}$$

and formulate the update function in terms of η_k^{comb}

$$\begin{pmatrix} q_{k+1} \\ p_{k+1} \end{pmatrix} = \begin{pmatrix} \bar{q}_{k+1} \\ \bar{p}_{k+1} \end{pmatrix} + \begin{pmatrix} a' \\ 1 \end{pmatrix} f'\eta^{\mathrm{comb}} \tag{32}$$

with $\bar{q}_{k+1} = q_k + (a' + a'd'd')p_k + a'd'b(q_k + a'p_k)$ and $\bar{p}_{k+1} = d'd'p_k + d'b(q_k + a'p_k)$ (see supplementary material). The AOBOA method first generates a deterministic update and moves the system to the support point $(\bar{q}_{k+1}, \bar{p}_{k+1})$, and then randomizes the position and momentum along a line with slope $(a', 1)$. Thus, the image of this update function is a line L_{1d} through the state space Γ (see Fig. 2). Note that any combination of $\eta_k^{(1)}$ and $\eta_k^{(2)}$ that yields the same value η_k^{comb}, will yield the same updated state (q_{k+1}, p_{k+1}).

V. ABSOLUTE CONTINUITY AND PATH REWEIGHTING FACTOR

The notion of absolute continuity is closely related to the image of update function. Recall that absolute continuity implies that the same regions of path space are sampled by the dynamics at $\widetilde{V}(x)$ and by the dynamics at $V(x)$. If the image of the update function depends on the potential energy, transitions $(q_k, p_k) \to (q_{k+1}, p_{k+1})$ that are possible at V are impossible at $\widetilde{V}$. Thus, the corresponding path probabilities are not absolutely continuous with respect to each other, and $M[\mathbf{x}|x_0]$ does not exist for the corresponding integrators. Among the integrators we considered here, this is the case for BAOAB and BAOA/GSD (Tab. I). Phase-space trajectories generated by these two integrators cannot be reweighted.

By contrast, the images of the update functions of ABO, ABOBA, AOBOA, BOAOB and OBABO/BP do no depend on the potential energy function. Consequently, any transition $(q_k, p_k) \to (q_{k+1}, p_{k+1})$ that is possible at V is also possible at $\widetilde{V}$. The corresponding path probabilities are absolutely continuous with respect to each other, and $M[\mathbf{x}|x_0]$ exists. Phase-space trajectories generated by these integrators can be reweighted (Tab. I).

Having identified integrators of underdamped Langevin dynamics for which Girsanov reweighting is possible, we next derive computable expressions for $M[\mathbf{x}|x_0]$ using the

integrator	**update** u	**image at** V **and** $\widetilde{V}$	**absolute continuity**	**reweighting in phase space**
ABO	$\mathbb{R} \to L_{1d}$	$L_{1d} = \widetilde{L}_{1d}$	yes	$\Delta\eta_k = \frac{d}{f}\Delta t \nabla U(q_{k+1})$
ABOBA	$\mathbb{R} \to L_{1d}$	$L_{1d} = \widetilde{L}_{1d}$	yes	$\Delta\eta_k = \frac{(d+1)}{f}\frac{\Delta t}{2}\nabla U(q_{k+1/2})$
BAOAB	$\mathbb{R} \to C_{1d}$	$C_{1d} \neq \widetilde{C}_{1d}$	no	n/a
BAOA/GSD	$\mathbb{R} \to L_{1d}$	$L_{1d} \neq \widetilde{L}_{1d}$	no	n/a
AOBOA	$\mathbb{R}^2 \to L_{1d}$	$L_{1d} = \widetilde{L}_{1d}$	yes	$\Delta\eta_k^{\mathrm{comb}} = \frac{d'}{f'}\Delta t \nabla U(q_{k+1/2})$ $\eta_k^{\mathrm{comb}} = d'\eta_k^{(1)} + \eta_k^{(2)}$
BOAOB	$\mathbb{R}^2 \to \Gamma$	Γ in both cases	yes	$\Delta\eta_k^{(1)} = \frac{d'}{f'}\frac{\Delta t}{2}\nabla U(q_k)$ $\Delta\eta_k^{(2)} = \frac{1}{f'}\frac{\Delta t}{2}\nabla U(q_{k+1})$
OBABO/BP	$\mathbb{R}^2 \to \Gamma$	Γ in both cases	yes	$\Delta\eta_k^{(1)} = \frac{1}{f'}\frac{\Delta t}{2}\nabla U(q_k)$ $\Delta\eta_k^{(2)} = \frac{d'}{f'}\frac{\Delta t}{2}\nabla U(q_{k+1})$
OABAO	depends on V and $\widetilde{V}$.			

TABLE I. Image of integrator update function and corresponding expressions for the random number difference

reweighting-on-the-fly approach (eqs. 18 and 21). The mathematically formal way to derive an expression for $\Delta\eta_k = \widetilde{\eta}_k - \eta_k$ (eq. 17) goes as follows. We denote the update function of integrator I at the simulation potential by $\mathcal{U}_I(\eta_k; x_k, V)$, and the update function of the same integrator at the target potential by $\mathcal{U}_I(\widetilde{\eta}_k; x_k, \widetilde{V})$. We require that both update operators yield the same update $(q_{k+1}, p_{k+1})^\top$ given the initial state $x_k = (q_k, p_k)^\top$, i.e. the path remains unchanged,

$$\begin{pmatrix} q_{k+1} \\ p_{k+1} \end{pmatrix} = \mathcal{U}_I(\eta_k; x_k, V) = \mathcal{U}_I(\widetilde{\eta}_k; x_k, \widetilde{V})\,. \tag{33}$$

Thus, we need to solve

$$\begin{pmatrix} 0 \\ 0 \end{pmatrix} = \mathcal{U}_I(\eta_k; x_k, V) - \mathcal{U}_I(\widetilde{\eta}_k; x_k, \widetilde{V}) \tag{34}$$

for $\Delta\eta_k$, i.e. we determine the change in the random number that yields the same path even though the potential has changed.

A. One random number per integration time step

We again use the ABO method to illustrate how to derive an expression for $\Delta\eta_k$. Its update function at the simulation potential V is eq. 27, and at the target potential $\widetilde{V}(q)$ it is

$$\begin{pmatrix} q_{k+1} \\ p_{k+1} \end{pmatrix} = \mathcal{U}_{\mathrm{ABO}}(\widetilde{\eta}_k; x_k, \widetilde{V}) = \begin{pmatrix} q_k + a p_k \\ d p_k + d\widetilde{b}(q_k + a p_k) + f\widetilde{\eta}_k \end{pmatrix}, \tag{35}$$

where

$$\widetilde{b}(q) = b(q) - \Delta t \nabla U(q)\,. \tag{36}$$

Inserting eq. 27 and 35 into eq. 34 yields

$$\begin{aligned}\begin{pmatrix}0\\0\end{pmatrix} &= \mathcal{U}_{\mathrm{ABO}}(\eta_k; x_k, V) - \mathcal{U}_{\mathrm{ABO}}(\widetilde{\eta}_k; x_k, \widetilde{V}) \\ &= \begin{pmatrix}0\\ d\cdot\left(b(q_k + ap_k) - \widetilde{b}(q_k + ap_k)\right) + f\cdot(\eta_k - \widetilde{\eta}_k)\end{pmatrix} \\ &= \begin{pmatrix}0\\ d\Delta t\nabla U(q_{k+1}) - f\cdot\Delta\eta_k\end{pmatrix}, \end{aligned} \tag{37}$$

where, in the last line, we replaced $q_k + ap_k$ by q_{k+1} (eq. 26a). Thus, for

$$\Delta\eta_k = \frac{d}{f}\Delta t\nabla U(q_{k+1}), \tag{38}$$

the two update functions yield the same state $(q_{k+1}, p_{k+1})^\top$.
The same calculation for ABOBA yields

$$\Delta\eta_k = \frac{(d+1)}{f}\frac{\Delta t}{2}\nabla U(q_{k+1/2}) \tag{39}$$

(see supplementary material). The relative conditional path probability densities $M[\mathbf{x}|x_0]$ for these two integrators can now be calculated according to eq. 18.

B. Two random numbers per integration time step

The condition

$$\begin{pmatrix}0\\0\end{pmatrix} = \mathcal{U}_{\mathrm{BOAOB}}(\eta_k^{(1)}, \eta_k^{(2)}; x_k, V) - \mathcal{U}_{\mathrm{BOAOB}}(\widetilde{\eta}_k^{(1)}, \widetilde{\eta}_k^{(2)}; x_k, \widetilde{V}) \tag{40}$$

yields the random number differences for the BOAOB method

$$\Delta\eta_k^{(1)} = \frac{d'}{f'}\frac{\Delta t}{2}\nabla U(q_k) \tag{41a}$$

$$\Delta\eta_k^{(2)} = \frac{1}{f'}\frac{\Delta t}{2}\nabla U(q_{k+1}). \tag{41b}$$

Similarly, the condition

$$\begin{pmatrix}0\\0\end{pmatrix} = \mathcal{U}_{\mathrm{OBABO}}(\eta_k^{(1)}, \eta_k^{(2)}; x_k, V) - \mathcal{U}_{\mathrm{OBABO}}(\widetilde{\eta}_k^{(1)}, \widetilde{\eta}_k^{(2)}; x_k, \widetilde{V}) \tag{42}$$

yields the random number differences for the OBABO/BP method

$$\Delta\eta_k^{(1)} = \frac{1}{f'}\frac{\Delta t}{2}\nabla U(q_k) \tag{43a}$$

$$\Delta\eta_k^{(2)} = \frac{d'}{f'}\frac{\Delta t}{2}\nabla U(q_{k+1}). \tag{43b}$$

For both methods, the intermediate steps of this calculation are reported in the supplementary material. The relative conditional path probability densities $M[\mathbf{x}|x_0]$ for these two integrators can now be calculated according to eq. 21.

C. AOBOA: two random numbers, but one-dimensional image

The condition

$$\begin{pmatrix} 0 \\ 0 \end{pmatrix} = \mathcal{U}_{\mathrm{AOBOA}}(\eta_k^{\mathrm{comb}}; x_k, V) - \mathcal{U}_{\mathrm{AOBOA}}(\widetilde{\eta}_k^{\mathrm{comb}}; x_k, \widetilde{V}) \,, \tag{44}$$

where $\mathcal{U}_{\mathrm{AOBOA}}(\eta_k^{\mathrm{comb}}; x_k, V)$ is given by eq. 32, yields the difference of the combined random number

$$\Delta\eta_k^{\mathrm{comb}} = \frac{d'}{f'} \Delta t \nabla U(q_{k+1/2}) \,. \tag{45}$$

The intermediate steps of this calculation are reported in the supplementary material.
To reweight trajectories generated by the AOBOA integrator, we need to formulate $M[\mathbf{x}|x_0]$ as a function of the combined random numbers η_k^{comb}. From the update function of AOBOA (eq. 32), it follows that the conditional path probability is

$$\mathcal{P}[\mathbf{x}|x_0] = \mathcal{P}[\boldsymbol{\eta}^{\mathrm{comb}}] = \frac{1}{\sqrt[n]{2(d'^2+1)\pi}} \exp\left(-\sum_{k=0}^{n-1} \frac{\left(\eta_k^{\mathrm{comb}}\right)^2}{2(d'^2+1)} \right) . \tag{46}$$

Note that the probability density of the weighted sum of two normally distributed random numbers is again a normal distribution with adjusted mean μ and variance σ^2. For the combined random number (eq. 31): $\mu^{\mathrm{comb}} = d'\mu^{(1)} + \mu^{(2)} = 0$ and $(\sigma^{\mathrm{comb}})^2 = d'^2(\sigma^{(1)})^2 + (\sigma^{(2)})^2 = d'^2 + 1$. The relative conditional path probability density for AOBOA is

$$M[\mathbf{x}|x_0] = \frac{\mathcal{P}[\widetilde{\boldsymbol{\eta}}^{\mathrm{comb}}]}{\mathcal{P}[\boldsymbol{\eta}^{\mathrm{comb}}]} = \exp\left(-\sum_{k=0}^{n-1} \frac{\eta_k^{\mathrm{comb}} \cdot \Delta\eta_k^{\mathrm{comb}}}{d'^2+1} \right) \cdot \exp\left(-\sum_{k=0}^{n-1} \frac{\left(\Delta\eta_k^{\mathrm{comb}}\right)^2}{2(d'^2+1)} \right) . \tag{47}$$

The random numbers $\eta_k^{(1)}$ and $\eta_k^{(2)}$ are recorded during the simulation at V. The combined random number η_k^{comb} is calculated according to eq. 31, and the expression for $\Delta\eta_k^{\mathrm{comb}}$ is given by eq. 45.

VI. GRAPHICAL REPRESENTATION OF LANGEVIN INTEGRATORS

In this section, we introduce a graphical representation of splitting methods for Langevin integrators. This representation helps in reasoning why some methods have potential-independent images, and why others do not. It also shows which parts of the integration algorithm are affected by a change in the potential and how this influences $\Delta\eta_k$.
Fig. 3 illustrates this graphical representation for the ABO method. The graphs show the phase space (q,p), and the black dots represent the initial state $(q_k, p_k)^\top$ and the state $(q_{k+1}, p_{k+1})^\top$ after one iteration of the ABO method. The left-hand graph shows the update from (q_k, p_k) to (q_{k+1}, p_{k+1}) for the simulation potential V decomposed into the three update operators $\mathcal{A}$, $\mathcal{B}$, and $\mathcal{O}$. The $\mathcal{A}$-step depends on the momentum p_k and updates the position from q_k to q_{k+1}. This is followed by two momentum updates: the $\mathcal{B}$-step which depends on the updated position q_{k+1} and potential V and yields the intermediate momentum $p_{k+1/2}$, followed by an $\mathcal{O}$-step which depends on this intermediate momentum and a random number. The graph in the middle shows how the same update from (q_k, p_k) to (q_{k+1}, p_{k+1}) is achieved at the target potential. Update operators and intermediate results that are affected by the change in potential are shown in colour. The $\mathcal{A}$-step only depends on the initial momentum p_k and therefore does not change. The $\mathcal{B}$-step evaluates the gradient of the potential and thus yields a different intermediate momentum $p_{k+1/2}$, shown in blue. In order to reach the state (q_{k+1}, p_{k+1}), the random number in the $\mathcal{O}$-step needs to be adjusted such that $\mathcal{O}$ covers the remaining distance to p_{k+1}. Colloquially: we have to adjust the random number in the $\mathcal{O}$-step such that $\sqrt{k_B T m (1 - e^{-2\xi\Delta t})}\Delta\eta_k$ compensates

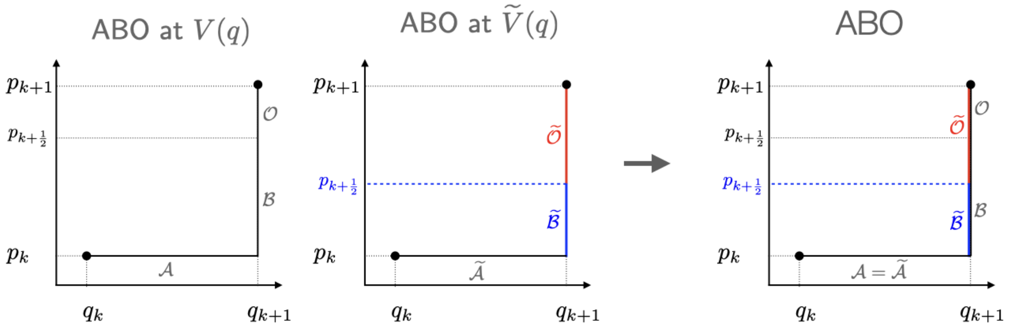

FIG. 3. Update from (q_k, p_k) to (q_{k+1}, p_{k+1}) for the ABO method at the simulations potential $V(x)$ and at the target potential $\widetilde{V}(x) = V(x) + U(x)$. Update operators and intermediate results that are affected by the change in potential are shown in colour.

"for the mess that $-\nabla U$ created". The right-hand graph combines the two previous graphs, so that the update at $V(x)$ and at $\widetilde{V}(x)$ can be compared directly.

Because the $\mathcal{A}$-step in the ABO method is unaffected by a change in the potential, the equation to determine $\Delta\eta_k$ simplifies. Instead of the condition

$$\left[\mathcal{OBA} - \widetilde{\mathcal{O}}\widetilde{\mathcal{B}}\widetilde{\mathcal{A}}\right]\begin{pmatrix} q_k \\ p_k \end{pmatrix} = \begin{pmatrix} 0 \\ 0 \end{pmatrix} \tag{48}$$

we only need to solve the condition

$$\left[\mathcal{OB} - \widetilde{\mathcal{O}}\widetilde{\mathcal{B}}\right]\begin{pmatrix} q_{k+1} \\ p_k \end{pmatrix} = \begin{pmatrix} 0 \\ 0 \end{pmatrix} . \tag{49}$$

which yields the same expression for $\Delta\eta_k$ as eq. 38.

Fig. 4 shows the graphical representation of the six symmetric splitting methods[46–49]. as well as for BAOA/GSD. These Langevin integrators can be classified according to the route they take through phase space during an integration time step from (q_k, p_k) to (q_{k+1}, p_{k+1}). In the integrators in the first columns of Fig. 4, the position update occurs in two steps, and in between the steps the momentum is updated. Stochastic position Verlet (SPV)[68], a splitting method that has been proposed prior to the symmetric splitting methods, takes the same route through phase space. In the algorithm in the second column, the momentum update occurs in two steps, and in between the steps the position is updated. Also in this case, there is an older algorithm that takes the same route through phase space: stochastic velocity Verlet (SVV)[68]. Algorithms in which neither position nor momentum update is calculated in one go, but position and momentum update are interspersed, are shown in the third column.

Using Fig. 4, one can derive simplified conditions for $\Delta\eta_k$ by considering which sub-steps in the integrator are affected by a change in V. In the ABOBA method, the first $\mathcal{A}$-step depends only on p_k and is not affected by a change in the potential. Therefore also the intermediate result $p_{k+1/2}$ is not affected by a change in the potential. The momentum update $p_k \to p_{k+1}$ is contained in the sequence of steps $\mathcal{BOB}$ (vertical line in Fig. 4), where the $\mathcal{B}$-step is affected by a change in the potential. In order to obtain the same momentum update in both potentials, the following condition for the two random numbers needs to be fulfilled:

$$\left[\mathcal{B}'\mathcal{O}\mathcal{B}' - \widetilde{\mathcal{B}}'\widetilde{\mathcal{O}}\widetilde{\mathcal{B}}'\right]\begin{pmatrix} q_{k+1/2} \\ p_k \end{pmatrix} = \begin{pmatrix} 0 \\ 0 \end{pmatrix} \tag{50}$$

The final $\mathcal{A}$-step only depends on p_{k+1} and is the same in both potentials if p_{k+1} remains the same. Solving eq. 50 yields the same $\Delta\eta_k$ as defined in eq. 39. Similarly, in the AOBOA

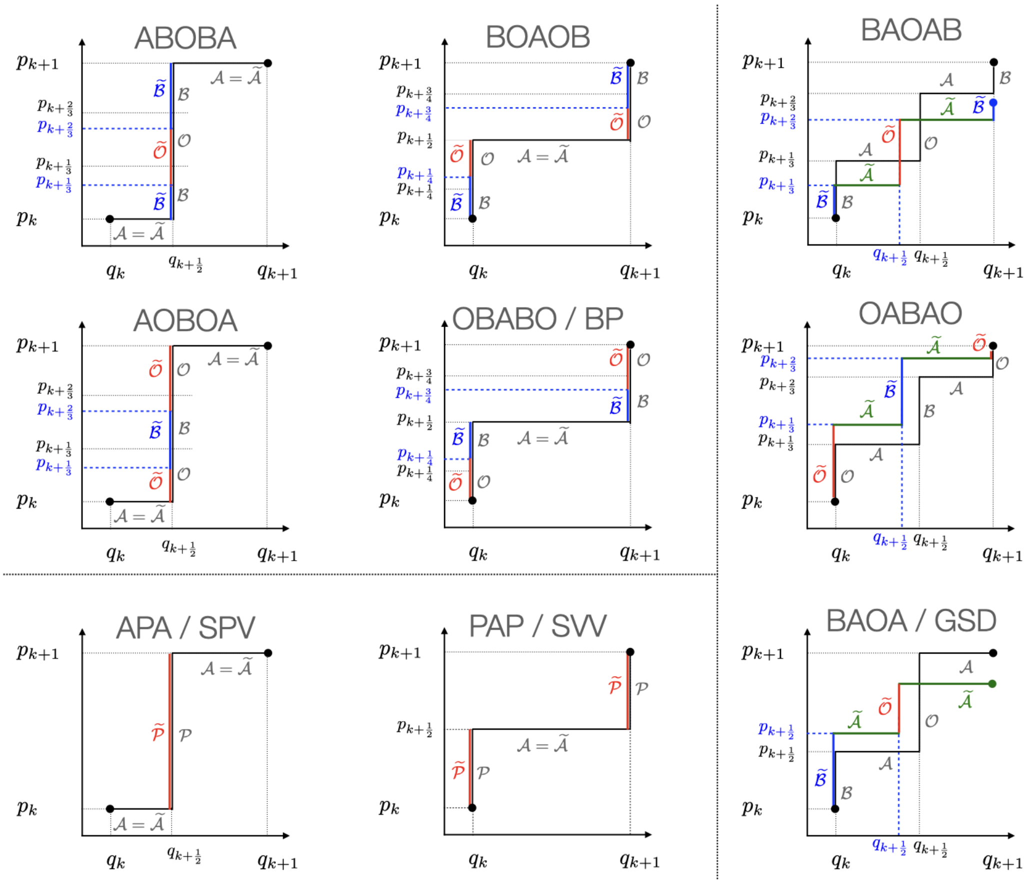

FIG. 4. Decomposition of the transition from (q_k, p_k) to (q_{k+1}, p_{k+1}) for Langevin integrators derived via the operator splitting method. Methods that are not suited to reweight position trajectories are highlighted in gray.

method it suffices to solve

$$\left[\mathcal{O}'\mathcal{B}\mathcal{O}' - \widetilde{\mathcal{O}}'\widetilde{\mathcal{B}}\widetilde{\mathcal{O}}'\right]\begin{pmatrix} q_{k+1/2} \\ p_k \end{pmatrix} = \begin{pmatrix} 0 \\ 0 \end{pmatrix} \tag{51}$$

to obtain eq. 45 for $\Delta\eta_k^{\mathrm{cond}}$.

Consider the algorithms in the second column. In the BOAOB method, the update of the positions $q_k \rightarrow q_{k+1}$ is contained in a single $\mathcal{A}$-step, which depends on the intermediate momentum result $p_{k+1/2}$. If $p_{k+1/2}$ is altered, q_{k+1} will change. In order to obtain the same path at the simulation and at the target potential, $p_{k+1/2}$ has to be the same in both potentials. This is the case, if the updates $p_k \rightarrow p_{k+1/2}$ and $p_{k+1/2} \rightarrow p_{k+1}$ (vertical lines in Fig. 4) are the same in both potentials. Thus, we have two separate conditions, one for each random number:

$$\left[\mathcal{O}'\mathcal{B}' - \widetilde{\mathcal{O}}'\widetilde{\mathcal{B}}'\right]\begin{pmatrix} q_k \\ p_k \end{pmatrix} = \begin{pmatrix} 0 \\ 0 \end{pmatrix} \tag{52a}$$

$$\left[\mathcal{B}'\mathcal{O}' - \widetilde{\mathcal{B}}'\widetilde{\mathcal{O}}'\right]\begin{pmatrix} q_{k+1} \\ p_{k+1/2} \end{pmatrix} = \begin{pmatrix} 0 \\ 0 \end{pmatrix} \tag{52b}$$

which lead to eqs. 41a and 41b for $\eta_k^{(1)}$ and $\eta_k^{(2)}$. (Note that the operators act from right to left, and thus their order is reversed compared to the name of the method.) Similarly, the conditions for OBABO/BP are

$$\left[\mathcal{B}'\mathcal{O}' - \widetilde{\mathcal{B}'}\widetilde{\mathcal{O}'}\right]\begin{pmatrix} q_k \\ p_k \end{pmatrix} = \begin{pmatrix} 0 \\ 0 \end{pmatrix} \tag{53a}$$

$$\left[\mathcal{O}'\mathcal{B}' - \widetilde{\mathcal{O}'}\widetilde{\mathcal{B}'}\right]\begin{pmatrix} q_{k+1} \\ p_{k+1/2} \end{pmatrix} = \begin{pmatrix} 0 \\ 0 \end{pmatrix} \tag{53b}$$

which lead to eqs. 43a and 43b for $\eta_k^{(1)}$ and $\eta_k^{(2)}$.

BAOAB and BAOA/GSD in the third column in Fig. 4 do not allow for reweighting in phase space. Consider BAOA/GSD to understand why. The first two steps in the algorithm are deterministic and the $\mathcal{B}$-step is affected by a change in V. Consequently, at $\widetilde{V}$ the intermediate state $(q_{k+1/2}, p_{k+1/2})$ will be different from the intermediate state at V. One can now choose the value of η_k such that the $\mathcal{O}$-step reaches p_{k+1}. In that case, the subsequent $\mathcal{A}$-step will not reach q_{k+1}. Or one can scale to a momentum $\widetilde{p}_{k+1}$ that is sufficient to bridge the remaining gap between $q_{k+1/2}$ and q_{k+1}, but this $\widetilde{p}_{k+1}$ will not be equal to the original p_{k+1}. Thus, one can reach either p_{k+1} or q_{k+1}, but not both. The equations for the corresponding values of $\Delta\eta_k$ are reported in the supplementary material. Note that this in principles allows for reweighting path expected values, in which the path observable $s[\mathbf{x}]$ only depends on the positions or only depends on the momenta. However, the resulting reweighted estimators might have a large variance or even a bias. An analogous reasoning applies to BAOAB. We provide the equations for $\Delta\eta_k$ for separately reweighting in position and momentum space in the supplementary material, and give the same warning.

For the OBABO method reweighting should in principle be possible, because we have two random numbers to adjust the updated position and the updated momentum. However, since pathological cases in which the image of the update function changes with the potential can be constructed (see supplementary material), we do not derive the equations for the random number differences here.

VII. CONCLUSION

We have introduced a strategy to derive the relative path-probability ratio for Langevin integrators. To achieve this, we adapted the method to derive the random number difference $\Delta\eta_k$ as presented in Ref. 45. With the random numbers differences presented in Tab. I it is now possible to use Girsanov reweighting with underdamped Langevin dynamics. This removes a major road block to study rare events by combining biased simulations with dynamical reweighting.

Besides reweighting enhanced sampling simulations, the relative path probability ratio for underdamped Langevin integrators can also be use in other contexts such as searching and sampling in path space[83–85] or force-field optimization[86]. It might also help in understanding the relation between molecular models that rely on path sampling and models that are derived from a direct discretization of the Fokker-Planck equation[78].

The analysis revealed that some algorithms violate absolute continuity, because the image of their update changes when the potential is change. As a consequence single-step transitions $(q_k, p_k) \to (q_{k+1}, p_{k+1})$ that are possible at the simulation potential are no longer possible at the target potential. Our condition for the absolute continuity of the single-step transitions (eq. 14) is a very strict condition and guarantees the Girsanov reweighting in the full phase space is possible. However, path observables usually either depend on the positions or on the momenta, rarely on both. Thus, for algorithms that violate eq. 14 reweighting in position space or in path space might still be possible. In fact, we report random number difference for these approaches for BAOA/GSD in the supplementary material. Whether these equations yield accurate results has yet to be tested. Another interesting question is how the absolute continuity of a Langevin integrator relates to the accuracy with which it reproduces transport properties[74,75]. Finally, in some cases one might be able to relax the absolute continuity over a single integration time-step to an absolute continuity over a larger lag time of several integration time steps, and thereby link Girsanov reweighting to dynamical reweighting methods that assume a Markov state model[20–24].

VIII. ACKNOWLEDGEMENTS

This research has been funded by Deutsche Forschungsgemeinschaft (DFG) through grant SFB 1114 "Scaling Cascades in Complex Systems" - project number 235221301, and through grant GRK 2473 "Bioactive Peptides" - project number 392923329. S.G. acknowledges funding by the Einstein Center of Catalysis/BIG-NSE.

IX. REFERENCES

[1] M. Karplus and J. A. McCammon, "Molecular dynamics simulations of biomolecules," Nat. Struct. Biol. **9**, 646–652 (2002).

[2] R. O. Dror, R. M. Dirks, J. Grossman, H. Xu, and D. E. Shaw, "Biomolecular simulation: a computational microscope for molecular biology," Annu Rev Biophys **41**, 429–452 (2012).

[3] T. J. Lane, D. Shukla, K. A. Beauchamp, and V. S. Pande, "To milliseconds and beyond: challenges in the simulation of protein folding," Curr. Opin. Struct. Biol. **23**, 58–65 (2013).

[4] T. Huber, A. Torda, and W. van Gunsteren, "Local elevation: A method for improving the searching properties of molecular dynamics simulation," J. Comput. Aided Mol. Des. **8**, 695 (1994).

[5] H. Grubmüller, "Predicting slow structural transitions in macromolecular systems: Conformational flooding," Physical Review E **52**, 2893 (1995).

[6] E. Darve and A. Pohorille, "Calculating free energies using average force," The Journal of chemical physics **115**, 9169–9183 (2001).

[7] A. Laio and M. Parrinello, "Escaping free-energy minima," Proc. Natl. Acad. Sci. U.S.A. **99**, 12562–12566 (2002).

[8] A. Barducci, G. Bussi, and M. Parrinello, "Well-tempered metadynamics: a smoothly converging and tunable free-energy method," Phys. Rev. Lett. **100**, 020603 (2008).

[9] G. M. Torrie and J. P. Valleau, "Nonphysical sampling distributions in monte carlo free-energy estimation: Umbrella sampling," J. Comput. Phys. **23**, 187–199 (1977).

[10] J. Kästner and W. Thiel, "Bridging the gap between thermodynamic integration and umbrella sampling provides a novel analysis method: "umbrella integration"," J. Chem. Phys. **123**, 144104 (2005).

[11] R. H. Swendsen, J.-S. Wang, and A. M. Ferrenberg, "New monte carlo methods for improved efficiency of computer simulations in statistical mechanics," The Monte Carlo method in condensed matter physics , 75–91 (1992).

[12] S. Kumar, J. M. Rosenberg, D. Bouzida, R. H. Swendsen, and P. A. Kollman, "The weighted histogram analysis method for free-energy calculations on biomolecules. i. the method," Journal of computational chemistry **13**, 1011–1021 (1992).

[13] S. Kieninger, L. Donati, and B. G. Keller, "Dynamical reweighting methods for markov models," Curr. Opin. Struct. Biol. **61**, 124–131 (2020).

[14] C. A. F. De Oliveira, D. Hamelberg, and J. A. McCammon, "Estimating kinetic rates from accelerated molecular dynamics simulations: Alanine dipeptide in explicit solvent as a case study," J. Chem. Phys. **127**, 11B605 (2007).

[15] U. Doshi and D. Hamelberg, "Extracting realistic kinetics of rare activated processes from accelerated molecular dynamics using kramers' theory," Journal of Chemical Theory and Computation **7**, 575–581 (2011).

[16] P. Tiwary and M. Parrinello, "From metadynamics to dynamics," Phys. Rev. Lett. **111**, 230602 (2013).

[17] A. T. Frank and I. Andricioaei, "Reaction coordinate-free approach to recovering kinetics from potential-scaled simulations: application of kramers' rate theory," The Journal of Physical Chemistry B **120**, 8600–8605 (2016).

[18] K. Palacio-Rodriguez, H. Vroylandt, L. S. Stelzl, F. Pietrucci, G. Hummer, and P. Cossio, "Transition rates and efficiency of collective variables from time-dependent biased simulations," The Journal of Physical Chemistry Letters **13**, 7490–7496 (2022).

[19] D. Bicout and A. Szabo, "Electron transfer reaction dynamics in non-debye solvents," The Journal of chemical physics **109**, 2325–2338 (1998).

[20] H. Wu, A. S. Mey, E. Rosta, and F. Noé, "Statistically optimal analysis of state-discretized trajectory data from multiple thermodynamic states," The Journal of Chemical Physics **141**, 12B629_1 (2014).

[21] A. S. Mey, H. Wu, and F. Noé, "xtram: Estimating equilibrium expectations from time-correlated simulation data at multiple thermodynamic states," Physical Review X **4**, 041018 (2014).

[22] E. Rosta and G. Hummer, "Free energies from dynamic weighted histogram analysis using unbiased markov state model," J. Chem. Theory Comput. **11**, 276–285 (2015).

[23] H. Wu, F. Paul, C. Wehmeyer, and F. Noé, "Multiensemble markov models of molecular thermodynamics and kinetics," Proc. Natl. Acad. Sci. U.S.A **113**, E3221 (2016).

[24] L. S. Stelzl, A. Kells, E. Rosta, and G. Hummer, "Dynamic histogram analysis to determine free energies and rates from biased simulations," Journal of chemical theory and computation **13**, 6328–6342 (2017).

[25] L. Onsager and S. Machlup, "Fluctuations and irreversible processes," Phys. Rev. **91**, 1505 (1953).

[26] I. V. Girsanov, "On transforming a certain class of stochastic processes by absolutely continuous substitution of measures," Theory Probab. Its Appl. **5**, 285 (1960).

[27] B. Øksendal, *Stochastic Differential Equations: An Introduction with Applications*, 6th ed. (Springer Verlag, Berlin, 2003).

[28] P. E. Kloeden and E. Platen, *Numerical Solution of Stochastic Differential Equations*, 1st ed. (Springer, Berlin, 1992).

[29] O. Mazonka, C. Jarzyński, and J. Błocki, "Computing probabilities of very rare events for langevin processes: a new method based on importance sampling," Nuclear Physics A **641**, 335–354 (1998).

[30] T. B. Woolf, "Path corrected functionals of stochastic trajectories: towards relative free energy and reaction coordinate calculations," Chem. Phys. Lett. **289**, 433–441 (1998).

[31] D. M. Zuckerman and T. B. Woolf, "Dynamic reaction paths and rates through importance-sampled stochastic dynamics," J. Chem. Phys. **111**, 9475–9484 (1999).

[32] D. M. Zuckerman and T. B. Woolf, "Efficient dynamic importance sampling of rare events in one dimension," Phys. Rev. E **63**, 016702 (2000).

[33] A. B. Adib, "Stochastic actions for diffusive dynamics: Reweighting, sampling, and minimization," J. Phys. Chem. B **112**, 5910–5916 (2008).

[34] H. Jang and T. B. Woolf, "Multiple pathways in conformational transitions of the alanine dipeptide: an application of dynamic importance sampling," Journal of computational chemistry **27**, 1136–1141 (2006).

[35] C. Schütte, A. Nielsen, and M. Weber, "Markov state models and molecular alchemy," Mol. Phys. **113**, 69–78 (2015).

[36] P. Bolhuis, Z. Brotzakis, and B. Keller, "Force field optimization by imposing kinetic constraints with path reweighting," arXiv preprint arXiv:2207.04558 (2022).

[37] G. A. Huber and J. A. McCammon, "Brownian dynamics simulations of biological molecules," Trends in chemistry **1**, 727–738 (2019).

[38] T. Cholko, S. Kaushik, K. Y. Wu, R. Montes, and C.-e. A. Chang, "Geombd3: Brownian dynamics simulation software for biological and engineered systems," Journal of chemical information and modeling **62**, 2257–2263 (2022).

[39] P. H. Hünenberger, "Thermostat algorithms for molecular dynamics simulations," in *Advanced Computer Simulation: Approaches for Soft Matter Sciences I* (Springer Berlin Heidelberg, 2005) pp. 105–149.

[40] C. Kwon and H. K. Lee, "Thermodynamic uncertainty relation for underdamped dynamics driven by time-dependent protocols," New Journal of Physics **24**, 013029 (2022).

[41] M. Athenes, "A path-sampling scheme for computing thermodynamic properties of a many-body system in a generalized ensemble," The European Physical Journal B-Condensed Matter and Complex Systems **38**, 651–663 (2004).

[42] C. Xing and I. Andricioaei, "On the calculation of time correlation functions by potential scaling," J. Chem. Phys. **124**, 034110 (2006).

[43] L. Donati, C. Hartmann, and B. G. Keller, "Girsanov reweighting for path ensembles and markov state models," J. Chem. Phys. **146**, 244112 (2017).

[44] L. Donati and B. G. Keller, "Girsanov reweighting for metadynamics simulations," J. Chem. Phys. **149**, 072335 (2018).

[45] S. Kieninger and B. G. Keller, "Path probability ratios for langevin dynamics—exact and approximate," J. Chem. Phys. **154**, 094102 (2021).

[46] G. Bussi and M. Parrinello, "Accurate sampling using Langevin dynamics." Phys. Rev. E Stat. Nonlin. Soft Matter Phys. **75**, 056707 (2007).

[47] B. Leimkuhler and C. Matthews, "Rational Construction of Stochastic Numerical Methods for Molecular Sampling," Appl Math Res Express **48**, 278 (2012).

[48] B. Leimkuhler and C. Matthews, "Robust and efficient configurational molecular sampling via Langevin dynamics," J. Chem. Phys. **138**, 174102 (2013).

[49] D. A. Sivak, J. D. Chodera, and G. E. Crooks, "Using Nonequilibrium Fluctuation Theorems to Understand and Correct Errors in Equilibrium and Nonequilibrium Simulations of Discrete Langevin Dynamics," Phys. Rev. X **3**, 011007 (2013).

[50] S. Kieninger and B. G. Keller, "Gromacs stochastic dynamics and baoab are equivalent configurational sampling algorithms," Journal of Chemical Theory and Computation **18**, 5792–5798 (2022).

[51] N. Bou-Rabee and H. Owhadi, "Long-run accuracy of variational integrators in the stochastic context," SIAM J Numer Anal **48**, 278–297 (2010).

[52] N. Goga, A. Rzepiela, A. De Vries, S. Marrink, and H. Berendsen, "Efficient algorithms for langevin and dpd dynamics," J. Chem. Theory Comput. **8**, 3637–3649 (2012).

[53] P. Eastman, J. Swails, J. D. Chodera, R. T. McGibbon, Y. Zhao, K. A. Beauchamp, L.-P. Wang, A. C. Simmonett, M. P. Harrigan, C. D. Stern, *et al.*, "Openmm 7: Rapid development of high performance algorithms for molecular dynamics," PLoS Comput. Biol. **13**, e1005659 (2017).

[54] D. A. Case, T. E. Cheatham III, T. Darden, H. Gohlke, R. Luo, K. M. Merz Jr, A. Onufriev, C. Simmerling, B. Wang, and R. J. Woods, "The amber biomolecular simulation programs," J. Comput. Chem **26**, 1668–

1688 (2005).

[55]D. Van Der Spoel, E. Lindahl, B. Hess, G. Groenhof, A. E. Mark, and H. J. Berendsen, "Gromacs: fast, flexible, and free," J. Comput. Chem **26**, 1701–1718 (2005).

[56]B. Leimkuhler and C. Matthews, *Molecular Dynamics, With Deterministic and Stochastic Numerical Methods*, 1st ed. (Springer Cham Heidelberg New York Dordrecht London, 2015).

[57]D. A. Sivak, J. D. Chodera, and G. E. Crooks, "Time step rescaling recovers continuous-time dynamical properties for discrete-time Langevin integration of nonequilibrium systems." J. Phys. Chem. B **118**, 6466–6474 (2014).

[58]B. Leimkuhler, C. Matthews, and G. Stoltz, "The computation of averages from equilibrium and nonequilibrium langevin molecular dynamics," IMA Journal of Numerical Analysis **36**, 13–79 (2016).

[59]J. Fass, D. A. Sivak, G. E. Crooks, K. A. Beauchamp, B. Leimkuhler, and J. D. Chodera, "Quantifying Configuration-Sampling Error in Langevin Simulations of Complex Molecular Systems," Entropy **20**, 318 (2018).

[60]A. Brünger, C. L. Brooks III, and M. Karplus, "Stochastic boundary conditions for molecular dynamics simulations of st2 water," Chem. Phys. Lett. **105**, 495–500 (1984).

[61]W. F. Van Gunsteren and H. J. Berendsen, "A leap-frog algorithm for stochastic dynamics," Molecular Simulation **1**, 173–185 (1988).

[62]R. W. Pastor, B. R. Brooks, and A. Szabo, "An analysis of the accuracy of langevin and molecular dynamics algorithms," Molecular Physics **65**, 1409–1419 (1988).

[63]E. Hershkovitz, "A fourth-order numerical integrator for stochastic langevin equations," J. Chem. Phys. **108**, 9253 (1998).

[64]M. G. Paterlini and D. M. Ferguson, "Constant temperature simulations using the langevin equation with velocity verlet integration," Chem. Phys. **236**, 243 (1998).

[65]R. D. Skeel and J. A. Izaguirre, "An impulse integrator for langevin dynamics," Mol. Phys. **100**, 3885 (2002).

[66]A. Ricci and G. Ciccotti, "Algorithms for brownian dynamics," Molecular Physics **101**, 1927–1931 (2003).

[67]E. Vanden-Eijnden and G. Ciccotti, "Second-order integrators for langevin equations with holonomic constraints," Chem. Phys. Lett. **429**, 310 (2006).

[68]S. Melchionna, "Design of quasisymplectic propagators for langevin dynamics," J. Chem. Phys. **127**, 044108 (2007).

[69]J. A. Izaguirre, C. R. Sweet, and V. S. Pande, "Multiscale dynamics of macromolecules using normal mode Langevin." Pacific Symp. Biocomput. , 240–251 (2010).

[70]H. Jia and K. Li, "A third accurate operator splitting method," Math Comput Model. **53**, 387–396 (2011).

[71]N. Grønbech-Jensen and O. Farago, "A simple and effective verlet-type algorithm for simulating langevin dynamics," Mol. Phys. **111**, 983 (2013).

[72]E. J. F. Peters, N. Goga, and H. J. Berendsen, "Stochastic dynamics with correct sampling for constrained systems," Journal of chemical theory and computation **10**, 4208–4220 (2014).

[73]Z. Zhang, X. Liu, K. Yan, M. E. Tuckerman, and J. Liu, "Unified efficient thermostat scheme for the canonical ensemble with holonomic or isokinetic constraints via molecular dynamics," J. Phys. Chem. A **123**, 6056 (2019).

[74]N. Grønbech-Jensen, "Complete set of stochastic verlet-type thermostats for correct langevin simulations," Molecular Physics **118**, e1662506 (2020).

[75]J. Finkelstein, C. Cheng, G. Fiorin, B. Seibold, and N. Grønbech-Jensen, "Bringing discrete-time langevin splitting methods into agreement with thermodynamics," J. Chem. Phys. **155**, 184104 (2021).

[76]T. C. Beutler, A. E. Mark, R. C. van Schaik, P. R. Gerber, and W. F. Van Gunsteren, "Avoiding singularities and numerical instabilities in free energy calculations based on molecular simulations," Chemical physics letters **222**, 529–539 (1994).

[77]M. Zacharias, T. Straatsma, and J. McCammon, "Separation-shifted scaling, a new scaling method for lennard-jones interactions in thermodynamic integration," The Journal of chemical physics **100**, 9025–9031 (1994).

[78]L. Donati, M. Weber, and B. G. Keller, "A review of girsanov reweighting and of square root approximation for building molecular markov state models," Journal of Mathematical Physics **63**, 123306 (2022).

[79]H. F. Trotter, "On the product of semi-groups of operators," Proc Am Math Soc **10**, 545–551 (1959).

[80]M. Tuckerman, B. J. Berne, and G. J. Martyna, "Reversible multiple time scale molecular dynamics," J. Chem. Phys. **97**, 1990–2001 (1992).

[81]B. Leimkuhler and C. Matthews, "Efficient molecular dynamics using geodesic integration and solvent–solute splitting," Proc. R. Soc. A: Math. Phys. Eng. Sci. **472**, 20160138 (2016).

[82]T. Arens, F. Hettlich, C. Karpfinger, U. Kockelkorn, K. Lichtenegger, and H. Stachel, "Kurven und flächen–von krümmung, torsion und längenmessung," in *Mathematik* (Springer, 2018) pp. 955–991.

[83]H. Fujisaki, M. Shiga, K. Moritsugu, and A. Kidera, "Multiscale enhanced path sampling based on the onsager-machlup action: Application to a model polymer," J. Chem. Phys. **139**, 08B607_1 (2013).

[84]J. Lee, I.-H. Lee, I. Joung, J. Lee, and B. R. Brooks, "Finding multiple reaction pathways via global optimization of action," Nature Communications **8**, 15443 (2017).

[85]E. K. Peter, J.-E. Shea, and A. Schug, "Core-md, a path correlated molecular dynamics simulation method," The Journal of Chemical Physics **153**, 084114 (2020).

[86]P. G. Bolhuis, D. Chandler, C. Dellago, and P. L. Geissler, "Transition path sampling: Throwing ropes," Annu. Rev. Phys. Chem **53**, 291–318 (2002).

Appendix A: Langevin integration methods

For the update operators we use the following abbreviations:

$$\begin{aligned} a &= \Delta t \frac{1}{m} && \text{(A1a)} \\ b(q_k) &= -\Delta t \nabla V(q_k) && \text{(A1b)} \\ d &= e^{-\xi \Delta t} && \text{(A1c)} \\ f &= \sqrt{k_B T m (1 - e^{-2\xi\Delta t})}\,. && \text{(A1d)} \end{aligned}$$

and for half time steps

$$\begin{aligned} a' &= \frac{\Delta t}{2}\frac{1}{m} && \text{(A2a)} \\ b'(q_k) &= -\frac{\Delta t}{2} \nabla V(q_k) && \text{(A2b)} \\ d' &= e^{-\xi \frac{\Delta t}{2}} && \text{(A2c)} \\ f' &= \sqrt{k_B T m (1 - e^{-2\xi\frac{\Delta t}{2}})}\,. && \text{(A2d)} \end{aligned}$$

We will further use that

$$\widetilde{\eta_k} - \eta_k = \Delta\eta_k \tag{A3}$$

and that

$$\begin{aligned} \widetilde{b}(q_k) - b(q_k) &= -\Delta t \nabla \widetilde{V}(q_k) + \Delta t \nabla V(q_k) \\ &= -\Delta t (\nabla V(q_k) + \nabla U(q_k)) + \Delta t \nabla V(q_k) \\ &= -\Delta t \nabla U(q_k) && \text{(A4)} \end{aligned}$$

and analogously for half-time steps.

1. ABOBA

a. Algorithm

$$\begin{aligned} q_{k+1/2} &= q_k + \frac{\Delta t}{2m} p_k && \text{(A5a)} \\ p_{k+1/3} &= p_k - \frac{\Delta t}{2} \nabla V(q_{k+1/2}) && \text{(A5b)} \\ p_{k+2/3} &= e^{-\xi\Delta t} p_{k+1/3} + \sqrt{k_B T m (1 - e^{-2\xi\Delta t})}\, \eta_k && \text{(A5c)} \\ p_{k+1} &= p_{k+2/3} - \frac{\Delta t}{2} \nabla V(q_{k+1/2}) && \text{(A5d)} \\ q_{k+1} &= q_{k+1/2} + \frac{\Delta t}{2m} p_{k+1} && \text{(A5e)} \end{aligned}$$

The algorithm has been reported in Refs. 47 and in 57. Compared to Ref. 48, we changed the notation as follows: $n \to k$, $R_n \to \eta_k$, $\delta t \to \Delta t$, $M \to m$, $\gamma \to \xi$, $F \to -\nabla V$.

b. Update operator

$$\begin{aligned}
\mathcal{A}'\mathcal{B}'\mathcal{O}\mathcal{B}'\mathcal{A}'\begin{pmatrix} q_k \\ p_k \end{pmatrix} &= \mathcal{A}'\mathcal{B}'\mathcal{O}\mathcal{B}'\begin{pmatrix} q_k + a'p_k \\ p_k \end{pmatrix} \\
&= \mathcal{A}'\mathcal{B}'\mathcal{O}\begin{pmatrix} q_k + a'p_k \\ p_k + b'(q_k + a'p_k) \end{pmatrix} \\
&= \mathcal{A}'\mathcal{B}'\begin{pmatrix} q_k + a'p_k \\ dp_k + db'(q_k + a'p_k) + f\eta_k \end{pmatrix} \\
&= \mathcal{A}'\begin{pmatrix} q_k + a'p_k \\ dp_k + db'(q_k + a'p_k) + f\eta_k + b'(q_k + a'p_k) \end{pmatrix} \\
&= \begin{pmatrix} q_k + a'p_k + a'[dp_k + db'(q_k + a'p_k) + f\eta_k + b'(q_k + a'p_k)] \\ dp_k + db'(q_k + a'p_k) + f\eta_k + b'(q_k + a'p_k) \end{pmatrix} \qquad \text{(A6)}
\end{aligned}$$

c. Update function

$$\begin{pmatrix} q_{k+1} \\ p_{k+1} \end{pmatrix} = \mathcal{U}_{\mathrm{ABOBA}}(\eta_k; x_k, V) = \begin{pmatrix} \bar{q}_{k+1} \\ \bar{p}_{k+1} \end{pmatrix} + \begin{pmatrix} a'f \\ f \end{pmatrix}\eta_k \qquad \text{(A7)}$$

with $\bar{q}_{k+1} = q_k + a'(1+d)p_k + a'(d+1)b'(q_k + a'p_k)$ and $\bar{p}_{k+1} = dp_k + (d+1)b'(q_k + a'p_k)$. Thus,

$$\begin{aligned}
\mathcal{U}_{\mathrm{ABOBA}} &: \ \mathbb{R} \to L_{1d} \subset \Gamma \\
\mathcal{U}_{\mathrm{ABOBA}} &: \ \eta_k \mapsto x_{k+1}\,, \qquad \text{(A8)}
\end{aligned}$$

where L_{1d} denotes a line in Γ.

d. Image at V and $\widetilde{V}$

$$\begin{aligned}
\begin{pmatrix} 0 \\ 0 \end{pmatrix} &= \mathcal{U}_{\mathrm{ABOBA}}(\eta_k; x_k, V) - \mathcal{U}_{\mathrm{ABOBA}}(\widetilde{\eta}_k; x_k, \widetilde{V}) \\
&= \begin{pmatrix} q_k + a'p_k + a'(dp_k + db'(q_k + a'p_k) + f\eta_k + b'(q_k + a'p_k)) \\ dp_k + db'(q_k + a'p_k) + f\eta_k + b'(q_k + a'p_k) \end{pmatrix} - \\
&\quad \begin{pmatrix} q_k + a'p_k + a'(dp_k + d\widetilde{b}'(q_k + a'p_k) + f\widetilde{\eta}_k + \widetilde{b}'(q_k + a'p_k)) \\ dp_k + d\widetilde{b}'(q_k + a'p_k) + f\widetilde{\eta}_k + \widetilde{b}'(q_k + a'p_k) \end{pmatrix} \\
&= \begin{pmatrix} a'[d \cdot b'(q_k + a'p_k) + f\eta_k + b'(q_k + a'p_k)] \\ db'(q_k + a'p_k) + f\eta_k + b'(q_k + a'p_k) \end{pmatrix} - \\
&\quad \begin{pmatrix} a'[d \cdot \widetilde{b}'(q_k + a'p_k) + f\widetilde{\eta}_k + \widetilde{b}'(q_k + a'p_k)] \\ d\widetilde{b}'(q_k + a'p_k) + f\widetilde{\eta}_k + \widetilde{b}'(q_k + a'p_k) \end{pmatrix} \\
&= \begin{pmatrix} a' \\ 1 \end{pmatrix}[d \cdot b'(q_k + a'p_k) + f\eta_k + b'(q_k + a'p_k)] - \\
&\quad \begin{pmatrix} a' \\ 1 \end{pmatrix}[d \cdot \widetilde{b}'(q_k + a'p_k) + f\widetilde{\eta}_k + \widetilde{b}'(q_k + a'p_k)] \\
&= \begin{pmatrix} a' \\ 1 \end{pmatrix}[d \cdot b'(q_k + a'p_k) + f\eta_k + b'(q_k + a'p_k) - d \cdot \widetilde{b}'(q_k + a'p_k) - f\widetilde{\eta}_k - \widetilde{b}'(q_k + a'p_k)] \\
&= \begin{pmatrix} a' \\ 1 \end{pmatrix}[(d+1) \cdot b'(q_k + a'p_k) - (d+1) \cdot \widetilde{b}'(q_k + a'p_k) + f(\eta_k - \widetilde{\eta}_k)]
\end{aligned}$$

$$= \begin{pmatrix} a' \\ 1 \end{pmatrix} \left[(d+1)\cdot\frac{\Delta t}{2}\nabla U(q_{k+1/2}) - f\Delta\eta_k\right] \tag{A9}$$

is fulfilled if

$$\Delta\eta_k = \frac{(d+1)}{f}\frac{\Delta t}{2}\nabla U(q_{k+1/2})\,, \tag{A10}$$

where we substituted $q_{k+1/2} = q_k + a'p_k$ (eq. A5a) and used eqs. **??** and eq. A4. Thus, $\mathcal{U}_{\mathrm{ABOBA}}(\eta_k; x_k, V)$ and $\mathcal{U}_{\mathrm{ABOBA}}(\widetilde{\eta_k}; x_k, \widetilde{V})$ have the same image

$$L_{1d} = \widetilde{L}_{1d}\,.$$

2. BAOAB

a. Algorithm

$$p_{k+1/3} = p_k - \frac{\Delta t}{2}\nabla V(q_k) \tag{A11a}$$

$$q_{k+1/2} = q_k + \frac{\Delta t}{2m}p_{k+1/3} \tag{A11b}$$

$$p_{k+2/3} = e^{-\xi\Delta t}p_{k+1/3} + \sqrt{k_B T m(1-e^{-2\xi\Delta t})}\,\eta_k \tag{A11c}$$

$$q_{k+1} = q_{k+1/2} + \frac{\Delta t}{2m}p_{k+2/3} \tag{A11d}$$

$$p_{k+1} = p_{k+2/3} - \frac{\Delta t}{2}\nabla V(q_{k+1}) \tag{A11e}$$

The algorithm has been reported in Refs. 47 and 57. Compared to Ref. 48, we changed the notation as follows: $n \to k$, $R_n \to \eta_k$, $\delta t \to \Delta t$, $M \to m$, $\gamma \to \xi$, $F \to -\nabla V$.

b. Update operator

$$\begin{aligned}
\mathcal{B}'\mathcal{A}'\mathcal{O}\mathcal{A}'\mathcal{B}'\begin{pmatrix} q_k \\ p_k \end{pmatrix} &= \mathcal{B}'\mathcal{A}'\mathcal{O}\mathcal{A}'\begin{pmatrix} q_k \\ p_k + b'(q_k) \end{pmatrix} \\
&= \mathcal{B}'\mathcal{A}'\mathcal{O}\begin{pmatrix} q_k + a'p_k + a'b'(q_k) \\ p_k + b'(q_k) \end{pmatrix} \\
&= \mathcal{B}'\mathcal{A}'\begin{pmatrix} q_k + a'p_k + a'b'(q_k) \\ dp_k + db'(q_k) + f\eta_k \end{pmatrix} \\
&= \mathcal{B}'\begin{pmatrix} q_k + a'p_k + a'b'(q_k) + a'dp_k + a'db'(q_k) + a'f\eta_k \\ dp_k + db'(q_k) + f\eta_k \end{pmatrix} \\
&= \begin{pmatrix} q_k + a'p_k + a'b'(q_k) + a'dp_k + a'db'(q_k) + a'f\eta_k \\ dp_k + db'(q_k) + f\eta_k + b'(q_k + a'p_k + a'b'(q_k) + a'dp_k + a'db'(q_k) + a'f\eta_k) \end{pmatrix}
\end{aligned} \tag{A12}$$

c. Update function

$$\begin{pmatrix} q_{k+1} \\ p_{k+1} \end{pmatrix} = \mathcal{U}_{\mathrm{BAOAB}}(\eta_k; x_k, V) = \begin{pmatrix} \bar{q}_{k+1} \\ \bar{p}_{k+1} \end{pmatrix} + \begin{pmatrix} 0 \\ b'(\bar{q}_{k+1} + a'f\eta_k) \end{pmatrix} + \begin{pmatrix} a'f \\ f \end{pmatrix}\eta_k \tag{A13}$$

with $\bar{q}_{k+1} = q_k + a'p_k + a'b'(q_k) + a'dp_k + a'db'(q_k) = q_k + a'(1+d)p_k + a'(1+d)b'(q_k)$ and $\bar{p}_{k+1} = dp_k + db'(q_k)$. Thus,

$$\begin{aligned} \mathcal{U}_{\mathrm{BAOAB}} &: \ \mathbb{R} \rightarrow C_{1d} \subset \Gamma \\ \mathcal{U}_{\mathrm{BAOAB}} &: \ \eta_k \mapsto x_{k+1}\,, \end{aligned} \tag{A14}$$

where C_{1d} denotes a curve in Γ.

d. Image at V and $\widetilde{V}$

$$\begin{aligned} \begin{pmatrix} 0 \\ 0 \end{pmatrix} &= \mathcal{U}_{\mathrm{BAOAB}}(\eta_k; x_k, V) - \mathcal{U}_{\mathrm{BAOAB}}(\widetilde{\eta}_k; x_k, \widetilde{V}) \\ &= \begin{pmatrix} q_k + a'(1+d)p_k + a'(1+d)b'(q_k) + a'f\eta_k \\ dp_k + d\cdot b'(q_k) + f\eta_k + b'(q_k + a'(1+d)p_k + a'(1+d)b'(q_k) + a'f\eta_k) \end{pmatrix} - \\ &\quad \begin{pmatrix} q_k + a'(1+d)p_k + a'(1+d)\widetilde{b}'(q_k) + a'f\widetilde{\eta}_k \\ dp_k + d\cdot \widetilde{b}'(q_k) + f\widetilde{\eta}_k + \widetilde{b}'(q_k + a'(1+d)p_k + a'(1+d)\widetilde{b}'(q_k) + a'f\widetilde{\eta}_k) \end{pmatrix} \\ &= \begin{pmatrix} a'(d+1)\cdot b'(q_k) + a'f\eta_k \\ d\cdot b'(q_k) + b'(q_k + a'(d+1)p_k + a'(d+1)\cdot b'(q_k) + a'f\eta_k) + f\eta_k \end{pmatrix} - \\ &\quad \begin{pmatrix} a'(d+1)\cdot \widetilde{b}'(q_k) + a'f\widetilde{\eta}_k \\ d\cdot \widetilde{b}'(q_k) + \widetilde{b}'(q_k + a'(d+1)p_k + a'(d+1)\cdot \widetilde{b}'(q_k) + a'f\widetilde{\eta}_k) + f\widetilde{\eta}_k \end{pmatrix} . \end{aligned} \tag{A15}$$

η_k appears linearly in the update of the positions. It appears as the argument of the function $b(q)$ in the update of the momenta which is typically a non-linear function (eq. A1b). Therefore, one cannot find an analytical expression for $\Delta\eta_k$ that solves both lines of the equation.

One can however find an expression for $\Delta\eta_k^{\mathrm{pos}}$, for which the two update functions yield the same positions:

$$\begin{aligned} 0 &= a'(d+1)\cdot b'(q_k) + a'f\eta_k - a'(d+1)\cdot \widetilde{b}'(q_k) - a'f\widetilde{\eta}_k \\ &= a'(d+1)\cdot \frac{\Delta t}{2}\nabla U(q_k) - a'f\Delta\eta_k^{\mathrm{pos}} \\ &\Updownarrow \\ \Delta\eta_k^{\mathrm{pos}} &= \frac{d+1}{f}\frac{\Delta t}{2}\nabla U(q_k)\,. \end{aligned} \tag{A16}$$

Then

$$\begin{aligned} q_{k+1} &= q_k + a'(d+1)p_k + a'(d+1)\cdot b'(q_k) + a'f\eta_k \\ &= q_k + a'(d+1)p_k + a'(d+1)\cdot \widetilde{b}'(q_k) + a'f\widetilde{\eta}_k\,, \end{aligned} \tag{A17}$$

and we can make the following substitution in the equation above

$$\begin{aligned} \begin{pmatrix} 0 \\ 0 \end{pmatrix} &= \begin{pmatrix} 0 \\ d\cdot b'(q_k) + b'(q_{k+1}) + f\eta_k - d\cdot \widetilde{b}'(q_k) - \widetilde{b}'(q_{k+1}) - f\widetilde{\eta}_k \end{pmatrix} \\ &= \begin{pmatrix} 0 \\ d\frac{\Delta t}{2}\nabla U(q_k) + \frac{\Delta t}{2}\nabla U(q_{k+1}) - f\Delta\eta_k^{\mathrm{pos}} \end{pmatrix} . \end{aligned} \tag{A18}$$

One can now see that the equation for the momenta is not fulfilled, because

$$\begin{aligned} 0 &\neq d\frac{\Delta t}{2}\nabla U(q_k) + \frac{\Delta t}{2}\nabla U(q_{k+1}) - f\Delta\eta_k^{\mathrm{pos}} \\ 0 &\neq d\frac{\Delta t}{2}\nabla U(q_k) + \frac{\Delta t}{2}\nabla U(q_{k+1}) - (d+1)\frac{\Delta t}{2}\nabla U(q_k) \\ \nabla U(q_{k+1}) &\neq \nabla U(q_k)\,. \end{aligned} \tag{A19}$$

Thus, $\mathcal{U}_{\mathrm{BAOAB}}(\eta_k; x_k, V)$ and $\mathcal{U}_{\mathrm{BAOAB}}(\widetilde{\eta}_k; x_k, \widetilde{V})$ parameterise different curves in state space

$$C_{1d} \neq \widetilde{C}_{1d}\,.$$

3. BAOA/ Gromacs stochastic dynamics

BAOA is equivalent to Gromacs stochastic dynamics (GSD)[50,52].

a. Algorithm

$$
\begin{aligned}
p_{k+\frac{1}{2}} &= p_k - \Delta t \nabla V(q_k) && \text{(A20a)}\\
q_{k+\frac{1}{2}} &= q_k + \frac{\Delta t}{2m} p_{k+\frac{1}{2}} && \text{(A20b)}\\
p_{k+1} &= e^{-\xi \Delta t} p_{k+\frac{1}{2}} + \sqrt{k_B T m \left(1 - e^{-2\xi\Delta t}\right)} \eta_k && \text{(A20c)}\\
q_{k+1} &= q_{k+\frac{1}{2}} + \frac{\Delta t}{2m} p_{k+1}. && \text{(A20d)}
\end{aligned}
$$

b. Update operator

$$
\begin{aligned}
\mathcal{A}'\mathcal{O}\mathcal{A}'\mathcal{B}\begin{pmatrix} q_k \\ p_k \end{pmatrix} &= \mathcal{A}'\mathcal{O}\mathcal{A}'\begin{pmatrix} q_k \\ p_k + b(q_k) \end{pmatrix}\\
&= \mathcal{A}'\mathcal{O}\begin{pmatrix} q_k + a'p_k + a'b(q_k) \\ p_k + b(q_k) \end{pmatrix}\\
&= \mathcal{A}'\begin{pmatrix} q_k + a'p_k + a'b(q_k) \\ dp_k + db(q_k) + f\eta_k \end{pmatrix}\\
&= \begin{pmatrix} q_k + a'p_k + a'b(q_k) + a'dp_k + a'db(q_k) + a'f\eta_k \\ dp_k + db(q_k) + f\eta_k \end{pmatrix} \qquad \text{(A21)}
\end{aligned}
$$

c. Update function

$$
\begin{pmatrix} q_{k+1} \\ p_{k+1} \end{pmatrix} = \mathcal{U}_{\mathrm{BAOA}}(\eta_k; x_k, V) = \begin{pmatrix} \bar{q}_{k+1} \\ \bar{p}_{k+1} \end{pmatrix} + \begin{pmatrix} a'f \\ f \end{pmatrix} \eta_k \qquad \text{(A22)}
$$

with $\bar{q}_{k+1} = q_k + a'p_k + a'b(q_k) + a'dp_k + a'db(q_k) = q_k + a'(1+d)p_k + a'(1+d)b(q_k)$ and $\bar{p}_{k+1} = dp_k + db(q_k)$. Thus,

$$
\begin{aligned}
\mathcal{U}_{\mathrm{BAOA}} &: \ \mathbb{R} \to L_{1d} \subset \Gamma\\
\mathcal{U}_{\mathrm{BAOA}} &: \ \eta_k \mapsto x_{k+1}\,, \qquad \text{(A23)}
\end{aligned}
$$

where L_{1d} denotes a line in Γ.

d. Image at V and $\widetilde{V}$

$$
\begin{aligned}
\begin{pmatrix} 0 \\ 0 \end{pmatrix} &= \mathcal{U}_{\mathrm{BAOA}}(\eta_k; x_k, V) - \mathcal{U}_{\mathrm{BAOA}}(\widetilde{\eta_k}; x_k, \widetilde{V})\\
&= \begin{pmatrix} q_k + a'(1+d)p_k + a'(1+d)b(q_k) + a'f\eta_k \\ dp_k + d\cdot b(q_k) + f\eta_k \end{pmatrix} -
\end{aligned}
$$

$$
\begin{aligned}
&\begin{pmatrix} q_k + a'(1+d)p_k + a'(1+d)\widetilde{b}(q_k) + a' f \widetilde{\eta}_k \\ dp_k + d \cdot \widetilde{b}(q_k) + f\widetilde{\eta}_k \end{pmatrix} \\
&= \begin{pmatrix} a'(1+d)\cdot b(q_k) + a' f \eta_k \\ d \cdot b(q_k) + f\eta_k \end{pmatrix} - \begin{pmatrix} a'(1+d)\cdot \widetilde{b}(q_k) + a' f \widetilde{\eta}_k \\ d \cdot \widetilde{b}(q_k) + f\widetilde{\eta}_k \end{pmatrix} \\
&= \begin{pmatrix} a'(1+d)\cdot \Delta t \nabla U(q_k) - a' f \Delta\eta_k \\ d \cdot \Delta t \nabla U(q_k) - f\Delta\eta_k \end{pmatrix}
\end{aligned}
\tag{A24}
$$

The two update functions yield the same positions if

$$
\begin{aligned}
0 &= a'(1+d)\cdot \Delta t \nabla U(q_k) - a' f \Delta \eta_k^{\mathrm{pos}} \\
&\Updownarrow \\
\Delta \eta_k^{\mathrm{pos}} &= \frac{1+d}{f} \cdot \Delta t \nabla U(q_k)\,.
\end{aligned}
\tag{A25}
$$

Substituting η_k^{pos} for η_k in eq. A24 yields

$$
\begin{aligned}
\begin{pmatrix} 0 \\ 0 \end{pmatrix} &= \begin{pmatrix} 0 \\ d \cdot \Delta t \nabla U(q_k) - f \Delta \eta_k^{\mathrm{pos}} \end{pmatrix} \\
&= \begin{pmatrix} 0 \\ d \cdot \Delta t \nabla U(q_k) - (1+d)\Delta t \nabla U(q_k) \end{pmatrix}
\end{aligned}
\tag{A26}
$$

which shows that the equation for the momenta is not fulfilled with $\Delta\eta_k^{\mathrm{pos}}$, because

$$
d \cdot \Delta t \nabla U(q_k) \neq (1+d)\Delta t \nabla U(q_k)\,. \tag{A27}
$$

Thus, $\mathcal{U}_{\mathrm{BAOA}}(\eta_k; x_k, V)$ and $\mathcal{U}_{\mathrm{BAOA}}(\widetilde{\eta}_k; x_k, \widetilde{V})$ parameterise different curves in state space

$$
L_{1d} \neq \widetilde{L}_{1d}\,.
$$

Because η_k appears linearly in the update of the positions as well as in the update of the momenta, one can solve eq. A24 for the momentum update

$$
\begin{aligned}
0 &= d \cdot \Delta t \nabla U(q_k) - f \Delta \eta_k^{\mathrm{mom}} \\
&\Updownarrow \\
\Delta \eta_k^{\mathrm{mom}} &= \frac{d}{f} \cdot \Delta t \nabla U(q_k)\,.
\end{aligned}
\tag{A28}
$$

Note that $\Delta\eta_k^{\mathrm{mom}} \neq \Delta\eta_k^{\mathrm{pos}}$.

4. AOBOA

a. Algorithm

$$
q_{k+1/2} = q_k + \frac{\Delta t}{2m} p_k \tag{A29a}
$$

$$
p_{k+1/3} = e^{-\frac{\xi \Delta t}{2}} p_k + \sqrt{k_B T m (1 - e^{-\xi \Delta t})}\, \eta_k^{(1)} \tag{A29b}
$$

$$
p_{k+2/3} = p_{k+1/3} - \Delta t \nabla V(q_{k+1/2}) \tag{A29c}
$$

$$
p_{k+1} = e^{-\frac{\xi \Delta t}{2}} p_{k+2/3} + \sqrt{k_B T m (1 - e^{-\xi \Delta t})}\, \eta_k^{(2)} \tag{A29d}
$$

$$
q_{k+1} = q_{k+1/2} + \frac{\Delta t}{2m} p_{k+1}\,. \tag{A29e}
$$

Here, two random numbers $\eta_k^{(1)} \sim \mathcal{N}(0,1)$ and $\eta_k^{(2)} \sim \mathcal{N}(0,1)$ need to be drawn per full update cycle.

b. Update operator

$$\begin{aligned}
\mathcal{A}'\mathcal{O}'\mathcal{B}\mathcal{O}'\mathcal{A}' \begin{pmatrix} q_k \\ p_k \end{pmatrix} &= \mathcal{A}'\mathcal{O}'\mathcal{B}\mathcal{O}' \begin{pmatrix} q_k + a'p_k \\ p_k \end{pmatrix} \\
&= \mathcal{A}'\mathcal{O}'\mathcal{B} \begin{pmatrix} q_k + a'p_k \\ d'p_k + f'\eta_k^{(1)} \end{pmatrix} \\
&= \mathcal{A}'\mathcal{O}' \begin{pmatrix} q_k + a'p_k \\ d'p_k + f'\eta_k^{(1)} + b(q_k + a'p_k) \end{pmatrix} \\
&= \mathcal{A}' \begin{pmatrix} q_k + a'p_k \\ d'd'p_k + d'f'\eta_k^{(1)} + d'b(q_k + a'p_k) + f'\eta_k^{(2)} \end{pmatrix} \\
&= \begin{pmatrix} q_k + a'p_k + a'\Big(d'd'p_k + d'f'\eta_k^{(1)} + d'b(q_k + a'p_k) + f'\eta_k^{(2)}\Big) \\ d'd'p_k + d'f'\eta_k^{(1)} + d'b(q_k + a'p_k) + f'\eta_k^{(2)} \end{pmatrix}
\end{aligned} \tag{A30}$$

c. Update function

$$\begin{pmatrix} q_{k+1} \\ p_{k+1} \end{pmatrix} = \mathcal{U}_{\mathrm{AOBOA}}(\eta_k^{\mathrm{comb}}; x_k, V) = \begin{pmatrix} \bar{q}_{k+1} \\ \bar{p}_{k+1} \end{pmatrix} + \begin{pmatrix} a' \\ 1 \end{pmatrix} f'\eta_k^{\mathrm{comb}} \tag{A31}$$

with $\bar{q}_{k+1} = q_k + (a' + a'd'd')p_k + a'd'b(q_k + a'p_k)$ and $\bar{p}_{k+1} = d'd'p_k + d'b(q_k + a'p_k)$ and a combined random number

$$\eta_k^{\mathrm{comb}} = d'\eta_k^{(1)} + \eta_k^{(2)} \sim \mathcal{N}(0, d'^2 + 1)\,. \tag{A32}$$

Thus,

$$\begin{aligned}
\mathcal{U}_{\mathrm{AOBOA}} :&\quad \mathbb{R} \to L_{1d} \subset \Gamma \\
\mathcal{U}_{\mathrm{AOBOA}} :&\quad \eta_k^{\mathrm{comb}} \mapsto x_{k+1},
\end{aligned} \tag{A33}$$

where L_{1d} denotes a line in Γ.

d. Image at V and $\widetilde{V}$

$$\begin{aligned}
\begin{pmatrix} 0 \\ 0 \end{pmatrix} &= \mathcal{U}_{\mathrm{AOBOA}}(\eta_k^{\mathrm{comb}}; x_k, V) - \mathcal{U}_{\mathrm{AOBOA}}(\widetilde{\eta}_k^{\mathrm{comb}}; x_k, \widetilde{V}) \\
&= \begin{pmatrix} q_k + (a' + a'd'd')p_k + a'd'b(q_k + a'p_k) \\ d'd'p_k + d'b(q_k + a'p_k) \end{pmatrix} + \begin{pmatrix} a' \\ 1 \end{pmatrix} f'\eta_k^{\mathrm{comb}} - \\
&\quad \begin{pmatrix} q_k + (a' + a'd'd')p_k + a'd' \cdot \widetilde{b}(q_k + a'p_k) \\ d'd'p_k + d' \cdot \widetilde{b}(q_k + a'p_k) \end{pmatrix} - \begin{pmatrix} a' \\ 1 \end{pmatrix} f'\widetilde{\eta}_k^{\mathrm{comb}} \\
&= \begin{pmatrix} a'd'b(q_k + a'p_k) \\ d'b(q_k + a'p_k) \end{pmatrix} - \begin{pmatrix} a'd' \cdot \widetilde{b}(q_k + a'p_k) \\ d' \cdot \widetilde{b}(q_k + a'p_k) \end{pmatrix} - \begin{pmatrix} a' \\ 1 \end{pmatrix} f'\Delta\eta_k^{\mathrm{comb}} \\
&= \begin{pmatrix} a' \\ 1 \end{pmatrix} d' \Big[b(q_k + a'p_k) - \widetilde{b}(q_k + a'p_k)\Big] - \begin{pmatrix} a' \\ 1 \end{pmatrix} f'\Delta\eta_k^{\mathrm{comb}} \\
&= \begin{pmatrix} a' \\ 1 \end{pmatrix} d'\Delta t \nabla U(q_k + a'p_k) - \begin{pmatrix} a' \\ 1 \end{pmatrix} f'\Delta\eta_k^{\mathrm{comb}}
\end{aligned} \tag{A34}$$

is fulfilled if

$$\Delta\eta_k^{\mathrm{comb}} = \frac{d'}{f'}\Delta t \nabla U(q_{k+1/2}) \tag{A35}$$

where we substituted $q_{k+1/2} = q_k + a' p_k$ (eq. A29a). Thus, $\mathcal{U}_{\mathrm{AOBOA}}(\eta_k; x_k, V)$ and $\mathcal{U}_{\mathrm{AOBOA}}(\widetilde{\eta}_k; x_k, \widetilde{V})$ have the same image

$$L_{1d} = \widetilde{L}_{1d}\,.$$

5. BOAOB

a. Algorithm

$$\begin{aligned}
p_{k+1/4} &= p_k - \frac{\Delta t}{2}\nabla V(q_k) && \text{(A36a)}\\
p_{k+2/4} &= e^{-\frac{\xi \Delta t}{2}}\, p_{k+1/4} + \sqrt{k_B T m\,(1-e^{-\xi\Delta t})}\,\eta_k^{(1)} && \text{(A36b)}\\
q_{k+1} &= q_k + \frac{\Delta t}{m} p_{k+2/4} && \text{(A36c)}\\
p_{k+3/4} &= e^{-\frac{\xi \Delta t}{2}}\, p_{k+2/4} + \sqrt{k_B T m\,(1-e^{-\xi\Delta t})}\,\eta_k^{(2)} && \text{(A36d)}\\
p_{k+1} &= p_{k+3/4} - \frac{\Delta t}{2}\nabla V(q_{k+1})\,. && \text{(A36e)}
\end{aligned}$$

Here, two random numbers $\eta_k^{(1)} \sim \mathcal{N}(0,1)$ and $\eta_k^{(2)} \sim \mathcal{N}(0,1)$ need to be drawn per full update cycle.

b. Update operator

$$\begin{aligned}
\mathcal{B}'\mathcal{O}'\mathcal{A}\mathcal{O}'\mathcal{B}' \begin{pmatrix} q_k \\ p_k \end{pmatrix} &= \mathcal{B}'\mathcal{O}'\mathcal{A}\mathcal{O}' \begin{pmatrix} q_k \\ p_k + b'(q_k) \end{pmatrix}\\
&= \mathcal{B}'\mathcal{O}'\mathcal{A} \begin{pmatrix} q_k \\ d'p_k + d'b'(q_k) + f'\eta_k^{(1)} \end{pmatrix}\\
&= \mathcal{B}'\mathcal{O}' \begin{pmatrix} q_k + ad'p_k + ad'b'(q_k) + af'\eta_k^{(1)} \\ d'p_k + d'b'(q_k) + f'\eta_k^{(1)} \end{pmatrix}\\
&= \mathcal{B}' \begin{pmatrix} q_k + ad'p_k + ad'b'(q_k) + af'\eta_k^{(1)} \\ d'd'p_k + d'd'b'(q_k) + d'f'\eta_k^{(1)} + f'\eta_k^{(2)} \end{pmatrix}\\
&= \begin{pmatrix} q_k + ad'p_k + ad'b'(q_k) + af'\eta_k^{(1)} \\ d'd'p_k + d'd'b'(q_k) + d'f'\eta_k^{(1)} + f'\eta_k^{(2)} + b'\Big(q_k + ad'p_k + ad'b'(q_k) + af'\eta_k^{(1)}\Big) \end{pmatrix}
\end{aligned} \tag{A37}$$

c. Update function

$$\begin{aligned}
\begin{pmatrix} q_{k+1} \\ p_{k+1} \end{pmatrix} &= \mathcal{U}_{\mathrm{BOAOB}}(\eta_k^{(1)}, \eta_k^{(2)}; x_k, V)\\
&= \begin{pmatrix} \bar{q}_{k+1} \\ \bar{p}_{k+1} \end{pmatrix} + \begin{pmatrix} 0 \\ b'\Big(\bar{q}_{k+1} + af'\eta_k^{(1)}\Big) \end{pmatrix} + \begin{pmatrix} af' \\ d'f' \end{pmatrix}\eta_k^{(1)} + \begin{pmatrix} 0 \\ f' \end{pmatrix}\eta_k^{(2)}
\end{aligned} \tag{A38}$$

with $\bar{q}_{k+1} = q_k + ad'p_k + ad'b'(q_k)$ and $\bar{p}_{k+1} = d'd'p_k + d'd'b'(q_k)$. Thus,

$$\begin{aligned}
\mathcal{U}_{\mathrm{BOAOB}} :&\quad \mathbb{R}^2 \to \Gamma\\
\mathcal{U}_{\mathrm{BOAOB}} :&\quad (\eta_k^{(1)}, \eta_k^{(2)}) \mapsto x_{k+1}\,.
\end{aligned} \tag{A39}$$

d. Derivation of $\Delta\eta_k^{(1)}$ and $\Delta\eta_k^{(2)}$

We derive $\Delta\eta_k^{(1)}$ and $\Delta\eta_k^{(2)}$ from the condition

$$\begin{pmatrix} 0 \\ 0 \end{pmatrix} = \mathcal{U}_{\mathrm{BOAOB}}(\eta_k^{(1)}, \eta_k^{(2)}; x_k, V) - \mathcal{U}_{\mathrm{BOAOB}}(\widetilde{\eta}_k^{(1)}, \widetilde{\eta}_k^{(2)}; x_k, \widetilde{V}) \tag{A40}$$

Inserting eq. A38 yields

$$\begin{aligned}
\begin{pmatrix} 0 \\ 0 \end{pmatrix} = & \begin{pmatrix} q_k + ad'p_k + ad'b'(q_k) \\ d'd'p_k + d'd'b'(q_k) \end{pmatrix} + \begin{pmatrix} 0 \\ b'(q_{k+1}) \end{pmatrix} + \begin{pmatrix} af' \\ d'f' \end{pmatrix} \eta_k^{(1)} + \begin{pmatrix} 0 \\ f' \end{pmatrix} \eta_k^{(2)} \\
& - \begin{pmatrix} q_k + ad'p_k + ad'\widetilde{b}'(q_k) \\ d'd'p_k + d'd'\widetilde{b}'(q_k) \end{pmatrix} - \begin{pmatrix} 0 \\ \widetilde{b}'(\widetilde{q}_{k+1}) \end{pmatrix} - \begin{pmatrix} af' \\ d'f' \end{pmatrix} \widetilde{\eta}_k^{(1)} - \begin{pmatrix} 0 \\ f' \end{pmatrix} \widetilde{\eta}_k^{(2)} \\
= & \begin{pmatrix} ad'\frac{\Delta t}{2}\nabla U(q_k) \\ d'd'\frac{\Delta t}{2}\nabla U(q_k) \end{pmatrix} + \begin{pmatrix} 0 \\ b'(q_{k+1}) - \widetilde{b}'(\widetilde{q}_{k+1}) \end{pmatrix} - \begin{pmatrix} af' \\ d'f' \end{pmatrix} \Delta\eta_k^{(1)} - \begin{pmatrix} 0 \\ f' \end{pmatrix} \Delta\eta_k^{(2)}
\end{aligned} \tag{A41}$$

where we used eqs. A3 and A4. The second term evaluates the potential at the updated position which, a priori, might differ in V and $\widetilde{V}$. Solving the line for the position in the above equation yields

$$\Delta\eta_k^{(1)} = \frac{d'}{f'}\frac{\Delta t}{2}\nabla U(q_k)\,. \tag{A42}$$

With this $q_{k+1} = \widetilde{q}_{k+1}$, and thus $b'(q_{k+1}) - \widetilde{b}'(\widetilde{q}_{k+1}) = \frac{\Delta t}{2}\nabla U(q_{k+1})$. Then the line for the momentum yields

$$\begin{aligned}
0 &= d'd'\frac{\Delta t}{2}\nabla U(q_k) + \frac{\Delta t}{2}\nabla U(q_{k+1}) - d'f' \cdot \frac{d'}{f'}\frac{\Delta t}{2}\nabla U(q_k) - f'\Delta\eta_k^{(2)} \\
&= \frac{\Delta t}{2}\nabla U(q_{k+1}) - f'\Delta\eta_k^{(2)} \\
&\Updownarrow \\
\Delta\eta_k^{(2)} &= \frac{1}{f'}\frac{\Delta t}{2}\nabla U(q_{k+1})
\end{aligned} \tag{A43}$$

6. OBABO method / Bussi-Parrinello thermostat

a. Algorithm

$$p_{k+1/4} = e^{-\frac{\xi\Delta t}{2}}\,p_k + \sqrt{k_B T m\,(1 - e^{-\xi\Delta t})}\,\eta_k^{(1)} \tag{A44a}$$

$$p_{k+2/4} = p_{k+1/4} - \frac{\Delta t}{2}\nabla V(q_k) \tag{A44b}$$

$$q_{k+1} = q_k + \frac{\Delta t}{m}p_{k+2/4} \tag{A44c}$$

$$p_{k+3/4} = p_{k+2/4} - \frac{\Delta t}{2}\nabla V(q_{k+1}) \tag{A44d}$$

$$p_{k+1} = e^{-\frac{\xi\Delta t}{2}}\,p_{k+3/4} + \sqrt{k_B T m\,(1 - e^{-\xi\Delta t})}\,\eta_k^{(2)}\,. \tag{A44e}$$

Here, two random numbers $\eta_k^{(1)} \sim \mathcal{N}(0,1)$ and $\eta_k^{(2)} \sim \mathcal{N}(0,1)$ need to be drawn per full update cycle. The algorithm is equal to the Bussi-Parrinello thermostat[46]. Compared to Ref. 48, we changed the notation as follows: $n \to k$, $R_n \to \eta_k$, $\delta t \to \Delta t$, $M \to m$, $\gamma \to \xi$, $F \to -\nabla V$.

b. Update operator

$$\begin{aligned}
\mathcal{O}'\mathcal{B}'\mathcal{A}\mathcal{B}'\mathcal{O}'\begin{pmatrix} q_k \\ p_k \end{pmatrix} &= \mathcal{O}'\mathcal{B}'\mathcal{A}\mathcal{B}'\begin{pmatrix} q_k \\ d'p_k + f'\eta_k^{(1)} \end{pmatrix} \\
&= \mathcal{O}'\mathcal{B}'\mathcal{A}\begin{pmatrix} q_k \\ d'p_k + f'\eta_k^{(1)} + b'(q_k) \end{pmatrix} \\
&= \mathcal{O}'\mathcal{B}'\begin{pmatrix} q_k + ad'p_k + af'\eta_k^{(1)} + ab'(q_k) \\ d'p_k + f'\eta_k^{(1)} + b'(q_k) \end{pmatrix} \\
&= \mathcal{O}'\begin{pmatrix} q_k + ad'p_k + af'\eta_k^{(1)} + ab'(q_k) \\ d'p_k + f'\eta_k^{(1)} + b'(q_k) + b'\Big(q_k + ad'p_k + af'\eta_k^{(1)} + ab'(q_k)\Big) \end{pmatrix} \\
&= \begin{pmatrix} q_k + ad'p_k + af'\eta_k^{(1)} + ab'(q_k) \\ d'd'p_k + d'f'\eta_k^{(1)} + d'b'(q_k) + d'b'\Big(q_k + ad'p_k + af'\eta_k^{(1)} + ab'(q_k)\Big) + f'\eta_k^{(2)} \end{pmatrix}
\end{aligned} \tag{A45}$$

c. Update function

$$\begin{aligned}
\begin{pmatrix} q_{k+1} \\ p_{k+1} \end{pmatrix} &= \mathcal{U}_{\mathrm{OBABO}}(\eta_k^{(1)}, \eta_k^{(2)}; x_k, V) \\
&= \begin{pmatrix} \bar{q}_{k+1} \\ \bar{p}_{k+1} \end{pmatrix} + \begin{pmatrix} 0 \\ d'b'(\bar{q}_{k+1} + af'\eta_k^{(1)}) \end{pmatrix} + \begin{pmatrix} af' \\ d'f' \end{pmatrix}\eta_k^{(1)} + \begin{pmatrix} 0 \\ f' \end{pmatrix}\eta_k^{(2)}
\end{aligned} \tag{A46}$$

with $\bar{q}_{k+1} = q_k + ad'p_k + ab'(q_k)$ and $\bar{p}_{k+1} = d'd'p_k + d'b'(q_k)$. Thus,

$$\begin{aligned}
\mathcal{U}_{\mathrm{OBABO}} :&\quad \mathbb{R}^2 \to \Gamma \\
\mathcal{U}_{\mathrm{OBABO}} :&\quad (\eta_k^{(1)}, \eta_k^{(2)}) \mapsto x_{k+1}\,.
\end{aligned} \tag{A47}$$

d. Derivation of $\Delta\eta_k^{(1)}$ and $\Delta\eta_k^{(2)}$

We derive $\Delta\eta_k^{(1)}$ and $\Delta\eta_k^{(2)}$ from the condition

$$\begin{pmatrix} 0 \\ 0 \end{pmatrix} = \mathcal{U}_{\mathrm{OBABO}}(\eta_k^{(1)}, \eta_k^{(2)}; x_k, V) - \mathcal{U}_{\mathrm{OBABO}}(\widetilde{\eta}_k^{(1)}, \widetilde{\eta}_k^{(2)}; x_k, \widetilde{V}) \tag{A48}$$

Inserting eq. A46 yields

$$\begin{aligned}
\begin{pmatrix} 0 \\ 0 \end{pmatrix} =&\ \begin{pmatrix} q_k + ad'p_k + ab'(q_k) \\ d'd'p_k + d'b'(q_k) \end{pmatrix} + \begin{pmatrix} 0 \\ d'b'(q_{k+1}) \end{pmatrix} + \begin{pmatrix} af' \\ d'f' \end{pmatrix}\eta_k^{(1)} + \begin{pmatrix} 0 \\ f' \end{pmatrix}\eta_k^{(2)} \\
&- \begin{pmatrix} q_k + ad'p_k + a\widetilde{b}'(q_k) \\ d'd'p_k + d'\widetilde{b}'(q_k) \end{pmatrix} - \begin{pmatrix} 0 \\ d'\widetilde{b}'(\widetilde{q}_{k+1}) \end{pmatrix} - \begin{pmatrix} af' \\ d'f' \end{pmatrix}\widetilde{\eta}_k^{(1)} - \begin{pmatrix} 0 \\ f' \end{pmatrix}\widetilde{\eta}_k^{(2)} \\
=&\ \begin{pmatrix} a\frac{\Delta t}{2}\nabla U(q_k) \\ d'\frac{\Delta t}{2}\nabla U(q_k) \end{pmatrix} + \begin{pmatrix} 0 \\ d'b'(q_{k+1}) - d'\widetilde{b}'(\widetilde{q}_{k+1}) \end{pmatrix} - \begin{pmatrix} af' \\ d'f' \end{pmatrix}\Delta\eta_k^{(1)} - \begin{pmatrix} 0 \\ f' \end{pmatrix}\Delta\eta_k^{(2)}
\end{aligned} \tag{A49}$$

where we used eqs. A4 and A3. The second term evaluates the potential at the updated position which, a priori, might differ in V and $\widetilde{V}$. Solving the line for the position in the above equation yields

$$\Delta\eta_k^{(1)} = \frac{1}{f'}\frac{\Delta t}{2}\nabla U(q_k)\,. \tag{A50}$$

With this $q_{k+1} = \widetilde{q}_{k+1}$, and thus $d'b'(q_{k+1}) - d'\widetilde{b}'(\widetilde{q}_{k+1}) = d'\frac{\Delta t}{2}\nabla U(q_{k+1})$. Then the line for the momentum yields

$$\begin{aligned}
0 &= d'\frac{\Delta t}{2}\nabla U(q_k) + d'\frac{\Delta t}{2}\nabla U(q_{k+1}) - d'f'\cdot\frac{1}{f'}\frac{\Delta t}{2}\nabla U(q_k) - f'\Delta\eta_k^{(2)} \\
&= d'\frac{\Delta t}{2}\nabla U(q_{k+1}) - f'\Delta\eta_k^{(2)} \\
&\Updownarrow \\
\Delta\eta_k^{(2)} &= \frac{d'}{f'}\frac{\Delta t}{2}\nabla U(q_{k+1})
\end{aligned} \tag{A51}$$

7. OABAO

a. Algorithm

$$p_{k+1/3} = e^{-\frac{\xi\Delta t}{2}}\,p_k + \sqrt{k_BTm(1-e^{-\xi\Delta t})}\,\eta_k^{(1)} \tag{A52a}$$

$$q_{k+1/2} = q_k + \frac{\Delta t}{2m}\,p_{k+1/3} \tag{A52b}$$

$$p_{k+2/3} = p_{k+1/3} - \Delta t\nabla V(q_{k+1/2}) \tag{A52c}$$

$$q_{k+1} = q_{k+1/2} + \frac{\Delta t}{2m}\,p_{k+2/3} \tag{A52d}$$

$$p_{k+1} = e^{-\frac{\xi\Delta t}{2}}\,p_{k+2/3} + \sqrt{k_BTm(1-e^{-\xi\Delta t})}\,\eta_k^{(2)} \tag{A52e}$$

Here, two random numbers $\eta_k^{(1)} \sim \mathcal{N}(0,1)$ and $\eta_k^{(2)} \sim \mathcal{N}(0,1)$ need to be drawn per full update cycle.

b. Update operator

$$\begin{aligned}
\mathcal{O}'\mathcal{A}'\mathcal{B}\mathcal{A}'\mathcal{O}'\begin{pmatrix} q_k \\ p_k \end{pmatrix} &= \mathcal{O}'\mathcal{A}'\mathcal{B}\mathcal{A}'\begin{pmatrix} q_k \\ d'p_k + f'\eta_k^{(1)} \end{pmatrix} \\
&= \mathcal{O}'\mathcal{A}'\mathcal{B}\begin{pmatrix} q_k + a'd'p_k + a'f'\eta_k^{(1)} \\ d'p_k + f'\eta_k^{(1)} \end{pmatrix} \\
&= \mathcal{O}'\mathcal{A}'\begin{pmatrix} q_k + a'd'p_k + a'f'\eta_k^{(1)} \\ d'p_k + f'\eta_k^{(1)} + b(q_k + a'd'p_k + a'f'\eta_k^{(1)}) \end{pmatrix} \\
&= \mathcal{O}'\begin{pmatrix} q_k + a'd'p_k + a'f'\eta_k^{(1)} + a'd'p_k + a'f'\eta_k^{(1)} + a'b(q_k + a'd'p_k + a'f'\eta_k^{(1)}) \\ d'p_k + f'\eta_k^{(1)} + b(q_k + a'd'p_k + a'f'\eta_k^{(1)}) \end{pmatrix} \\
&= \begin{pmatrix} q_k + a'd'p_k + a'f'\eta_k^{(1)} + a'd'p_k + a'f'\eta_k^{(1)} + a'b(q_k + a'd'p_k + a'f'\eta_k^{(1)}) \\ d'd'p_k + d'f'\eta_k^{(1)} + d'b(q_k + a'd'p_k + a'f'\eta_k^{(1)}) + f'\eta_k^{(2)} \end{pmatrix}
\end{aligned} \tag{A53}$$

c. Update function

$$\begin{pmatrix} q_{k+1} \\ p_{k+1} \end{pmatrix} = \mathcal{U}_{\mathrm{OABAO}}(\eta_k^{(1)}, \eta_k^{(2)}; x_k, V)$$

$$= \begin{pmatrix} \bar{q}_{k+1} \\ \bar{p}_{k+1} \end{pmatrix} + \begin{pmatrix} a'b(q_k + a'd'p_k + a'f'\eta_k^{(1)}) \\ d'b(q_k + a'd'p_k + a'f'\eta_k^{(1)}) \end{pmatrix} + \begin{pmatrix} 2a'f' \\ d'f' \end{pmatrix} \eta_k^{(1)} + \begin{pmatrix} 0 \\ f' \end{pmatrix} \eta_k^{(2)} \tag{A54}$$

with $\bar{q}_{k+1} = q_k + 2a'd'p_k$ and $\bar{p}_{k+1} = d'd'p_k$. Thus for most potentials,

$$\begin{aligned} \mathcal{U}_{\mathrm{OABAO}}: &\quad \mathbb{R}^2 \to \Gamma \\ \mathcal{U}_{\mathrm{OABAO}}: &\quad (\eta_k^{(1)}, \eta_k^{(2)}) \mapsto x_{k+1}\,. \end{aligned} \tag{A55}$$

If e.g. $a'b(q_k + a'd'p_k + a'f'\eta_k^{(1)}) = -2a'f'\eta_k^{(1)}$, the contribution of $\eta_k^{(1)}$ to the position update cancels, and the the image of $\mathcal{U}_{\mathrm{OABAO}}$ is a line parallel to the p-axis.

3.4 Supporting Information for part B

The content of this section has not been published in any form prior to this thesis.

3.4.1 SI: Introduction

To further test Girsanov reweighting for splitting methods in underdamped Langevin dynamics, we conducted molecular simulations for the [Ca-Cl]$^+$ dimer in aqueous solvent. Dissociation rates were determined from molecular dynamics (MD) simulations, initially using the unbiased potential energy function. Calculations were then repeated using a repulsive bias applied in the bounded state to accelerate dissociation events. The biased dissociation rates were reweighted using Girsanov reweighting and compared to the reference rates from unbiased simulations. Successful Girsanov reweighting would yield reweighted rates close to the reference rates.

We tested Girsanov reweighting for four different integrators: ABOBA, AOBOA, BOAOB and OBABO. These integrators are named according to the sequence of application of the partial integration steps $\mathcal{A}$, $\mathcal{B}$ and $\mathcal{O}$, see Section 3.3. Steps that appear twice indicate two half partial steps. All integrators used in this study are symmetrical, meaning they have the same order when read forwards or backwards, which is why they are referred to as symmetric splitting methods. Expressions for random number differences $\Delta\eta_k$ necessary to calculate the relative path probabilities are provided in Tab. 1 of the paper in Section 3.3.

3.4.2 SI: Results

MD simulations of a [Ca-Cl]$^+$ dimer surrounded by explicit water in a cubic box were carried out at a temperature of 300 K using a parametrized force field (see computational details in Section 3.4.4). For dissociation events, the ion-ion distance d effectively describes the reactant (bounded) and product (unbounded) states. Consequently, the progression of d can be used to register dissociation events and measure escape times (Section 2.3.1). Additionally, dissociation can be accelerated by biasing the potential at d values corresponding to the reactant state.

Trajectories were started from configurations equilibrated in the bounded state A and propagated until the unbounded state B was reached. From each trajectory, an escape time was determined. Repeating the experiment a sufficient number of times yields a statistically representative distribution of escape times, from which a mean first passage time (MFPT) and dissociation rate k_{AB}^{MFPT} can be calculated (Eqs. 2.41-2.42). For each integrator, k_{AB}^{MFPT} was computed from 3000 trajectories using the unbiased potential, which we also refer to as the target potential. The free energy as a function of ion-ion distance d for the target potential is given in Fig. 3.1.a (green). The corresponding distribution of escape times from trajectories generated using the ABOBA integrator is shown in Fig. 3.1.b (green). The

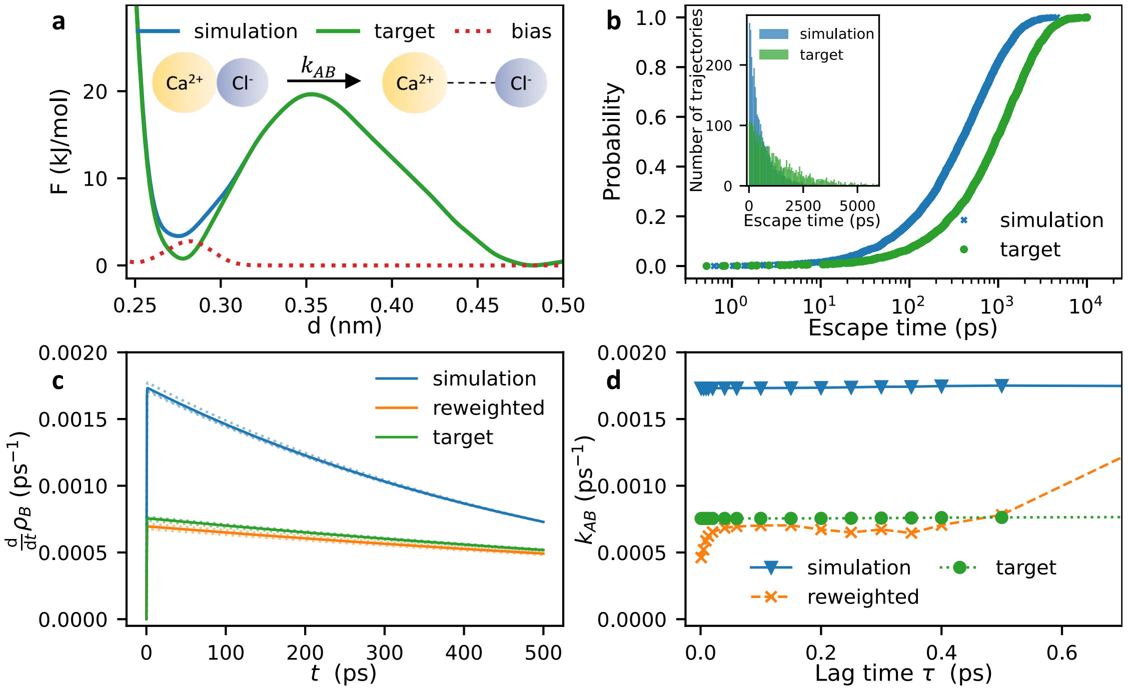

Figure 3.1: **a:** Free energy profile for ion-ion distance d of $[\text{Ca-Cl}]^+$ model system for the unbiased (target, green) and biased (simulation, blue) potentials. **b:** Cumulative distribution function and histogram of escape times for 3000 trajectories in the biased (simulation, blue) and 3000 trajectories in the unbiased potential (target, green) using the ABOBA integrator. **c:** Time derivative of the product state probability $\rho_B(t)$ propagated by transition matrices (lag time $\tau = 0.06\,\text{ps}$) at the simulation (blue) and target (green) potential, as well as by a reweighted transition matrix (orange) using the ABOBA integrator. Full lines correspond to sets of 3000 trajectories, dotted lines correspond to different sets of 1000 trajectories. **d:** Dissociation rates as a function of lag time τ for simulation (blue) and target (green) potentials, as well as for reweighted dynamics (orange) using the ABOBA integrator.

distribution of escape times and the shape of the empirical cumulative distribution function (ECDF) corresponds to what we expect for a first order Poisson process[85]. The resulting rates k_{AB}^{MFPT} for all integrators are given in Tab. 3.1. All results are between 7.3×10^{-4} and $7.6 \times 10^{-4}\,\text{ps}^{-1}$, with rates varying slightly between integrators. ABOBA and OBABO produce faster rates, while for AOBOA dissociation is slightly slower.

It is our intention to examine if we can speed up dissociation by biasing the potential, but retrieve the actual, unbiased rate using Girsanov reweighting. Accordingly, a bias $U(d)$ (Fig. 3.1.a, red) was added destabilizing the bounded state, resulting in a new potential which we refer to as the simulation potential (Fig. 3.1.a, blue). 3000 new trajectories were propagated for each integrator. The distribution of escape times for the ABOBA integrator is also shown in Fig. 3.1.b (blue). Similarly as for the target potential, the distribution of escape times and shape of the ECDF correspond to what is anticipated for a first order Poisson process. As expected, escape times are on average shorter than for the target potential, with the ECDF shifted left to smaller values. The dissociation rate k_{AB}^{MFPT} at the simulation potential is between 1.65×10^{-3} and $1.74 \times 10^{-3}\,\text{ps}^{-1}$ (Tab. 3.1), about 2.3 times higher

	Simulation			**Target**	
	$\mathbf{k_{AB}^{MFPT}}$ [ps^{-1}]	$\mathbf{k_{AB}^{prop}}$ [ps^{-1}]	$\mathbf{k_{AB}^{rew}}$ [ps^{-1}]	$\mathbf{k_{AB}^{MFPT}}$ [ps^{-1}]	$\mathbf{k_{AB}^{prop}}$ [ps^{-1}]
ABOBA	1.74×10^{-3}	1.73×10^{-3}	6.95×10^{-4}	7.56×10^{-4}	7.55×10^{-4}
AOBOA	1.65×10^{-3}	1.65×10^{-3}	6.59×10^{-4}	7.32×10^{-4}	7.31×10^{-4}
BOAOB	1.68×10^{-3}	1.68×10^{-3}	6.77×10^{-4}	7.41×10^{-4}	7.40×10^{-4}
OBABO	1.69×10^{-3}	1.68×10^{-3}	6.79×10^{-4}	7.54×10^{-4}	7.54×10^{-4}

Table 3.1: Rates from mean first passage times (k_{AB}^{MFPT}) and from density propagation (k_{AB}^{prop}) for the simulation and target potentials and using dynamical reweighting (k_{AB}^{rew}).

than at the target potential. This means the total simulation time to estimate rates at the simulation potential is about a factor of 2.3 smaller.

As an alternative to calculating MFPTs, the trajectories can be used in Markov State Models (MSM) to build transition matrices $\mathbf{T}(\tau)$ (Section 2.3.3) using d as collective variable (CV). Transition matrices can be used to propagate probability densities (Eqs. 2.50-2.51). Starting from an initial probability density representing local equilibrium in the bounded state (and being zero everywhere else), ion-ion dissociation is depicted by the transfer of probability density towards the unbounded state over time. The dissociation rate k_{AB}^{prop} can then be estimated from the time derivative of the probability to be in the product state $\rho_B(t)$ (Eq. 3.7, Section 3.4.4). Time derivatives for density propagation as a function of simulation time $\frac{\mathrm{d}}{\mathrm{d}t}\rho_B(t)$ propagated by transition matrices built from 3000 trajectories using the ABOBA integrator are shown in Fig. 3.1.c (full blue and green lines for simulation and target potentials, respectively). Similar curves for other integrators are shown in Fig. 3.2.a,b,c. Maxima of these curves estimate k_{AB}^{prop}. The resulting rates are provided in Tab. 3.1 and match rates from MFPTs very closely for all integrators at both simulation and target potentials. This indicates dissociation rates can reliably be computed employing analysis of density propagation by transition matrices (Section 3.4.4).

Using Girsanov reweighting (Section 2.4.2), we estimated a transition matrix $\mathbf{T}(\tau)$ for the target potential from trajectories simulated at the simulation potential. Similarly as before, this matrix was used to propagate a well-chosen starting probability density, from which the product state probability $\rho_B(t)$ was determined as a function of time. The evolution of $\frac{\mathrm{d}}{\mathrm{d}t}\rho_B(t)$ from the reweighted transition matrix (Fig. 3.1.c, full orange line) approximates the reference at target potential (Fig. 3.1.c, full green line) well. This was also observed for other integrators in Fig. 3.2.a,b,c. The resulting reweighted dissociation rate k_{AB}^{rew} (Tab. 3.1) ranged from 6.6×10^{-4} to $7.0 \times 10^{-4}\,\mathrm{ps}^{-1}$, close to reference values at the target potential. More precisely, reweighted rates underestimate target rates by about 8 to 10%. This promising result demonstrates that Girsanov reweighting effectively recovers unbiased rates even when the simulation potential produces dissociation rates approximately 2.3 times higher than the target potential.

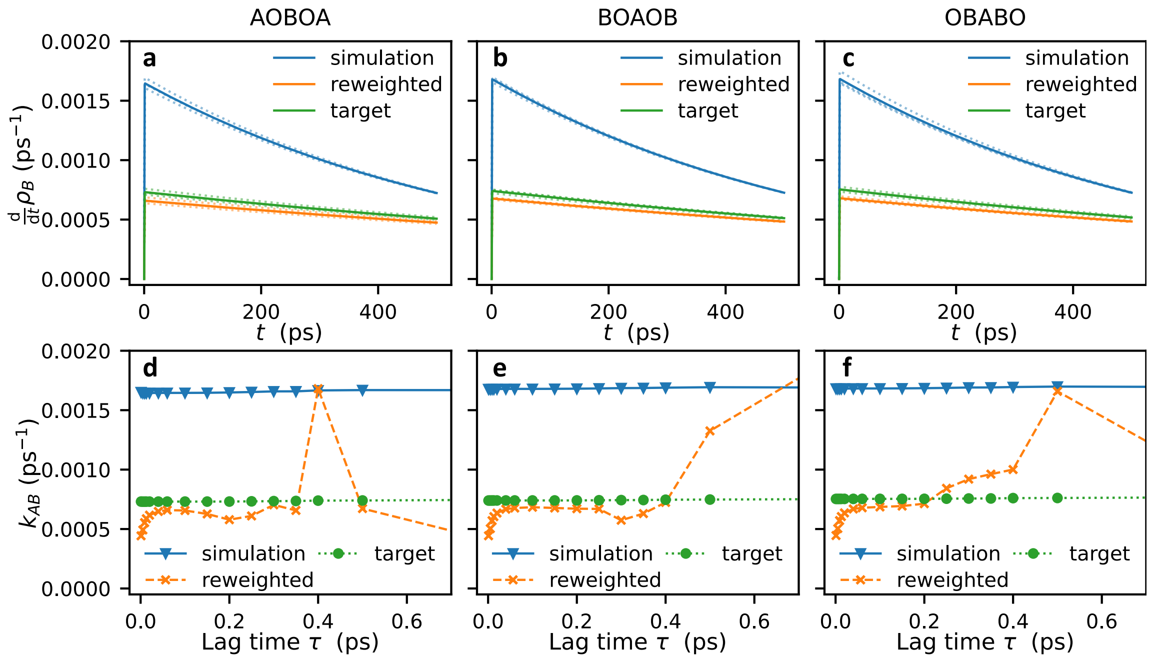

Figure 3.2: **Top:** Time derivative of the product state probability $\rho_B(t)$ propagated by transition matrices (lag time $\tau = 0.06\,\text{ps}$) at the simulation (blue) and target (green) potential, as well as by a reweighted transition matrix (orange) for different integrators AOBOA (**a**), BOAOB (**b**) and OBABO (**c**). Full lines correspond to sets of 3000 trajectories, dotted lines correspond to different sets of 1000 trajectories. **Bottom:** Dissociation rates as a function of lag time τ for simulation (blue) and target (green) potentials as well as for reweighted dynamics (orange) for different integrators AOBOA (**d**), BOAOB (**e**) and OBABO (**f**).

3.4.3 SI: Outlook

Lag times for transition matrices from path reweighting have been chosen carefully. Rates as a function of lag times are shown in Fig. 3.1.d for the ABOBA integrator and Fig. 3.1.d,e,f for the other integrators. At very short lag times, reweighted rates underestimate the target rates, while at long lag times, reweighting breaks down completely. In between, there is a plateau region of lag times where reweighting is stable and performs well. While more extensive investigation is required for a detailed understanding of this behavior, the following remarks could be a starting point:

- Breakdown of reweighting at high lag times could be caused by insufficient sampling of the path ensemble. As paths get longer, the path probabilities generally become smaller, making reweighting more challenging. Sufficiently sampling of paths at the simulation potential to reweight so a path ensemble at the target potential is emulated is expected to require more data. Simulating more dissociation trajectories is expected to improve reweighting at higher lag times.

- High precision libraries might be necessary to implement the computation of ratios of very small numbers.

- Biasing and subsequent Girsanov reweighting in combination with MSMs might be sen-

> sitive to the choice of CV along which the bias is applied as well as the CV space on which the MSM is built[104, 106]. In the current setup, d is used for both, although correlated motion in the explicit water solvent might be involved. The coordination number of the ions has been identified in literature[141, 142] as a CV exhibiting correlations.

For the current model system, the chosen lag time is sufficient to predict accurate rates, evidenced by the proximity of rates calculated from density propagation to those calculated from mean first passage times (Tab. 3.1). Notice that this is not a given for more involved processes, as many processes require molecular relaxation times τ_{mol} for the system to relax in the product state. At times smaller than τ_{mol}, orthogonal degrees of freedom are expected to exhibit correlated motion with the MSM collective variables, leading to correlation functions and corresponding transition matrices that are unreliable. While transitions in the current system evidently can be accurately described using transition matrices at small lag times, this might not be the case for processes in systems that are more involved. Consequently, more research is necessary towards the convergence of path reweighting at higher lag times.

On a more general level, error estimation for path reweighting would be beneficial. There is a trade off between gain in computational time through biasing, but loss of precision. It would be of interest to optimize biasing functions that facilitate reliable reweighting of the dynamics with maximal speed up. Path reweighting of course has the advantage that from trajectories at a single simulation potentials, dynamics can be reweighted to different target potentials.

3.4.4 SI: Methods

Computational Details for Dynamics

A cubic box of solvent of cell size 1.25 nm including one Ca^{2+} and one Cl^{-} ion, similar as in Ref. 141, was generated using GROMACS'[41] *solvate* and *genion* functionalities. Subsequently, the *tleap* and *parmed* programs of AmberTools22[143] were used to generate input and topology files, using the TIP4P-EW[144] water model and with corresponding Amber ion parameters using 12-6-4 Lennard-Jones (LJ) parameters for the calcium[145] and chloride[142] ions. These parameters have been documented to have superior structural features over the traditionally used 12-6 LJ parameters. All dynamics were performed in OpenMM[40]. The ABOBA, AOBOA, BOAOB and OBABO integrators for Langevin dynamics were implemented using OpenMM's *CustomIntegrator* class, which allows definition of new variables and customized application of integration steps necessary for writing out all data required for the path reweighting. Dynamics were carried out with an integration time step of 1 fs at a temperature of 300 K with a friction rate of 2 ps^{-1} and using periodic boundary conditions with the particle mesh Ewald (PME) scheme and a cutoff of 0.6 nm for non-bonded interactions. Notice that PME can technically only be applied to systems of neutral net charge. Administering it to the calcium chloride dimer in water is done by implicitly introducing a uniform background charge density which effectively neutralizes the system[146]. This is an unphysical approximation, and leads to artificial dynamics. Furthermore, the small cell size is expected to perturb the solvation free energy of the ions, as well as the ion-ion interactions[147]. These effects are expected to have a significant influence on the dissociation rate, yet in a way that is similar for the target and simulation potential. Consequently, while dynamics of this small system are not a completely reliable physical representation of true calcium chloride dissociation, they are nevertheless useful to demonstrate the performance of dynamical reweighting methods in molecular dynamics simulations, and reweighting is expected to perform similarly in larger, more realistic model systems.

Free Energy Profile

In order to get an idea of the population distribution along d, a 100 ns well-tempered metadynamics simulation was carried out using the ABOBA integrator, biasing d at a deposition rate of $2\,\mathrm{ps}^{-1}$ or every 500 time steps, and using Gaussians of initial height of $0.4\,\mathrm{kJ\,mol}^{-1}$ and a standard deviation of 0.01 nm, while using a biasing factor of 8. During metadynamics, a one-sided harmonic barrier of $1000\,\mathrm{kJ\,mol}^{-1}\mathrm{nm}^{-2}$ was put at $d = 0.55\,\mathrm{nm}$. The resulting free energy surface is shown in Fig. 3.1.a (green) and corresponds to the target potential for which we aim to calculate dissociation rates.

Unbiased Trajectories

Unbiased reference trajectories were initialized in the bounded state and equilibrated for 400 ps. To avoid escape from the bounded state during equilibration, the PLUMED[148] software package was applied to put one-sided harmonic restraints (i.e. walls) on the ion-ion distance d at 0.33 nm with a spring constant of $5000\,\mathrm{kJ\,mol}^{-1}\mathrm{nm}^{-2}$ as well as on the coordination number at 6.5 with a spring constant of $3000\,\mathrm{kJ\,mol}^{-1}$ per unit of coordination number squared. The UPPER_WALLS keyword was used for the one-sided harmonic restraints while the COORDINATION keyword was used to define the coordination number, which calls the default switching function in PLUMED to do so. After equilibration, restraints were removed and trajectories were run up until a dissociation event was recorded, using PLUMED's committor functionality to stop trajectories once an ion-ion distance of larger than 0.45 nm was registered. Ion-ion distances were written out at every time step.

Biased Trajectories

To generate a bias in the bounded state, a short well-tempered metadynamics simulation was performed using the ABOBA integrator in combination with PLUMED. After equilibration in the bounded state as described above, metadynamics were started, biasing the ion-ion distance d at a deposition rate of $0.1\,\mathrm{ps}^{-1}$, depositing Gaussian biases of height $0.4\,\mathrm{kJ\,mol}^{-1}$ and standard deviation $0.01\,\mathrm{nm}$ while using a biasing factor of 6. Metadynamics were interrupted after deposition of just ten Gaussians, with the reactant state only partially filled and thus long before a conventional metadynamics experiment would be completed. The positions and heights of the deposited Gaussians are saved to file, and can subsequently be used as a constant bias in the bounded state. In other words, we performed an incomplete metadynamics simulation in the bounded state solely for the purpose of constructing a small reactant state bias.

Biased trajectories were initialized and equilibrated in the bounded state in an equivalent way as for the unbiased reference trajectories, i.e. using the same restraints and equilibration times. Similarly as before, restraints were removed after equilibration and a committor function was used to stop simulations when trajectories reach the unbounded product state. For the biased trajectories, the ion-ion distance d and the bias at the current step are saved at every time step using PLUMED. Additionally, the terms

$$\eta_k \cdot \Delta\eta_k + \frac{1}{2}(\Delta\eta_k)^2 \tag{3.1}$$

necessary for calculating $M\left[\mathrm{x}\,|\,\mathbf{x}_0\right]$ (Eq. 2.91) are computed using OpenMM's *CustomIntegrator* class and written out at every time step using OpenMM's reporter functionalities. The expression of $\Delta\eta_k$ depends on the integrator used (Section 3.3).

Calculation of k_{AB}^{MFPT}

3000 trajectories were simulated at both the target and simulation potential. For each trajectory, the escape time was determined by measuring the time it took for the trajectory to reach a predetermined border value of d on the product side, which we chose to be relatively close to the barrier peak at $d = 0.40\,\mathrm{nm}$. Notice that due to partly neglected recrossing, this can lead to an overestimation of the rate. This effect is expected to influence the target and simulation escape rates similarly, and thus dynamically reweighting rates from trajectories at the simulation potential should still be a good estimate for rates at the target potential, as long as the border value is applied consistently. Mean first passage times and corresponding dissociation rates can then be calculated using Eqs. 2.41 and 2.42. The distributions of escape times for target and simulation potential are shown in Fig. 3.1.b.

Calculation of k_{AB}^{prop}

For both potentials, all 3000 trajectories were truncated after the first trajectory point exceeding the border value of $d = 0.40\,\mathrm{nm}$, and combined to generate a transition matrix, similar to what is typically done in Markov State Models. The ion-ion distance d was discretized in 100 bins, where the lower border of the last bin was made to correspond to the border value of

0.40 nm. In this way, the last bin functions as a sink state representing the product state B, and trajectories are assumed to stay in that state once it has been reached. After choosing a lag time τ, count matrices can be built for each trajectory, and subsequently added together and row normalized to obtain a transition matrix $\mathbf{T}(\tau)$. Detailed balance is not enforced in doing so. Transition matrices can be used to propagate densities

$$\mathbf{p}^T(t + a\tau) \approx \mathbf{p}^T(t)\mathbf{T}^a(\tau)\,, \tag{3.2}$$

which is an approximation compared to the continuous propagation of densities[106] because Markovianity is not guaranteed (Section 2.3.3). An initial density is chosen to match local equilibrium in the bounded state, i.e. for $d \leq 0.32\,\mathrm{nm}$, and zero everywhere else, and is propagated using the transition matrix constructed from the escape trajectories. From the evolution of the probability density in time (Fig. 3.3), transition rates can be estimated using conventional rate theory.

For a first order non-reversible reaction $A \rightarrow B$, the rate equation can be written in terms of the reaction constant k_{AB}:

$$-\frac{\mathrm{d}c_A(t)}{\mathrm{d}t} = \frac{\mathrm{d}c_B(t)}{\mathrm{d}t} = k_{AB}c_A(t)\,. \tag{3.3}$$

Using $c_A(t) = \rho_A(t)N/V$, where $\rho_A(t) = \int_{x \in A} \rho(x,t)\mathrm{d}x$ is the probability to be in state A and equivalent for B, this can be rewritten in probability densities

$$-\frac{\mathrm{d}\rho_A(t)}{\mathrm{d}t} = \frac{\mathrm{d}\rho_B(t)}{\mathrm{d}t} = k_{AB}\rho_A(t) \tag{3.4}$$

and solved as

$$\rho_A(t) = \rho_A(0)e^{-k_{AB}t}\,. \tag{3.5}$$

Since we've initiated the density in local equilibrium at the reactant state A and zero everywhere else, we let $\rho_A(0) = 1$. Furthermore, we assume $\rho_A(t) + \rho_B(t) = 1$ as we expect very low probability densities in the transition zone between reactant and product state at any time. Correspondingly, Eq. 3.5 can be expressed in terms of the product state B as:

$$\rho_B(t) = 1 - e^{-k_{AB}t}\,. \tag{3.6}$$

Taking the time derivative yields

$$\frac{\mathrm{d}}{\mathrm{d}t}\rho_B(t) = k_{AB}e^{-k_{AB}t} \tag{3.7}$$

from which the rate constant can be obtained directly through $k_{AB} = \max\left(\frac{\mathrm{d}}{\mathrm{d}t}\rho_B(t)\right)$.

From the discretized probabilities $\mathbf{p}(t)$ propagated using Eq. 3.2, $\rho_B(t)$ can be estimated

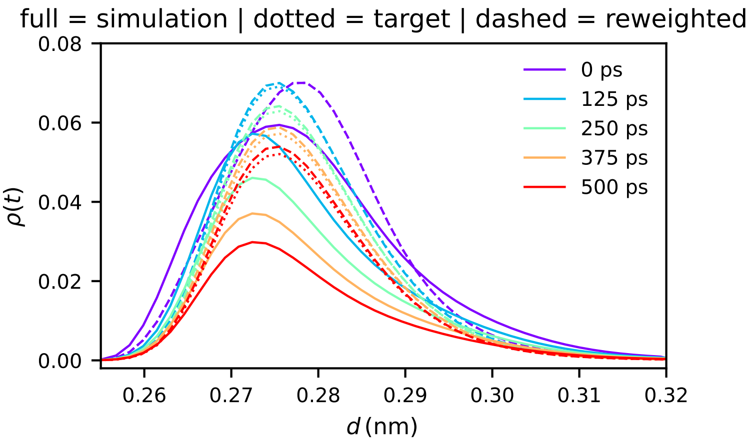

Figure 3.3: Evolution of probabilities $\mathbf{p}(t)$ in the reactant state A as a function of time, propagated using Eq. 3.2 with transition matrices at lag time $\tau = 0.06\,\mathrm{ps}$ built from trajectories at the simulation potential (full) and target potential (dotted), as well as with reweighted transition matrices (dashed). Propagation from reweighted dynamics follows propagation at target potential closely.

using

$$\rho_B(t) = \mathbf{p}^T(t) \cdot \mathbf{h_B} \tag{3.8}$$

where $\mathbf{h_B}$ is a reactant state mask array with unit elements in the bins associated with the product state and zero elsewhere. In our case, the reactant state B corresponds to the sink state in the last bin, so $\mathbf{h_B}$ is zero everywhere except for its last element, which is one, and $\rho_B(t)$ simply corresponds to the last element of $\mathbf{p}(t)$. For propagation with a transition matrix of lag time τ, the time derivative was calculated as

$$\frac{\mathrm{d}}{\mathrm{d}t}\rho_B(t) \approx \frac{\rho_B(t+\tau) - \rho_B(t)}{\tau} \tag{3.9}$$

from which k_{AB}^{prop} was estimated by finding the maximum value.

For calculation of rates from density propagation k_{AB}^{prop}, a lag time of $\tau = 0.06\,\mathrm{ps}$ was used. Figures showing time derivatives of propagation of product state densities $\frac{\mathrm{d}}{\mathrm{d}t}\rho_B(t)$ (Fig. 3.1.c and Fig. 3.1.a,b,c) were generated using transition matrices with the same lag time.

Calculation of k_{AB}^{rew}

Reweighted transition matrices modeling dynamics at the target potential from trajectories simulated at the simulation potential were calculated using path reweighting formulations as delineated in Section 2.4.2. MSMs are built similarly as above for k_{AB}^{prop}, with the addition that each count in the count matrix is weighted by thermodynamical reweighting factor $g(\mathbf{x}_0)$ and dynamical reweighting factor $M\left[\mathrm{x}\,|\,\mathbf{x}_0\right]$ for the corresponding path x of length τ (Eq. 2.97). This can be achieved straightforwardly at little extra cost using the terms in Eq. 3.1 saved during simulation of the biased trajectories. Once the reweighted transition matrix was calculated, density propagation and rate estimation were carried out as before (Eqs. 3.2-3.9).

Since transition matrices model dynamics at the target potential, the initial density should match local equilibrium in the unbiased bounded state. As can be seen in Fig. 3.3, density propagation by the reweighted transition matrix follows that by the transition matrix at the target potential closely. Dissociation rates from Girsanov reweighting (k_{AB}^{rew}, Tab. 3.1) and corresponding figures for time derivatives of product state densities (Fig. 3.1.a,b,c in orange) were generated with transition matrices of lag times $\tau = 0.06\,\mathrm{ps}$.

Chapter 4

Conclusions

This work has explored the potential for estimating reaction rates of high activation energy processes using molecular dynamics (MD) simulations combined with enhanced sampling techniques. Eyring's Transition State Theory (TST) remains the most widely used method for estimating reaction rate constants as it relies only on key thermodynamic quantities, bypassing the need for full dynamical trajectories. However, TST assumes a single, well-defined transition state in quasi-equilibrium with the reactant state—a simplification that can lead to inaccuracies in systems with complex reaction pathways, dynamic fluctuations or strong solvent effects. In contrast, MD-based approaches rely on explicit simulations of molecular trajectories and capture the detailed molecular pathways and fluctuations, offering potentially higher accuracy for complex reaction environments. This shift from TST to MD-based methods marks a fundamental change in theoretical approach, highlighting the need to examine the applicability and reliability of MD-based rate estimates, especially for processes with high energy barriers. Through a series of case studies, this work evaluates the efficacy of MD-based rare event methods, and additionally explores dynamical reweighting techniques to enhance their applicability and accuracy.

Part A The study begins by investigating the thermal cis-trans isomerization of retinal, a rare event that plays a key role in the photocylce of biological light responses. Density functional tight-binding (DFTB) was used to model the potential energy surfaces (PES) of two retinal analogues in vacuum. In the gas phase, ground-state isomerization exhibits a well-defined, high energy transition state for which Eyring's TST is expected to provide accurate rate constants. Consequently, TST can serve as a reference to evaluate reaction rates from MD-based methods. Rare event methods based on numerical sampling, such as infrequent metadynamics, yielded rate constants consistent with TST in the classical limit. However, effective dynamics-based methods like Kramers' theory produced rate constants that were several orders of magnitude higher. This discrepancy is attributed to the limitations of the dihedral angle to function as a one-dimensional reaction coordinate. Notably, out-of-plane wagging of substituents on the double bond showed strong correlation with the dihedral angle, suggesting that the isomerization mechanism involves coordinated motions beyond mere rotation. This indicates the need for a multidimensional approach to accurately model the reaction dynamics.

To investigate this further, MD simulations were set up for a retinal analogue modeled by a classical force field. Consistent with the DFTB findings, effective dynamics along the dihedral angle reaction coordinate produced rates significantly higher than those from infrequent metadynamics. An enhanced reaction coordinate was converged by incorporating correlated degrees of freedom using the path adaptive sampling approach. This path-based approach improved the accuracy of rate estimations, revealing higher free energy barriers and yielding rates closer to those from infrequent metadynamics. Similarly, grid-based models, such as the square-root approximation, applied to multidimensional free energy surfaces, produced rates in excellent agreement with those from infrequent metadynamics.

As systems become more complex, with rugged PES and less clearly defined transition states, the assumptions of TST become less viable. This is likely the case, for example, if more of the protein environment around the retinal cofactor were to be included in the simulations. In such scenarios, rare event methods utilizing MD simulations become crucial. Our study demonstrates that MD simulations can yield reasonable rate constants, even when using ab-initio MD, despite the enormous difference between achievable simulation times and actual reaction times. Recent advances in potential energy models, including reactive force fields[29], neural network potentials[30], semi-empirical electronic structure methods[31–33] and QM/MM approaches[34], make it increasingly feasible to model complex reaction dynamics using MD. Coupled with rate theory and enhanced sampling techniques, MD is now applicable to a broader array of processes, including reactions in complex solvent environments[149], enzyme catalysis[150, 151] or polymer rearrangement[152].

Not all methods are straightforward to apply, however, with methods based in effective dynamics proving highly sensitive to the choice of reaction coordinate. An intuitive one-dimensional reaction coordinate, even with clear timescale separation and a well-defined distinction among reactant, transition, and product states, was ultimately inadequate; rate estimates differed by several orders of magnitude from those obtained via numerical simulation. While optimized reaction coordinates yielded more accurate rates, identifying reliable candidates is nontrivial. Various methods have been developed to address this[23,89,153–155]. Infrequent metadynamics also faces limitations in more complex systems, particularly where slow processes occur orthogonal to the biased coordinate[85, 122] or where the reactant state exhibits multiple subminima[156, 157]. Grid-based methods offer a promising alternative, supporting multidimensional effective dynamics and producing rates very close to those from numerical simulation.

While this study primarily focuses on infrequent metadynamics and effective dynamics-based methods, other rate methods are valuable for capturing complex reaction dynamics.

One notable example is Variational Transition State Theory (VTST)[158, 159], an extension of TST that refines the transition state by minimizing the reaction rate, thereby adapting the dividing surface to better match the true dynamic behavior of the system. Methods based on the generalized Langevin equation[38] including Grote-Hynes (GH) theory[160] address another limitation of TST. New approaches[161, 162] incorporate the effects of friction and solvent dynamics by introduction of a memory kernel, allowing more accurate modeling of rates in condensed phases and in systems where environmental interactions significantly impact the barrier crossing. Other approaches, such as transition path sampling (TPS)[14, 78] and weighted ensemble (WE)[163, 164] methods are useful for reactions with long timescales and complex intermediates, as they emphasize the sampling of critical reaction paths and weighted trajectory segments. Finally, reactive flux (RF)[79,165] methods account for recrossing corrections by refining the initial TST rate calculation, improving accuracy in dynamic environments where barrier crossing events are prevalent. Furthermore, quantum effect such as tunneling and zero-point energy are not incorporated in classical MD methods, but can significantly impact rates in reactions involving light atoms, low temperatures or narrow barriers. Quantum dynamics approaches like ring polymer molecular dynamics (RPMD)[166,167] allow more explicit treatment of quantum behavior, though at higher computational cost.

Part B The second part of the thesis focuses on Girsanov reweighting, a technique that allows for the estimation of dynamical properties at a target potential from trajectories simulated at a different, simulation potential. This method is particularly useful for accelerating the sampling of rare events. The research investigates the applicability of Girsanov reweighting for various integrators from splitting methods for underdamped Langevin dynamics, a common framework for MD simulations at constant temperature. By analyzing the image of update operators for the integrators, the study establishes conditions for absolute continuity, ensuring that any path possible at the target potential is also possible at the simulation potential. This ensures that the reweighting is valid and can be reliably used to estimate dynamical properties at the target potential. The study formulates a general method for deriving computable expressions for relative path probabilities of various integrators using the reweighting-on-the-fly approach. It could be extended to other splitting methods such as stochastic position Verlet (SPV)[168] and stochastic velocity Verlet (SVV)[168].

The reweighting expressions for various integrators are tested through MD simulations of a $[\text{Ca-Cl}]^+$ dimer in aqueous solvent. By comparing dissociation rates obtained from simulations at an unbiased potential with those reweighted from biased simulations, we confirm that Girsanov reweighting can accurately recover unbiased rates. This is evident across various integrators, with reweighted rates consistently within 8-10 % of the reference rates, despite the simulation potential displaying dissociation rates approximately 2.3 times higher. These findings validate the reliability of Girsanov reweighting in recovering true dissociation rates and underscore its potential for enhancing the efficiency of molecular dynamics simulations.

Overall, this thesis underscores the challenges and complexities associated with estimating reaction rates for rare events using MD simulations. While traditional methods like TST provide valuable benchmarks, enhanced sampling techniques and reweighting methods have the potential to offer significant improvements in applicability, accuracy and efficiency. The insights gained from retinal isomerization studies demonstrate the capacity of MD simulations in combination with enhanced sampling techniques to yield accurate rate constants, even when achievable simulation times and actual reaction times are substantially different. This emphasizes the potential of these methods in a wide range of applications. Furthermore, the importance of the choice of reaction coordinates to capture the full dynamics of complex processes is highlighted. The development of Girsanov reweighting formulations for underdamped Langevin dynamics addresses a critical need for reliable reweighting in MD simulations, enabling more accurate estimations of dynamical properties.

Appendix A

Derivations for the Reactive Flux Formalisms

A.1 Derivation of Linear Rate Relation from Onsager's Regression Hypothesis

The linear relationship between the correlation function in Eq. 2.43 and the microscopic rate can be derived from a more fundamental principle called *Onsager's regression hypothesis*. The regression hypothesis states the relaxation of macroscopic nonequilibrium disturbances is governed by the same laws as the regression of spontaneous microscopic fluctuations in an equilibrium system[4]. It is assumed that nonequilibrium disturbances are in the linear regime, that is, that deviations from equilibrium are linearly related to the perturbations that move the system away from equilibrium. This is in most cases a good approximation for nonequilibrium deviations which remain close to or slightly removed from equilibrium[4]. Onsager's regression hypothesis can be considered a special formulation of the so-called *fluctuation-dissipation theorem.*

For a general dynamical variable $X(t) = X(\mathbf{q}(t), \mathbf{p}(t))$, spontaneous fluctuations at equilibrium are denoted as

$$\delta X(t) = X(t) - \langle X \rangle \ . \tag{A.1}$$

While the fluctuations themselves are expected to average out at equilibrium conditions, i.e. $\langle \delta X(t) \rangle = 0$, one can obtain important information on the dynamics of the system by studying equilibrium correlations between the fluctuations, i.e. $\langle \delta X(t) \delta X(0) \rangle$ for correlations at a time t. More specifically, the regression hypothesis relates decay of these correlations to nonequilibrium relaxation. Say $X(t)$ has been prepared in a nonequilibrium state at $t = 0$. According to the regression hypothesis, relaxation can be written down mathematically as

$$\frac{\Delta \bar{X}(t)}{\Delta \bar{X}(0)} = \frac{\langle \delta X(0) \delta X(t) \rangle}{\left\langle (\delta X(0))^2 \right\rangle} \tag{A.2}$$

where $\Delta \bar{X}(t) = \langle X(t) \rangle_{\text{ne}} - \langle X \rangle$ is the average nonequilibrium decay to equilibrium. The regression hypothesis thus proposes an equivalence between relaxation from spontaneous fluctuations from equilibrium on one hand (right side of Eq. A.2) and deviations that have been externally prepared on the other hand (left side of Eq. A.2).

Onsager's regression hypothesis can be applied to a two-state reaction A $\rightleftharpoons$ B by making use of the occupation functions defined in Eq. 2.38. Inserting $h_A(t)$ as dynamical variable in Eq. A.2, we obtain

$$\frac{\langle h_A(t) \rangle_{\text{ne}} - \langle h_A \rangle}{\langle h_A(0) \rangle_{\text{ne}} - \langle h_A \rangle} = \frac{\langle \delta h_A(0) \delta h_A(t) \rangle}{\left\langle (\delta h_A(0))^2 \right\rangle} \,. \tag{A.3}$$

Assuming separation of timescales ($\tau_{\text{mol}} \ll \tau_{\text{rxn}}$), the nonequilibrium relaxation is expected to follow the linear rate laws of Section 2.3.1, for which solutions were given in Eq. 2.40. Comparing to the left hand side of Eq. A.3, we can write

$$\exp(-kt) = \frac{\langle \delta h_A(0) \delta h_A(t) \rangle}{\left\langle (\delta h_A(0))^2 \right\rangle} \qquad \text{for} \qquad t > \tau_{\text{mol}} \,. \tag{A.4}$$

This is a remarkable result, as the phenomenological rate k is written directly in terms of microscopic equilibrium correlation functions, allowing us to compute macroscopic rate constants directly from microscopic equilibrium dynamics such as the dynamics obtained from molecular dynamics simulations. Notice the exponential relation will only hold for times larger than the molecular relaxation time, i.e. for $t > \tau_{\text{mol}}$, since for smaller times the correlation functions on the right-hand side will represent correlations in microscopic motions including recrossings from state B to A before committing to one of the two states[14]. The right-hand side can be rewritten as

$$\frac{\langle \delta h_A(0) \delta h_A(t) \rangle}{\left\langle (\delta h_A(0))^2 \right\rangle} = \frac{\langle h_A(0) h_A(t) \rangle - \langle h_A \rangle^2}{\langle h_A \rangle - \langle h_A \rangle^2} \tag{A.5a}$$

$$= \frac{\langle h_A(0)\left(1 - h_B(t)\right) \rangle - \langle h_A \rangle^2}{\langle h_A \rangle \left(1 - \langle h_A \rangle\right)} \tag{A.5b}$$

$$= \frac{\langle h_A \rangle - \langle h_A(0) h_B(t) \rangle - \langle h_A \rangle^2}{\langle h_A \rangle \langle h_B \rangle} \tag{A.5c}$$

$$= \frac{\langle h_A \rangle \left(1 - \langle h_A \rangle\right)}{\langle h_A \rangle \langle h_B \rangle} - \frac{\langle h_A(0) h_B(t) \rangle}{\langle h_A \rangle \langle h_B \rangle} \tag{A.5d}$$

$$= 1 - \frac{\langle h_A(0) h_B(t) \rangle}{\langle h_A \rangle \langle h_B \rangle} \tag{A.5e}$$

where we have used the fact that $h_A^2(t) = h_A(t)$ and $h_B(t) = 1 - h_A(t)$. Combining and rearranging yields

$$C_{AB}(t) \equiv \frac{\langle h_A(0) h_B(t) \rangle}{\langle h_A \rangle} = \langle h_B \rangle \left[1 - \exp(-kt)\right] \qquad \text{for} \qquad t > \tau_{\text{mol}} \tag{A.6}$$

where $C_{AB}(t)$ corresponds to the time correlation function defined in the reactive flux formalisms of Section 2.3.2. For small times $t \ll \tau_{\mathrm{rxn}}$ where $\tau_{\mathrm{rxn}} = 1/k$, the exponential can be approximated by its first-order expansion $\exp(-kt) \approx 1 - kt$ giving

$$C_{AB}(t) = \langle h_B \rangle kt \qquad \text{for} \qquad \tau_{\mathrm{mol}} < t \ll \tau_{\mathrm{rxn}} \,. \tag{A.7}$$

Using the definition $k = k_{AB} + k_{BA}$ in combination with the detailed balance relation $k_{AB} \langle h_A \rangle = k_{BA} \langle h_B \rangle$, this can be rewritten in terms of microscopic rates:

$$C_{AB}(t) = k_{AB} t \qquad \text{for} \qquad \tau_{\mathrm{mol}} < t \ll \tau_{\mathrm{rxn}} \tag{A.8}$$

and equivalent for $k_{BA}t$.

A.2 Time Derivation of the Correlation Function

The reactive flux is defined as the time derivative of the time correlation function

$$k_{AB}^{\mathrm{RF}}(t) = \frac{\mathrm{d}}{\mathrm{d}t} C_{AB}(t) = \frac{\mathrm{d}}{\mathrm{d}t} \frac{\langle h_A(0) h_B(t) \rangle}{\langle h_A \rangle} \,. \tag{A.9}$$

In principle the time derivative can be brought into the ensemble averaging directly giving $\left\langle h_A(0) \dot{h}_B(t) \right\rangle / \langle h_A \rangle$ where the dot indicates a time derivative. One could then continue from there by expressing the time derivation of $h_B(t)$ directly. We end up with a more intuitive expression, however, if we first shift the time back according to $t' \to t' - t$ for any time t'. At equilibrium conditions, a constant time shift should not influence the correlation functions, and consequently

$$k_{AB}^{\mathrm{RF}}(t) = \frac{\mathrm{d}}{\mathrm{d}t} \frac{\langle h_A(-t) h_B(0) \rangle}{\langle h_A \rangle} = -\frac{\left\langle \dot{h}_A(-t) h_B(0) \right\rangle}{\langle h_A \rangle} \tag{A.10}$$

where the minus sign appears because generally $\frac{\mathrm{d}}{\mathrm{d}x}[f(-x)] = -\frac{\mathrm{d}f}{\mathrm{d}x}(-x)$. Remember the dependence of the occupation functions on time is implicit, $h_A(t) = h_A(s(t))$. Consequently, the chain rule has to be used to express the time derivative

$$\dot{h}_A(t) = \frac{\mathrm{d}}{\mathrm{d}t} h_A(s(t)) = \dot{s}(t) \frac{\mathrm{d}}{\mathrm{d}s} h_A(s(t)) = -\dot{s}(t) \delta\left(s(t) - s^\ddagger\right) \tag{A.11}$$

where $\delta(s)$ is the Dirac delta function. Filling in in Eq.A.10 yields

$$k_{AB}^{\mathrm{RF}}(t) = \frac{\left\langle \dot{s}(-t) \delta\left(s(-t) - s^\ddagger\right) h_B(0) \right\rangle}{\langle h_A \rangle} \,. \tag{A.12}$$

After shifting back time $t' \to t' + t$ the expression in Eq. 2.45 is obtained:

$$k_{AB}^{\mathrm{RF}}(t) = \frac{\left\langle \dot{s}(0) \delta\left(s(0) - s^\ddagger\right) h_B(t) \right\rangle}{\langle h_A \rangle} \,. \tag{A.13}$$

A.3 From the Reactive Flux Formalism to Transition State Theory

A relatively simple and commonly used expression for the rate constant can be formulated in the transition state theory (TST) framework introduced in Section 2.3.4. In TST, two additional assumptions are added starting from the reactive flux formulations:

3. States on the dividing surface are populated as though at equilibrium with reactants
4. Trajectories that cross the dividing surface lead directly to products with no recrossing events

The numbering has been copied to comply with the complete list of assumptions made in TST listed in Section 2.3.4.

The fourth assumption is introduced by considering the limit of $t \to 0+$ in the reactive flux formulation. Evaluating the reactive flux $k_{AB}^{\mathrm{RF}}(t)$ in this limit corresponds to assigning the end state (either B or A) of any trajectory initiated at the transition state by evaluating which state it is in an infinitesimal time interval later, i.e. by evaluating $h_B(t \to 0+)$ in Eq. A.13. In other words, a trajectory at the transition state at time $t = 0$ going towards product state B at that time is assumed to lead directly to the product state and relax there without recrossing. For trajectories initiated at the transition state, the state at an infinitesimal time later is perfectly determined by the initial velocity along s[4,6]. If $\dot{s}(0) > 0$, the trajectory ends up in B and $h_B(t \to 0+) = 1$, whereas if $\dot{s}(0) < 0$, the trajectory ends up in A and $h_B(t \to 0+) = 0$. Consequently, the numerator of the reactive flux in Eq. A.13 will be

$$\left\langle \dot{s}(0)\delta\left(s(0) - s^{\ddagger}\right) h_B(t \to 0+)\right\rangle = \begin{cases} \left\langle \dot{s}(0)\delta\left(s(0) - s^{\ddagger}\right)\right\rangle & \text{if} \quad \dot{s}(0) > 0 \\ 0 & \text{if} \quad \dot{s}(0) < 0 \end{cases} \tag{A.14}$$

Finally, the third assumption is introduced to further simplify this expression. Assuming the transition state is at thermal equilibrium with the reactant state, the ensemble distribution of $\dot{s}$ at the dividing surface corresponds to the Maxwell-Boltzmann distribution (Eq. 2.7) and thus is even around zero. Furthermore, thermal equilibrium predicts distributions of position s and velocity $\dot{s}$ are uncorrelated. Consequently, the numerator can be rewritten as

$$\left\langle \dot{s}(0)\delta\left(s(0) - s^{\ddagger}\right) h_B(t \to 0+)\right\rangle = \left\langle \frac{1}{2}\left|\dot{s}\right|\right\rangle_{\ddagger} \left\langle \delta\left(s(0) - s^{\ddagger}\right)\right\rangle \tag{A.15}$$

where $\langle \dots \rangle_{\ddagger}$ denotes an ensemble average over all points on the dividing surface, i.e. where

s is constrained at $s^\ddagger$. The reactive flux in the limit $t \to 0+$ can then be written as

$$k_{AB}^{\mathrm{RF}}(t \to 0+) = \frac{1}{2} \left\langle |\dot{s}| \right\rangle_\ddagger \frac{\left\langle \delta\left(s(0) - s^\ddagger\right)\right\rangle}{\left\langle h_A \right\rangle} \tag{A.16}$$

$$= \frac{1}{2} \left\langle |\dot{s}| \right\rangle_\ddagger \frac{\exp\left(-\beta F(s^\ddagger)\right)}{\exp\left(-\beta F_A\right)} \tag{A.17}$$

$$= \frac{1}{2} \left\langle |\dot{s}| \right\rangle_\ddagger \exp\left(-\beta \Delta F^\ddagger\right) . \tag{A.18}$$

This is the TST rate k_{AB}^{TST} in Eq. 2.59.

Appendix B

Rate and Transition Matrices

B.1 Spectral Decomposition of the Transition Matrix

The transition matrix can, as any diagonalizable matrix, be written as a linear combination of the left eigenvectors, right eigenvectors and eigenvalues:

$$\mathbf{T}(\tau) = \sum_{i=0}^{n_c-1} \lambda_i(\tau)\mathbf{l}^{(i)} \left(\mathbf{r}^{(i)}\right)^T \tag{B.1}$$

where $\mathbf{l}^{(i)} \in \mathbb{R}^{n_c}\,\forall i = 0,\ldots,n_c-1$ are the left eigenvectors, $\mathbf{r}^{(i)} \in \mathbb{R}^{n_c}\,\forall i = 0,\ldots,n_c-1$ the right eigenvalues and $\lambda_i(\tau)$ the eigenvalues of transition matrix $\mathbf{T}(\tau)$. The eigenvalue decomposition, also called the spectral decomposition, can be considered a principle component analysis of the dynamics, where the principle modes (the eigenvectors with the largest eigenvalues) represent the main modes of probability flow between the system's metastable substates. The magnitudes of the corresponding eigenvalues express how slow or fast the probability flow occurs. Because the transition matrix is a row-stochastic matrix[169], it always has one eigenvalue which is equal to one, with all other eigenvalues guaranteed to be smaller, $1 = \lambda_0 > |\lambda_1| \geq |\lambda_2| \geq \cdots \geq |\lambda_{n_c-1}| \geq 0$. For dynamics satisfying the detailed balance condition, the left and right eigenvectors are related by the stationary distribution[105, 106]

$$\mathbf{l}^{(i)} = \mathrm{diag}\left(\boldsymbol{\pi}\right)\mathbf{r}^{(i)} \quad \forall i\,, \tag{B.2}$$

and are orthogonal to one other

$$\mathbf{l}^{(i)} \cdot \mathbf{r}^{(j)} = \left(\mathbf{l}^{(i)}\right)^T \mathbf{r}^{(j)} = \delta_{i,j} \quad \forall i,j\,. \tag{B.3}$$

For the case of repeated application of the transition matrix to predict propagation over a time $a\tau$, the matrix power in Eq. 2.51 can thus be written as

$$\mathbf{T}^a(\tau) = \sum_{i=0}^{n_c-1} [\lambda_i(\tau)]^a \, \mathbf{l}^{(i)} \left(\mathbf{r}^{(i)}\right)^T . \tag{B.4}$$

Since for $i \neq 0$ all eigenvalues $|\lambda_i| < 1$, the factors $[\lambda_i(\tau)]^a$ for $i \neq 0$ will decay to zero exponentially for increasing value of a. For exponential decay, the lifetime t_i is defined as the time it takes for the population to reduce by a factor $1/e$. This happens at a value of a where $[\lambda_i(\tau)]^a = 1/e$ or, in other words where $a = -1/\ln\lambda_i(\tau)$. The corresponding propagation time necessary to reduce the population by $1/e$ is the process lifetime

$$t_i = a\tau = -\frac{\tau}{\ln\lambda_i(\tau)} \tag{B.5}$$

which is the definition of the implied timescale of the process also given in Eq. 2.52. Raising the eigenvalue $\lambda_0 = 1$ to the power a does not change the weight of the corresponding process, and thus for high values of a the term for $i = 0$ will be the only one remaining. The eigenvectors for $i = 0$ hence represent the stationary process, with $\mathbf{l}^{(0)} = \boldsymbol{\pi}$ while $\mathbf{r}^{(0)}$ is a vector where every element is one. As a result, applying Eq. 2.51 to any starting distribution $\boldsymbol{\rho}(0)$ will yield $\boldsymbol{\pi}$ as $a \to \infty$.

B.2 Rate and Transition Matrix for the Two-State System

For a two-state system and assuming Markovianity, the rate matrix $\mathbf{Q}$ is written as[102]

$$\mathbf{Q} = \begin{pmatrix} -k_{AB} & k_{AB} \\ k_{BA} & -k_{BA} \end{pmatrix} . \tag{B.6}$$

The eigenvalues of $\mathbf{Q}$ are $\theta_0 = 0$ and $\theta_1 = -(k_{AB} + k_{BA}) = -k$ with k the phenomenological rate constant introduced in Section 2.3.1. Using Eq. 2.53, the first implied timescale is

$$t_1 = -\frac{1}{\theta_1} = \frac{1}{k} = \tau_{\text{rxn}} \tag{B.7}$$

where τ_{rxn} is the reaction time introduced in Section 2.3.1. For a two state system under Markovian conditions, the first implied timescale thus corresponds to the reaction time. The eigenvalues of the transition matrix $\mathbf{T}(\tau) = \exp(\tau\mathbf{Q})$ are $\lambda_0 = 1$ and $\lambda_1 = \exp(-k\tau)$.

Bibliography

[1] D. Frenkel and B. Smit, Understanding molecular simulation: from algorithms to applications. Elsevier, 2023.

[2] A. R. Leach, Molecular Modelling: Principles and Applications. Pearson Education, 2001.

[3] B. Leimkuhler and C. Matthews, Molecular Dynamics: With Deterministic and Stochastic Numerical Methods. Springer International Publishing, 2015.

[4] D. Chandler, Introduction to Modern Statistical Mechanics. Oxford University Press, 1987.

[5] B. Roux, Computational Modeling and Simulations of Biomolecular Systems. World Scientific, 2021.

[6] B. Peters, Reaction Rate Theory and Rare Events. Elsevier, 2017.

[7] C. Dellago and P. G. Bolhuis, “Transition path sampling and other advanced simulation techniques for rare events,” Advanced computer simulation approaches for soft matter sciences III, pp. 167–233, 2009.

[8] P. Hänggi, P. Talkner, and M. Borkovec, “Reaction-rate theory: fifty years after Kramers,” Rev. Mod. Phys., vol. 62, no. 2, p. 251, 1990.

[9] G. Henkelman, B. P. Uberuaga, and H. Jónsson, “A climbing image nudged elastic band method for finding saddle points and minimum energy paths,” J. Chem. Phys., vol. 113, no. 22, pp. 9901–9904, 2000.

[10] C. Peng and B. H. Schlegel, “Combining synchronous transit and quasi-newton methods to find transition states,” Isr. J. Chem., vol. 33, no. 4, pp. 449–454, 1993.

[11] J. Hénin, T. Lelièvre, M. Shirts, O. Valsson, and L. Delemotte, “Enhanced sampling methods for molecular dynamics simulations [article v1. 0],” LiveCoMS, vol. 4, no. 1, pp. 1583–1583, 2022.

[12] L. Maragliano, A. Fischer, E. Vanden-Eijnden, and G. Ciccotti, “String method in collective variables: Minimum free energy paths and isocommittor surfaces,” J. Chem. Phys., vol. 125, no. 2, p. 024106, 2006.

[13] D. Branduardi, F. L. Gervasio, and M. Parrinello, "From A to B in free energy space," J. Chem. Phys., vol. 126, no. 5, p. 054103, 2007.

[14] P. G. Bolhuis, D. Chandler, C. Dellago, and P. L. Geissler, "Transition path sampling: Throwing ropes over rough mountain passes, in the dark," Annu. Rev. Phys. Chem., vol. 53, no. 1, pp. 291–318, 2002.

[15] K. Schulten and S. Hayashi, "Quantum biology of retinal," in Quantum Effects in Biology, pp. 237–263, Cambridge University Press, 2014.

[16] R. R. Birge, "Nature of the primary photochemical events in rhodopsin and bacteriorhodopsin," Biochim. Biophys. Acta, vol. 1016, no. 3, pp. 293–327, 1990.

[17] P. Tavan, K. Schulten, and D. Oesterhelt, "The effect of protonation and electrical interactions on the stereochemistry of retinal Schiff bases," Biophys. J., vol. 47, no. 3, pp. 415–430, 1985.

[18] A. Hermone and K. Kuczera, "Free-energy simulations of the retinal cis→trans isomerization in bacteriorhodopsin," Biochemistry, vol. 37, no. 9, pp. 2843–2853, 1998.

[19] R. Hubbard, "The stereoisomerization of 11-cis-retinal," J. Biol. Chem., vol. 241, no. 8, pp. 1814–1818, 1966.

[20] Y. Koyama, K. Kubo, M. Komori, H. Yasuda, and Y. Mukai, "Effect of protonation on the isomerization properties of n-butylamine Schiff base of isomeric retinal as revealed by direct HPLC analyses: Selection of isomerization pathways by retinal proteins," Photochem. Photobiol., vol. 54, no. 3, pp. 433–443, 1991.

[21] J. Kuhne, J. Vierock, S. A. Tennigkeit, M.-A. Dreier, J. Wietek, D. Petersen, K. Gavriljuk, S. F. El-Mashtoly, P. Hegemann, and K. Gerwert, "Unifying photocycle model for light adaptation and temporal evolution of cation conductance in Channelrhodopsin-2," PNAS, vol. 116, no. 19, pp. 9380–9389, 2019.

[22] B. G. Keller and P. G. Bolhuis, "Dynamical reweighting for biased rare event simulations," Annu. Rev. Phys. Chem, vol. 75, no. 1, pp. 137–162, 2024.

[23] I. V. Girsanov, "On transforming a certain class of stochastic processes by absolutely continuous substitution of measures," Theory Probab. Appl., vol. 5, no. 3, pp. 285–301, 1960.

[24] B. Øksendal and B. Øksendal, Stochastic differential equations. Springer, 2003.

[25] A. B. Adib, "Stochastic actions for diffusive dynamics: Reweighting, sampling, and minimization," J. Phys. Chem. B., vol. 112, no. 19, pp. 5910–5916, 2008.

[26] L. Donati, C. Hartmann, and B. G. Keller, "Girsanov reweighting for path ensembles and Markov state models," J. Chem. Phys., vol. 146, no. 24, p. 244112, 2017.

[27] S. Kieninger and B. G. Keller, "Path probability ratios for Langevin dynamics—Exact and approximate," J. Chem. Phys., vol. 154, no. 9, p. 094102, 2021.

[28] H. Eyring, "The activated complex in chemical reactions," J. Chem. Phys., vol. 3, no. 2, pp. 107–115, 1935.

[29] T. P. Senftle, S. Hong, M. M. Islam, S. B. Kylasa, Y. Zheng, Y. K. Shin, C. Junkermeier, R. Engel-Herbert, M. J. Janik, H. M. Aktulga, et al., "The ReaxFF reactive force-field: development, applications and future directions," Npj Comput. Mater., vol. 2, no. 1, pp. 1–14, 2016.

[30] P. Gkeka, G. Stoltz, A. Barati Farimani, Z. Belkacemi, M. Ceriotti, J. D. Chodera, A. R. Dinner, A. L. Ferguson, J.-B. Maillet, H. Minoux, et al., "Machine learning force fields and coarse-grained variables in molecular dynamics: application to materials and biological systems," J. Chem. Theory Comput., vol. 16, no. 8, pp. 4757–4775, 2020.

[31] M. Gaus, Q. Cui, and M. Elstner, "DFTB3: Extension of the self-consistent-charge density-functional tight-binding method (SCC-DFTB)," J. Chem. Theory Comput., vol. 7, no. 4, pp. 931–948, 2011.

[32] P. Pracht, F. Bohle, and S. Grimme, "Automated exploration of the low-energy chemical space with fast quantum chemical methods," Phys. Chem. Chem. Phys., vol. 22, no. 14, pp. 7169–7192, 2020.

[33] R. Schade, T. Kenter, H. Elgabarty, M. Lass, T. D. Kühne, and C. Plessl, "Breaking the exascale barrier for the electronic structure problem in ab-initio molecular dynamics," Int. J. High Perform. Comput. Appl., vol. 37, no. 5, pp. 530–538, 2023.

[34] H. M. Senn and W. Thiel, "QM/MM methods for biomolecular systems," Angew. Chem. Int. Ed., vol. 48, no. 7, pp. 1198–1229, 2009.

[35] D. J. Tannor, Introduction to Quantum Mechanics: a Time-Dependent Perspective. University Science Books, 2007.

[36] A. Szabo and N. Ostlund, Modern Quantum Chemistry: Introduction to Advanced Electronic Structure Theory. Dover Publications, 2012.

[37] H. Goldstein, Classical Mechanics. Pearson, 2011.

[38] R. Zwanzig, Nonequilibrium Statistical Mechanics. Oxford University Press, 2001.

[39] L. Donati, Reweighting Methods for Molecular Dynamics. PhD thesis, Freie Universität Berlin, 2019.

[40] P. Eastman, J. Swails, J. D. Chodera, R. T. McGibbon, Y. Zhao, K. A. Beauchamp, L.-P. Wang, A. C. Simmonett, M. P. Harrigan, C. D. Stern, et al., "OpenMM 7: Rapid development of high performance algorithms for molecular dynamics," PLoS Comput. Biol., vol. 13, no. 7, p. e1005659, 2017.

[41] M. J. Abraham, T. Murtola, R. Schulz, S. Páll, J. C. Smith, B. Hess, and E. Lindahl, "GROMACS: High performance molecular simulations through multi-level parallelism from laptops to supercomputers," SoftwareX, vol. 1, pp. 19–25, 2015.

[42] G. Bussi and A. Laio, "Using metadynamics to explore complex free-energy landscapes," Nat. Rev. Phys., vol. 2, no. 4, pp. 200–212, 2020.

[43] B. Peters, "Reaction coordinates and mechanistic hypothesis tests," Annu. Rev. Phys. Chem., vol. 67, pp. 669–690, 2016.

[44] H. Risken and T. Frank, The Fokker-Planck Equation: Methods of Solution and Applications. Springer Berlin Heidelberg, 1996.

[45] G. Hummer, "Position-dependent diffusion coefficients and free energies from Bayesian analysis of equilibrium and replica molecular dynamics simulations," New J. Phys., vol. 7, no. 1, p. 34, 2005.

[46] A. Berezhkovskii and A. Szabo, "One-dimensional reaction coordinates for diffusive activated rate processes in many dimensions," J. Chem. Phys., vol. 122, no. 1, p. 014503, 2005.

[47] B. Peters, P. G. Bolhuis, R. G. Mullen, and J.-E. Shea, "Reaction coordinates, one-dimensional Smoluchowski equations, and a test for dynamical self-consistency," J. Chem. Phys., vol. 138, no. 5, p. 054106, 2013.

[48] K. Palacio-Rodriguez and F. Pietrucci, "Free energy landscapes, diffusion coefficients, and kinetic rates from transition paths," J. Chem. Theory Comput., vol. 18, no. 8, pp. 4639–4648, 2022.

[49] S. Jungblut and C. Dellago, "Pathways to self-organization: Crystallization via nucleation and growth," Eur. Phys. J. E, vol. 39, pp. 1–38, 2016.

[50] B. C. Knott, N. Duff, M. F. Doherty, and B. Peters, "Estimating diffusivity along a reaction coordinate in the high friction limit: Insights on pulse times in laser-induced nucleation," J. Chem. Phys., vol. 131, no. 22, p. 224112, 2009.

[51] W. Im and B. Roux, "Ions and counterions in a biological channel: a molecular dynamics simulation of OmpF porin from Escherichia coli in an explicit membrane with 1 M KCl aqueous salt solution," J. Mol. Biol., vol. 319, no. 5, pp. 1177–1197, 2002.

[52] F. Sicard, V. Koskin, A. Annibale, and E. Rosta, "Position-dependent diffusion from biased simulations and Markov state model analysis," J. Chem. Theory Comput., vol. 17, no. 4, pp. 2022–2033, 2021.

[53] G. D. Leines and B. Ensing, "Path finding on high-dimensional free energy landscapes," Phys. Rev. Lett., vol. 109, no. 2, p. 020601, 2012.

[54] G. M. Torrie and J. P. Valleau, "Nonphysical sampling distributions in Monte Carlo free-energy estimation: Umbrella sampling," J. Comput. Phys., vol. 23, no. 2, pp. 187–199, 1977.

[55] A. Laio and M. Parrinello, "Escaping free-energy minima," PNAS, vol. 99, no. 20, pp. 12562–12566, 2002.

[56] G. Ciccotti and M. Ferrario, "Blue moon approach to rare events," Mol. Simul., vol. 30, no. 11-12, pp. 787–793, 2004.

[57] H. Grubmüller, "Predicting slow structural transitions in macromolecular systems: Conformational flooding," Phys. Rev. E., vol. 52, no. 3, p. 2893, 1995.

[58] T. Huber, A. E. Torda, and W. F. Van Gunsteren, "Local elevation: a method for improving the searching properties of molecular dynamics simulation," J. Comput. Aided Mol. Des., vol. 8, no. 6, pp. 695–708, 1994.

[59] S. Kumar, J. M. Rosenberg, D. Bouzida, R. H. Swendsen, and P. A. Kollman, "The weighted histogram analysis method for free-energy calculations on biomolecules. I. the method," J. Comput. Chem., vol. 13, no. 8, pp. 1011–1021, 1992.

[60] G. Bussi and G. A. Tribello, "Analyzing and biasing simulations with PLUMED," in Biomolecular Simulations, pp. 529–578, Springer, 2019.

[61] Z. Tan, E. Gallicchio, M. Lapelosa, and R. M. Levy, "Theory of binless multi-state free energy estimation with applications to protein-ligand binding," J. Chem. Phys., vol. 136, no. 14, p. 04B608, 2012.

[62] J. Kästner and W. Thiel, "Analysis of the statistical error in umbrella sampling simulations by umbrella integration," J. Chem. Phys., vol. 124, no. 23, p. 234106, 2006.

[63] B. Efron, The Jackknife, the Bootstrap and Other Resampling Plans. SIAM, 1982.

[64] J. S. Hub, B. L. De Groot, and D. Van Der Spoel, "g_wham a free weighted histogram analysis implementation including robust error and autocorrelation estimates," J. Chem. Theory Comput., vol. 6, no. 12, pp. 3713–3720, 2010.

[65] A. Barducci, G. Bussi, and M. Parrinello, "Well-tempered metadynamics: a smoothly converging and tunable free-energy method," Phys. Rev. Lett., vol. 100, no. 2, p. 020603, 2008.

[66] J. F. Dama, M. Parrinello, and G. A. Voth, "Well-tempered metadynamics converges asymptotically," Phys. Rev. Lett., vol. 112, no. 24, p. 240602, 2014.

[67] M. Bonomi, A. Barducci, and M. Parrinello, "Reconstructing the equilibrium Boltzmann distribution from well-tempered metadynamics," J. Comput. Chem., vol. 30, no. 11, pp. 1615–1621, 2009.

[68] P. Tiwary and M. Parrinello, "A time-independent free energy estimator for metadynamics," J. Phys. Chem. B., vol. 119, no. 3, pp. 736–742, 2015.

[69] D. Branduardi, G. Bussi, and M. Parrinello, "Metadynamics with adaptive Gaussians," J. Chem. Theory Comput., vol. 8, no. 7, pp. 2247–2254, 2012.

[70] S. Piana and A. Laio, "A bias-exchange approach to protein folding," J. Phys. Chem. B., vol. 111, no. 17, pp. 4553–4559, 2007.

[71] J. Pfaendtner and M. Bonomi, "Efficient sampling of high-dimensional free-energy landscapes with parallel bias metadynamics," J. Chem. Theory Comput., vol. 11, no. 11, pp. 5062–5067, 2015.

[72] E. Weinan, W. Ren, E. Vanden-Eijnden, et al., "Finite temperature string method for the study of rare events," J. Phys. Chem. B, vol. 109, no. 14, pp. 6688–6693, 2005.

[73] M. Bonomi, D. Branduardi, F. L. Gervasio, and M. Parrinello, "The unfolded ensemble and folding mechanism of the C-terminal GB1 β-hairpin," J. Am. Chem. Soc., vol. 130, no. 42, pp. 13938–13944, 2008.

[74] A. Pérez de Alba Ortíz, J. Vreede, and B. Ensing, "The adaptive path collective variable: a versatile biasing approach to compute the average transition path and free energy of molecular transitions," in Biomolecular Simulations, pp. 255–290, Springer, 2019.

[75] D. Wales et al., Energy Landscapes: Applications to Clusters, Biomolecules and Glasses. Cambridge University Press, 2003.

[76] G. Henkelman and H. Jónsson, "A dimer method for finding saddle points on high dimensional potential surfaces using only first derivatives," J. Chem. Phys., vol. 111, no. 15, pp. 7010–7022, 1999.

[77] N. Govind, M. Petersen, G. Fitzgerald, D. King-Smith, and J. Andzelm, "A generalized synchronous transit method for transition state location," Comput. Mater. Sci., vol. 28, no. 2, pp. 250–258, 2003.

[78] C. Dellago, P. G. Bolhuis, and D. Chandler, "On the calculation of reaction rate constants in the transition path ensemble," J. Chem. Phys., vol. 110, no. 14, pp. 6617–6625, 1999.

[79] D. Chandler, "Statistical mechanics of isomerization dynamics in liquids and the transition state approximation," J. Chem. Phys., vol. 68, no. 6, pp. 2959–2970, 1978.

[80] C. H. Bennett, "Molecular dynamics and transition state theory: the simulation of infrequent events," ACS Publications, 1977.

[81] J. B. Anderson, "Predicting rare events in molecular dynamics," Adv. Chem. Phys., vol. 91, pp. 381–432, 1995.

[82] P. E. Smith, B. M. Pettitt, and M. Karplus, "Stochastic dynamics simulations of the alanine dipeptide using a solvent-modified potential energy surface," J. Phys. Chem., vol. 97, no. 26, pp. 6907–6913, 1993.

[83] D. S. Chekmarev, T. Ishida, and R. M. Levy, "Long-time conformational transitions of alanine dipeptide in aqueous solution: Continuous and discrete-state kinetic models," J. Phys. Chem. B., vol. 108, no. 50, pp. 19487–19495, 2004.

[84] C. A. F. De Oliveira, D. Hamelberg, and J. A. McCammon, “Estimating kinetic rates from accelerated molecular dynamics simulations: Alanine dipeptide in explicit solvent as a case study,” J. Chem. Phys., vol. 127, no. 17, p. 11B605, 2007.

[85] M. Salvalaglio, P. Tiwary, and M. Parrinello, “Assessing the reliability of the dynamics reconstructed from metadynamics,” J. Chem. Theory Comput., vol. 10, no. 4, pp. 1420–1425, 2014.

[86] P. G. Bolhuis, C. Dellago, and D. Chandler, “Reaction coordinates of biomolecular isomerization,” PNAS, vol. 97, no. 11, pp. 5877–5882, 2000.

[87] L. Donati and B. G. Keller, “Girsanov reweighting for metadynamics simulations,” J. Chem. Phys., vol. 149, no. 7, p. 072335, 2018.

[88] L. Donati, M. Heida, B. G. Keller, and M. Weber, “Estimation of the infinitesimal generator by square-root approximation,” J. Phys. Condens. Matter, vol. 30, no. 42, p. 425201, 2018.

[89] R. B. Best and G. Hummer, “Reaction coordinates and rates from transition paths,” PNAS, vol. 102, no. 19, pp. 6732–6737, 2005.

[90] F. Noé, C. Schütte, E. Vanden-Eijnden, L. Reich, and T. R. Weikl, “Constructing the equilibrium ensemble of folding pathways from short off-equilibrium simulations,” PNAS, vol. 106, no. 45, pp. 19011–19016, 2009.

[91] W. Du and P. G. Bolhuis, “Sampling the equilibrium kinetic network of Trp-cage in explicit solvent,” J. Chem. Phys., vol. 140, no. 19, p. 05B616_1, 2014.

[92] N. J. Bruce, G. K. Ganotra, D. B. Kokh, S. K. Sadiq, and R. C. Wade, “New approaches for computing ligand–receptor binding kinetics,” Curr. Opin. Struct. Biol., vol. 49, pp. 1–10, 2018.

[93] K. Ahmad, A. Rizzi, R. Capelli, D. Mandelli, W. Lyu, and P. Carloni, “Enhanced-sampling simulations for the estimation of ligand binding kinetics: current status and perspective,” Front. mol. biosci., vol. 9, 2022.

[94] M. Garcia-Viloca, J. Gao, M. Karplus, and D. G. Truhlar, “How enzymes work: analysis by modern rate theory and computer simulations,” Science, vol. 303, no. 5655, pp. 186–195, 2004.

[95] A. Nunes-Alves, D. B. Kokh, and R. C. Wade, “Recent progress in molecular simulation methods for drug binding kinetics,” Curr. Opin. Struct. Biol., vol. 64, pp. 126–133, 2020.

[96] O. K. Dudko, G. Hummer, and A. Szabo, “Theory, analysis, and interpretation of single-molecule force spectroscopy experiments,” PNAS, vol. 105, no. 41, pp. 15755–15760, 2008.

[97] L.-T. Da and J. Yu, “Base-flipping dynamics from an intrahelical to an extrahelical state exerted by thymine DNA glycosylase during DNA repair process,” Nucleic Acids Res., vol. 46, no. 11, pp. 5410–5425, 2018.

[98] S.-D. Wang, R.-B. Zhang, and L. A. Eriksson, "Markov state models elucidate the stability of DNA influenced by the chiral 5S-Tg base," Nucleic Acids Res., vol. 50, no. 16, pp. 9072–9082, 2022.

[99] A. Arjun and P. Bolhuis, "Molecular understanding of homogeneous nucleation of CO2 hydrates using transition path sampling," J. Phys. Chem. B., vol. 125, no. 1, pp. 338–349, 2020.

[100] A. Arjun and P. G. Bolhuis, "Homogeneous nucleation of crystalline methane hydrate in molecular dynamics transition paths sampled under realistic conditions," J. Chem. Phys., vol. 158, no. 4, p. 044504, 2023.

[101] G. T. Beckham and B. Peters, "Optimizing nucleus size metrics for liquid–solid nucleation from transition paths of near-nanosecond duration," J. Phys. Chem. Letters, vol. 2, no. 10, pp. 1133–1138, 2011.

[102] J. D. Chodera, P. J. Elms, W. C. Swope, J.-H. Prinz, S. Marqusee, C. Bustamante, F. Noé, and V. S. Pande, "A robust approach to estimating rates from time-correlation functions," arXiv preprint arXiv:1108.2304, 2011.

[103] L. Onsager, "Reciprocal relations in irreversible processes. I.," Phys. Rev., vol. 37, no. 4, p. 405, 1931.

[104] L. Donati, M. Weber, and B. G. Keller, "Markov models from the square root approximation of the Fokker–Planck equation: calculating the grid-dependent flux," J. Phys. Condens. Matter, vol. 33, no. 11, p. 115902, 2021.

[105] G. Bowman, V. Pande, and F. Noé, An Introduction to Markov State Models and Their Application to Long Timescale Molecular Simulation. Advances in Experimental Medicine and Biology, Springer Netherlands, 2013.

[106] J.-H. Prinz, H. Wu, M. Sarich, B. Keller, M. Senne, M. Held, J. D. Chodera, C. Schütte, and F. Noé, "Markov models of molecular kinetics: Generation and validation," J. Chem. Phys., vol. 134, no. 17, p. 174105, 2011.

[107] W. C. Swope, J. W. Pitera, and F. Suits, "Describing protein folding kinetics by molecular dynamics simulations. 1. Theory," J. Phys. Chem. B., vol. 108, no. 21, pp. 6571–6581, 2004.

[108] S. Röblitz and M. Weber, "Fuzzy spectral clustering by PCCA+: application to Markov state models and data classification," Adv. Data Anal. Classif., vol. 7, pp. 147–179, 2013.

[109] M. Weber, "Implications of PCCA+ in molecular simulation," Computation, vol. 6, no. 1, p. 20, 2018.

[110] G. H. Vineyard, "Frequency factors and isotope effects in solid state rate processes," J. Phys. Chem. Solids, vol. 3, no. 1-2, pp. 121–127, 1957.

[111] W. H. Miller, "Beyond transition-state theory: a rigorous quantum theory of chemical reaction rates," Acc. Chem. Res., vol. 26, no. 4, pp. 174–181, 1993.

[112] J. W. Ochterski, "Thermochemistry in Gaussian," 2000.

[113] S. Ghysbrecht and B. G. Keller, "Thermal isomerization rates in retinal analogues using ab-initio molecular dynamics," J. Comput. Chem., vol. 45, no. 16, pp. 1390–1403, 2024.

[114] J. W. Ochterski, "Vibrational analysis in Gaussian," 1999.

[115] H.-H. Carstensen and A. M. Dean, "Rate constant rules for the automated generation of gas-phase reaction mechanisms," J. Phys. Chem. A, vol. 113, no. 2, pp. 367–380, 2009.

[116] J. Dokic, M. Gothe, J. Wirth, M. V. Peters, J. Schwarz, S. Hecht, and P. Saalfrank, "Quantum chemical investigation of thermal cis-to-trans isomerization of azobenzene derivatives: substituent effects, solvent effects, and comparison to experimental data," J. Phys. Chem. A, vol. 113, no. 24, pp. 6763–6773, 2009.

[117] M. K. Sabbe, M.-F. Reyniers, V. Van Speybroeck, M. Waroquier, and G. B. Marin, "Carbon-centered radical addition and β-scission reactions: modeling of activation energies and pre-exponential factors," ChemPhysChem, vol. 9, no. 1, pp. 124–140, 2008.

[118] L. Pontryagin, A. Andronov, and A. Vitt, "On the statistical investigation of dynamic systems," Zh. Eksp. Teor. Fiz, vol. 3, p. 165, 1933.

[119] A. M. Berezhkovskii and A. Szabo, "Committors, first-passage times, fluxes, Markov states, milestones, and all that," J. Chem. Phys., vol. 150, no. 5, p. 054106, 2019.

[120] P. Tiwary and M. Parrinello, "From metadynamics to dynamics," Phys. Rev. Lett., vol. 111, no. 23, p. 230602, 2013.

[121] A. F. Voter, "Hyperdynamics: Accelerated molecular dynamics of infrequent events," Phys. Rev. Lett., vol. 78, no. 20, p. 3908, 1997.

[122] O. Valsson, P. Tiwary, and M. Parrinello, "Enhancing important fluctuations: Rare events and metadynamics from a conceptual viewpoint," Annu. Rev. Phys. Chem, vol. 67, no. 1, pp. 159–184, 2016.

[123] D. M. Zuckerman and T. B. Woolf, "Dynamic reaction paths and rates through importance-sampled stochastic dynamics," J. Chem. Phys., vol. 111, no. 21, pp. 9475–9484, 1999.

[124] C. Schütte, A. Nielsen, and M. Weber, "Markov state models and molecular alchemy," Mol. Phys., vol. 113, no. 1, pp. 69–78, 2015.

[125] J. A. Izaguirre, C. R. Sweet, and V. S. Pande, "Multiscale dynamics of macromolecules using normal mode Langevin," in Pac. Symp. Biocomput., pp. 240–251, 2010.

[126] P. Bolhuis, Z. Brotzakis, and B. Keller, “Force field optimization by imposing kinetic constraints with path reweighting,” arXiv preprint arXiv:2207.04558, 2022.

[127] K. Shmilovich and A. L. Ferguson, “Girsanov reweighting enhanced sampling technique (GREST): On-the-fly data-driven discovery of and enhanced sampling in slow collective variables,” J. Phys. Chem. A, 2023.

[128] M. Elstner, “The SCC-DFTB method and its application to biological systems,” Theor. Chem. Acc., vol. 116, pp. 316–325, 2006.

[129] C. Lee, W. Yang, and R. G. Parr, “Development of the Colle-Salvetti correlation-energy formula into a functional of the electron density,” Phys. Rev. B, vol. 37, no. 2, p. 785, 1988.

[130] A. D. Becke, “Density-functional exchange-energy approximation with correct asymptotic behavior,” Phys. Rev. A, vol. 38, no. 6, p. 3098, 1988.

[131] W. J. Hehre, R. Ditchfield, and J. A. Pople, “Self-consistent molecular orbital methods. XII. further extensions of Gaussian-type basis sets for use in molecular orbital studies of organic molecules,” J. Chem. Phys., vol. 56, pp. 2257–2261, 1972.

[132] H. Zhou, E. Tajkhorshid, T. Frauenheim, S. Suhai, and M. Elstner, “Performance of the AM1, PM3, and SCC-DFTB methods in the study of conjugated Schiff base molecules,” Chem. Phys., vol. 277, no. 2, pp. 91–103, 2002.

[133] A.-N. Bondar, M. Knapp-Mohammady, S. Suhai, S. Fischer, and J. C. Smith, “Ground-state properties of the retinal molecule: from quantum mechanical to classical mechanical computations of retinal proteins,” Theor. Chem. Acc., vol. 130, pp. 1169–1183, 2011.

[134] N. Elghobashi-Meinhardt, P. Phatak, A.-N. Bondar, M. Elstner, and J. C. Smith, “Catalysis of ground state cis-trans isomerization of bacteriorhodopsin’s retinal chromophore by a hydrogen-bond network,” J. Membr. Biol., vol. 251, no. 3, pp. 315–327, 2018.

[135] E. Malmerberg, Z. Omran, J. S. Hub, X. Li, G. Katona, S. Westenhoff, L. C. Johansson, M. Andersson, M. Cammarata, M. Wulff, et al., “Time-resolved WAXS reveals accelerated conformational changes in iodoretinal-substituted proteorhodopsin,” Biophys. J., vol. 101, no. 6, pp. 1345–1353, 2011.

[136] S. A. Paz and C. F. Abrams, “Testing convergence of different free-energy methods in a simple analytical system with hidden barriers,” Computation, vol. 6, no. 2, p. 27, 2018.

[137] S. Kieninger and B. G. Keller, “GROMACS stochastic dynamics and BAOAB are equivalent configurational sampling algorithms,” J. Chem. Theory Comput., vol. 18, no. 10, pp. 5792–5798, 2022.

[138] B. Leimkuhler and C. Matthews, “Robust and efficient configurational molecular sampling via Langevin dynamics,” J. Chem. Phys., vol. 138, no. 17, 2013.

[139] D. A. Sivak, J. D. Chodera, and G. E. Crooks, "Time step rescaling recovers continuous-time dynamical properties for discrete-time langevin integration of nonequilibrium systems," J. Phys. Chem. B., vol. 118, no. 24, pp. 6466–6474, 2014.

[140] B. Leimkuhler, C. Matthews, and G. Stoltz, "The computation of averages from equilibrium and nonequilibrium Langevin molecular dynamics," IMA J. Numer. Anal., vol. 36, no. 1, pp. 13–79, 2016.

[141] T. Martinek, E. Duboué-Dijon, Š. Timr, P. E. Mason, K. Baxová, H. E. Fischer, B. Schmidt, E. Pluhařová, and P. Jungwirth, "Calcium ions in aqueous solutions: Accurate force field description aided by ab initio molecular dynamics and neutron scattering," J. Chem. Phys., vol. 148, no. 22, p. 222813, 2018.

[142] P. Li and K. M. Merz Jr, "Taking into account the ion-induced dipole interaction in the nonbonded model of ions," J. Chem. Theory Comput., vol. 10, no. 1, pp. 289–297, 2014.

[143] D. A. Case, T. E. Cheatham III, T. Darden, H. Gohlke, R. Luo, K. M. Merz Jr, A. Onufriev, C. Simmerling, B. Wang, and R. J. Woods, "The Amber biomolecular simulation programs," J. Comput. Chem, vol. 26, no. 16, pp. 1668–1688, 2005.

[144] H. W. Horn, W. C. Swope, J. W. Pitera, J. D. Madura, T. J. Dick, G. L. Hura, and T. Head-Gordon, "Development of an improved four-site water model for biomolecular simulations: TIP4P-Ew," J. Chem. Phys., vol. 120, no. 20, pp. 9665–9678, 2004.

[145] P. Li, L. F. Song, and K. M. Merz Jr, "Systematic parameterization of monovalent ions employing the nonbonded model," J. Chem. Theory Comput., vol. 11, no. 4, pp. 1645–1657, 2015.

[146] J. S. Hub, B. L. de Groot, H. Grubmueller, and G. Groenhof, "Quantifying artifacts in Ewald simulations of inhomogeneous systems with a net charge," J. Chem. Theory Comput., vol. 10, no. 1, pp. 381–390, 2014.

[147] P. H. Hünenberger and J. A. McCammon, "Ewald artifacts in computer simulations of ionic solvation and ion–ion interaction: a continuum electrostatics study," J. Chem. Phys., vol. 110, no. 4, pp. 1856–1872, 1999.

[148] G. A. Tribello, M. Bonomi, D. Branduardi, C. Camilloni, and G. Bussi, "PLUMED 2: New feathers for an old bird," Comput. Phys. Commun., vol. 185, no. 2, pp. 604–613, 2014.

[149] H. Zhang, V. Juraskova, and F. Duarte, "Modelling chemical processes in explicit solvents with machine learning potentials," Nat. Commun., vol. 15, no. 1, p. 6114, 2024.

[150] J. D. McGeagh, K. E. Ranaghan, and A. J. Mulholland, "Protein dynamics and enzyme catalysis: insights from simulations," Biochim. Biophys. Acta, vol. 1814, no. 8, pp. 1077–1092, 2011.

[151] D. Platero-Rochart, T. Krivobokova, M. Gastegger, G. Reibnegger, and P. A. Sánchez-Murcia, "Prediction of enzyme catalysis by computing reaction energy barriers via steered qm/mm molecular dynamics simulations and machine learning," J. Chem. Inf. Model., vol. 63, no. 15, pp. 4623–4632, 2023.

[152] N. Shahidi, J. A. Laub, K. D. Vogiatzis, and M. Doxastakis, "Multiscale modeling of vinyl-addition polynorbornenes: The effect of stereochemistry," Polymers, vol. 16, no. 16, p. 2243, 2024.

[153] B. Peters and B. L. Trout, "Obtaining reaction coordinates by likelihood maximization," J. Chem. Phys., vol. 125, no. 5, 2006.

[154] L. Mouaffac, K. Palacio-Rodriguez, and F. Pietrucci, "Optimal reaction coordinates and kinetic rates from the projected dynamics of transition paths," J. Chem. Theory Comput., vol. 19, no. 17, pp. 5701–5711, 2023.

[155] H. Jung, R. Covino, and G. Hummer, "Artificial intelligence assists discovery of reaction coordinates and mechanisms from molecular dynamics simulations," arXiv:1901.04595, 2019.

[156] B. M. Dickson, "Erroneous rates and false statistical confirmations from infrequent metadynamics and other equivalent violations of the hyperdynamics paradigm," J. Chem. Theory Comput., vol. 15, no. 1, pp. 78–83, 2018.

[157] S. A. Khan, B. M. Dickson, and B. Peters, "How fluxional reactants limit the accuracy/efficiency of infrequent metadynamics," J. Chem. Phys., vol. 153, no. 5, 2020.

[158] J. C. Keck, "Variational theory of chemical reaction rates applied to three-body recombinations," J. Chem. Phys., vol. 32, no. 4, pp. 1035–1050, 1960.

[159] D. G. Truhlar and B. C. Garrett, "Variational transition state theory," Annu. Rev. Phys. Chem., vol. 35, no. 1, pp. 159–189, 1984.

[160] R. F. Grote and J. T. Hynes, "The stable states picture of chemical reactions. ii. rate constants for condensed and gas phase reaction models," J. Chem. Phys., vol. 73, no. 6, pp. 2715–2732, 1980.

[161] H. Vroylandt, L. Goudenège, P. Monmarché, F. Pietrucci, and B. Rotenberg, "Likelihood-based non-markovian models from molecular dynamics," PNAS, vol. 119, no. 13, 2022.

[162] C. Ayaz, L. Tepper, F. N. Brünig, J. Kappler, J. O. Daldrop, and R. R. Netz, "Non-markovian modeling of protein folding," PNAS, vol. 118, no. 31, 2021.

[163] G. A. Huber and S. Kim, "Weighted-ensemble brownian dynamics simulations for protein association reactions," Biophys. J., vol. 70, no. 1, pp. 97–110, 1996.

[164] D. M. Zuckerman and L. T. Chong, "Weighted ensemble simulation: review of methodology, applications, and software," Annu. Rev. Biophys., vol. 46, no. 1, pp. 43–57, 2017.

[165] T. S. Van Erp, “Dynamical rare event simulation techniques for equilibrium and nonequilibrium systems,” Adv. Chem. Phys., vol. 151, p. 27, 2012.

[166] I. R. Craig and D. E. Manolopoulos, “Quantum statistics and classical mechanics: Real time correlation functions from ring polymer molecular dynamics,” J. Chem. Phys., vol. 121, no. 8, pp. 3368–3373, 2004.

[167] J. O. Richardson and S. C. Althorpe, “Ring-polymer molecular dynamics rate-theory in the deep-tunneling regime: Connection with semiclassical instanton theory,” J. Chem. Phys., vol. 131, no. 21, 2009.

[168] S. Melchionna, “Design of quasisymplectic propagators for Langevin dynamics,” J. Chem. Phys., vol. 127, no. 4, 2007.

[169] P. Deuflhard, W. Huisinga, A. Fischer, and C. Schütte, “Identification of almost invariant aggregates in reversible nearly uncoupled Markov chains,” Linear Algebra Appl., vol. 315, no. 1-3, pp. 39–59, 2000.